ANALYSIS OF PMM DATA FOR UNDERWATER VEHICLES

Brendon J. Anderson, BSc.

Submitted in fulfilment of the requirements
For the degree of
Master of Engineering Science
University of Tasmania
February 1999

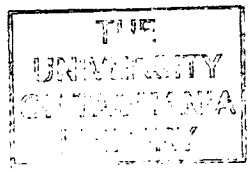

Declaration

The following Thesis contains no material which has been accepted for a degree or diploma by the University or any other institution, except by way of background information and duly acknowledged in the in the Thesis, and to the best of the Candidate's knowledge and belief no material previously published or written by another person except where due acknowledgment is made in the text of the Thesis.

Candidate Signature:  Date: 13 October 1999

Candidate Name: Brendon Anderson

Authority of Access

This thesis may be made available for loan and limited copying in accordance with the Copyright Act 1968.

Candidate Signature:  Date: 13 October 1999

Candidate Name: Brendon Anderson

Abstract

The following thesis studies techniques for determining the manoeuvring performance of unmanned underwater vehicles (UUVs). The use of UUVs is increasing in both commercial and military applications. These craft, which are unmanned, are controlled and powered through an umbilical cable in the case of remotely operated vehicles; for autonomous UUVs, they are powered and controlled from suitable on-board equipment.

Often the expense of operating UUVs over numerous scenarios and environmental conditions restricts opportunities for developing operational use of these craft. Hence the capability to simulate the manoeuvring performance of particular UUVs is desirable.

The development of mathematical models and software functions to simulate a manoeuvring UUV are given in this work. The thesis also addresses the requirement of these mathematical models for hydrodynamic coefficients that characterise a vehicle's performance. Experimental techniques based on planar motion mechanism (PMM) measurements for determining hydrodynamic coefficients are considered here.

The development of a horizontal planar motion mechanism (HPMM) by the Australian Maritime Engineering Cooperative Research Centre (AME) provided the basis for an extensive experimental program. The work reported here includes results from tests on a 1/3rd scale model of the Royal Australian Navy's Mine Disposal Vehicle, PAP104. The HPMM is an electromechanical device that is mounted in either a towing tank or a circulating water channel, enabling scale models to be oscillated in a water flow. Hydrodynamic loads are measured together with the displacement of the model, allowing the hydrodynamic coefficients to be determined.

Techniques are reviewed for the analysis of HPMM data. The Systems Identification technique is developed into software routines that are used to determine hydrodynamic coefficients for the 1/3rd PAP104 model.

Experimental considerations for model testing are discussed together with the equipment and facilities used. Recommendations are proposed for the design of the

model test program, which includes commentary on frequency and blockage related effects that occur with oscillatory testing.

A circulating water channel (CWC) was used in conjunction with the HPMM for the continuous testing of the submerged models. An evaluation of this facility with respect to flow quality is given together with results of the work undertaken to improve the flow uniformity.

Validation data was provided by independent vertical planar motion mechanism tests that were conducted on a full size PAP104 vehicle. These data show good agreement with the results obtained from the HPMM tests conducted on the 1/3rd scale model of the PAP104.

An error analysis was conducted on the experimental procedure and HPMM data analysis method to determine accuracy of individual hydrodynamic coefficients. A sensitivity analysis was also conducted using the UUV simulation to investigate the effect of individual errors in the hydrodynamic coefficients on the navigational accuracy of a manoeuvring UUV.

Acknowledgements

The completion of this piece of work required the support and patience of many individuals to whom I owe my gratitude.

To my wife Liz, for her understanding and patience, especially in the final months where I spent many hours writing the Thesis.

To my supervisors, Dr. Greg Walker of the University of Tasmania, and Dr. Martin Renilson of the Australian Maritime College, for their guidance and encouragement during the course of the work.

To my superiors at the Defence Science & Technology Organisation, Frank May and Janis Cocking, for their support throughout the course of the work, particular during the write up of the Thesis.

To all my friends, family and colleagues, for their encouragement at different stages of the journey.

To the Defence Science & Technology Organisation, Australian Maritime Engineering Collaborative Research Centre, and the Australian Maritime College, for their roles in providing the funding for facilities and travel required to undertake the work.

Nomenclature

a	length of the semi-major axis of an ellipsoid
b, c	lengths of the semi-minor axes of an ellipsoid
fs1, fs2, fs3	flow conditioning screen identifyer
x, y, z	body-fixed coordinate axes
x_B, y_B, z_B	coordinates of centre of buoyancy of body relative to body-fixed origin
x_E, y_E, z_E	earth-fixed coordinate axes
x_G, y_G, z_G	coordinates of centre of gravity of body relative to body-fixed origin
i	components of the velocity potential with values 1,..,6
j,k,l	indices with values 1,2,3
k_1	Lamb's coefficient for a prolate ellipsoid moving in axial flow
k_2	Lamb's coefficient for a prolate ellipsoid moving in a cross-flow
m	body mass
$\overline{m}$	mass of the displaced fluid
m_{11}	added mass of the hull for acceleration in the x-axis direction
$m_{22}^{(2)}(x)$	two dimensional added mass at a point x regarding movement in the Y body axis direction.
$m_{33}^{(2)}(x)$	two dimensional added mass at a point x regarding movement in the Z direction
$m_{44}^{(2)}(x)$	added moment of inertia per unit length at a point x for an axis of rotation parallel to the x-axis through the centre of the added mass $m_{22}^{(2)}(x)$
n	normal vector to the surface

p	propeller pitch
s_b	maximum cross-sectional area of the body
t_i	ith time increment
t_a	axial direction of thruster
t_n	normal direction of thruster
$u,\ v,\ w,\ p,\ q,\ r$	vehicle velocities relative to body axes
	vehicle accelerations relative to body axes
u_r, v_r, w_r	relative velocities of the vehicle to the flow
$\dot{u}_s, \dot{v}_s, \dot{w}_s, \dot{u}_s, \dot{v}_s, \dot{w}_s$	flow accelerations and velocities, relative to body axes
x_{AP}	x-axial position of the aft perpendicular
x_{FP}	x-axial position of the forward perpendicular
$z_s(x)$	z-coordinate of the centre of added mass $m_{22}^{(2)}(x)$
z_{so}	z-coordinate of the wetted hull surface
A	average aperture of a screen wire
A	propeller duct cross sectional area
$\boldsymbol{A}_o$	momentary acceleration of the body at time t_o
$\boldsymbol{A}_i$	acceleration of the body at the ith time increment
B	buoyancy of the body
C_f	friction coefficient
C_r	form drag coefficient
CB	body centre of buoyancy
CG	body centre of gravity
D	diameter of screen wire
D	propeller diameter
$\boldsymbol{D}_{M_i}$	momentum drag of the ith thruster
$\boldsymbol{D}_t$	transformation matrix
$\boldsymbol{F}$	net body force
$\boldsymbol{F}_o$	net body force at initial time, t_o
$\boldsymbol{F}_d$	rigid body kinematic force vector
$\boldsymbol{F}_G$	hydrostatic force vector
$\boldsymbol{F}_H$	hydrodynamic force vector

$\boldsymbol{F}^{(H)}$	hydrodynamic force due to hull
$\boldsymbol{F}^{(HI)}$	hydrodynamic force on the hull due to inviscid components
$\boldsymbol{F}^{(HL)}$	hydrodynamic force on the hull due to lifting foil theory
$\boldsymbol{F}^{(HV)}$	hydrodynamic force on the hull due to viscous flow
$\boldsymbol{F}_P$	hydrodynamic pressure force
$\boldsymbol{F}^{(P)}$	hydrodynamic force due to propeller or propulsors
$\boldsymbol{F}_S$	inertial force vector due to unsteady fluid motion
$\boldsymbol{F}_T$	thruster force vector
$\boldsymbol{F}_U$	umbilical force vector
$\boldsymbol{F}^{(W)}$	hydrodynamic force due to wings and appendages
$I_{xx}, I_{xy}, I_{xz}, I_{yx}, I_{yy}, I_{yz}, I_{zx}, I_{zy}, I_{zz}$	moments and cross products of inertia
K, M, N	components of the net moment along the body axes
$K_{\mathrm{d}}, M_{\mathrm{d}}, N_{\mathrm{d}}$	components of rigid body moment along body axes
K_G, M_G, N_G	components of the hydrostatic moment along body axes
Kt_o	normalised thrust coefficient at zero advance
K	blockage constant
L	length of screen wire
$\boldsymbol{M}$	mass inertia matrix
$\boldsymbol{M}_d$	rigid body moment along body axes
$\boldsymbol{M}_P$	pressure moment acting on surface S
$\boldsymbol{M}_T$	net thrust moment
N	number of apertures in screen wire
OAR	open area ratio of screen wire
O	origin of body fixed axes
$\boldsymbol{R}_B$	position vector of the body's centre of buoyancy
$\boldsymbol{R}_G$	position vector of body centre of gravity from the body-fixed origin
R_n	is the Reynolds number
$\mathrm{Rn}_{\text{free air}}$	Reynolds number in free air
Rn_{exp}	Reynolds number in experiment

Rn_{eff}	effective Reynolds number
$\boldsymbol{R}_t$	position vector of the thruster from the body-fixed origin
S	surface of integration
S_B	surface of the body
T	thrust output magnitude
TF	turbulence factor
$\boldsymbol{U}$	velocity of origin of body axes
$\boldsymbol{U}_G$	velocity of body CG
$\boldsymbol{U}_r$	velocity of the body relative to the flow
$\boldsymbol{U}_s$	fluid velocity relative to body axes
$\boldsymbol{U}_{ta}$	axial flow velocity at the thruster
$\boldsymbol{U}_{tn}$	normal flow velocity at the thruster
V	duct volume
$\boldsymbol{V}_B$	vector in the body fixed coordinate system
$\boldsymbol{V}_E$	vector in the earth fixed coordinate system
$\boldsymbol{V}_i$	velocity vector of the body at the ith time increment
X, Y, Z	components of the net force along the body axes
$\boldsymbol{X}_i$	position vector of the body at the ith time increment
$X_d \quad Y_d \quad Z_d$	components of rigid body force along body axes
X_G, Y_G, Z_G	components of the hydrostatic force along body axes
W	body weight
ϕ	velocity potential
ϕ, θ, ψ	Euler angles; orientation of body relative to earth-fixed axes
$\dot{\phi}, \dot{\theta}, \dot{\psi}$	angular velocities relative to earth-fixed axes
η	propeller efficiency
ρ	density of the fluid
τ	input torque
Ω	angular velocity about body origin
Ω_t	propeller angular velocity

Contents

Chapter 1. Introduction

The use of unmanned underwater vehicles (UUVs) in both commercial and military applications is increasing. These craft are controlled and powered through an umbilical cable in which case they are known as remotely operated vehicles. Alternatively they may be powered and controlled from suitable on-board equipment in which case they are known as autonomous UUVs.

The applications of UUVs includes inspection, payload delivery, surveillance, and reconnaissance. Typically the design for a particular UUV relies on its operational requirements. The designer considers the size and shape of the vehicle, taking into account payload, endurance and manoeuvrability requirements.

The shape of these craft varies significantly, for instance, the shapes may be geometrically similar to long cylinders, boxes, or small spheres. These craft are also provided with a combination of thrusters and control surfaces to propel them, and control their heading and attitude through the undersea environment.

Missions performed by UUVs vary in complexity and duration. Some require skilled operators who are knowledgable about both the environment and the vehicle's operational envelopes. Realistic simulation software is used for operator training in the absence of the vehicle as well as the provision of performance information which in turn enables the development of operational scenarios.

In this thesis techniques for determining the hydrodynamic characteristics and the associated manoeuvring performance of unmanned underwater vehicles (UUVs) are studied. The performance of an underwater vehicle is determined through time domain simulation. An experimental approach for the determination of hydrodynamic coefficients is given.

The development of a horizontal planar motion mechanism (HPMM) by the Australian Maritime Engineering Cooperative Research Centre (AME) provided the basis for an extensive experimental program in this thesis. The HPMM is an electro-mechanical device that can oscillate models suspended in a water flow, in a controlled cyclic manner. Loads on the model are measured concurrently with the angular and positional displacement in the flow. The force and moment data are used to determine the manoeuvring behaviour of the model, which is characterised by 'hydrodynamic coefficients' or 'derivatives'. Two servomotors are used to provide the HPMM motions: one is dedicated to providing translation and the other rotation.

Chapter Two describes a mathematical model for the simulation of an underwater vehicle. The forces acting on a submerged body are given. In particular, the hydrodynamic force is described, with the form of the model given by potential flow theory, which assumes inviscid flow conditions. Forces due to viscous effects are considered separately and are accounted for by additional terms to the inviscid model. Hydrodynamic terms used in addition to the inviscid model are given. The mathematical model is also developed into the software package Uuv6dof using Matlab Version 4 and the Simulink Toolbox.

Chapter Three describes the AME HPMM, the model mounting arrangements, the load cell used in the experiments, the development of the HPMM motion equations and validation of its performance. The development of the motion equations for the HPMM was undertaken as part of the thesis. The validation of the AME HPMM motions is given together with details of the method of analysis.

The Australian Maritime College (AMC) circulating water channel (CWC) was used in conjunction with the HPMM for the continuous testing of the submerged models. Chapter Four contains an evaluation of this facility with respect to flow quality. Methods for improving the flow quality are investigated and several are implemented. The results of this work are also described.

Chapter Five describes the design of an experimental program for the AME HPMM. It describes effects due to changes in frequency of oscillation, blockage and surface roughness of the model on the measured drag values. The requirements for scale

models in the test tank are given, with guidelines developed from the literature. The test program outlines the tests required to determine the inertial properties of the model, and gives the frequency and amplitude of the motions to determine the hydrodynamic properties of the body.

Chapter Six reviews several methods for the analysis of data derived from HPMM tests, including Discrete Analysis, Fourier Integration, Switched Integration and Systems Identification. Each method is developed into software functions and the performance of each is compared. An ideal model of a force is developed and each method is used to identify the coefficients while noise, sampling frequency and data requirements are varied.

Chapter Seven contains experimental results from HPMM tests of the HPMM testing of a 1/3rd scale model of the PAP104. Some validation data is provided by independent vertical planar motion mechanism tests that were conducted on a full size PAP104 vehicle in the United Kingdom.

Chapter Eight describes the errors involved the experimental procedure and HPMM data analysis method. The accuracy of individual hydrodynamic coefficients is given and a sensitivity analysis is conducted using the UUV simulation to investigate the affect of these errors on the simulated performance of the UUV.

Chapter 2. Mathematical Model of a UUV

2.1 Model Form

Mathematical modelling of unmanned underwater vehicles (UUVs) is complex. The dynamics are highly non-linear with cross-coupled terms and, due to the relatively dense nature of the operating environment, must contain expressions for forces due to the fluid and its relative motion (Dand 1985 & 1988, Feldman 1975 & 1979, Gertler 1967, Goheen 1990, Greenshields 1987, Imlay 1961, Lewis 1984, and Newman 1977).

Numerous hydrodynamic characteristics are required to describe the manoeuvring performance of unmanned underwater vehicles . The vehicle body may be bluff and have large regions of separation as a consequence of on-board features such as lights, cameras, sonars and manipulator arms. Such features decrease the ability to simplify the equations of motion, which would be possible if the vehicle was symmetrical. Furthermore, since the vehicles are also frequently required to perform tasks along any of their axes, within the same order of speed, linearising about any one predominant axial motion is not suitable (Dand 1985, Lewis 1984).

The open loop mathematical model of these vehicles is comprised of many components. These include: hydrostatics; rigid body dynamics; hydrodynamics of the hull and any control surfaces; propulsion dynamics from the propellers or propulsors; and for tethered vehicles, the dynamics of the umbilical cable.

The basic geometry of a UUV is modelled as a rigid body, free to move in all six degrees of freedom. The equations of motion for the rigid body are based on Newton's Second Law of Motion. They assume the body is made up of a system of particles that are connected via a massless rigid framework, the distance between each of these particles being fixed during the motions of the body. Equal and opposite reaction forces are formed between the particles which are in equilibrium with each other, they have no influence on the net force (Smart, 1951).

Newton's Second Law of motion states that the net force $\boldsymbol{F}$ acting on a body is proportional to the rate of change of momentum of the centre of gravity of the body, $\boldsymbol{U}_G$. ie.

$$\boldsymbol{F} = m\frac{\mathrm{d}\boldsymbol{U}_G}{\mathrm{dt}} \tag{2.1}$$

where the constant of proportionality is given by the body mass m.

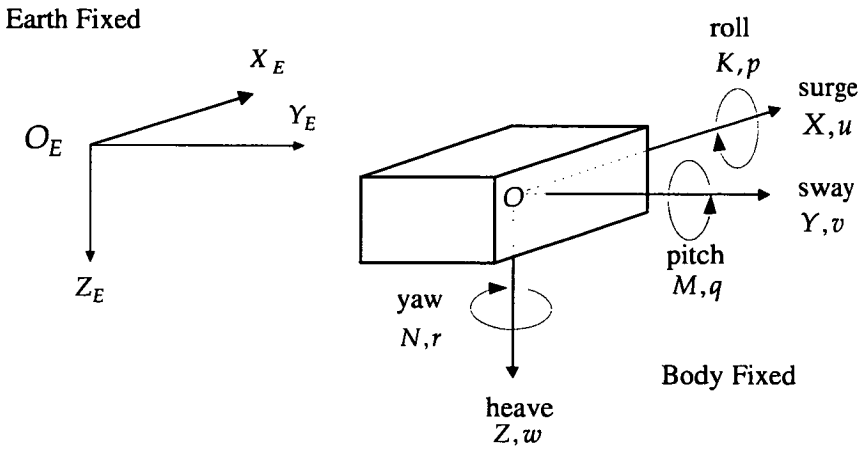

Figure. 2.1. Generalised co-ordinate system for a rigid body

In order that forces are easily expressed, the equations of motion are given relative to a set of coordinate axes fixed to the body. An absolute reference to the body coordinate system is also necessary. This reference is external to the body and is normally based on a non-accelerating earth reference frame, as illustrated in Figure 2.1. The axes are denoted by X_E, Y_E, Z_E. The convention given by SNAME (1962) and Abkowitz (1969) suggests that the coordinate system be a right-handed orthogonal set with X_E and Y_E in the horizontal plane, and Z_E vertical downward, as shown in Figure 2.1.

The expression for the net force acting on the vehicle can be divided into its component forces which allows each one to be treated separately. As mentioned above, linearising about one particular component of the UUV motion is inappropriate, since the UUV may be required to manoeuvre in any direction in order to perform a task. Consequently, the expression for the motion of the UUV is dependent on six motion components, three of which are translational accelerations while the other are three rotational accelerations.

$$M\begin{bmatrix} \dot{u} \\ \dot{v} \\ \dot{w} \\ \dot{p} \\ \dot{q} \\ \dot{r} \end{bmatrix} = \begin{matrix} F_d(u,v,w,p,q,r)+ \\ F_H(u_r,v_r,w_r,p,q,r)+ \\ F_S\left(\dot{u}_s,\dot{v}_s,\dot{w}_s,u_s,v_s,w_s,p,q,r\right)+ \\ F_G(\phi,\theta,\psi)+ \\ F_U + \\ F_T \end{matrix}$$

(2. 2)

where

$u,\ v,\ w,\ p,\ q,\ r$	are the vehicle velocities referred to body axes,
u_r, v_r, w_r	relative velocities to the flow, referred to body axes
$\dot{u},\ \dot{v},\ \dot{w},\ \dot{p},\ \dot{q}$, and $\dot{r}$	are the vehicle accelerations relative to body axes,
$\dot{u}_s, \dot{v}_s, \dot{w}_s, u_s, v_s, w_s$	are the flow accelerations and velocities, referred to body axes,
F_d	is the rigid body kinematic force vector,
F_G	is the hydrostatic force vector,
F_H	is the hydrodynamic force vector,
F_S	is the inertial force vector due to unsteady fluid motion,
F_T	is the thruster force vector,
F_U	is the umbilical force vector,
M	is the mass inertia matrix, and
ϕ, θ, and ψ	are the Euler angles; orientation of body referred to earth-fixed axes.

The umbilical force is not examined further in this formulation. However, these forces are significant for UUVs that are connected by cables to its host platform and should therefore be included when assessing the UUV's overall performance (Dand 1983).

The unsteady inertial fluid force, F_S, and the hydrodynamic force, F_H, are included in the expression to account for the pressure and shear forces that act on a body immersed in a fluid where there exists either an unsteady motion in the fluid or relative acceleration of the body with respect to the flow. This is discussed further in Section 2.4.

The complete derivation of the inertial force equations is given in Appendix 1. The development of the equations is generalised so that an arbitrary origin, separate from the body centre of gravity, is selected and included in the development. An arbitrary origin is occasionally helpful where the centre of gravity of a geometrically symmetric body does not lie in one of the planes of symmetry.

An examination of the expressions for the rigid body kinematic forces reveals terms that contain both accelerations and velocities. The terms containing acceleration reside in the mass inertia matrix M, while terms that contain velocities are given in the rigid body vector F_d. The rigid body force vector contains terms that are due to the decision to place the point of reference (ie. the coordinate axes) arbitrarily, with the body-fixed origin being offset from the centre of gravity of the vehicle.

The components of the net force vector acting along each of the body axes, shown on the right side of Equation (2.2), are denoted by X, Y and Z in Figure 2.1. These components are expressed as,

$$\begin{aligned} X &= X_G + X_H + X_d + X_S + X_T \\ Y &= Y_G + Y_H + Y_d + Y_S + Y_T \\ Z &= Z_G + Z_H + Z_d + Z_S + Z_T \end{aligned} \tag{2.3}$$

Similarly the components of the net moment vector are given by K, M and N and are expressed as,

$$\begin{aligned} K &= K_G + K_H + K_d + K_S + K_T \\ M &= M_G + M_H + M_d + M_S + M_T \\ N &= N_G + N_H + N_d + N_S + N_T \end{aligned} \tag{2.4}$$

where the subscripts G, H, d, S, and T refer to hydrostatics, hydrodynamics, rigid body dynamics, fluid inertia, and thrust force components respectively.

2. 2 Rigid Body Kinematic Forces

In this section the kinematic forces on a UUV are established. The results of a detailed derivation, given in Appendix 1., are summarised below. If the components of the rigid body force vector F_d are given by $(X_d \quad Y_d \quad Z_d)$, the expressions for the forces are given by,

$$X_d = -m\left((qw - rv) - x_G\left(r^2 + q^2\right) + p(qy_G + rz_G)\right)$$

$$Y_d = -m\left((ru - pw) - y_G\left(p^2 + r^2\right) + q(px_G + rz_G)\right)$$

$$Z_d = -m\left((pv - qu) - z_G\left(p^2 + q^2\right) + r(px_G + qy_G)\right) \tag{2. 5}$$

where

m	is the body mass,
$\boldsymbol{R}_G = (x_G \quad y_G \quad z_G)$	is the position vector of body centre of gravity from the body-fixed origin,
$\boldsymbol{U} = (u \quad v \quad w)$	is the velocity of origin of body axes, and
$\boldsymbol{\Omega} = (p \quad q \quad r)$	is the angular velocity about body origin.

The inertial equations for the moment are developed by considering the rate of change of angular momentum of the mass particles which make up the body (Greenshields, 1987). The components of acceleration are considered separately. The remaining terms, when coupled with velocity form the rigid body moment about the origin of the fixed axes located on the body, O. The components of the moment along the axes of the body are denoted by

$$\boldsymbol{M}_d = (K_d, M_d, N_d) \tag{2. 6}$$

The expressions for the rigid body moment are derived in Appendix 1. The results for the components of rigid body moment along the body axes are shown in Equation (2.7).

$$K_d = I_{zx}pq + I_{zy}q^2 - I_{zz}qr - I_{yx}pr + I_{yy}qr - I_{yz}r^2 - m[y_G(pv - qu) - z_G(ru - pw)]$$

$$M_d = -I_{xx}pr + I_{xy}qr + I_{xz}r^2 - I_{zx}p^2 - I_{zy}pq + I_{zz}pr - m[z_G(qw - rv) - x_G(pv - qu)]$$

$$N_d = I_{yx}p^2 - I_{yy}pq + I_{yz}pr + I_{xx}qp - I_{xy}q^2 - I_{xz}qr \\ - m[x_G(ru - pw) - y_G(qw - rv)] \tag{2.7}$$

where $I_{xx}, I_{xy}, I_{xz}, I_{yx}, I_{yy}, I_{yz}, I_{zx}, I_{zy}, I_{zz}$ are the moments and cross products of inertia.

2. 3 Transformation Matrices

Transformation matrices are necessary to relate the velocities described in terms of the body-fixed coordinate system back to earth-fixed coordinates. Hooft (1986) gives the following relationship between body-fixed and earth-fixed coordinate vectors.

$$\begin{aligned} \boldsymbol{V}_B &= \boldsymbol{D}_\phi \cdot \boldsymbol{D}_\theta \cdot \boldsymbol{D}_\psi \cdot \boldsymbol{V}_E \\ \Rightarrow \boldsymbol{V}_B &= \boldsymbol{D}_t \cdot \boldsymbol{V}_E \end{aligned} \tag{2.8}$$

where

$\boldsymbol{V}_B$ is the vector in the body-fixed coordinate system,

$\boldsymbol{V}_E$ is the vector in the earth-fixed coordinate system,

$\boldsymbol{D}_t$ is the transformation matrix, and

$$\boldsymbol{D}_\phi = \begin{bmatrix} 1 & 0 & 0 \\ 0 & \cos\phi & \sin\phi \\ 0 & -\sin\phi & \cos\phi \end{bmatrix} \tag{2.9}$$

$$\boldsymbol{D}_\theta = \begin{bmatrix} \cos\theta & 0 & -\sin\theta \\ 0 & 1 & 0 \\ \sin\theta & 0 & \cos\theta \end{bmatrix} \tag{2.10}$$

$$\boldsymbol{D}_\psi = \begin{bmatrix} \cos\psi & \sin\psi & 0 \\ -\sin\psi & \cos\psi & 0 \\ 0 & 0 & 1 \end{bmatrix} \tag{2.11}$$

The relationship between the earth fixed velocities $\dot{\phi}, \dot{\theta}, \dot{\psi}$ and the body fixed velocities p, q, r is given by the following equation.

$$\begin{bmatrix} p \\ q \\ r \end{bmatrix} = \boldsymbol{D}_{\phi} \cdot \boldsymbol{D}_{\theta} \cdot \begin{bmatrix} 0 \\ 0 \\ \dot{\psi} \end{bmatrix} + \boldsymbol{D}_{\phi} \begin{bmatrix} 0 \\ \dot{\theta} \\ 0 \end{bmatrix} + \begin{bmatrix} \dot{\phi} \\ 0 \\ 0 \end{bmatrix} \tag{2. 12}$$

This relationship can be expanded, Greenshields (1987), to give a single transformation matrix relating the body velocities to the velocities in terms of earth-fixed axes. This is shown in Equation (2.13).

$$\begin{bmatrix} \cos\psi\cos\theta & \cos\psi\sin\theta\sin\phi - \sin\psi\cos\phi & \cos\psi\sin\theta\cos\phi + \sin\psi\sin\phi \\ \sin\psi\cos\theta & \sin\psi\sin\theta\sin\phi + \cos\psi\cos\phi & \sin\psi\sin\theta\cos\phi - \cos\psi\sin\phi \\ -\sin\theta & \cos\theta\sin\phi & \cos\theta\cos\phi \end{bmatrix} \tag{2. 13}$$

Similarly, a transformation matrix for the rotational velocities of the body to the angular velocities relative to the earth-fixed axes can be derived as shown in Equation (2.14).

$$\begin{bmatrix} 1 & \sin\phi\tan\theta & \cos\phi\tan\theta \\ 0 & \cos\phi & -\sin\phi \\ 0 & \sin\phi\sec\theta & \cos\phi\sec\theta \end{bmatrix} \tag{2. 14}$$

2. 4 Hydrodynamic Force

2.4.1 Introduction

The manoeuvring of submarines has been a driving force for the development of many hydrodynamic models. For example, the hydrodynamic equations by Feldman (1975), Feldman (1979), and Gertler (1967) were developed for simulation of submarines. Kalske (1989), Aage (1994), Bohlmann (1991), Feldman (1966), Friswell (1985), Fyfe (1979), Greenshields (1987) and He (1990) also describe hydrodynamic models for a variety of vehicles, although some have considerably different shapes to that of traditional submarines. A discussion on the development of the hydrodynamic force equations follows.

Hydrodynamic force or drag of deeply submerged bodies is made up of several components. Hoerner (1958) gives a thorough discussion on the elements of drag. In

summary, the total drag on a body in a real flow is equal to the sum of the frictional drag and the form or resistance drag. The resultant force of the drag is along the line of motion of the body. It can be resolved into two components, a normal stress or pressure force, and a tangential stress or skin friction. A real flow is considered to be viscous. It causes friction between particles and is responsible for the presence of boundary layers over bodies. The development of boundary layers and the separation of flow gives rise to the viscous stress forces.

If the fluid flow is considered inviscid or ideal, then the pressure force can be derived. This produces the general form of the hydrodynamic force equations. This form alone however, does not account for the effect of viscosity. Lewis (1984) developed a mathematical model for an underwater vehicle in which the components of the force due to the viscous and inviscid effects were considered separately. Lewis noted that care must be taken when evaluating hydrodynamic derivatives from experimental data to ensure consistency with the mathematical model. Additional terms are frequently added to the mathematical model to allow for the viscous effects not accounted for in the inviscid mathematical model. Several examples are given in Section 2.4.4.

The force on an arbitrary body moving in an inviscid flow is due to either unsteady motion of the body in a stationary flow or unsteady motion of the flow around an otherwise stationary body. Imlay (1961) describes both the basis for the forces and the complete equations that describe the Added Mass of a body.

The total pressure force in an inviscid fluid, $\boldsymbol{F}_P$, is given here as the sum of the forces due to the motion of a body in undisturbed flow, $\boldsymbol{F}_A$, and $\boldsymbol{F}_S$, the force on the otherwise stationary body, due to the unsteady, uniformly accelerating fluid flow.

$$\boldsymbol{F}_P = \boldsymbol{F}_A + \boldsymbol{F}_S \tag{2. 15}$$

'Added Mass' is one of the many names assigned to the added inertia when the body accelerates relative to the fluid around it; other names include 'Apparent Mass', 'Added Virtual Mass', 'Virtual Mass', 'Apparent Mass' or 'Hydrodynamic Mass'. The force $\boldsymbol{F}_A$ is proportional to the relative accelerations of the body where the constants of proportionality are based on the geometry and mass distribution of the body.

The force on the body due to the unsteady fluid flow F_S, is considered to be like a buoyancy force (Imlay, 1961). The uniform accelerating fluid sets up a pressure gradient that is opposite to the acceleration and has a magnitude equal to the product of the fluid density and the acceleration. The force acting on the body due to the pressure gradient, is given by the product of the fluid density, by the volume of the fluid displaced, and by the acceleration of the fluid.

The total hydrodynamic pressure force F_P and moment, M_P, that act on a body immersed in a fluid, are given by the integration of the pressure p over the entire body surface S such that,

$$F_P = \iint_{S_B} p\boldsymbol{n}\, dS \tag{2. 16}$$

and

$$M_P = \iint_{S_B} p(\boldsymbol{r} \times \boldsymbol{n})\, \mathrm{d}S \tag{2. 17}$$

2.4.2 Unsteady Body Motion

The following section considers the hydrodynamic pressure force due to the unsteady motion of the body in an otherwise stationary fluid flow.

Newman (1977) gives the expressions for the pressure force due to the body accelerating in an undisturbed fluid. The development is undertaken in an ideal fluid where viscosity is neglected. The result in tensor notation is given below:

$$F_{A_j} = -\dot{U}_i\, m_{ji} - \quad _{jkl} U_i \Omega_k m_{li} \tag{2. 18}$$

and

$$M_{A_j} = -\dot{U}_i\, m_{j+3,i} - \varepsilon_{jkl} U_i \Omega_k m_{l+3,i} - \varepsilon_{jkl} U_i U_k m_{li} \tag{2. 19}$$

The Added Mass term, denoted by m_{ij} is expressed as

$$m_{ji} = \rho \iint_{S_B} \phi_i \frac{\partial \phi_j}{\partial n} dS\,, \tag{2. 20}$$

where

ϕ	is the velocity potential
$\boldsymbol{n}$	is the normal vector to the surface
S_B	is the surface of the body
ρ	is the density of the fluid
S	is the surface of integration
j,k,l	are indices with values 1,2,3 and
i	denotes the six components of the velocity potential.

By noting the expressions given in Equations (2.18) and (2.19), the Added Mass tensor can be related to the conventional notation for hydrodynamic coefficients as follows,

$$m_{ji} = -\frac{\partial \boldsymbol{F}_j}{\partial \dot{\boldsymbol{U}}_i} \tag{2. 21}$$

where i and j are both indices ranging from 1 to 6.

Given the results provided by Equations (2.18), (2.19), (2.20) and (2.21), the complete 'Added Mass' expressions for a body in an undisturbed flow are as follows (Imlay, 1961):

$$\left.\begin{aligned} X_A = {} & X_{\dot{u}}\dot{u} + X_w\left(\dot{w} + uq\right) + X_{\dot{q}}\dot{q} + Z_{wq}wq + Z_{qq}q^2 + X_{\dot{v}}\dot{v} + X_{\dot{p}}\dot{p} + X_{\dot{r}}\dot{r} - Y_{vr}vr \\ & - Y_{rp}rp - Y_{rr}r^2 - X_{ur}ur - Y_{wr}wr + Y_{wq}vq + Z_{pq}pq - \left(Y_{\dot{q}} - Z_{\dot{r}}\right)qr \end{aligned}\right\} \tag{2. 22}$$

$$\left.\begin{aligned} Y_A = {} & X_{\dot{u}}\dot{u} + Y_{\dot{w}}\dot{w} + Y_{\dot{q}}\dot{q} + Y_{\dot{v}}\dot{v} + Y_{\dot{p}}\dot{p} + Y_{\dot{r}}\dot{r} + X_{vr}vr - Y_{wp}vp + X_{rr}r^2 \\ & + \left(X_{\dot{p}} - Z_{\dot{r}}\right)rp - Z_{pp}p^2 - X_{uw}\left(up - wr\right) + X_{ur}ur - Z_{wp}wp - Z_{pq}pq + X_{qr}qr \end{aligned}\right\} \tag{2. 23}$$

$$\left.\begin{aligned} Z_A = {} & X_{w}\left(\dot{u} - wq\right) + Z_{\dot{w}}\dot{w} + Z_{\dot{q}}\dot{q} - X_{uq}uq - X_{qq}q^2 + Y_{\dot{v}}\dot{v} + Z_{\dot{p}}\dot{p} + Z_{\dot{r}}\dot{r} + Y_{vp}vp \\ & + Y_{rp}rp + Y_{pp}p^2 + X_{up}up + Y_{wp}wp - X_{vq}vq - \left(X_{\dot{p}} - Y_{\dot{q}}\right)pq - X_{qr}qr \end{aligned}\right\} \tag{2. 24}$$

$$
\left.\begin{aligned}
K_A = {} & X_p^{\bullet}u + Z_p^{\bullet}w + K_q^{\bullet}q - X_v wu + X_r uq - Y_w w^2 - \left(Y_q - Z_r\right)wq + M_r q^2 + Y_p^{\bullet}v \\
& + K_p^{\bullet}p + K_r^{\bullet}r + Y_w v^2 - \left(Y_q - Z_r\right)vr + Z_p vp - M_r r^2 - K_q rp + X_w uv - \left(Y_v - Z_w\right)vw \\
& - \left(Y_r + Z_q\right)wr - Y_p wp - X_q ur + \left(Y_r + Z_q\right)vq + K_r pq - \left(M_q - N_r\right)qr
\end{aligned}\right\} \quad (2.25)
$$

$$
\left.\begin{aligned}
M_A = {} & X_q\left(\dot{u} + wq\right) + Z_q\left(\dot{w} - uq\right) + M_q^{\bullet}q - X_w\left(u^2 - w^2\right) - \left(Z_w - X_u\right)wu + Y_q^{\bullet}v + K_q^{\bullet}p \\
& + M_r^{\bullet}r + Y_p vr - Y_r vp - K_r\left(p^2 - r^2\right) + \left(K_p - N_r\right)rp - X_w uv + X_v vw \\
& - \left(X_r + Z_p\right)\left(up - wr\right) + \left(X_p - Z_r\right)\left(wp + ur\right) - M_r pq + K_q qr
\end{aligned}\right\} \quad (2.26)
$$

$$
\left.\begin{aligned}
N_A = {} & X_r^{\bullet}u + Z_r^{\bullet}w + M_r^{\bullet}q + X_v u^2 + Y_w wu - \left(X_p - Y_q\right)uq - Z_p wq - K_q q^2 - X_v v^2 \\
& - X_r vr - \left(X_p - Y_q\right)vp + Y_r^{\bullet}v + K_r^{\bullet}p + N_r^{\bullet}r - \left(X_u - Y_v\right)uv - X_w vw + \left(X_q + Y_p\right)up \\
& + Y_r ur + M_r rp + K_q p^2 + Z_q wp - \left(X_q + Y_p\right)vq - \left(K_p - M_q\right)pq - K_r qr
\end{aligned}\right\} \quad (2.27)
$$

Appendix 2 summarises the hydrodynamic coefficient relationships for a body in a potential flow.

The accelerations and velocities given in these examples are relative to a flow that is otherwise undisturbed. Therefore, account must be made for the body motion in a flow where there exists a flow field of some description. In order to achieve this the dynamic variables in Equations (2.22) to (2.27) should be replaced by

$$
\left(\dot{u}_r, \dot{v}_r, \dot{w}_r\right) \text{ and } \left(u_r, v_r, w_r\right)
$$

where

$$
\left.\begin{aligned}
\dot{u}_r &= \dot{u} - \dot{u}_s \\
\dot{v}_r &= \dot{v} - \dot{v}_s \\
\dot{w}_r &= \dot{w} - \dot{w}_s \\
u_r &= u - u_s \\
v_r &= v - v_s \\
w_r &= w - w_s
\end{aligned}\right\} \quad (2.28)
$$

and

$$\left(\dot{u}_s, \dot{v}_s, \dot{w}_s\right) \text{and} \left(u_s, v_s, w_s\right)$$

are the acceleration and velocity of the sea current with respect to the body axes respectively. The additional terms required to represent the presence of an unsteady fluid flow are discussed below.

2.4.3 Unsteady Fluid Motion

In this section the remaining force terms required to specify the motion of the body relative to an accelerating fluid flow are given. The buoyancy-like force described by Imlay (1961) is given by

$$\boldsymbol{F}_S = \overline{m}\frac{\mathrm{d}}{\mathrm{dt}}\boldsymbol{U}_s \tag{2. 29}$$

where the fluid velocity is given by

$$\boldsymbol{U}_s = \begin{pmatrix} u_s & v_s & w_s \end{pmatrix}$$

Note that the unsteady angular flow velocity is assumed to be negligible in this formulation.

and the mass of the displaced fluid is denoted by $\overline{m}$.

The components of the force are

$$X_S = \overline{m}\left(\dot{u}_s + qw_s - rv_s\right) \tag{2. 30}$$

$$Y_S = \overline{m}\left(\dot{v}_s + ru_s - pw_s\right) \tag{2. 31}$$

$$Z_S = \overline{m}\left(\dot{w}_s + pv_s - qu_s\right) \tag{2. 32}$$

$$K_S = \overline{m}\left[\left(y_B\dot{w}_s - z_B\dot{v}_s\right) + y_B\left(pv_s - qu_s\right) - z_B\left(ru_s - pw_s\right)\right] \tag{2. 33}$$

$$M_S = \overline{m}\left[\left(z_B\dot{u}_s - x_B\dot{w}_s\right) + z_B\left(qw_s - rv_s\right) - x_B\left(pv_s - qu_s\right)\right] \tag{2. 34}$$

$$N_S = \overline{m}\left[\left(x_B \dot{v}_s - y_B \dot{u}_s\right) + x_B(ru_s - pw_s) - y_B(qw_s - rv_s)\right] \tag{2.35}$$

where

$\overline{m}$ is the mass of the displaced fluid, and

(x_B, y_B, z_B) defines the position of the centre of buoyancy of the body.

The Added Mass components of the pressure force, $\boldsymbol{F}_A$, are separated in the equations of motion. The terms that contain body accelerations are placed in the mass inertia matrix and these are addressed in Section 2.5.

The terms that contain flow acceleration are added to the unsteady fluid force vector. The components of the unsteady fluid force follow:

$$X_S = \overline{m}\left(\dot{u}_s + qw_s - rv_s\right) - X_{\dot{u}}\dot{u}_s - X_{\dot{v}}\dot{v}_s - X_{\dot{w}}\dot{w}_s \tag{2.36}$$

$$Y_S = \overline{m}\left(\dot{v}_s + ru_s - pw_s\right) - X_{\dot{v}}\dot{u}_s - Y_{\dot{v}}\dot{v}_s - Y_{\dot{w}}\dot{w}_s \tag{2.37}$$

$$Z_S = \overline{m}\left(\dot{w}_s + pv_s - qu_s\right) - X_{\dot{w}}\dot{u}_s - Y_{\dot{w}}\dot{v}_s - Z_{\dot{w}}\dot{w}_s \tag{2.38}$$

$$K_S = \overline{m}\left[\left(y_B \dot{w}_s - z_B \dot{v}_s\right) + y_B(pv_s - qu_s) - z_B(ru_s - pw_s)\right] - X_{\dot{p}}\dot{u}_s - Y_{\dot{p}}\dot{v}_s - Z_{\dot{p}}\dot{w}_s \tag{2.39}$$

$$M_S = \overline{m}\left[\left(z_B \dot{u}_s - x_B \dot{w}_s\right) + z_B(qw_s - rv_s) - x_B(pv_s - qu_s)\right] - X_{\dot{q}}\dot{u}_s - Y_{\dot{q}}\dot{v}_s - Z_{\dot{q}}\dot{w}_s \tag{2.40}$$

$$N_S = \overline{m}\left[\left(x_B \dot{v}_s - y_B \dot{u}_s\right) + x_B(ru_s - pw_s) - y_B(qw_s - rv_s)\right] - X_{\dot{r}}\dot{u}_s - Y_{\dot{r}}\dot{v}_s - Z_{\dot{r}}\dot{w}_s \tag{2.41}$$

The results given in Section 2.4.2 and 2.4.3 combine to give the result obtained in Lewis (1984).

2.4.4 Resultant Force Vector

The remaining velocity terms in the vector $\boldsymbol{F}_A$ represent the inviscid damping forces and will form the basis of the hydrodynamic force vector $\boldsymbol{F}_H$. The result for the X axial hydrodynamic force is

$$\begin{aligned} X_H &= \underset{w}{X_{\cdot}} u_r q + \underset{w}{Z_{\cdot}} w_r q + \underset{q}{Z_{\cdot}} q^2 - \underset{v}{Y_{\cdot}} v_r r - \underset{p}{Y_{\cdot}} rp - \underset{r}{Y_{\cdot}} r^2 - \underset{v}{X_{\cdot}} u_r r - \underset{w}{Y_{\cdot}} w_r r + \underset{w}{Y_{\cdot}} v_r q \\ &+ \underset{p}{Z_{\cdot}} pq - \left(\underset{q}{Y_{\cdot}} - \underset{r}{Z_{\cdot}} \right) qr \end{aligned} \tag{2.42}$$

or

$$\begin{aligned} X_H &= X_{uq} u_r q + X_{wq} w_r q + X_{qq} q^2 + X_{vr} v_r r + X_{rp} rp + X_{rr} r^2 + X_{ur} u_r r + X_{wr} w_r r \\ &+ X_{vq} v_r q + X_{pq} pq + X_{qr} qr \end{aligned} \tag{2.43}$$

where

$$X_{uq} = \underset{w}{X_{\cdot}}, X_{wq} = \underset{w}{Z_{\cdot}}, X_{qq} = \underset{q}{Z_{\cdot}}, X_{vr} = -\underset{v}{Y_{\cdot}}, X_{rp} = -\underset{p}{Y_{\cdot}}, X_{rr} = -\underset{r}{Y_{\cdot}}, X_{ur} = -\underset{v}{X_{\cdot}}, X_{wr} = -\underset{w}{Y_{\cdot}},$$

$$X_{vq} = \underset{w}{Y_{\cdot}}, X_{pq} = \underset{p}{Z_{\cdot}}, \text{ and } X_{qr} = -\left(\underset{q}{Y_{\cdot}} - \underset{r}{Z_{\cdot}} \right)$$

Similarly the expressions for the inviscid part of the remaining components of the hydrodynamic force are

$$\left.\begin{aligned} Y_H &= Y_{vr} v_r r + Y_{vp} v_r p + Y_{rr} r^2 + Y_{rp} rp + Y_{pp} p^2 + Y_{up} u_r p + Y_{wr} w_r r + Y_{ur} u_r r \\ &+ Y_{wp} w_r p + Y_{pq} pq + Y_{qr} qr \end{aligned}\right\} \tag{2.44}$$

$$\left.\begin{aligned} Z_H &= Z_{wq} w_r q + Z_{uq} u_r q + Z_{qq} q^2 + Z_{vp} v_r p + Z_{rp} rp + Z_{pp} p^2 + Z_{up} u_r p + Z_{wp} w_r p \\ &+ Z_{vq} v_r q + Z_{pq} pq + Z_{qr} qr \end{aligned}\right\} \tag{2.45}$$

$$\left.\begin{aligned} K_H &= K_{wu} w_r u + K_{uq} u_r q + K_{ww} w_r^2 + K_{wq} w_r q + K_{qq} q^2 + K_{vv} v_r^2 + K_{vr} v_r r \\ &+ K_{vp} v_r p + K_{rr} r^2 + K_{rp} rp + K_{uv} u_r v_r + K_{vw} v_r w_r + K_{wr} w_r r + K_{wp} w_r p + K_{ur} u_r r \\ &+ K_{vq} v_r q + K_{pq} pq + K_{qr} qr \end{aligned}\right\} \tag{2.46}$$

$$\left.\begin{aligned} M_H &= M_{wq} w_r q + M_{uq} u_r q + M_{uu} u_r^2 + M_{ww} w_r^2 + M_{wu} w_r u_r + M_{vr} v_r r \\ &+ M_{vp} v_r p + M_{pp} p^2 + M_{rr} r^2 + M_{rp} rp + M_{uv} u_r v_r + M_{vw} v_r w_r + M_{up} u_r p \\ &+ M_{wr} w_r r + M_{wp} w_r p + M_{ur} u_r r + M_{pq} pq + M_{qr} qr \end{aligned}\right\} \tag{2.47}$$

$$\left.\begin{aligned} N_H &= N_{uu}u_r^2 + N_{wu}w_r u_r + N_{uq}u_r q + N_{wq}w_r q + N_{qq}q^2 + N_{vv}v_r^2 \\ &+ N_{vr}v_r r + N_{vp}v_r p + N_{uv}u_r v_r + N_{vw}v_r w_r + N_{up}u_r p + N_{ur}u_r r + N_{rp}rp \\ &+ N_{pp}p^2 + N_{wp}w_r p + N_{vq}v_r q + N_{pq}pq + N_{qr}qr \end{aligned}\right\} \quad (2.48)$$

The equations may also contain further terms that account for viscous effects on the body. Simplification of the expressions may be possible if the body exhibits symmetry about an axis (Imlay 1961). Feldman (1979), Gertler and Hagen (1967) proposed mathematical models to describe the resultant hydrodynamic force on an underwater body, such as a submarine, that exhibits symmetry along the XZ body plane. The equations are similar to those expressed above, but are due to the symmetry of the body. These authors also made an allowance for viscous effects not incorporated into the above expressions. The suggestions made by these authors could be used additionally to the terms provided in the inviscid formulation above. The expressions are given below, note in some cases alternative expressions for the same force disturbance are given:

Surge Force, X_H: $X_{uu}u_r u_r$, $X_{uU}u_r U_r$, $X_{u|u|}u_r|u_r|$, $X_{uw}u_r w_r$, $X_{u|r|}u_r|r|$, $X_{u|v|}u_r|v|$,

$X_{vv}v_r v_r$, $X_{UU}U_r^2$, $X_{w|w|}w_r|w_r|$, $X_{ww}w_r w_r$, $X_{pp}pp$, $X_{rrv}\frac{r^2 v_r}{U_r}$,

$X_{wwq}\frac{w_r^2 q}{U_r}$, $X_{pv}pv_r$, $X_{ppv}\frac{p^2 v_r}{U_r}$, $X_{|v|}|v_r|$, $X_w w_r$, $X_r r$, $X_p p$

Sway Force, Y_H: $Y_{p|p|}p|p|$, $Y_{v|v|}v_r\left|\left(v_r^2 + w_r^2\right)^{1/2}\right|$, $Y_{vU}v_r U_r$, $Y_{v|r|}v_r|r|$, $Y_{rvv}\frac{v_r^2 r}{U_r}$,

$Y_{rrv}\frac{r^2 v_r}{U_r}$, $Y_{r|r|}r|r|$, $Y_{pU}pU_r$, $Y_{v|v|}v_r|v_r|$, $Y_{r|u|}r|u_r|$, $Y_{qv}qv_r$, $Y_v v_r$, $Y_{uv}uv_r$,

$Y_{vw}vw$, $Y_{uu}u_r u_r$, $Y_p p$, $Y_r r$, $Y_{up}u_r p$, $Y_{ur}u_r r$

Heave Force, Z_H: $Z_{|w|}u_r|w_r|$, $Z_{ww}\left|w_r\left(v_r^2 + w_r^2\right)^{1/2}\right|$, $Z_{wU}w_r U_r$, $Z_{UU}U_r^2$, $Z_{|v|U}|v_r|U_r$,

$Z_{uw}u_r w_r$, $Z_{wvv}\frac{w_r v_r^2}{U_r}$, $Z_{rr}rr$, $Z_{ru}u_r r$, $Z_{rrv}\frac{r^2 v}{U_r}$, $Z_{w|q|}|q|w_r$, $Z_{|u|w}|u_r|w_r$,

$Z_{|u|q}|u_r|q$, $Z_{u|u|}u_r|u_r|$, $Z_{qw}|q|\left(v_r^2 + w_r^2\right)^{1/2}(sign(w_r))$, $Z_{vr}v_r r$, $Z_{vv}v_r^2$,

$Z_{uu}u_r^2$, $Z_{w|w|}w_r|w_r|$, $Z_w w_r$, $Z_q q$

Roll Moment, K_H: $K_{p|p|}p|p|^2$, $K_{v|v|}v_r\left|\left(v_r^2+w_r^2\right)^{1/2}\right|$, $K_{vU}v_rU_r$, $K_{rrv}\frac{r^2v_r}{U_r}$,

$K_{wvv}\frac{w_rv_r^2}{U_r}$, $K_{r|r|}r|r|$, $K_{vvr}\frac{v_r^2r}{U_r}$, $K_{|u|v}|u_r|v_r$, $K_{pu}pu_r$, K_pp, K_rr,

K_vv_r, $K_{v|v|}v_r|v_r|$, $K_{vw}v_rw_r$

Pitch Moment, M_H: $M_{q|q|}q|q|$, $M_{q|w|}\left|q\left(v_r^2+w_r^2\right)^{1/2}\right|$, $M_{w|w|}w_r\left|\left(v_r^2+w_r^2\right)^{1/2}\right|$, $M_{|w|}u_r|w_r|$

$M_{wU}w_rU_r$, $M_{UU}U_r^2$, $M_{uuu}\frac{u_r^3}{U_r}$, $M_{vvr}\frac{v_r^2r}{U_r}$, $M_{rrv}\frac{r^2v_r}{U_r}$, $M_{|w|q}|w_r|q$,

$M_{wwq}\frac{w_r^2q}{U_r}$, $M_{|u|w}|u_r|w_r$, $M_{|u|q}|u_r|q$, $M_{pU}pU_r$, $M_{u|u|}u_r|u_r|$, $M_{vv}v_r^2$,

$M_{uU}u_rU_r$, M_qq, M_ww_r, $M_{w|w|}w_r|w_r|$

Yaw Moment, N_H: $N_{r|r|}r|r|$, $N_{r|v|}r\left|\left(v_r^2+w_r^2\right)^{1/2}\right|$, $N_{v|v|}v_r\left|\left(v_r^2+w_r^2\right)^{1/2}\right|$, $N_{vU}v_rU_r$,

$N_{v|r|}v_r|r|$, $N_{rrv}\frac{r^2v_r}{U_r}$, $N_{pU}pU_r$, $N_{v|u|}v_r|u_r|$, $N_{r|u|}r|u_r|$, $N_{wr}w_rr$, N_pp,

$N_{p|p|}p|p|$, N_rr, N_vv_r, $N_{v|v|}v_r|v_r|$, $N_{|v|r}|v_r|r$

2. 5 Mass Inertia Matrix

The equations of motion developed for the rigid body contain many terms that are dependent on the acceleration of the body. In order to solve for these accelerations the terms are collected in a mass inertia matrix M. The matrix contains the mass, moments of inertia, cross products of inertia and the Added Mass coefficients that are coupled with the acceleration terms. The following is the full expression for the mass inertia matrix. This expression has not been simplified to take into account parameters which have zero value due to symmetry of the body (Lewis, 1984).

$$M = \begin{bmatrix} m - X_{\dot{u}} & -X_{\dot{v}} & -X_{\dot{w}} & -X_{\dot{p}} & mz_G - X_{\dot{q}} & -my_G - X_{\dot{r}} \\ -Y_{\dot{u}} & m - Y_{\dot{v}} & -Y_{\dot{w}} & -mz_G - Y_{\dot{p}} & -Y_{\dot{q}} & mx_G - Y_{\dot{r}} \\ -Z_{\dot{u}} & -Z_{\dot{v}} & m - Z_{\dot{w}} & my_G - Z_{\dot{p}} & -mx_G - Z_{\dot{q}} & -Z_{\dot{r}} \\ -K_{\dot{u}} & -x_G m - K_{\dot{v}} & y_G m - K_{\dot{w}} & I_{xx} - K_{\dot{p}} & -I_{xy} - K_{\dot{q}} & -I_{xz} - K_{\dot{r}} \\ z_G m - M_{\dot{u}} & -M_{\dot{v}} & -x_G m - M_{\dot{w}} & -I_{yx} - M_{\dot{p}} & I_{yy} - M_{\dot{q}} & -I_{yz} - M_{\dot{r}} \\ -y_G m - N_{\dot{u}} & x_G m - N_{\dot{v}} & -N_{\dot{w}} & -I_{zx} - N_{\dot{p}} & -I_{zy} - N_{\dot{q}} & I_{zz} - N_{\dot{r}} \end{bmatrix} \quad (2.49)$$

2. 6 Weight and Buoyancy Force

Imlay (1964) gives complete expressions for the buoyancy and weight force on a rigid body. The hydrostatic forces in each of the body coordinate axes, denoted by $X_G, Y_G, Z_G, K_G, M_G, N_G$ are

$$\begin{aligned} X_G &= -(W - B)\sin\theta \\ Y_G &= (W - B)\cos\theta\sin\phi \\ Z_G &= (W - B)\cos\theta\cos\phi \\ K_G &= (y_G W - y_B B)\cos\theta\cos\phi - (z_G W - z_B B)\cos\theta\sin\phi \\ M_G &= -(x_G W - x_B B)\cos\theta\cos\phi - (z_G W - z_B B)\sin\theta \\ N_G &= (x_G W - x_B B)\cos\theta\sin\phi + (y_G W - y_B B)\sin\theta \end{aligned} \quad (2.50)$$

where

W	is the body weight
B	is the buoyancy of the body
ϕ, θ, and ψ	are the body orientation angles, roll, pitch and yaw respectively.

2. 7 Thrust Force

The thrusters are critical to the operational performance of underwater vehicles. They determine the ability of the vehicle to overcome drag. The effectiveness of the thrusters has repercussions for many aspects of vehicle performance including its manoeuvrability, the maximum speed through the water and power usage.

The aim of this work is not to study the dynamics of thrusters. However the impact of the thrusters on underwater vehicle performance is such that a basic understanding is necessary, since a model of the thrusters is required to ensure accurate simulation of the behaviour of the vehicle.

The net thrust is equal to the summation of the individual thrust, $\boldsymbol{F}_{T_i}$, and momentum drag, $\boldsymbol{D}_{M_i}$, from each of the thrusters (Dand, 1983). This is expressed as follows:

$$\boldsymbol{F}_T = \sum_i \left(\boldsymbol{F}_{Ti} + \boldsymbol{D}_{Mi}\right) \tag{2.51}$$

The net thrust moment is equal to the cross product of the position vector of the ith thruster with the thrust and momentum drag. This is expressed in Equation (2.52).

$$\boldsymbol{M}_T = \sum_i \boldsymbol{R}_{Ti} \times \left(\boldsymbol{F}_{Ti} + \boldsymbol{D}_{Mi}\right) \tag{2.52}$$

Axial and cross-flow effects influence the performance of thrusters, these are a combination of interactions between individual thrusters, both with each other and with the hull. These effects are described in more detail in Dand (1983).

Yoerger et al. (1990) discusses the dynamics of thrusters and their influence on underwater vehicles. In his paper he develops a dynamic model for an electrically powered thruster which is torque controlled. The response of the thrusters to a demanded thrust level may be inadequate due to bandwidth constraints and limit cycling. Forms of control for thruster compensation are discussed in order to obtain the desired thruster performance. Yoerger concluded that for effective performance over the entire operating range and for compensation of uncertainties and degradation of the thruster, an adaptive sliding controller is necessary.

For simplicity the controller implemented in this work is a first order system. The dynamic thruster model proposed by Yoerger (1990) is given below in Equations (2.53) and (2.54).

$$\dot{\Omega}_t = \frac{1}{\eta^2 p^2 \rho V}\tau - \frac{\eta p A_D}{2V}\Omega_t|\Omega_t| \tag{2.53}$$

$$T = A_D \rho \eta^2 p^2 \Omega_t|\Omega_t| \tag{2.54}$$

where

T is the thrust output,

Ω_t is the propeller angular velocity (rads/s),

τ is the input torque,

η is the propeller efficiency $(\equiv 1 - \text{slip})$,

p is the pitch of the propeller,

A_D is the cross sectional area of the duct, and

V is the volume of the duct.

The simplified thrust equations are given in Equations (2.55) and (2.56).

$$\dot{\Omega}_t = \beta\tau - \alpha\Omega_t|\Omega_t| \tag{2.55}$$

$$T = C_t\Omega_t|\Omega_t| \tag{2.56}$$

Goheen (1990) describes thruster models developed by several authors, which include thruster interaction effects. Momentum drag is one such interaction effect; this occurs when the fluid velocity has a component that acts perpendicular to the axial direction of the thruster. The momentum drag, $\boldsymbol{D}_{M_i}$ is given by:

$$\boldsymbol{D}_{M_i} = \left(\frac{\pi}{2}\rho\Omega_t D^3 \boldsymbol{U}_{tn}\sqrt{\frac{Kt_o}{\pi}}\right)_i \tag{2.57}$$

where

D is the diameter of the propeller,

$\boldsymbol{U}_{tn}$ is the normal velocity at the thruster, and

Kt_o is the normalised thrust coefficient at zero advance.

Dand (1983) gives a similar expression for the momentum drag

$$\boldsymbol{D}_{M_i} = \left(K\rho A_D v_j U\right)_i \tag{2.58}$$

where

v_j is the thruster jet velocity,

U is the vehicle velocity, and

K is a coefficient determined from measured results.

Assuming no interaction effects, the normal flow velocity at the thruster is given by

$$\boldsymbol{U}_{t_n} = \left(\boldsymbol{U}_r + \boldsymbol{\Omega} \times \boldsymbol{R}_t\right) \cdot \boldsymbol{t}_n \tag{2.59}$$

where $\boldsymbol{t}_n = \boldsymbol{j} + \boldsymbol{k}$ is the normal vector to the axial direction of the thrusters.

Similarly, the axial inflow velocity is given by:

$$\boldsymbol{U}_{t_a} = \left(\boldsymbol{U}_r + \boldsymbol{\Omega} \times \boldsymbol{R}_t\right) \cdot \boldsymbol{t}_a \tag{2.60}$$

where $\boldsymbol{t}_a = \boldsymbol{i}$ is the axial direction of the thrust.

2. 8 Solution Technique

In order to determine the state of the body at each time step, Equation (2.2) is considered in the following form (Hooft, 1986)

$$\boldsymbol{A} = \boldsymbol{M}^{-1} \cdot \boldsymbol{F} \tag{2.61}$$

The initial conditions at t_0 are given for position and velocity, enabling the net force at t_0 to be determined. From this the following expression for the net force at t_0, denoted by $\boldsymbol{F}_o$, is derived.

$$\boldsymbol{F}_o = \boldsymbol{F}_o\left(t_o, \phi_o, \theta_o, \psi_o, x_o, y_o, z_o, u_o, v_o, w_o, p_o, q_o, r_o\right) \tag{2.62}$$

The momentary acceleration $\boldsymbol{A}_o$ is then determined using Equation (2.62), which is then integrated using a linear approximation to obtain the velocity at the next time

step. The result is integrated again to determine the position. The expressions for velocity and position are given in Equations (2.63) and (2.64) respectively.

$$V_{i+1} = A_i \cdot (t_{i+1} - t_i) + V_i \tag{2.63}$$

and

$$X_{i+1} = \frac{1}{2} A_i \cdot (t_{i+1} - t_i)^2 + V_i \cdot (t_{i+1} - t_i) + X_i \tag{2.64}$$

The procedure is repeated for the remaining duration of the simulation.

2. 9 Simulation Software

The mathematical model described in the previous sections was developed into a generic simulation for underwater vehicles. The software 'UUV6DOF', was designed using the mathematical package MATLAB 4.0 and the Simulink Toolbox from Mathworks Inc (Mathworks 1994). The Matlab/Simulink figures are given in Appendix 1.4.

The general aim of the software is to provide a tool that enables analyses of underwater vehicle manoeuvring behaviour to be performed. In the context of the work herein, it will enable a study to be performed that will identify the effect of various errors in hydrodynamic coefficient prediction, either from theory or experiment, on the overall simulated results.

2.10 Discussion

A description of the mathematical model for a rigid body was given in this chapter. In particular, the hydrodynamic force on a body in an deeply submerged, underwater environment is expressed as the sum of the pressure and shear forces. The form of the hydrodynamic model is developed around potential flow theory, where only normal pressure forces are determined. Allowance for the viscous shear force is made with the addition of terms that enable the inviscid model to more accurately fit the hydrodynamic performance of the body. Mathematical models for thrusters, unsteady fluid flow and hydrostatics are also presented.

A solution method for the mathematical model is developed in the software package, Uuv6dof. The software was developed under the Matlab Version 4 environment, using the Simulink Toolbox to enable time domain simulation of underwater bodies.

Chapter 3. The Planar Motion Mechanism

3.1 Introduction

The Planar Motion Mechanism (PMM) is an electro-mechanical device that can oscillate models suspended in a water flow, in a controlled cyclic manner. PMMs have been used to characterise the hydrodynamics of both surface and submerged vehicles, since the late 1950s. The water flow is generated by towing the model/PMM arrangement on a carriage in a water tank or by a facility such as a circulating water channel (CWC) in which the carriage is stationary and the water moves past the model.

Loads on the model are measured concurrently with the angular and positional displacement in the flow. The force and moment data are used to determine the model's manoeuvring behaviour, which is characterised by 'hydrodynamic coefficients' or 'derivatives'. These are scaled to the full dimensional size of the corresponding vehicle and used in simulation codes for determining the vehicle's stability and manoeuvring performance.

The recent installation of a PMM facility in Australia has established a capability that previously existed overseas. The PMM was designed and built by the Defence Science and Technology Organisation (DSTO), and completed as part of its contribution to the Australian Maritime Engineering (AME) Co-operative Research Centre (CRC). The PMM arrangement is shown in Figures 3.1 and 3.2. The facility was installed in the Australian Maritime College's Circulating Water Channel in Beauty Point, Tasmania.

The AME PMM, the data file format, the load cell and the model mounting arrangements are described in this chapter. The development of the motion equations for the AME PMM and validation are also included.

3.2 Description

The AME PMM operates only in the horizontal plane. It has two modes of operation; namely the 'static' and 'dynamic' modes. In the dynamic mode, the PMM moves in translation and rotation. The motions have been designed to produce pure translation and pure rotation relative to the water. The static mode allows the models to be held stationary relative to the moving flow at various angles of incidence.

Two servo-motors are used to provide the PMM motions: one is dedicated to providing translation and the other rotation. The motors are driven under closed loop control of an IBM PC. However, since the motors are independently controlled, the PMM is also capable of providing non-sinusoidal motions, within the limitations of the mechanism.

The maximum static rotation in the horizontal plane is ±45°. In the dynamic mode, the maximum peak to peak horizontal oscillation is 0.30m and the maximum peak to peak rotational oscillation is 30°. The oscillatory frequency ranges from 0.01 Hz to 0.20 Hz. The maximum translational rate is therefore 0.19 m/s.

A six-component strain gauge load cell is currently used to measure forces and moments on models on the AME PMM. The motions performed by the model under control of the PMM are measured with transducers fitted to the mechanism, at the point of the motor drive system, to measure the position and rotation displacements. Data is acquired on a separate PC-based data acquisition system.

Figures 3.1 and 3.2 show general arrangements of the AME PMM. In both the lifting frame attaches to the tank or carriage, and enables the PMM to be raised and lowered into the flow as required.

3.3 Model Mounting Arrangements

There are two methods currently available for mounting models to the AME PMM. The arrangement shown in Figure 3.1 shows the first method, with the AME PMM mounted onto the lifting frame. Attached to the PMM is the single vertical 'strut' from which models are mounted. The arrangement shown in Figure 3.2 shows the 'sting' attached to the PMM. This allows for models to be mounted from behind in their wake region, thus reducing flow interference due to the presence of the support.

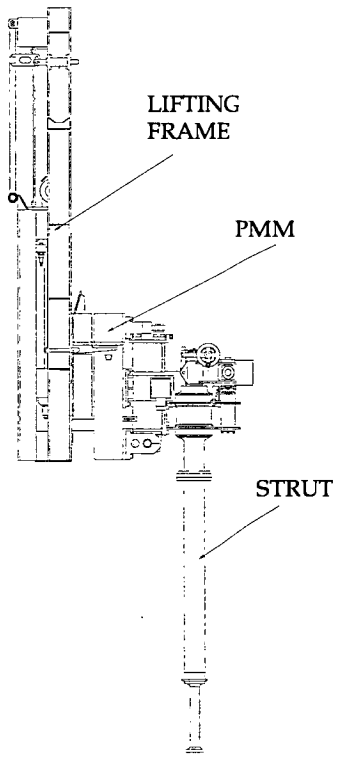

Figure 3.1 Strut mounting arrangement for the AME PMM.
(Modified ACAD Drawing NC-00-00.dwg.
Source: DSTO Engineering Services Archive)

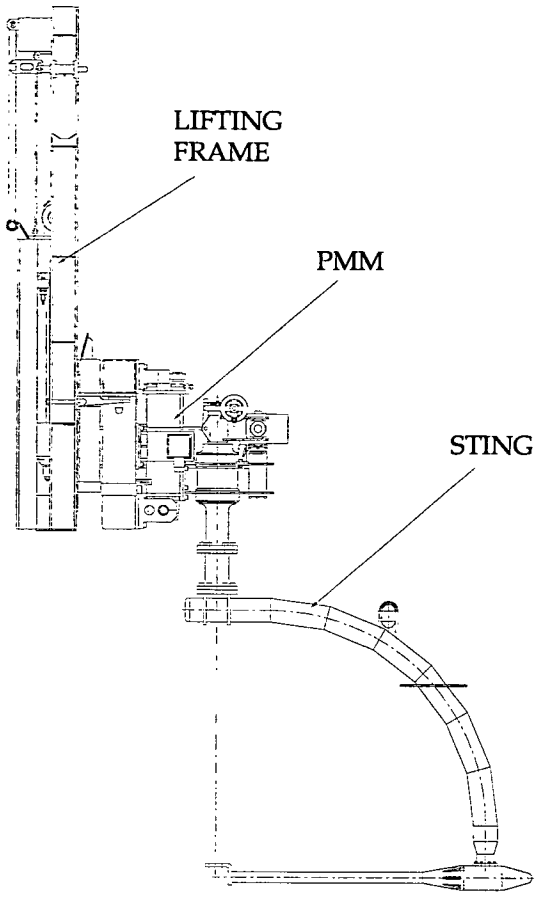

Figure 3.2 Sting mounting arrangement for the AME PMM.
(Modified ACAD Drawing NC-09-00.dwg.
Source: DSTO Engineering Services Archive)

3.4 The Load Cell

The Advanced Mechanical Technology Inc. (AMTI) load cell, serial number M3378 was used for the work described in this thesis. The load cell is comprised of bonded strain gauge transducers that incorporate special seals to prevent water and oil contamination. It is made of the aluminium alloy 7075-T6 which is anodised. Elastomeric O-ring seals provide internal protection of the strain gauges and wiring. The strain gauges are also potted (AMTI 1993). A schematic of the AMTI load cell is shown in Figure 3.3. Details of the load cell are given in Appendix 3.

The load cell is located at the interface between the test model and the mount arrangement, and is mounted internally to the model. This has the added advantage of protecting the load cell from external hydrodynamic forces.

The force transducer has 6 outputs, which correspond to measurements of the three forces along the X, Y, and Z body axes and the moments about the same. The load cell coordinate system is shown in Figure 3.3. The parameters that relate the input forces or moments on the instrument, to the output signal, are known as the load cell 'sensitivities'. A complete 'sensitivity matrix' for this load cell contains 36 numbers. Each channel has its own sensitivity, relating its input to the output voltage, and five other parameters that relate the effect of inputs from the other channels on the output channel. These are known as the 'cross-talk sensitivities'.

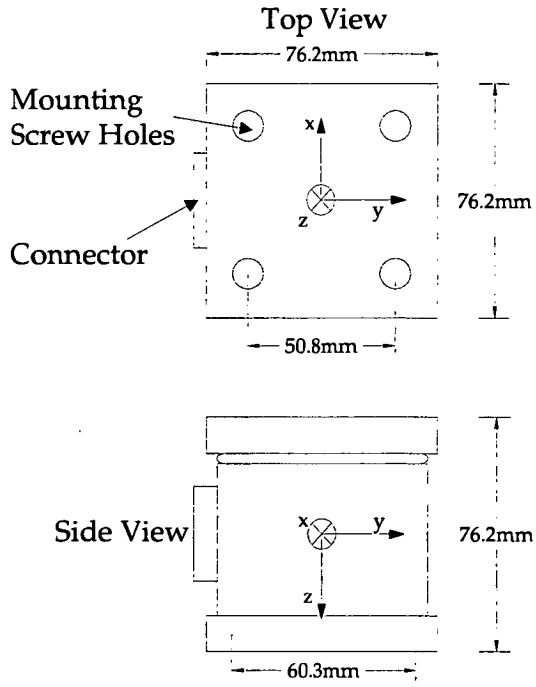

Figure 3.3 AMTI Load Cell M3378:
Dimensions and coordinate system; based on AMTI (1993)

An initial calibration of the AMTI load cell (ETRS 1995) confirmed the manufacturer's sensitivities to within 2.6% over all degrees of freedom. However, further testing of the load cell showed errors when loads were placed on large moment arms. It would appear that the manufacturer's data for the load cell

sensitivities were determined from calibration tests where small moment arms were applied. These errors are described in more detail in Heron (1998).

3.5 The Data File

An Ascii data file is created and stored to disk for each test run performed by the DSTO/AMECRC PMM. The file is created by the computer dedicated to data acquisition and is stored under a user defined directory. The file contains a header block that describes the variables for that run, followed by the data from the experiment. The information describing each run is manually entered into the software before each test is performed.

The header in each data file consists of the first 34 rows. The file format is illustrated in Appendix 3. The 12 channels of data recorded by the acquisition system are:

1. The sample number
2. Force, X
3. Force, Y
4. Force, Z
5. Moment, K
6. Moment, M
7. Moment N
8. Flow speed sensor 1
9. Flow speed sensor 2
10. Flow speed sensor 3
11. The translation displacement
12. The rotation displacement

The data recorded in the file are given in dimensional units. The conversion of the data from machine units to the dimensional units was completed as part of the acquisition process. The load cell calibration constants determined prior to the testing were used. The removal of offsets or zeros was performed later in the analysis procedure.

The order of the data channels given here relates directly to the load cell coordinate axes illustrated in Figure 3.3. For example; the load cell x-axis will be recorded in channel two, while the load cell y-axis data is recorded in channel three, and so on. It is important to note that the axes being used for the body may not be the same as for the load cell. The data file header can be amended to account for such changes, as can be seen in Appendix 3.

The data analysis algorithm removes the header and places the data contents of the file into a matrix A. The data in each channel is then a column vector. Therefore

$$A = A(i, j)$$

where

i ranges from 1 to N, the number of samples, and

j ranges from 1 to 12, the number of data channels.

3.6 PMM Motions

3.6.1 Introduction

The AME PMM motions are provided by two independently controlled servo-motors. As mentioned above, there are two ways in which the PMM is used to provide motions to the model. The dynamic mode produces a combination of cyclic translation and rotation motions while the static mode enables the models to be held stationary, at angles to the water flow.

The AME PMM provides horizontal plane motions similar to those described in Driscoll (1990) and Gill (1976). Typically 'pure yaw' and 'pure sway' dynamic motions, or 'pure heave' and pure pitch' for vertical PMMs (Booth 1973 and Fyfe 1979), are used as standard test motions. These motions are sinusoidal, requiring amplitude of displacement and frequency of oscillation to be specified for each test.

The manner in which the AME PMM provides a motion is quite different to those described by Driscoll (1990), Gill (1976), Booth (1973) and Fyfe (1979), in that independent translation and rotation are combined to provide the required motion.

For instance, the translation motor can provide cyclic lateral motions independently of the rotation motor that can provide cyclic angular motions. These are combined to give 'pure sway' and 'pure yaw'.

To understand the motions clearly, it is important to recognise the distinction between the model axes and the tank coordinate axes. The equations that drive the PMM motions are defined relative to the tank coordinate system. This provides a fixed reference for the displacement of the model.

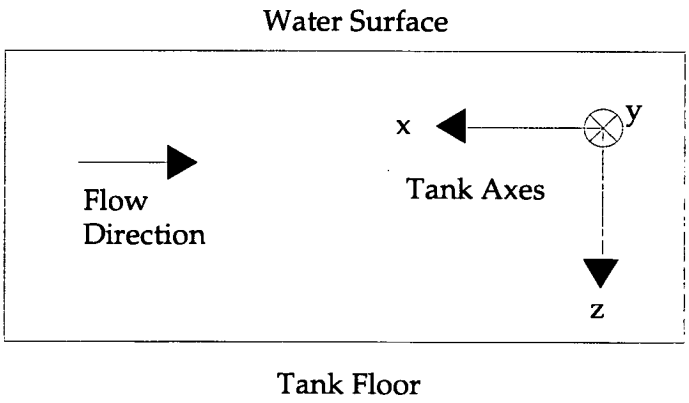

Figure 3.4 Side view of the Tank Coordinate System:
x-axis facing into flow, y-axis positive into page and z positive downwards.

The motion definitions relate to the body coordinate system described in Figure 2.1. However, the motion equations that drive the PMM in the Circulating Water Channel (CWC) are given relative to the tank coordinate axes, shown in Figure 3.4. The reference point for the motions is given fixed to the centre of rotation, in the plane of movement, of the PMM shown in Figures 3.1 and 3.2.

3.6.2 Pure Sway

Pure sway is imparted to the model by oscillating it in the tank y-axis while its heading is set to zero. The motion imparted to the model is sinusoidal, and the lateral displacement y of the model is given by the expression

$$y = y_0 \sin \omega_t t \qquad (3.1)$$

where

y_0 is the amplitude of the sinusoidal motion

ω_t is the frequency of the translation oscillation and

t is the time

The translation velocity and acceleration of the body are then given by

$$v = \dot{y} = \omega_t y_0 \cos \omega_t t \tag{3.2}$$

and

$$\dot{v} = \ddot{y} = -\omega_t{}^2 y_0 \sin \omega_t t \tag{3.3}$$

where v is the lateral velocity of the model in the body co-ordinate axes.

The model heading to the flow ψ, is given by

$$\psi = 0 \tag{3.4}$$

The velocity of the model along the body x-axis is

$$u = U_f \tag{3.5}$$

Since the total model speed in the horizontal plane is

$$U = \sqrt{u^2 + v^2}$$

and substituting for the lateral velocity of the model v, the total speed of the model is

$$U = \sqrt{U_f{}^2 + (\omega_t y_0 \cos \omega_t t)^2} \tag{3.6}$$

An example of pure sway motion is given in Figure 3.5.

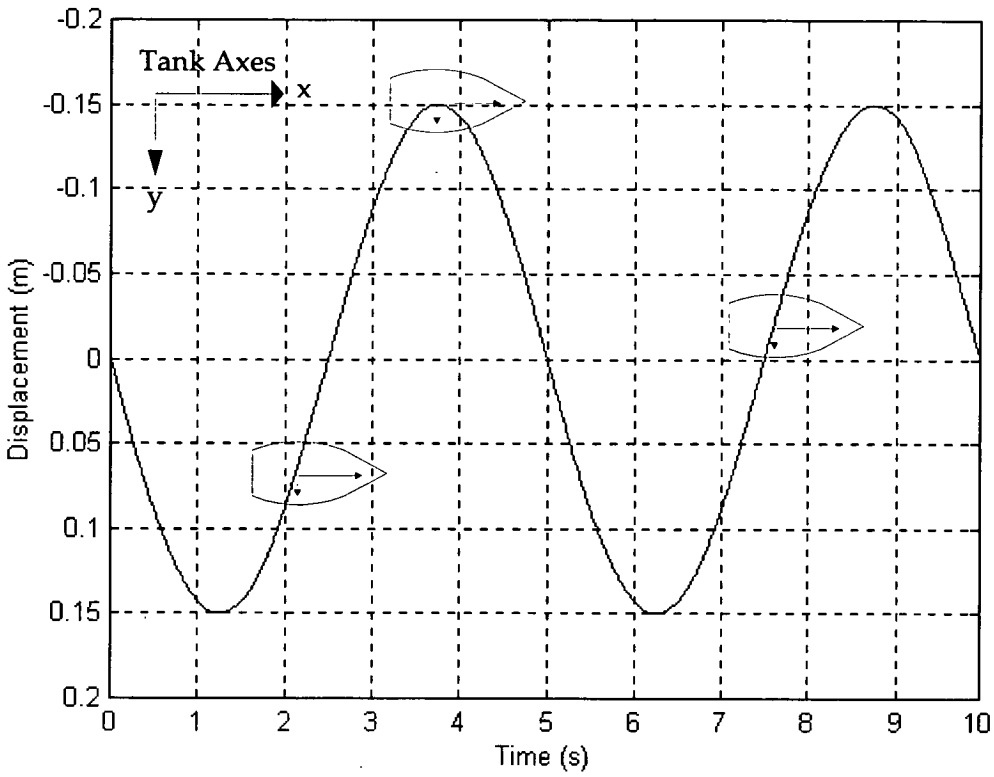

Figure 3.5 Simulated Pure Sway Motion: Displacement is along the tank y-axis with maximum amplitude of 0.15m and translation frequency of 0.20Hz. The model heading is zero with respect to tank x-axis.

3.6.3 Pure Yaw

Pure yaw motion involves oscillating the model cyclically in rotation and translation. However, for pure yaw to exist, the body x-axis must be coincident with the tangent of the model's path, ie.

$$\tan\psi = \frac{\dot{y}}{U_f} \tag{3.7}$$

where U_f is the tank water flow speed.

Solving for the translation velocity in pure yaw gives

$$\dot{y} = U_f \tan\psi \tag{3.8}$$

The angular displacement drives the yaw motion, with the model heading given by

$$\psi = \psi_0 \sin \omega_r t \tag{3. 9}$$

where

ψ_0 is the maximum amplitude of the angular oscillation, and

ω_r is the frequency of the angular oscillation.

Now substituting for ψ in Equation (3.8) and then integrating gives the y-axis displacement of the body as

$$y = U_f \int \tan(\psi_0 \sin \omega_r t) dt \tag{3. 10}$$

Further boundary conditions are derived to define the pure yaw motion. These are:

(1) At $t = \dfrac{(2k \pm 1)\pi}{2\omega_r}$; $y = \mp y_0$ and $\psi = 0$,

(2) At $t = \dfrac{2k\pi}{\omega_r}$; $y = 0$ and $\psi = -\psi_0$, and

(3) At $t = \dfrac{(2k-1)\pi}{\omega_r}$; y=0 and $\psi = \psi_0$

where $k = 1,2,...$ is the cycle number.

Equation (3.10) is modified to account for the boundary conditions, thus giving the y displacement of the body to be

$$y = U_f \int \tan\left(\psi_0 \sin\left(\omega_r t - \frac{\pi}{2}\right)\right) dt \tag{3. 11}$$

The displacement is then solved using a 4th order Runge Kutta numerical integration scheme. Therefore

$$y_{i+1} = y_i + \frac{1}{6}(k_1 + 2k_2 + 2k_3 + k_4) \tag{3. 12}$$

where $$k_1 = \Delta t \, \beta(t_i) \tag{3. 13}$$

$$k_2 = \Delta t \, \beta\left(t_i + \frac{1}{2}\Delta t\right) \tag{3. 14}$$

$$k_3 = \Delta t\, \beta\left(t_i + \frac{1}{2}\Delta t \right) \tag{3. 15}$$

$$k_4 = \Delta t\, \beta(t_i + \Delta t) \tag{3. 16}$$

and

$$\beta(t_i) = U_f \tan\left(\psi_0 \sin\left(\omega_r t_i - \frac{\pi}{2} \right) \right) \tag{3. 17}$$

The x-axial speed of the model is

$$u = U_f \sqrt{1 + \tan^2\left(\psi_0 \sin\left(\omega_r t - \frac{\pi}{2} \right) \right)} \tag{3. 18}$$

Since $v = 0$ in pure yaw, the total speed of the model is the same as the x-axial speed u of the model, therefore

$$U = u \tag{3. 19}$$

The software 'pureyaw.m' and 'beta.m' that generate the simulated results are available in Appendix 3. An example of pure yaw is demonstrated in Figure 3.6. Note in the figure that the body is shown to be coincident with the path of the vehicle, given by the solid line. The dashed line represents the heading of the vehicle.

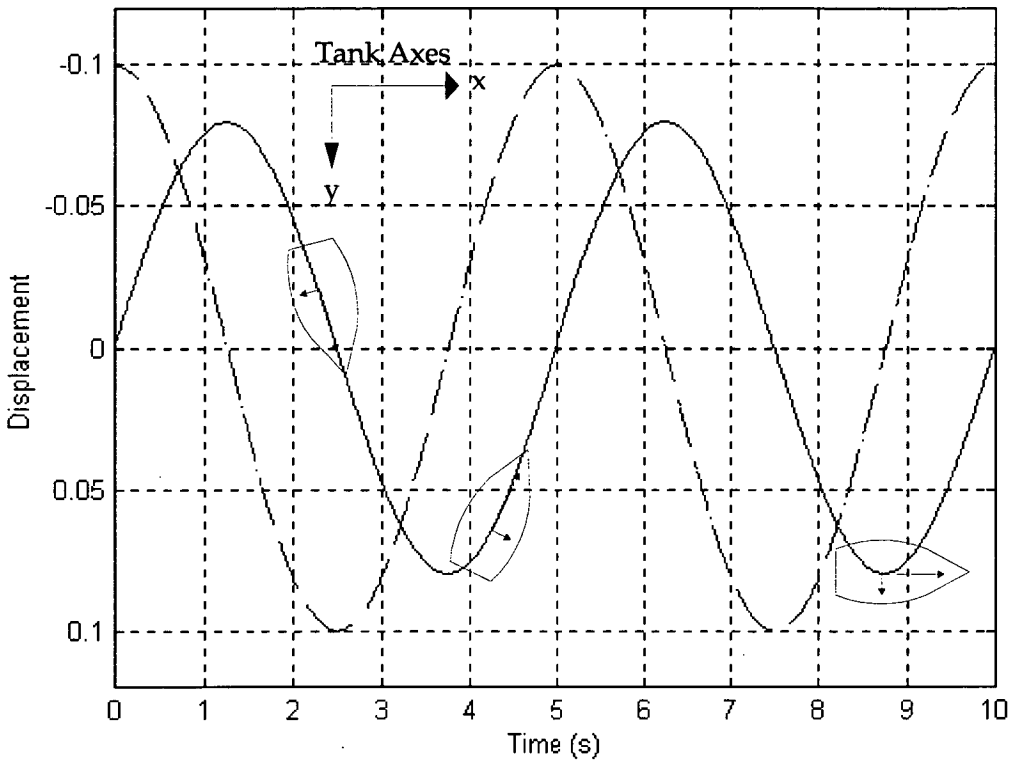

Figure 3.6 Pure Yaw Motion Simulation: The solid line represents the translation displacement, while the dashed line gives the rotation or heading of the body. Both curves use the same y axis in this example, where the units for translation are metres and those for rotation are radians. The maximum heading amplitude is 0.10 radians, while the frequency of rotation is 0.20 Hz. The resulting y-translation over time is shown.

3.6.4 Rotation Motion

A top view schematic of the AME PMM arrangement that produces the rotation motion is given in Figure 3.7. The simple view of the design shows the rotation motor fixed at a point A, about which it is allowed to rotate. Similarly the rotation assembly is fixed at a point B, about which it can also rotate. The screwjack is fixed to the rotation assembly at a point P; the length from B to P, denoted by b, is a constant. Similarly, the length from B to A, denoted by a, is constant. The motor revolutions are controlled to adjust the length of the screwjack arm L, the length between A and P, to produce angular rotation. The rotation assembly moves together with the motor to produce the motion.

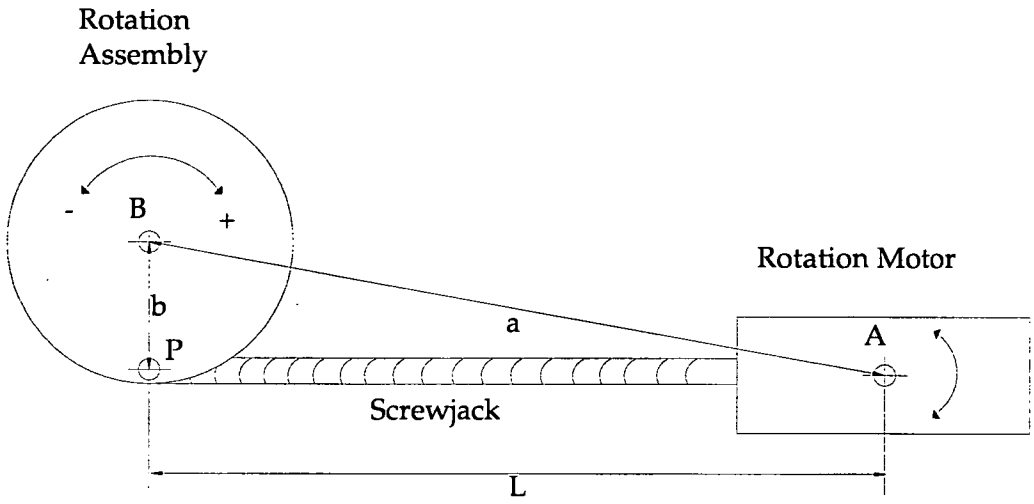

Figure 3.7 Top view schematic of the AME PMM arrangement for producing rotation motion.

The geometry of the arrangement is given in Figure 3.8. The angle ψ is by definition the rotation angle of the PMM, and is created by the angle that the line BP makes with BB′, where B′ is a fixed point also. The angle α is that which the line BA makes with BB′, thus α is constant.

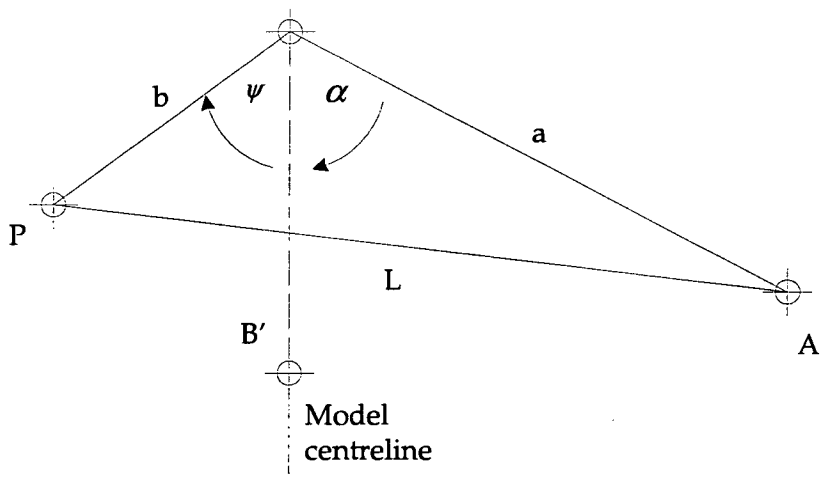

Figure 3.8 Rotation motion geometry.

The signal to the motor is given in steps, such that the number of revolutions the motor turns is

$$M_{revs} = \frac{n}{S} \tag{3. 20}$$

where

M_{revs} is the number of motor revolutions,

S is the number of steps for one complete revolution of the motor,

n is the number of steps.

If a gear ratio exists between the screwjack revolutions and the motor, then the screwjack revolutions can be given by

$$\begin{aligned} J_{revs} &= G\, M_{revs} \\ &= \frac{G\ n}{S} \end{aligned} \tag{3. 21}$$

where

J_{revs} is the number of screwjack revolutions, and

G is the gear ratio between the screwjack and the motor.

The amount of change in the length of the arm AP given by one revolution of the screwjack is given by L_1. Therefore the change in arm length of AP for n motor steps, is given by

$$\Delta L = \frac{G\, n\, L_1}{S} \tag{3. 22}$$

From the geometry the length L of AP is given by the expression

$$L = \sqrt{a^2 + b^2 - 2\, ab \cos(\alpha + \psi)} \tag{3. 23}$$

Note that when $\psi = 0 \quad L = L_0$, therefore

$$\alpha = \cos^{-1}\left(\frac{a^2 + b^2 - {L_0}^2}{2ab}\right) \tag{3. 24}$$

The number of motor steps n required to give the rotation ψ is therefore

$$n = \frac{S\left(\sqrt{a^2 + b^2 - 2\, ab \cos(\psi + \alpha)} - L_0\right)}{G\, L_1} \tag{3. 25}$$

where α is given by Equation (3.24).

The parameters for the AME PMM are:

$$a = 462.50\,\text{mm}$$
$$b = 300.00\,\text{mm}$$
$$L_0 = 352.00\,\text{mm}$$
$$L_1 = 5.08\,\text{mm}$$
$$G = 1.92$$
$$S = 8000$$

The relationship is shown in Figure 3.9.

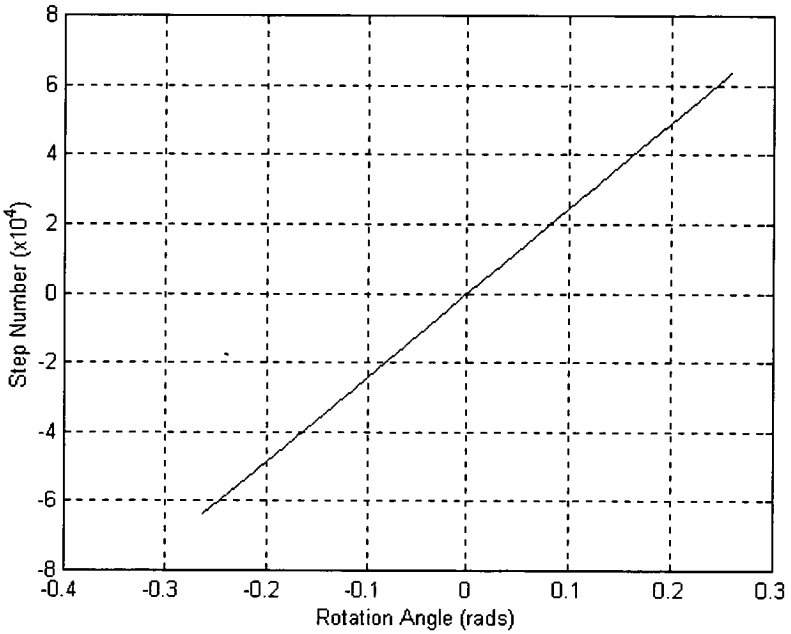

Figure 3.9 Relationship between the motor step number and the angular displacement given by the rotation assembly.

The software 'ROTATION_MOTION.M', used to generate the simulations of the rotation displacement, is given in Appendix 3.

3.6.5 Translation Motion

The translation motor on the AME PMM is identical to the rotation motor, thus the relationship between the motor steps and translation distance is similar to that given in Equation (3.22). Hence

$$n = \frac{S\,y}{G\,L_1} \tag{3.26}$$

where y is the translation displacement from the median position on the PMM carriage.

Note: A negative step value ie. $n < 0$ signals reverse motor operation.

3.7 Motion Analysis

3.7.1 Introduction

In order to validate the AME PMM motions, and as part of the initial analysis for hydrodynamic coefficient determination, it was necessary to determine the frequency and amplitude of the displacements directly from the measured data. Also, it was necessary to determine the start point at which the motions were recorded relative to a standard sinusoid. This allows the displacement signals to be regenerated without the inherent noise from transducers, thus allowing differential displacement signals to be generated.

The measured displacement outputs for two typical PMM tests are shown in Figures 3.11 and 3.12. Figure 3.11 illustrates the translation and rotation displacement for a pure sway test where the maximum amplitude is 0.02m and the frequency of oscillation is 0.20Hz. The rotation transducer data was recorded and is also given in Figure 3.11. This plot illustrates the effect of noise on measurements. Figure 3.12 illustrates the translation and rotation displacements for a pure yaw test where the maximum amplitude is 0.01 radians and 0.02Hz. The noise observed in these figures is attributed mainly to vibration in the PMM. Note that the data shown in these figures has been filtered at the point of acquisition by an anti-aliasing filter with a cut-off frequency of 10Hz.

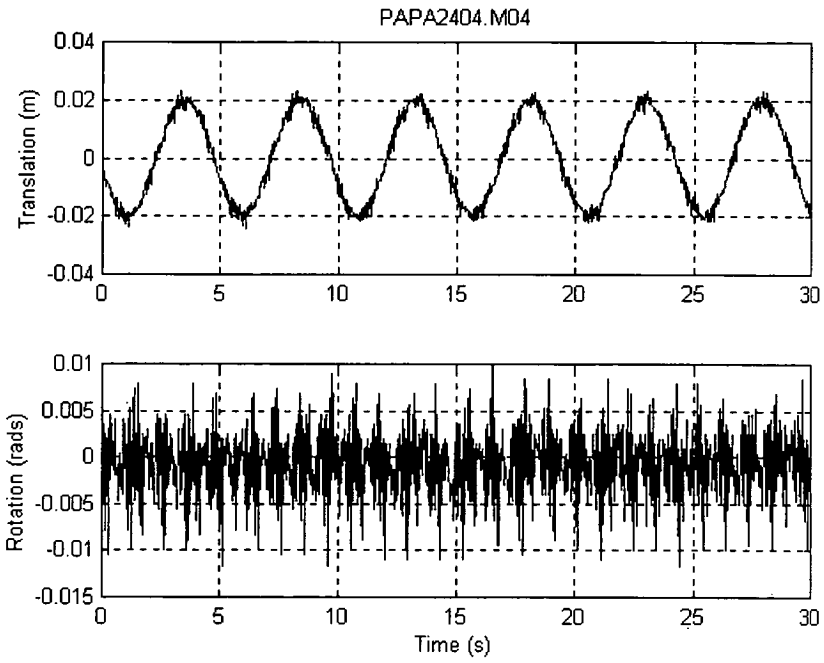

Figure 3.11 The translation and rotation plots shown for a typical test performed in pure sway with translation amplitude 0.02m and frequency 0.20Hz.

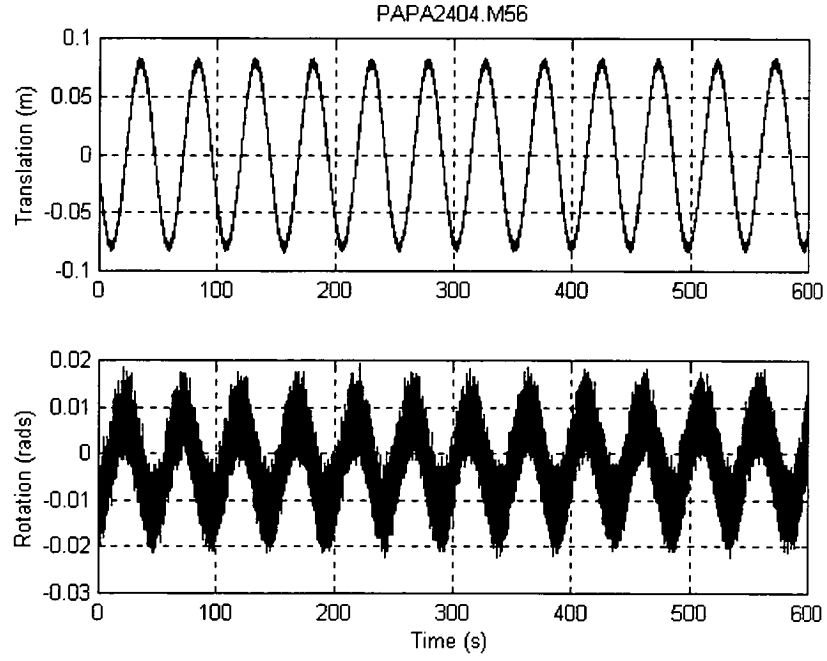

Figure 3.12 The translation and rotation plots shown for a typical test performed in pure yaw with rotation amplitude of 0.01rads and frequency 0.02Hz.

3.7.2 Fourier Transformation

The FFT algorithm is based on the Radix-2 method described in Bellanger (1986) and Rabiner (1975). The algorithm was implemented using the Matlab toolbox for signal processing (Krauss, 1994).

The discrete Fourier transformation is given by

$$YF(k+1)=\sum_{n=0}^{N-1} Y(n+1)\,W_N^{kn} \qquad (3.27)$$

where

YF is the transformed series of Y,

k is sample number,

$W_N = e^{-j(2\pi/N)}$, and

N = length(Y), ie. the length of the data vector.

The Matlab FFT command was applied to perform the Fourier transform. eg.

$$YF = fft(y,N)$$

The spectral response was determined by the following Matlab commands:

Line 1: YF=fft(y,N);

Line 2: Syy=yf.*conj (yf)/N; (3. 28)

where

YF is the frequency domain FFT response,

y is the time domain measurement data,

N is the number of samples to perform the FFT,

conj () is the Matlab command to determine the conjugate of the argument, and

fft is the Matlab command to implement the FFT algorithm.

To enable the Radix-2 method to be employed, the measured data was padded with zeroes, taking the total number of samples to a pre-defined number N such that

$$N = 2^a \qquad (3.29)$$

where a is an integer value greater than zero.

Since the sample rate f_s is fixed at 30.003 Hz for the HPMM data acquisition system, the spectral resolution was given by

$$\Delta f_r = \frac{30.003}{2^a} \tag{3. 30}$$

The frequency resolutions of the various values of a are given in Table 3.1.

a	Δf_r (Hz)
11	1.465×10^{-2}
12	7.325×10^{-3}
13	3.663×10^{-3}
14	1.831×10^{-3}
15	9.156×10^{-4}
16	4.578×10^{-4}
17	2.289×10^{-4}
18	1.145×10^{-4}
19	5.723×10^{-5}
20	2.861×10^{-5}

Table 3.1 Frequency resolution for various values of 'a' given by Equation (3.30).

3.7.3 Frequency Determination

The frequency was found by determining the sample at which the maximum energy magnitude of the power spectral density function occurs. This was determined using the Matlab 'FIND' function. The sample at which the maximum frequency occurs is

$$k = find(Syy == \max(Syy)) \tag{3. 31}$$

where k is the sample number and S_{yy}. is determined from the Matlab commands given in Equation (3.28).

The angular frequency, in rads/s, is given by

$$\omega = \frac{2\pi(k-1)f_s}{N} \tag{3.32}$$

The power spectral density function of the test data shown in Figures 3.11 and 3.12 was determined over the frequency range 0 to the nyquist cut-off frequency $f_s/2$. The energy density magnitude of the data is shown in Figures 3.13 and 3.14 over a small frequency range centred on the main frequency response.

The description of several data files is listed in Table 3.2. The files represent a series of tests performed using the AME PMM. The measured data output is analysed using the software 'motion_analysis.m', which is given in Appendix 3., and a comparison between the demanded and measured parameters is given.

The frequency response was found to be inaccurate compared to the specified frequency in all cases. This result is discussed further in the following section.

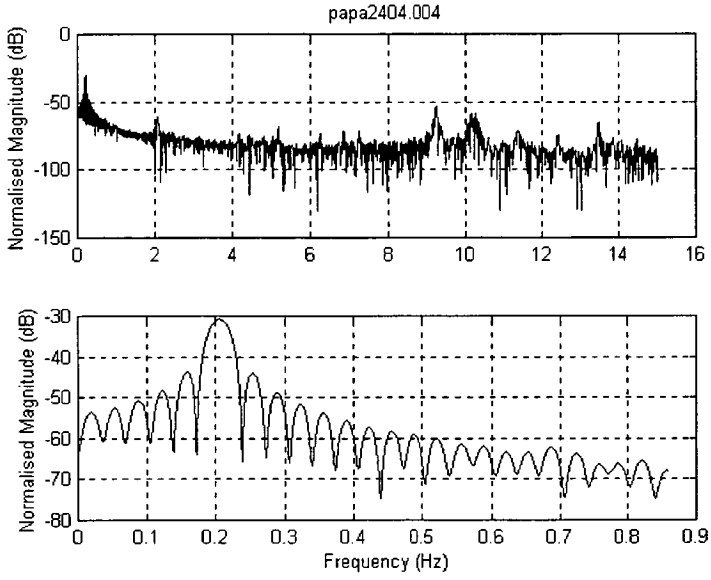

Figure 3.13 Normalised power spectral density function of the pure sway data shown in Figure 3.11. The first plot shows the response over the frequency range 0 to 15Hz, the nyquist frequency and the second over the range 0 to 0.9 Hz. The desired frequency response was 0.20 Hz.

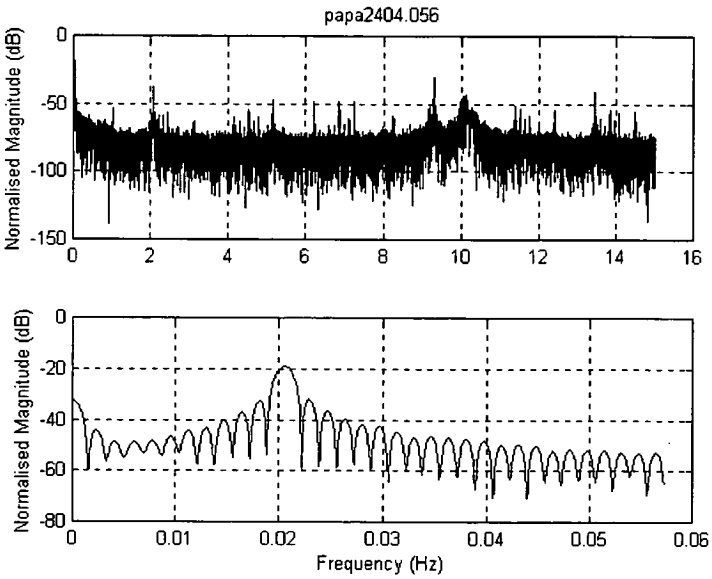

Figure 3.14 Normalised power spectral density function of the pure yaw data shown in Figure 3.12. The first plot shows the response over the frequency range 0 to 15Hz, the nyquist frequency, and the second over the range 0 to 0.06 Hz. The demanded frequency was 0.02 Hz.

3.7.4 Potential Sources of Frequency Error

It was apparent, from the calculated frequency values in Table 3.2 that significant errors in the frequency were present in the motions. Since the frequency was determined from measurements of displacement, it was important to confirm whether the error was due to motor performance or whether it was due to the analysis of the motor performance. If the performance of the two motors was significantly different then the pure yaw motion, which relies on the responses of the two motors being the same, would be affected. Pure sway motion would not be affected so long as the actual frequency of the system could be accurately identified.

On examination of the system, several errors were identified in the process for driving and measuring the oscillatory motions of the HPMM. These included:

- Software round-off in motor control software
- Motor time constant error
- Spectral leakage and interference
- Round-off noise in FFT due to word length
- Quantisation in FFT due to word length

No.	Name	Motion	Demanded Frequency		Measured Frequency	
			Trans.	Rot.	Trans	Rot.
1	Papa2404.m04	Sway	0.2000	n/a	0.2051	n/a
2	Papa2404.m10	Sway	0.2000	n/a	0.2054	n/a
3	Papa2404.m11	Sway	0.1600	n/a	0.1677	n/a
4	Papa2404.m17	Sway	0.1600	n/a	0.1739	n/a
5	Papa2404.m18	Sway	0.1200	n/a	0.1234	n/a
6	Papa2404.m24	Sway	0.1200	n/a	0.1229	n/a
7	Papa2404.m27	Sway	0.0800	n/a	0.0841	n/a
8	Papa2404.m29	Sway	0.0400	n/a	0.0410	n/a
9	Papa2404.m30	Sway	0.0200	n/a	0.0205	n/a
10	Papa2404.m31	Yaw	0.2000	0.2000	0.2054	0.2050
11	Papa2404.m39	Yaw	0.2000	0.2000	0.2056	0.2047
12	Papa2404.m40	Yaw	0.1600	0.1600	0.1670	0.1664
13	Papa2404.m47	Yaw	0.1600	0.1700	0.1740	0.1736
14	Papa2404.m48	Yaw	0.1200	0.1200	0.1229	0.1234
15	Papa2404.m53	Yaw	0.1200	0.1200	0.1229	0.1234
16	Papa2404.m54	Yaw	0.0800	0.0800	0.0824	0.0826
17	Papa2404.m55	Yaw	0.0400	0.0400	0.0410	0.0410
18	Papa2404.m56	Yaw	0.0200	0.0200	0.0205	0.0205

Table 3.2 Measured frequency results of several PMM test runs. The demanded and actual measured frequency of the translation and rotation motor is given, where it is used in the motion. The data were sampled using a rectangular window and were padded with zeroes so that the data record was length 2^{19}. *The FFT algorithm described in Equations (3.27) - (3.32) were applied to the data to determine the frequency.*

The first two errors are concerned with producing the motions while the third is concerned with the calculation of the frequency from the spectral response of the displacement measurements. The remaining round-off noise and quantisation errors were considered insignificant due to a word length of 32 bits.

3.7.5 Software Round-Off

The AME HPMM motor control software alters the specified value of frequency that is set at the graphical user interface. Due to constraints on the data requirements for the HPMM motors, manipulation of the input frequency is performed. The following lines of 'C' language code manipulate the set frequency (Marker, 1998):

```
Line 1:    period=1/freq;
Line 2:    num_packets=4*(int)(period/(4*0.032));
Line 3:    period=num_packets*0.032;
Line 4:    freq=1/period;
```

The first line converts the set frequency to a period. The second determines an integer number of packets for one oscillation, while ensuring that an integer number exists for one quarter of the oscillation. The time spacing between packets is given as 32 milliseconds. The resulting frequencies after software round-off are given in Table 3.3.

Desired Freq. (Hz)	Desired Period (s)	Software Period (s)	Software Freq. (Hz)
0.02000	50.00	49.92	0.0200
0.04000	25.00	24.96	0.0401
0.06000	16.67	16.64	0.0601
0.08000	12.50	12.42	0.0805
0.1000	10.00	9.984	0.1002
0.1200	8.333	8.320	0.1202
0.1400	7.143	7.040	0.1420
0.1600	6.250	6.144	0.1628
0.1800	5.556	5.504	0.1817
0.2000	5.000	4.992	0.2003

Table 3.3 Frequencies determined by HPMM motor control software, taking into account software round-off.

3.7.6 Motor Time Constant

The time spacing between the packets of data sent to the motors was specified to be 32 milliseconds. However, it was determined, and later confirmed by the manufacturer of the motors, that the actual spacing between data packets was 31.232 milliseconds. The error consistently appears in all HPMM experiments for both motors. The 2.4% error in the time spacing between packets is attributed to the accuracy in setting the motor clocks.

The scaled time constant effectively scales the frequency of the motors. Hence the actual frequencies driven by the motors are increased by 2.4% from those given in Table 3.3. The resulting frequencies for the desired motions, considering the software round–off error and the motor time constant error, are given in Table 3.4.

Desired Freq. (Hz)	Actual Freq. (Hz)
0.02000	0.0205
0.04000	0.0410
0.06000	0.0616
0.08000	0.0825
0.1000	0.1026
0.1200	0.1231
0.1400	0.1455
0.1600	0.1668
0.1800	0.1862
0.2000	0.2052

Table 3.4. Actual frequency of motors given the set frequency, taking into account the software round-off and motor time constant errors.

Still, the values for the corrected frequency in Table 3.4 do not compare to the measured results in Table 3.2. The next step was to look at the measurement technique, in particular, the affect of the FFT on the measured results.

3.7.7 Fast Fourier Transformation Effects on Frequency Determination

The sampling of the displacement data returns discrete values that are implicitly weighted by a value 1. The sampling process described here is called "windowing". The window, which has been applied to the data in this instance, is a rectangular box. Inside the window, the data is weighted by values of 1, and outside the window, the data is weighted with values of zero. The effect of sampling the data in this way is the same as convolving the frequency response of the displacement measurements, with a SINC function.

The discrete frequency domain implies the windowed data is folded in time to form an eternal waveform, creating discontinuities at the fold points. If the sampling frequency is not an integral multiple of the displacement frequency response then spreading of the spectra occurs. This effect is known as 'spectral leakage' (Technisearch, 1991). To produce the optimal waveform in the frequency domain requires an infinite amount of data points. This is not practical, however, spectral leakage can be reduced by the application of optimal window designs (Bellanger, 1986 and Rabiner, 1975).

An example of the effect of spectral leakage is shown in Table 3.5 where the results from the analysis of a data file generated by software are given. The generated data file represents a pure sway motion with an amplitude of 0.14 m and a frequency of 0.205300 Hz. The file is analysed with various values of N using the algorithm in Equation (3.29).

Table 3.5 shows that by increasing the number of cycles of data, the estimate of the expected frequency is improved. As the rectangular window extends to infinity (to 4000 in this example) the estimate tends to the set value. Improved resolution offers a more precise estimate, however does not reduce the effect of the spectral leakage.

The frequency values were not purely increasing or decreasing functions of resolution, instead it was observed that the frequency values tended to oscillate with resolution. However, this only occurred until the resolution was fine enough to resolve variations to the number of decimal places given.

a	cycles=5	cycles=5.5	cycles=10	cycles=15	cycles=30	cycles=4000
11	0.205099	0.205099	0.205099	0.205099	0.205099	0.205099
12	0.205099	0.205099	0.205099	0.205099	0.205099	0.205099
13	0.205099	0.205099	0.205099	0.205099	0.205099	0.205099
14	0.203267	0.205099	0.205099	0.205099	0.205099	0.205099
15	0.204183	0.204183	0.205099	0.205099	0.205099	0.205099
16	0.204183	0.204183	0.205099	0.205099	0.205099	0.205099
17	0.203954	0.204183	0.205099	0.205099	0.205328	0.205328
18	0.204069	0.204297	0.204984	0.205213	0.205213	0.205328
19	0.204069	0.204240	0.204984	0.205156	0.205270	0.205328
20	0.204040	0.204269	0.204984	0.205156	0.205270	0.205299

Table 3.5 Example of the effect of spectral leakage. Generated signal: Motion type = pure sway, amplitude=0.14m, frequency= 0.205300 Hz, and sample frequency=30.003 Hz. Variation of the number of samples for the FFT denoted by 'a', given in Equation (3.29), and the number of cycles of generated data, denoted by 'cycles'.

3.7.8 Hanning Window

To reduce the effects of spectral leakage an optimal window design, such as a Hanning Window, may be implemented instead of the rectangular window. The expression for the Hanning Window coefficients are given by Equation (3.33) and the resultant response is shown in Figure 3.15.

$$w(k)=0.5\left(1-\cos\left(2\pi\frac{k}{n+1}\right)\right), \quad k=1,....,n \tag{3.33}$$

where $w(k)$ is the weighting value of the kth sample.

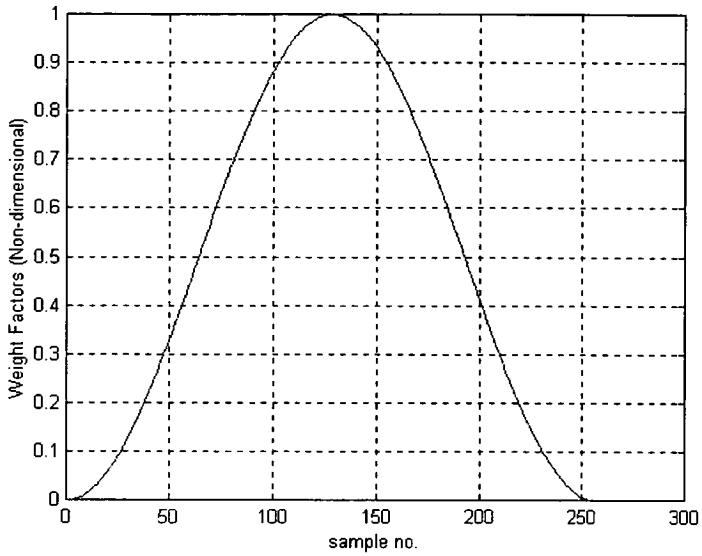

Figure 3.15 A 256 point Hanning Window

A Hanning Window was implemented in simulation using the same parameters as those used for the simulated results given in Table 3.5. Results from the analysis of the simulated data are using the Hanning Window are given in Table 3.6

a	cycles=10	Cycles=20
11	0.205078	0.205078
12	0.205078	0.205078
13	0.205078	0.205078
14	0.205078	0.205078
15	0.205078	0.205078
16	0.205078	0.205078
17	0.205078	0.205307
18	0.205307	0.205307
19	0.205307	0.205307
20	0.205307	0.205307

Table 3.6 Spectral analysis of simulated data using a Hanning Window to sample the data. Generated signal: Motion type = pure sway, amplitude=0.14m, frequency= 0.205300 Hz, and sample frequency=30.003 Hz.

Comparison of the results in Table 3.5 with those in Table 3.6 clearly indicates that the Hanning Window has reduced the spectral leakage and that the results are equivalent to the set frequency within the resolution given. It is worth noting also that the results were achieved in fewer cycles than required in those given in Table 3.5.

3.7.9 Data Requirements

The minimum requirement for experimental data was investigated using the simulation developed in the previous section. In these simulations the minimum number of cycles of data required to provide the best estimate of the frequency for the resolution given by a=20 were determined. The Rectangular Box and Hanning window methods were both simulated. The results are given in Table 3.7.

Set Freq. (Hz)	Actual Freq. (Hz) Rectangular Box	No. Cycles Rectangular Box	Actual Freq. (Hz) Hanning	No. Cycles Hanning
0.020500	0.020487	11	0.020514	3
0.041100	0.041088	16	0.041113	4
0.061600	0.061604	31	0.061598	5
0.082600	0.082606	39	0.082598	6
0.102700	0.102692	27	0.102711	5
0.123200	0.123208	55	0.123196	6
0.145600	0.145612	99	0.145597	6
0.166800	0.166786	30	0.166798	7
0.186200	0.186185	32	0.186195	7
0.205300	0.205299	46	0.205307	6

Table 3.7 Required minimum number of cycles to minimise the effect of spectral leakage and to achieve a spectral resolution of 2.861×10^{-5} *Hz. Simulated motion of pure sway with amplitude of 0.14m.*

The performance of the spectral analysis using the Hanning Window, given by the results in Table 3.7, is shown to be superior to that of the Rectangular Box Window. The results indicate that fewer cycles of data are required for the analysis procedure to accurately determine the frequency. The results are also indicative of the number of cycles that need to be recorded when undertaking PMM tests. A reanalysis of the test data described in Table 3.2 is given in Table 3.8. The results shown in the table are determined using a Hanning Window.

No.	Name	Motion	Demanded Frequency		Measured Frequency	
			Trans.	Rot.	Trans.	Rot.
1	Papa2404.m04	Sway	0.2052	n/a	0.2052	n/a
2	Papa2404.m10	Sway	0.2052	n/a	0.2052	n/a
3	Papa2404.m11	Sway	0.1668	n/a	0.1667	n/a
4	Papa2404.m17	Sway	0.1668	n/a	0.1741	n/a
5	Papa2404.m18	Sway	0.1231	n/a	0.1231	n/a
6	Papa2404.m24	Sway	0.1231	n/a	0.1232	n/a
7	Papa2404.m27	Sway	0.0825	n/a	0.0842	n/a
8	Papa2404.m29	Sway	0.0410	n/a	0.0410	n/a
9	Papa2404.m30	Sway	0.0205	n/a	0.0205	n/a
10	Papa2404.m31	Yaw	0.2052	0.2052	0.2052	0.2052
11	Papa2404.m39	Yaw	0.2052	0.2052	0.2051	0.2050
12	Papa2404.m40	Yaw	0.1668	0.1668	0.1667	0.1667
13	Papa2404.m47	Yaw	0.1668	0.1668	0.1739	0.1735
14	Papa2404.m48	Yaw	0.1231	0.1231	0.1231	0.1231
15	Papa2404.m53	Yaw	0.1231	0.1231	0.1231	0.1231
16	Papa2404.m54	Yaw	0.0825	0.0825	0.0825	0.0825
17	Papa2404.m55	Yaw	0.0410	0.0410	0.0410	0.0410
18	Papa2404.m56	Yaw	0.0205	0.0205	0.0205	0.0205

Table 3.8 Re-analysis of values given in Table 3.2. Measured frequency results of several PMM test runs using Hanning Window method and assuming actual frequency values accounting for software and motor time constant errors.

The results in Table 3.8 more closely reflect the demanded frequency, accounting for software and motor errors. The accuracy of the results indicates that further cycles of data were still required to obtain frequency values accurate to four decimal places. The test results in files 'papa2404.017' and 'papa2404.047' suggest that the demanded frequency was not as indicated in the table. Further testing with the parameters for these tests are required to determine the cause of the substantially larger error than was determined.

3.7 10 Amplitude Determination Using a Finite Impulse Response Filter

In order to determine the maximum amplitude of the displacement motion, a finite impulse response (FIR) filter was applied to the raw displacement data. A Kaiser Window was selected to window the data since it was finite length. Once the data is smoothed then the motion amplitude is easily determined using the Matlab function 'MAX' to determine the maximum peak eg. $A = \max(\textit{filtered data})$.

Since the maximum oscillation frequency is 0.2Hz, the cut-off frequency of the pass-band was chosen to be 0.5Hz. For a transition width of $\Delta\omega$ radians/sec and a side-lobe height of $-\alpha$ dB, the filter length was given by

$$n = \frac{\alpha - 8}{2.285\Delta\omega} + 1 \qquad (3.34)$$

The beta parameter (Mathworks, 1994), defined by the side-lobe height is given by

$$\beta = \begin{cases} 0.1102(\alpha - 8.7), & \alpha > 50 \\ 0.5842(\alpha - 21)^{0.4} + 0.07886(\alpha - 21), & 50 \geq \alpha \geq 21 \\ 0, & \alpha < 21 \end{cases} \qquad (3.35)$$

Since the filter is FIR and the phase response is linear in the pass-band region, n/2 points are required exactly to initialise the filter. A phase shift of n/2 points occurs when the filter is applied to the data.

The FIR filter was implemented in Matlab; the routine 'BFILT.M' was developed and is provided in Appendix 3. The impulse response of the filter is shown in Figure 3.16.

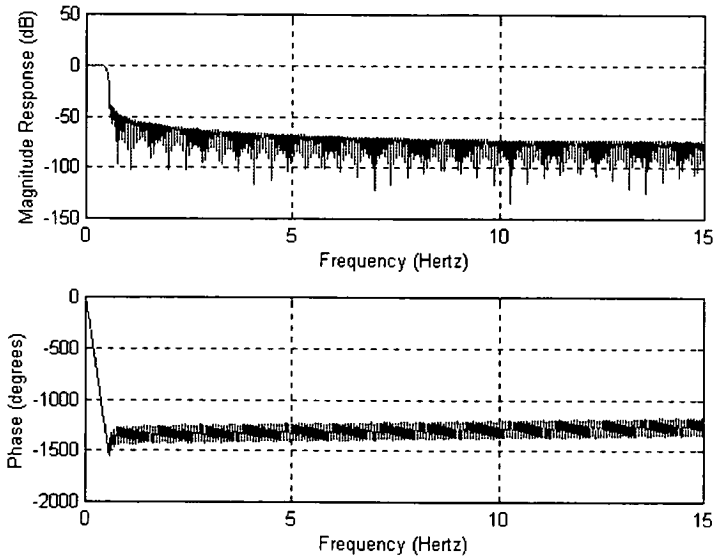

Figure 3.16 Magnitude and phase response of a FIR filter employing a Kaiser Window. The cut-off frequency is 0.5 Hz.

A closer inspection of the magnitude response in Figure 3.16, as shown in Figure 3.17, illustrates the undesirable feature of pass-band ripple. The amount of ripple is approximated by the value 0.008. However, the amount of ripple over the range in which HPMM tests were conducted was less than 0.005.

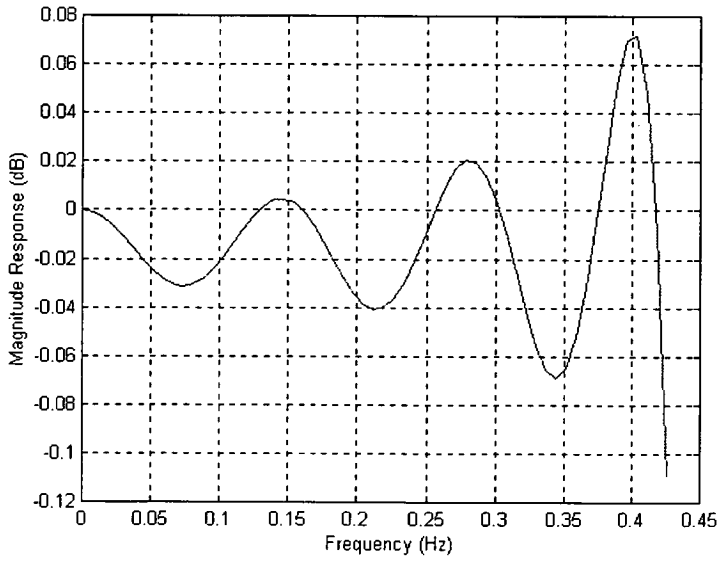

Figure 3.17 Magnitude response of FIR filter employing Kaiser Window as shown in Figure 3.16. The cut-off frequency is 0.5 Hz.

3.7 11 An Infinite Impulse Response Filter to Determine Signal Amplitude

The Butterworth IIR filter represents only one of the possibilities that could be employed to reduce the band–pass ripple. The response of a Butterworth filter, designed with a cut-off frequency of 0.5 Hz, is shown in Figure 3.18. It is apparent from an examination of Figure 3.18 that the roll-off in the stop-band does not reach 50 dB until the frequency is 2-3 Hz, which is significantly greater than for the Kaiser FIR filter. However, the measured signal to noise ratio is such that the roll-off response of the Butterworth filter is adequate. Figure 3.18 also shows the phase response to be nonlinear. However, this does not interfere with the determination of the signal amplitude.

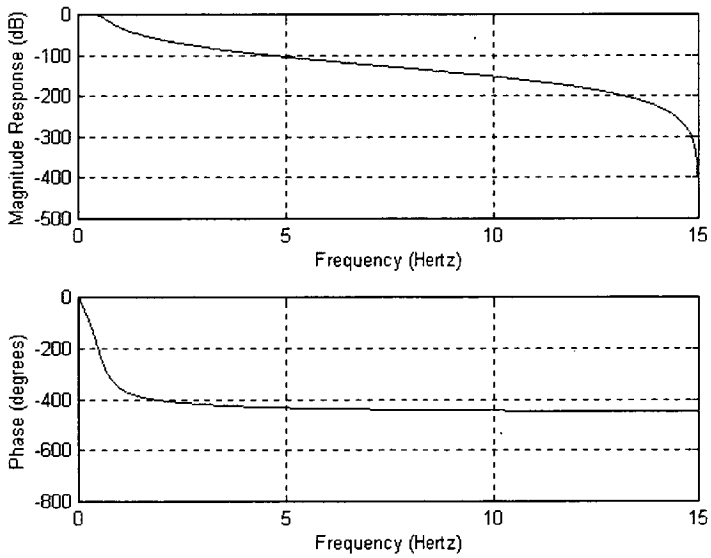

Figure 3.18 Magnitude and phase response of Butterworth low pass IIR filter. The filter cut-off frequency is 0.5 Hz. Frequency response given from 0 Hz to the nyquist frequency 15 Hz.

On closer inspection of the magnitude response of the Butterworth IIR filter, shown in Figure 3.19, it is apparent that the band-pass ripple is negligible. Thus the Butterworth filter presented is a potential option for reducing the processing error in determining the signal amplitude of the HPMM motors.

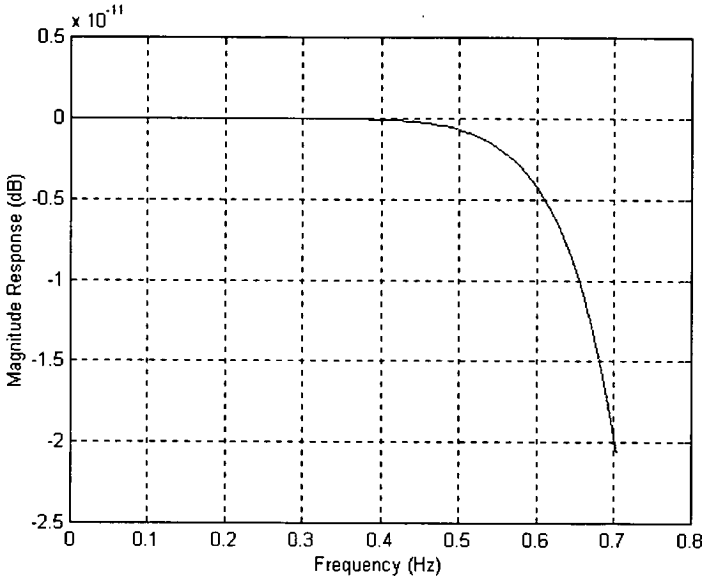

Figure 3.19 Magnitude response of Butterworth low pass IIR filter. The filter cut-off frequency is 0.5 Hz.

3.7.12 Validation

The resultant fitted curves to the motions specified in Figures 3.11 and 3.12 are given in Figures 3.20 and 3.21 respectively.

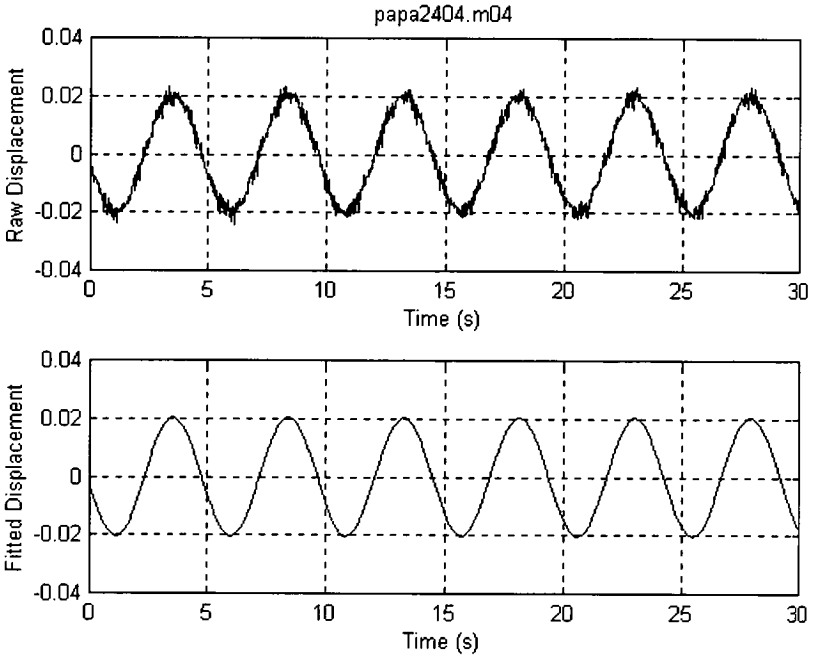

Figure 3.20 Regenerated translation displacement (metres) compared to the result in Figure 3.11.

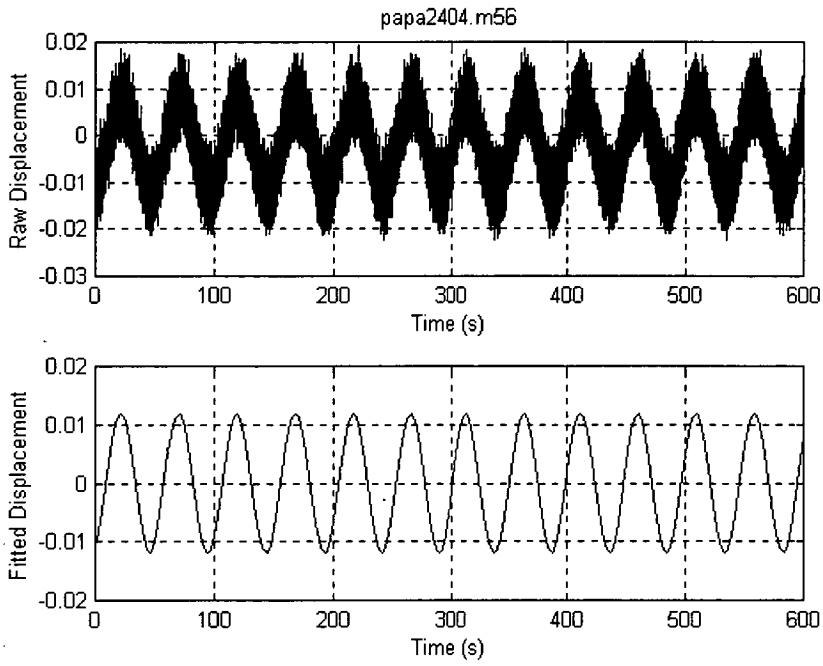

Figure 3.21 Regenerated rotation displacement (radians) compared to the result in Figure 3.12; based on parameters determined using the software function 'motion_analysis.m' on the data file 'papa2404.m56'.

The fitted curves for the tests detailed in Table 3.2 are given in Appendix 3.

3.8 Discussion

The HPMM described in this chapter was developed by the DSTO as part of its contribution to the AME CRC. The HPMM was designed to operate in the horizontal plane with two independent servo-motors being used to control motion in that plane. Motion control and data acquisition are provided by separate computers.

Scale models are attached to the AME HPMM by either of two mounting arrangements, the first being a strut – a vertical pole arrangement that pierces the model in mid-body and the second being a sting – a 'C' shaped arrangement that mounts the model from behind in its rear wake region. The latter arrangement was found useful for minimising the effect of the presence of the model mount on the flow around the body and thus the resultant measured hydrodynamic loads.

The commercially available, AMTI M3378 six component load cell was described in this chapter. An initial calibration of the load cell (ETRS, 1995) determined that the load cell constants were within 2.6% of manufacturers specifications, over all degrees of freedom. However, further work by Heron (1998) discovered that if forces were applied on large moment arms, up to 500 mm from the centre of the load cell, then cross-talk sensitivities were more significant than presented in ETRS (1995). It is recommended that future calibration of the load cell should include large moment arms if forces are to be applied at similar distances from the origin of the load cell.

The equations of motion for the AME HPMM are based on periodic functions. Pure sway is defined as pure translational motion of the body, with the heading fixed at zero angle of attack to the flow. The translational motion is a sinusoid function. Pure yaw is a combination of translation and rotation motions such that the x-axis of the body is coincident with the tangent of the path of the body. The rotation of the body was based on a sinusoid, while the translation of the body is determined from the condition of pure yaw.

A 4^{th} order Runge Kutta numerical scheme was implemented to solve the translation motion equation. While small angle approximations in the equation of motion would only have introduced small errors in the motion, the capacity of the servo-motors to process arbitrary motions meant that this was not necessary.

A correction factor was also introduced to account for errors produced when the mechanism operated the rotation motors. Once again, the errors were small - in the order of 1-2%, however, the equations of motion were simply modified to mitigate the error.

Analysis of the HPMM motions was required to determine the frequency and amplitude of an executed motion. The determined amplitude and frequency were then used to generate velocity and acceleration signals for each of the tests. It was important that the amplitude and frequency were known so that the parameters for the test could be validated and so that post-analysis of the results could consider frequency and speed related effects on the results.

A Fast Fourier Transformation was applied to several displacement records, given in Table 3.2, to determine the frequency of the motions. In determining the frequency, several errors were found. These included: Round-off in the motor control software, motor time constant error, frequency resolution and spectral leakage due to the windowing technique used and the amount of data in the record. The resultant frequencies, taking into account the combined errors, are given in Table 3.4.

It was shown via simulation that a Hanning Window provided more accurate results than a Rectangular Window for the same resolution and quantity of data. The Hanning Window also required less data than a Rectangular window to provide accurate results. Several HPMM displacement data files were analysed using a Rectangular Window, shown in Table 3.2, and compared to the same files analysed using a Hanning Window, given in Table 3.8. The result confirms the predictions made by simulation.

The simulation also gives an indication as to the amount of data required to determine an accurate result for both the Hanning and Rectangular Window techniques. The results shown in Table 3.8, while offering significant improvement over the results of the analysis given in Table 3.2, do not give the required frequency accurate to four decimal places. Comparing the data requirements with the amount of data recorded, indicated that further data was required for more accurate results.

A finite impulse response filter (FIR) employing a Kaiser Window was applied to the displacement data to remove noise. This enabled the amplitude of the motion to be determined. Errors in the pass-band region of the filter were found to be significant, prompting an investigation into alternative approaches. One such approach was found to be a Butterworth style, infinite impulse response filter (IIR). Pass-band characteristics of the Butterworth IIR were significantly improved over the Kaiser FIR, suggesting that future analysis to determine the amplitude of a motion should involve using a Butterworth IIR or an equivalent with similar pass-band properties.

Chapter 4. Circulating Water Channel

4.1 Introduction

This chapter describes an investigation of the flow quality in the Australian Maritime College's (AMC) circulating water channel (CWC). The Australian Maritime College (AMC) is located on campuses in Launceston and Beauty Point Tasmania. The college's experimental test facilities also include a towing tank. The CWC was used to support the PMM testing of scale models in the work described in this thesis. For reasons which will be explained later, the CWC was selected over the towing tank for conducting PMM tests.

The AMC CWC was commissioned in December 1983. It has a working section 17.2m long, 5.0m wide, and 2.5m deep, and forms a continuous circuit for 700,000 litres of water. Flow speeds up to a maximum of 1.5 m/s are generated in the working section by four 56.5kW axial flow pumps located at the downstream end of the test section. Water is pumped into a return channel beneath the test section, then through two 90^o cascade bends, and honeycomb and turbulence reduction screens, before entering the test section (Smith, 1984). A two dimensional, schematic of the AMC CWC is shown in Figure 4.1

The principal advantage of using a CWC for hydrodynamic testing is the unlimited run-time, which is not available in a towing tank facility. The water flow passes the model continuously and if the flow is steady, the duration of tests can be as long as necessary. This allows the HPMM testing to be extended to lower frequencies and thus reduces the need for extrapolation of the data.

An advantage of using the AMC CWC instead of the AMC towing tank was the significantly larger cross-section area of the CWC to the tow tank. It was more suitable for submerged model testing as it allowed more practical sized models to be tested. Model size is limited by 'blockage' and 'surface' or 'boundary' effects, these are discussed further in Chapter 6.

The turbulence level and spatial uniformity of flow can significantly influence the results of scale model tests. The water in tow tanks is typically allowed a settling time between runs and is assumed stationary before test runs. The speed of the water over the model is then controlled by the speed of the carriage moving down the tank. The water flow quality in CWCs is more difficult to control and, significantly, water flow uniformity and turbulence levels do not reach the same quality achieved in tow tanks. In the AMC CWC the working section inlet is preceded by an expansion, rather than a contraction, which exacerbates these problems.

The work reported in this chapter involved measuring flow profiles in the CWC at various water speeds. As the flow uniformity was initially found unacceptable, it was necessary to implement some modifications for improving the flow quality. In an effort to quantify the turbulence levels in the CWC, sphere drag measurements were performed in both the AMC CWC and the AMC tow tank. It was assumed no turbulence existed in the latter. From these tests it was possible to draw conclusions regarding the effective Reynolds number of the tests performed in the AMC CWC.

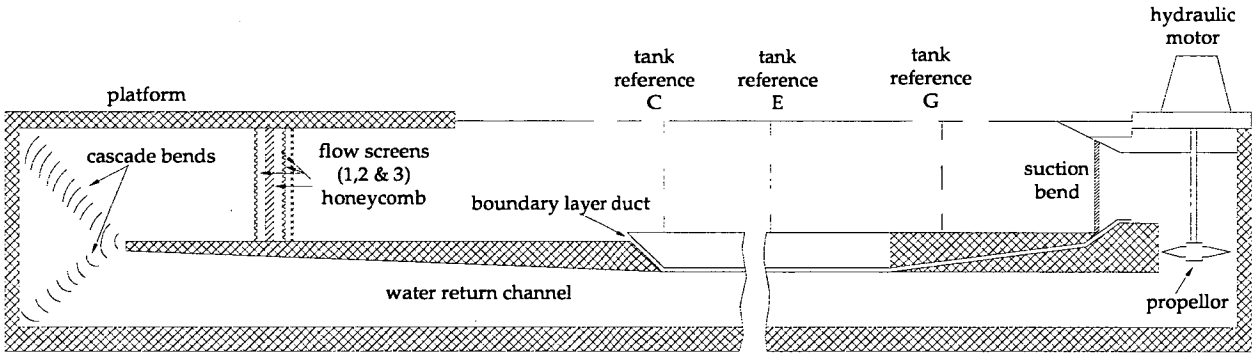

Figure 4. 1 Schematic of the AMC CWC.

4.2 Flow Uniformity in the AMC CWC

4.2.1 CWC Coordinate System

A coordinate system was arbitrarily assigned to the channel to provide a reference for flow measurements. Figure 4.2 shows the coordinate system, where the origin is attached to the window side of the working section, aligned with the right hand edge of the 'E' marking located on the CWC wall.

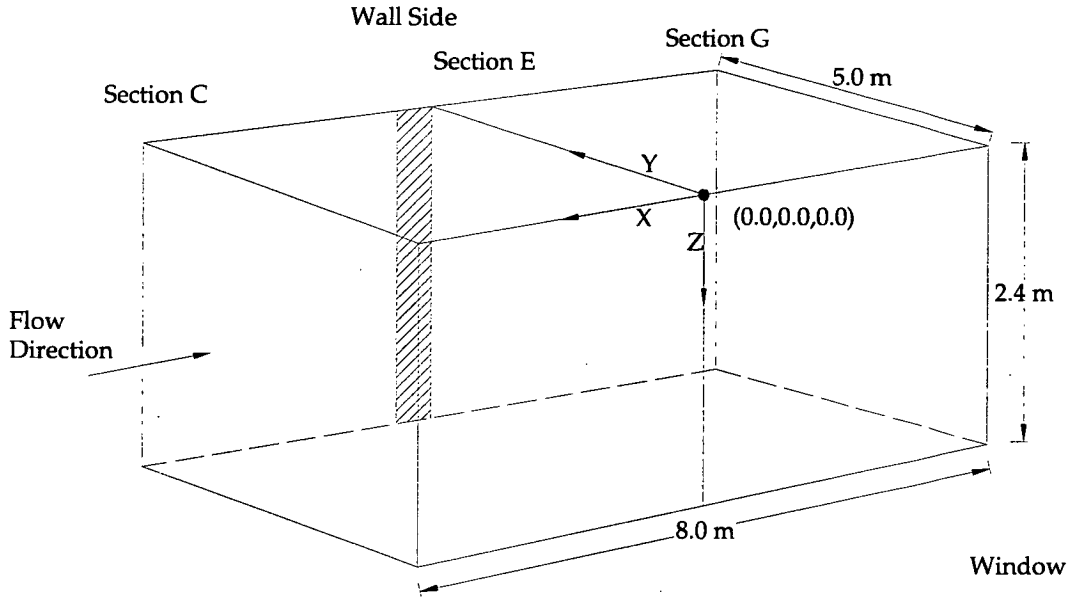

Figure 4.2 Definition of a co-ordinate system for the CWC working section.

4.2.2 Channel Configuration

The CWC configuration discussed here refers to the number and position of flow straightening screens and honeycombs installed in the channel upstream of the working section. The location and geometry of the screens are illustrated in Figures 4.1 and 4.3 respectively.

An initial inspection of the CWC revealed only one screen and honeycomb were installed in the channel. The flow screen was located immediately after the honeycomb, in position 'fs2' as indicated in Figure 4. 3.

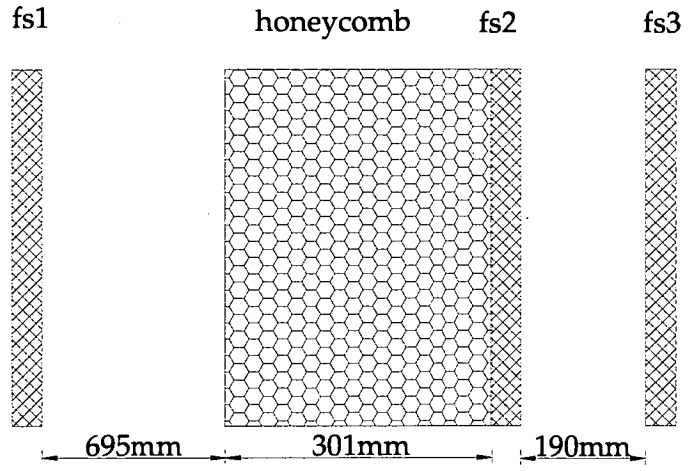

Figure 4. 3 AMC CWC: Positions of Honeycomb and Flow Straightening Screens relative to one another. The abbreviation 'fs' refers to the position of the flow screen, while the number refers to its order from left to right as shown in Figure 4. 1.

The AMC CWC honeycomb screen dimensions were width 5.0m and depth 2.4m, while the length along the channel X-axis was 0.301m, as shown in Figure 4. 3. The screen is comprised of a series of fixed cylinders, placed parallel to each other, and spanning the length of the screen. The inside diameter of each cylinder's was 0.038m and the wall thickness of the tube was 0.002m.

The open area ratio of the flow conditioning screen was 68% and was positioned at 'fs2'. Further description of the design of the screen is given in the following section.

4.2.3 Flow Conditioning Screens

Flow conditioning screens are typically made of woven wire mounted to a rigid frame. Their application in water tanks such as the CWC provides improved quality of the flow by dampening non-uniformities. To specify a flow-conditioning screen, the open-air ratio (OAR) of the woven wire must be given. This is generally determined from the open-air aperture, denoted by A, and the diameter of the wire strand D and is illustrated in Figure 4.4.

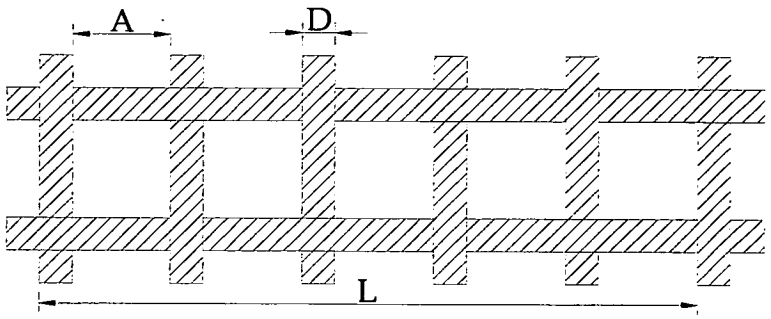

Figure 4.4 (Boral, 1994) Schematic depicts parameters describing woven wire used in production of flow conditioning screens.

The wire diameter can be determined using a micrometer. However the aperture is determined from the length L of a number of apertures, and then calculating an average.

The expression for the average aperture given by Boral (1994) is,

$$A = \frac{L}{N} - D \tag{4. 1}$$

For example, if wire is woven into square mesh, the total area covered by woven wire with $N \times N$ apertures is

$$N^2(A + D)^2$$

and the open area for the same dimensions is,

$$N^2A^2$$

The OAR is then given by

$$OAR = \frac{1}{\left(1 + \frac{D}{A}\right)^2} \tag{4. 2}$$

The results in Equations (4.1) and (4.2) were applied to the dimensions determined for the flow screen installed at position 'fs2' in the AMC CWC. The average aperture was 7.6mm while the diameter of the wire was 1.6mm. The OAR for that screen, as a percentage, was 68%.

4.2.4 Initial Flow Profile Measurements

The flow profile in the AMC CWC was recorded at a range of positions between 0.5m from each side-wall, and 0.1m from the surface and bottom. Measurements were made along each of the three channel axes X, Y, and Z, within these ranges. The 68% OAR flow screen was positioned at 'fs2' and the honeycomb was fitted as shown in Figure 4. *1.* A calibrated mechanical propellor log was used to measure the flow speeds. Data was recorded for 30 seconds at each position at a sample rate of 1Hz.

Results from the initial profile testing in the CWC are shown in Figure 4.5 and Figure 4.6. The vertical profile tests showed a significant variation in the flow speed with depth in the channel. Although the reference flow speed was set at 1.024m/s, the average flow speed measured in the vertical profile, shown in Figure 4.5, was 0.990m/s with a standard deviation of 0.100. As a percentage of the average flow speed, the standard deviation was therefore 10.1%.

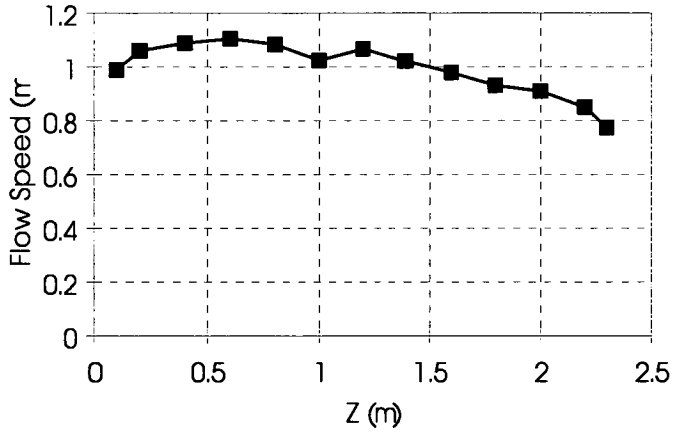

Figure 4.5 Measured flow speed in the AMC CWC. A vertical profile is given here. In this example the (X, Y) co-ordinates were fixed at X= -4.0m and Y= 2.5m, while the reference velocity was 1.024m/s at position (-4.0,2.5,1.4).

The horizontal flow profile, shown in Figure 4.6, also indicated significant non-uniformity in the flow speed. The calculated average over the horizontal range measured was 1.022m/s with a standard deviation of 0.031m/s or 3.0% of the average speed. It is interesting to observe that the shape of the curve in figure 4.6 correlates with the positioning of the four pumps in the CWC.

More significantly, the standard deviations obtained for a more defined region of the channel, where it is expected that force measurements would be conducted (ie. Y positions between 1.8m and 3.2m, and Z ranging between 0.6m and 1.8m) are 4.7% in the vertical and 3.5% in the horizontal profile.

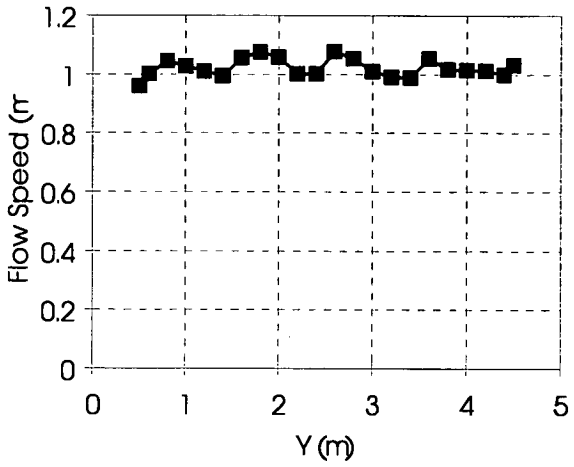

Figure 4.6 Measured flow speed in the AMC CWC. A horizontal profile is given here. In this example the (X, Z) co-ordinates were fixed at X= -4.0m and Z=1.2m, while the reference velocity was 1.027m/s at position (-4.0,2.5,1.4).

These results were only regarded as indicative of the levels of uniformity in the flow. Since there was unsteadiness in the pump flow, which was a result of no closed loop control on the pump motors, it was difficult to get repeatable results. The installation of closed loop controllers for the pump motors was undertaken. This is discussed further in the following section.

4.3 Methods For Improving Flow Speed Uniformity

4.3.1 Introduction

Various options for improving the flow speed uniformity for the AMC CWC were considered. These included examination of wind tunnel designs as discussed in Bradshaw and Pankhurst (1964) and Mehta (1977) to determine what methods might be applicable to water channel design. Methods readily applicable to the CWC

included graded or shaped wire screens (ie. flow conditioning screens), optimally designed honeycombs and optimal positioning of multiple flow screens relative to each other.

According to Mehta (1977 and 1979), if the yaw angle of the incoming flow is not more than 10°, honeycombs are to be preferred over screens for removing lateral velocity variations. Honeycombs will reduce the free-stream turbulence levels but their presence will contribute to turbulence. The build up of turbulence in a honeycomb is a result of boundary layer growth in the tube. The effect of the honeycomb turbulence can be dampened by the use of wire screens used downstream.

The design criteria for optimal honeycomb performance are a cell length of between 6 and 10 times the diameter of the cell. The cross-sectional size and shape of the cell is not critical, however a small cell is preferred as it reduces the generated turbulence.

Wire screens are used to improve the flow uniformity. Mehta (1977) gives three main effects that gauze screens have on the flow which passes through them:

(i) reduction of mean velocity variation – leading to the prevention of, or delay in, boundary layer separation;

(ii) reduction in turbulent fluctuations

(iii) refraction of inclined flow towards the local normal to the screen.

According to Mehta (1979) the static pressure drop as the fluid passes through the screen is proportional to the square of the velocity. This reduces the boundary layer in the channel and thus increases the resistance to the pressure gradient. This results in more uniform flow and a reduction in the turbulence intensity of the whole flow.

It is important to note that screens with OAR less than 0.57 are known to cause instabilities in the flow. Also, the optimum distance between wire screens placed consecutively after each other is approximately 500 times the diameter of the wire (Mehta, 1979).

Five aspects of the AMC CWC configuration were finally considered with respect to improving the flow uniformity in both the horizontal and vertical profiles and also the turbulence levels:

1. Wire Screen Design
2. Honeycomb Design
3. Cascade Bend Design
4. Boundary layer Duct Performance
5. Motor/Pump Performance

Feasible locations for screens in the AMC CWC were limited to the three positions shown in Figure 4. *1* and Figure 4. *3*. This restricted what was achievable by optimal placement of the screens. However, adding further screens of different OAR was possible. The existing honeycomb was considered optimally designed by the criteria given in Mehta (1979).

The discharge from the four pumps was also considered a major factor in the flow speed uniformity. It was realised through measurement of the pump motor discharge that the four pumps were operating independently of each other with no feed back reference to enable adequate control of the pump speeds.

The boundary layer duct and the cascade bend performance are the subject of ongoing research and their configuration was not altered.

Therefore, two approaches were implemented to improve the AMC CWC performance. These comprised of adding further flow conditioning screens and the installation of closed loop feedback control on the pump motors.

There were three possible positions for screens to be implemented in the channel. The original screen, placed in position 'fs2', had an open area ratio of 68%. Implementation of two further screens to fill positions 'fs1' and 'fs3' was completed.

A controller for the synchronisation of the hydraulic motors was implemented. This allowed the AMC CWC horizontal flow profile to be "tuned", with several options for the type of feedback given to the controllers. The horizontal spatial variation in the flow was further reduced by this method. The controller reference is also used to provide a standard reference for velocity measurements made in the channel.

4.3.2 Effect of New Flow Screens

The addition of further flow conditioning screens significantly improved the flow speed uniformity in both the horizontal and vertical profiles. A screen with an open area ratio of 64% was installed in position 'fs3'. The results, summarised in Table 4.1, show a significant reduction in the spatial non-uniformity in the flow.

The success of the new screen suggested that implementing a third screen in the remaining available position could further improve the flow quality. To investigate this proposition the screens were then repositioned or rewired in the following manner:

- The 64% screen from position 'fs3' was moved to position 'fs2';
- The 68% screen from position 'fs2' was rewired with 58% open area ratio and placed in position 'fs1', and
- A new screen was built and wired to 69% open area ratio and placed in position 'fs3'.

The new screen arrangement improved the flow variation significantly in the vertical profile. Fluctuations in the horizontal profile appeared to be marginally worse. It was considered that the latter could be an artefact of problems in setting uniform pump speeds.

Table 4.1 provides a summary of the results of flow profile tests taken in the AMC CWC as a function of three arrangements of screen installations. The values given in this table are the percentage standard deviations of time-mean velocity of the flow in the horizontal or vertical directions. TS refers to the standard deviation values for the horizontal range between 0.5m from both channel walls, and the range between 0.1m from the surface and floor in the vertical. The values given under WS indicate a more tightly defined region, this being 1.8m from the walls in the horizontal and 0.6m from surface and floor in the vertical. All measurements given in the table were taken at position E, where the x-coordinate is zero according to the axes shown in Figure 4.2.

Screen Open Area Ratio %			Horizontal % Standard Deviation		Vertical % Standard Deviation	
1	2	3	TS	WS	TS	WS
-	68	-	3.0	3.5	10.1	4.7
-	68	64	2.4	1.8	6.1	3.1
58	64	69	2.9	2.1	3.0	2.4

TABLE 4.1. AMC CWC: Measured Spatial Variation in Water Flow

4.3 3 Effect of Pump Motor Controllers

The pump motor settings were used to further optimise the flow uniformity. The final measurements of horizontal flow velocity distribution in the empty test section were made at the normal testing position, 1.2m above the channel floor, using a single pitot-static tube and differential pressure transducer. A series of flow velocity profiles were produced across the width of the test section. The pump settings required to produce these profiles were recorded, and used to reproduce the desired flow profile during model tests. The recorded flow speeds were found to be repeatable. Figure 4.7 shows the measured flow profiles for speeds from 0.3 to 1.1 m/s, along with the standard deviation for the test section of each profile.

The pump motor settings used for these tests were pump 1 = 0.95, pump 2 = 1.24, pump 3 = 1.01, and pump 4 = 1.16. The control demand that sets the reference demand for the four pump motors was plotted against flow speed measured at (-2.0,2.5,1.2). The relationship between flow speed at the reference point and the pump control demand is given Figure 4.8.

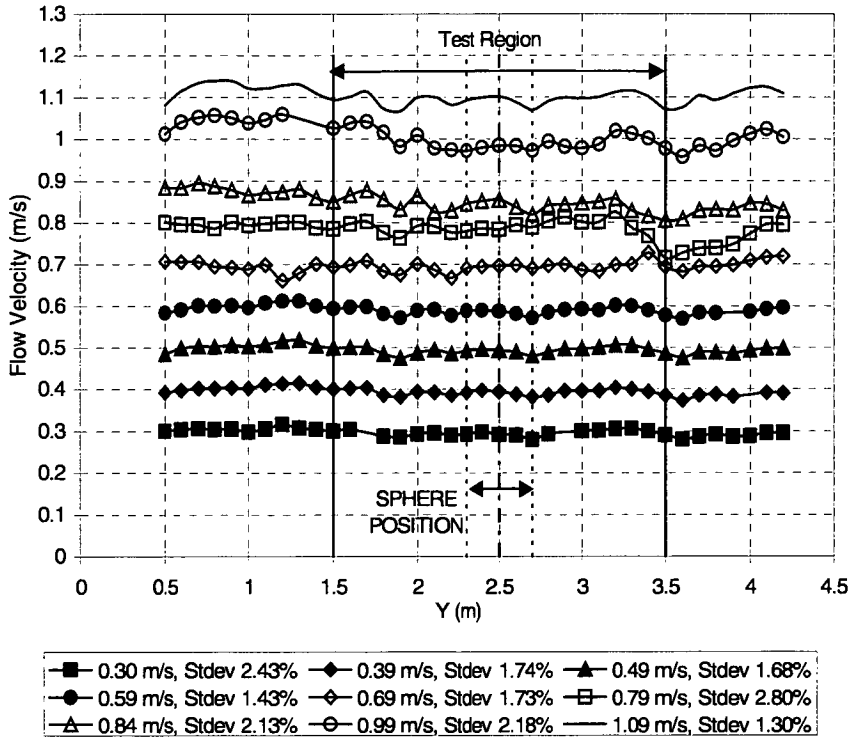

Figure 4.7 Flow velocity measurements in the horizontal profile; standard deviations from the average flow speed across the test section.

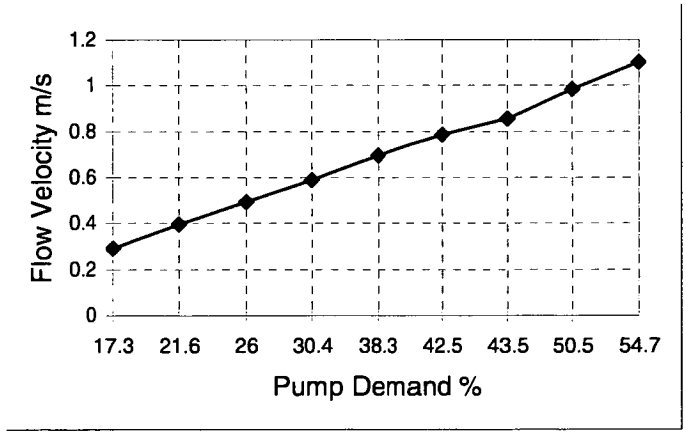

Figure 4. 8 Measured relationship between the pump motor controller demand percentage and the channel flow speed taken at channel position (-2.0,2.5,1.2).

4.4 Turbulence

4.4.1 Introduction

It is well known that turbulence in a testing environment affects drag measurements (Pope, 1954). It is therefore important to quantify the level of free-stream turbulence in the test environment to permit interpretation of the results. Turbulence causes the flow to be similar to that of non-turbulent flow at a higher Reynolds Number (Rn). This effect can be quantified by the "turbulence factor" defined by

$$TF = \frac{Rn_{free\ air.}}{Rn_{exp}} \tag{4. 3}$$

Since Reynolds numbers of spheres are well defined in free air, Equation (4.3) can be applied to experimental measurements on spheres to determine the flow environment's turbulence factor. The turbulence factor determined from the sphere, free air and measurement ratios, can then be used to determine the effective Reynolds number of experimental tests involving other shapes.

$$Rn_{eff} = TF \times Rn_{exp} \tag{4. 4}$$

Also, Hoerner (1958) states that the critical Rn decreases steadily as a function of the turbulence intensity.

One method of identifying the turbulence factor for a test environment is to determine the critical Rn of a sphere, defined as that at which the drag coefficient is 0.30 (Pope, 1954). The critical Rn in free (non-turbulent) air is 0.39×10^6 (Pope, 1954). A critical Rn as low as 0.15×10^6 was measured in the early stages of the NACA variable density wind tunnel (Hoerner, 1958), indicating a high turbulence level. Hoerner (1958) shows from experiment that above Rn = 1000, the drag coefficient of a sphere is a stable value of approximately 0.47, up to the critical Reynolds number, where it drops suddenly to about 0.1.

Therefore, the critical Reynolds number can give a qualitative indication of the turbulence intensity. It must be pointed out however, that other factors such as acoustical vibrations and mechanical vibrations in the model supports can also affect the critical Reynolds number.

4.4.2 Sphere Model Tests

Two separate sphere models of diameter D_s = 400mm were constructed for drag tests, one to be mounted by the strut and the other by the sting mount. In both models the origin of the load cell was located at the centre of the sphere.

The normal testing depth in the towing tank was 1.75 D_s while in the CWC it was 3.0 D_s. Note the load cell was positioned inside the models at the centre of volume. Therefore only forces applied directly to the model were measured. No direct forces on the mounting arrangements were measured.

The Rn range for the set of experiments was from 1.2×10^5 to 4.8×10^5. It was expected that the critical Reynolds number would lie within this range.

The drag coefficient given by

$$C_d = \frac{F}{\frac{1}{2}\rho A U^2} \tag{4.5}$$

where

F is the magnitude of the axial component of the force, and

A is the frontal area of the body,

was calculated for each of the measurements made in the tests. Figure 4.9 shows the drag coefficient plotted against the Reynolds number for the tests conducted using the strut mounting arrangement. The comparison in the plot is between the results from the CWC and the towing tank.

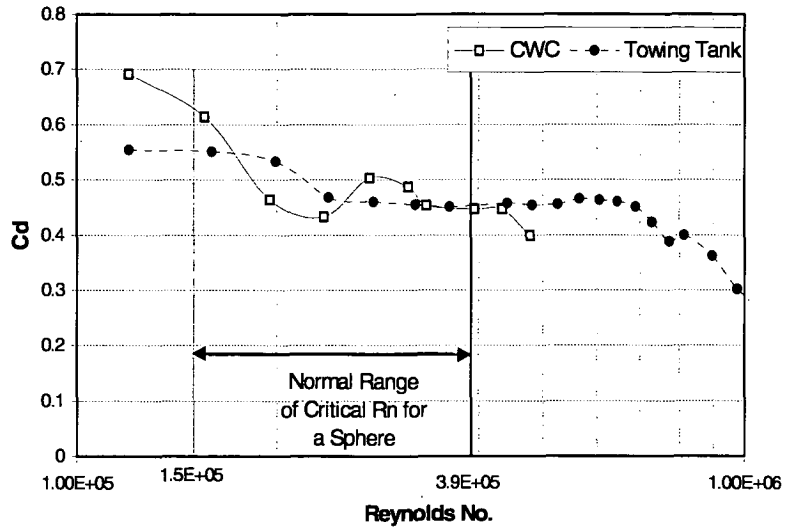

Figure 4.9 Comparison of sphere drag measurements made in AMC towing tank and CWC while mounted by the 'strut' mounting arrangement.

The results shown in Figure 4.10 were measured in the CWC. The sphere was tested with both the sting and strut mounting arrangement.

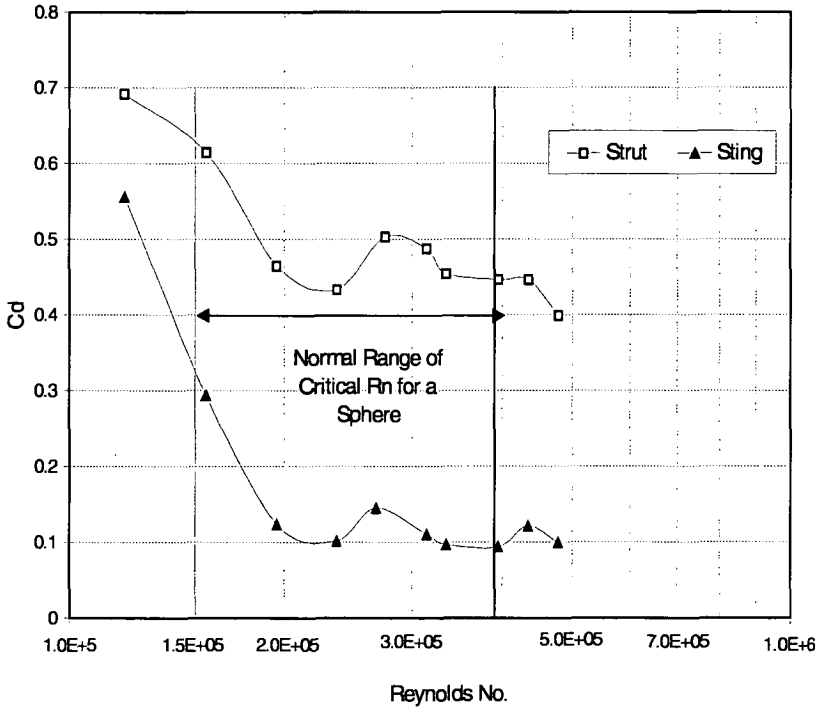

Figure 4.10 Comparison of sphere drag measurements in AMC CWC between 'strut' and 'sting' mounting arrangements.

4.4.3 Analysis

The sphere model was tested in both the CWC and the tow tank; mounted by both the sting and strut in the CWC and the strut only in the tow tank. Figure 4.10 illustrates that when the sphere model was mounted by the strut arrangement, it did not behave the same as an unrestricted sphere, as described by Hoerner (1958).

The measured drag values on the strut/CWC combination are high compared with those found in the literature. The additional drag on the sphere mounted by the strut is attributed to the interference caused by the presence of the strut. It is considered that the strut, which pierces the water surface, and extends straight down to the top of the sphere, produces its own wake. This arrangement creates a low pressure area on the top of the sphere, immediately behind the intersection with the strut, thus increasing the drag on the sphere.

To study the effect further, flow visualisation tests were conducted on the sphere with the strut/CWC combination, using a single wool tuft at the end of a slender rod. The tests indicated the presence of a low-pressure area behind the strut. Overall, except the slowest speeds tested, strong flow was detected upwards from the rear of the sphere towards the strut's wake.

The 'bump' in the CWC data at $Rn = 0.27 \times 10^6$ appears consistently in all test sets and has been attributed to a consistent flow anomaly.

While only a few measurements were made at the subcritical Reynolds number for the sting/CWC combination shown in Figure 4.10, the drag coefficient reached the critical value of 0.1. The flow over the sphere in the sting/CWC combination passes the transition drag coefficient of 0.30 at approximately $Rn = 0.16 \times 10^6$, indicating a high level of turbulence.

The sting that supports the sphere model from the downstream side has the advantage that it does not produce a wake that interferes with the flow around the sphere. Although its likely to be small, the effect of the sting's position in the wake of the

sphere should be considered, as it still occupies some of the volume that would normally be taken up by the sphere's wake.

If the transition drag coefficient of 0.30 is used here to determine the point of transition over the sphere in the results in Figure 4.9, then it would appear that transition for the channel/strut combination occurred at approximately $Rn = 0.98 \times 10^6$. It also appears that transition did not occur in the CWC/strut combination in the range tested. In this case transition would seem to have been delayed by the presence of the strut.

From Equation (4.3), the turbulence factor for the sphere tests described in this paper is 2.48. This corresponds to a turbulence level of approximately 1.75 % (Pope 1954). Pope (1954) states that turbulence factors in wind tunnels range from 1.0 to 3.0, but values above 1.4 may indicate that the air has too much turbulence for good testing results. Although high turbulence yields high effective Rn, the correction is not exact. If these comments were applied to the CWC, then it would seem that the turbulence levels are too high for good results.

4.5 Discussion

This chapter reported the details of an investigation into the flow properties of the AMC CWC. Flow uniformity and turbulence levels in particular were studied; in the former case study methods were implemented to improve the flow performance and, in the latter, measurements were made to permit interpretation of the affect of turbulence. Also, measurements illustrating the affect of the model mounting arrangement on the measured drag were completed.

Two methods were implemented to improve the uniformity of the flow in the AMC CWC, these included additional wire screens and pump motor controllers. The alterations to the CWC configuration improved the flow uniformity by 40% in the horizontal plane of the working section and by 49% in the vertical. The installation of the closed loop controllers for the pump motors enabled the CWC to be operated with repeatable flow uniformity.

Comparison of sphere drag measurements made in the AMC CWC and towing tank, and the literature, indicated the AMC CWC to have a turbulence intensity of

approximately 1.75%. Pope (1954) stated that such a result for a wind tunnel would indicate too much turbulence for good results to be obtainable. However, it would appear from the results obtained in the AMC CWC for the sphere model, that reasonable results are possible. However, the effective Reynolds number must be accounted for.

The validity of using the turbulence factor to correct the effective Reynolds number for non-sphere shapes was not determined. However, it was useful for providing indication as to the effect of the turbulence in the flow on the drag measurements. Further work to characterise the turbulence level in the AMC CWC would provide a more accurate basis for assessing the effective Reynolds number of individual model tests.

Chapter 5. Experimental Program

5.1 Introduction

The design of an experimental program for PMM testing of underwater models on the AME HPMM at the AMC's CWC in Beauty Point, Tasmania is described in this chapter.

Numerous hydrodynamic coefficients are required for simulation of an underwater vehicle. However, it may not be feasible to determine all the possible coefficients. Realistically, only some will be determinable from experiment, while others may be determined from theory. The remaining undetermined coefficients form part of the simulation error.

There are a significant number of tests that could be undertaken using a PMM to determine hydrodynamic coefficients. Since the tests can be performed over a range of different flow speeds, motion types, model orientations, frequencies and amplitudes, it is important to define the operating range for which the hydrodynamic coefficients are to be valid and hence limit the various options.

Typically, most underwater vehicles with length of the order of 2m and operational speeds of about five knots, operate in subcritical through to transcritical flow regimes for drag variation (Achenbach, 1972). The drag coefficients will vary appreciably through these different flow regimes as the wake region alters (Sayer, 1986). This obviously places further requirements on the hydrodynamic testing as the same coefficients may have different values depending on the vehicle operation.

The design of the test model must consider its mass, mass distribution, weight in water, and its overall dimensions. It is also important to consider the location of the load cell inside the model. For the purpose of fixing the load cell to the model, it is necessary to have sufficient access to its internal regions. In specifying these

parameters, it is also necessary to consider the effects of blockage, boundaries and frequency on the results.

5.2 Reynolds Number

Surface effects are assumed to be negligible when modelling deep underwater vehicles. It is therefore considered appropriate to neglect gravitational forces when considering these bodies and to study their performance with respect to the applied inertial and viscous forces. Hence the non-dimensional relationship given by Reynolds number, the ratio of inertial to viscous forces, is used to scale underwater bodies and their motions.

5.3 Tank Effects

5.3.1 Frequency Effects

The measured forces on a model are generally assumed to be functions of the instantaneous velocities and accelerations of the body at that time. The term 'slow motion derivatives' (SMD) is applied to the resultant hydrodynamic coefficients determined under this assumption. Therefore no account is made of 'fluid memory' or 'frequency effect' (Gill, 1979). Dynamic tests using a PMM involve oscillating the model at several frequencies. Results from these tests are extrapolated to zero frequency to give the SMDs (Booth, 1973).

While a model being PMM tested is subject to frequency effects, it may not follow that the full size vehicle will exhibit the same response (Gill, 1979). During dynamic tests the model is oscillated from side to side, shedding vortices into the flow. If the model completes a cycle before the affected flow has passed the model length, then the model response will be affected. Some work has been undertaken by Bishop, Burcher and Price (1969, 1973a, and 1973b) to develop an analysis technique consistent with frequency affected measurements; this is discussed further in Chapter 6.

Booth (1973) suggests that the SMD assumption holds for oscillatory PMM tests if the body moves forward axially one model length at a faster rate than the PMM completes one cycle.

If the time taken for the model to travel axially by one body length is given by l/U_f and the time taken to oscillate one PMM cycle is given by T, where l is the length of the body and U_f is the tank flow speed, then the following relation expresses the requirement by Booth.

$$T > \frac{l}{U_f} \tag{5. 1}$$

Since the smallest dynamic oscillation period possible with the AME HPMM is 5 seconds, the relationship between the model length and the tank flow speed is given by

$$\frac{l}{U_f} < 5$$

If the model is to be tested at flow speeds as low as 0.3 m/s, then the requirement for length under the SMD assumption is

$$l < 1.5m \tag{5. 2}$$

Obviously the model length restriction is relaxed if the model tests are to be performed at larger flow speeds and lower frequencies on the HPMM. However, in designing for a range of test options, the largest HPMM test frequency and lowest water tank flow speed were considered.

5.3.2 Blockage

The effect of placing a model in a channel flow restricts the region in which the flow has to pass, thus creating 'solid blockage' (Sayer, 1986 and Bell, 1983). Other effects described by Bell (1983) include, wake blockage, and restriction of the wake geometry. These effects change the pressure gradient on the body, changing the effective flow speed around the body, which leads to early transition of the boundary layer, and a change in the point of separation, and can also alter the vortex shedding frequency.

The amount of blockage is quantified by the parameter K, which is the ratio of the cross-sectional area of the model to the cross-section area of the tank. Sayer (1986) suggests that blockage effects have negligible affect on drag measurements if $K < 0.004$, and also concludes that for underwater vehicles of similar length to breadth dimensions, $K < 0.02$ is satisfactory. Bell (1983) suggests that a correction for the actual

flow velocity experienced by the body can be made according to the following expression:

$$U = U_F(1+\varepsilon) \tag{5.3}$$

where

U is the velocity of the flow experienced by the body,

U_F is the velocity of the unrestricted flow, and

ε is a blockage correction factor.

Bell (1983) reports that various techniques have been investigated to determine correction factors, but most have been developed around streamlined bodies and airfoils, and would thus not be suitable for correcting blockage for bluff bodies.

Willetts (1980) performed a series of experiments on spheres to determine the effects of proximity of walls on lift measurements. Willetts found that for separations from a boundary of greater than two diameters of the spheres, the effects due to the presence of the boundary were negligible.

The approach taken in the work of this thesis relies on the guidelines from the literature for designing models and experiments so that blockage effects are minimised.

In order that the drag measurements are not affected by the free surface or the walls and floor of the tank, the model size must be selected so that its separation from the walls, floor and surface is greater than two body diameters (Sayer, 1986).

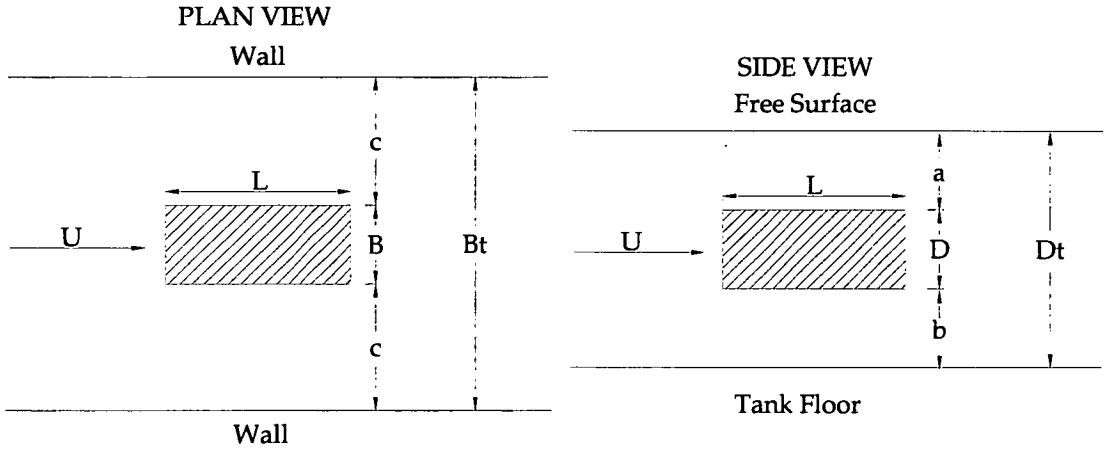

Figure 5.1 Views of an arbitrary model in a test tank.

The model/tank relationship is illustrated in Figure 5.1. The rectangular shaded box represents the model, taking into account the area traced by the maximum model dimensions. The parameters shown are: D, the depth of the model in vertical section; a, the vertical separation of the model from the free surface; b, the vertical separation of the model from the tank floor; Dt the vertical height of the tank, from the floor to the free surface; B, the breadth of the model; L, the length of the model; c, the horizontal plane separation from the walls; Bt, the breadth of the tank and U, the tank flow velocity.

According to the relationship given by Sayer (1986), the separation of the model from the surface should be

$$a > 2\,D \tag{5.4}$$

and similarly the separation of the model from the floor should be

$$b > 2\,D \tag{5.5}$$

The remaining condition to be satisfied is

$$a + b + D \leq Dt \tag{5.6}$$

Substituting Equations (5.4) and (5.5) into (5.6), a condition for the vertical height of the model to the height of the tank results as follows:

$$5\,D < Dt \tag{5.7}$$

Using the guidelines described above, the maximum height of the region that can be occupied by a model for minimal effect is 0.48 m, given that the vertical height of the AMC CWC from the floor to water surface is 2.4 m. Similarly, in the horizontal plane the maximum horizontal region that can be occupied by a model is 1.0 m since the distance between the CWC walls is 5.0 m. If the motions of the model are taken into account then its dimensions necessarily need to be smaller than these requirements.

The allowable vertical test region is quite small compared to the horizontal range. This factor was significant in considering the design of the AME HPMM and ultimately determined that the mechanism should be designed to operate in the horizontal plane rather than in the vertical.

To form a relationship that would assist in determining model parameters for HPMM experiments, it was assumed that the area traced by a model undergoing a motion

satisfies the guidelines described above. The shape of the model is assumed to be a rectangular box with length and breadth given by maximum model length and breadth characteristics.

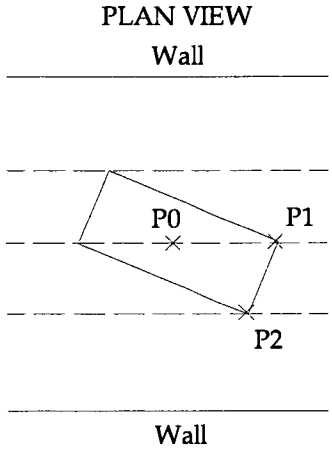

Figure 5.2 Model represented as a rectangular box, rotated in the tank.

The angle formed by the box centreline $\overline{P0P1}$, with the line $\overline{P0P2}$, is given by

$$\tan^{-1}\left(\frac{1}{AR}\right)$$

where $AR = \frac{L}{B}$.

If the box is rotated through an angle of ψ radians, the total angle between $\overline{P0P2}$ and the centreline of the tank is given by

$$\tan^{-1}\left(\frac{1}{AR}\right)+\psi$$

The projected breadth of the box under rotation is then given by

$$L\sin\left[\tan^{-1}\left(\frac{1}{AR}\right)+\psi\right]$$

Assuming that the maximum breadth allowable for the model is 1.0m, and if the translation motion of the body is also included, the following relationship expresses the guidelines as a function of the motion parameters:

$$L\sin\left[\tan^{-1}\left(\frac{1}{AR}\right)+\psi\right]+y\leq 1.0 \qquad (5.8)$$

where y is the total displacement of the model (m).

5.4 Model Specifications

5.4.1 Mass and Buoyancy

The limit on the mass and buoyancy of the model is determined here by the requirements set on the HPMM and the load cell. Coote (1998) gives a maximum model mass of 50kg, including all ballast materials. It is desirable that the model be as close to neutrally buoyant as possible so that the range on the load cell is not saturated with a static load. Mass, buoyancy, centre of mass and centre of buoyancy of the model are determined from inertia tests described in Section 5.7.

5.4.2 Location of load cell mount

The position of the load cell relative to the model is fixed, since it is impractical to change the load cell position during tests. The reference point for placement of the load cell in the model and measuring the hydrodynamic loads can be selected to be the same as for the full size vehicle, or a separate point. The positioning of the load cell within the model body relies upon the availability of space and access together with a consideration of the likely loads. If the loads are measured at a point different to the reference point in the full size vehicle, then a transformation of the forces is required. Booth (1973) gives the necessary coordinate transformation.

5.4.3 Dimensions

The potential to test small scale models rather than the full size vehicle offers several advantages. The required size of the tank does not have to be so large, nor does the size of the handling equipment. Also it is simpler to mount a purpose built model, where internal brackets have been designed, to a PMM, rather than a vehicle which may not readily offer internal space without some significant modification.

The minimum size of a model that could be validly tested is not well understood, assuming the requirement is for determining accurate drag coefficients at the appropriate Reynolds numbers. The approach taken in this work is to build the largest model which fits into the constraints determined in the previous section (5.3).

5.4.4 Surface Roughness

The effect of the surface roughness of the model on the Reynolds number is considered here. Since the turbulence levels in the tank are high compared to towing tanks, sphere model tests were conducted in the AMC CWC to investigate whether the roughness of the surface of the model would affect the drag measurements.

Achenbach (1973) describes the effect of increasing the fluid flow over a sphere in several stages:

- Sub-critical: The flow regime before critical range is reached.
- Critical: The range over which a small change in the Rn provides a significant decrease in the sphere drag coefficient, leading to a minimum value of drag coefficient called the critical Rn.
- Super-critical: The range extends from the critical Rn where the drag coefficient increases again with increasing Rn.
- Trans-critical: Following the super-critical range, the drag coefficient reaches an approximately steady state value. The point of transition between super-critical and trans-critical is not fixed.

Using this terminology, Achenbach (1973) discusses the effect of surface roughness on the drag of spheres and its relationship with Reynolds number (Rn) over the range $5\times10^4 < \mathrm{Rn} < 6\times10^6$. Experimental results shown by the author indicate that the surface roughness stimulates the boundary layer flow, causing it to transition to turbulent flow earlier than otherwise would be the case. The critical Rn is shown to decrease and the trans-critical drag coefficient over the sphere increases to approximately double that of a smooth sphere.

If the roughness ratio, given by

$$\frac{k}{D_s} \tag{5. 9}$$

where

k is the characteristics roughness length and

D_s is the diameter of the sphere,

and the value of the roughness ratio is increased sufficiently, the steady trans-critical drag coefficient reaches approximately 0.38 instead of 0.19 for a smooth sphere. Thus significant effects to the drag coefficient are expected with increase in surface roughness.

Tests were conducted in the AMC CWC to investigate the effect of roughness over a sphere model. The model was covered with a number of stimulators, where the roughness ratio given by Equation (5.9) was 0.0025. The results of the tests are given in Figure (5.3).

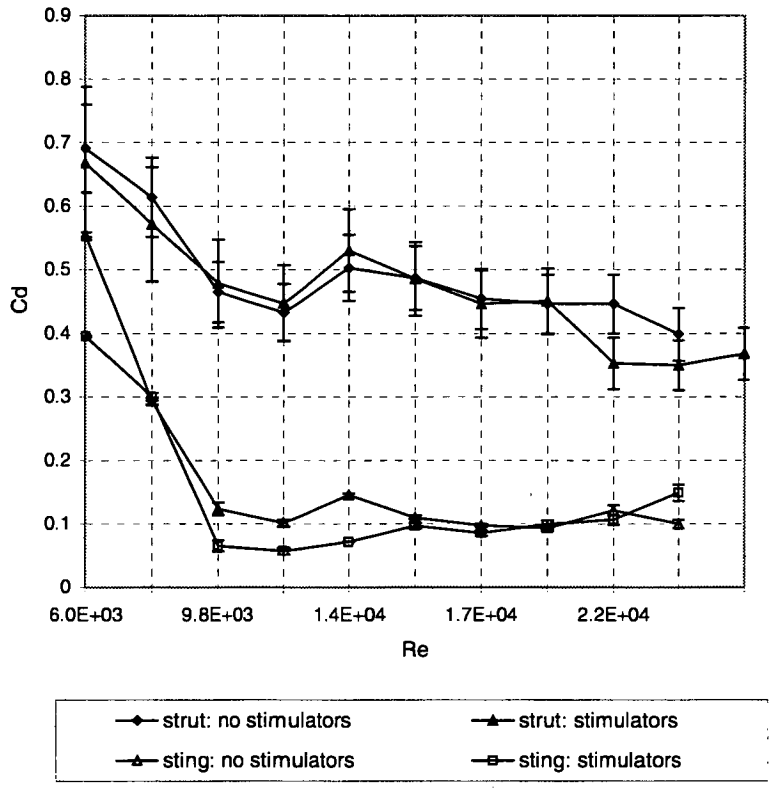

Figure 5.3 Sphere drag measurements in the AMC CWC. Comparison of drag coefficient between strut and sting mounted model, with and without flow turbulence stimulators. Error bars assume a force measurement error of ±3% and a velocity error of ±5%.

To investigate the significance of the results in Figure (5.3), an error analysis was conducted which led to the error bars shown in the figure. Since the expression for the drag coefficient was given by

$$C_d = \frac{F}{\frac{1}{2}\rho A U^2}$$

The error in the drag coefficient was expressed as

$$\delta C_d = \sqrt{\left(\frac{\delta F}{\frac{1}{2}\rho A U^2}\right)^2 + \left(\frac{4F\,\delta U}{\rho A U^3}\right)^2} \tag{5. 10}$$

Assuming a force measurement error of ±3% (Heron, 1998) and a velocity error of ±5% (see Chapter 4), the error in the drag coefficient was determined for each of the measurements.

It appears that the tank turbulence levels were sufficiently high that any effect on the drag measurements due to the use of stimulators was negligible.

5.5 Scaling Motions

The vehicle motions are scaled according to Reynolds number. If the model scale is given by r, such that

$$l = r \times l_m \tag{5. 11}$$

where

l is the vehicle length, and

l_m the model length.

then a vehicle velocity of v is scaled to the model velocity v_m by

$$v_m = r\,v \tag{5. 12}$$

The rotation rates are non-dimensionalised by

$$\dot{\psi}' = \dot{\psi}\left(\frac{l}{v}\right) \tag{5. 13}$$

where

$\dot{\psi}'$ is the non-dimensional vehicle velocity, and

$\dot{\psi}$ is the angular velocity of the vehicle.

Therefore the relationship between the angular velocity of the model and that of the full-scale vehicle is

$$\dot{\psi}_m = r^2 \dot{\psi} \tag{5.14}$$

where $\dot{\psi}_m$ is the angular velocity of the model.

5.6 Load Cell Calibration

It is important when measuring forces on a body that the results are an accurate representation of the applied loads. For this reason calibration of the load cell used in the measurement procedure is necessary. The AMTI load cell used in this work was described earlier in Chapter 3.

The early calibration of the AMTI load cell (ETRS, 1995) showed the manufacturer's sensitivities to be within 2.6% over all degrees of freedom. Further work by Heron (1998) showed the load cell to be sensitive to large moment arms.

The location of the centre of pressure due to the hydrodynamic loading varies as the model is translated and rotated in the flow, shown in Figure 5.4.

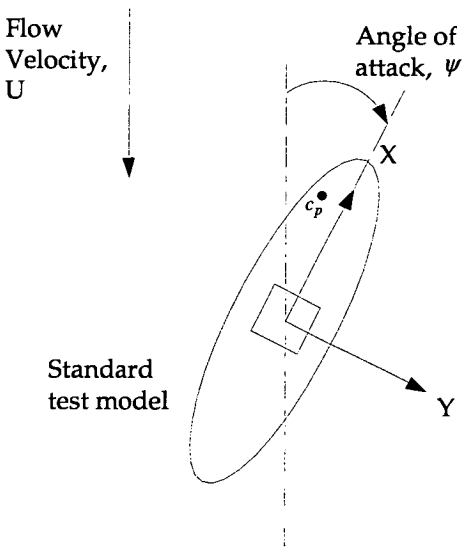

Figure 5.4 Schematic of a standard test model at angle to the flow. The position of the centre of pressure is shown not to coincide with the load cell origin.

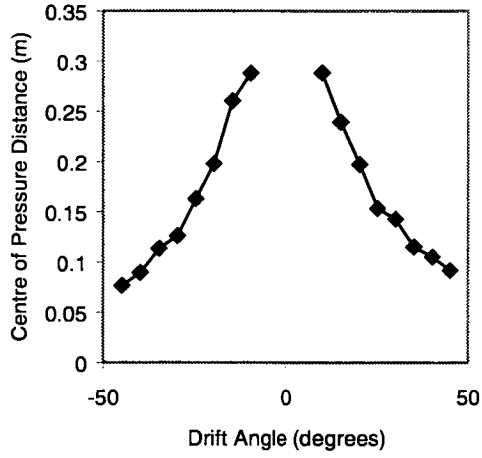

Figure 5.5 Typical data collected from static angle hydrodynamic tests. The data is from a standard ellipse test with flow velocity of 0.3m/s (Heron, 1998). The ellipse was 0.9m in length. and 0.18m diameter at maximum cross-section.

Figure (5.5) shows results from a series of tests where the angle of attack to the flow was varied. Post analysis showed that the centre of pressure moved as far forward as 300mm from the origin of the load cell.

Calibration of the load cell over moment arms up to 500mm showed the load cell to have errors that could be linearly correlated to the change in centre of pressure. A significant result was found to be the relative error in the Y force channel, which was as much as 15% at a moment arm of 500mm. Heron (1998) concludes by giving a technique, based on calibration results, for determining a correction factor to significantly reduce this error component.

5.7 Test Program Design

5.7.1 Introduction

The following experimental test program was designed for the AME HPMM, to be used in the AMC's CWC in Beauty Point, Tasmania. The program limits the number of frequencies and amplitudes to be tested in each of the modes of operation. As more experience is gained further refinement of the program will follow. An outline of the equipment and procedure is included in the description.

5.7.2 Equipment:

The following equipment was used during the AME HPMM tests:

1. HPMM Motion Control console
2. HPMM Data acquisition console
3. Strut/Sting mounting arrangement
4. Load cell
5. Load cell calibrator
6. Data storage/backup media (1.44Mb Disks/Iomega Zip Disks)
7. Test Model
8. Internal bracket to suit sting/strut
9. Bracket to allow model to be mounted on its side
10. Flow Measurement Device

5.7.3 Procedure

The following steps given here are a general schedule of activities developed for performing experiments using the AME HPMM:

1. Establish model design.
2. Build scale model.
3. Specify model test program (static and dynamic tests).
4. Calibrate the load cell.
5. Install AME HPMM Hardware.
6. Test all systems.
7. Mount load cell to HPMM mount.
8. Perform preliminary inertia tests ie. no model.
9. Mount model onto HPMM.
10. Conduct in-air inertia tests on the model.
11. Position carriage over required section in CWC.
12. Lower the model into the stationary flow.
13. Record a base measurement; a component of the inertia tests.

14. Initiate the required CWC water flow speed.
11. Conduct experimental program, as per step 3.
12. On completion, check load cell calibration.

The installation instructions, set-up and operation procedures for the AME HPMM are available in the user's manual by Coote (1998).

5.7.4 Inertia Tests

The following 'inertia tests' were completed to determine the centre of gravity, buoyancy, and the moment of inertia of the model about the vertical axis around the load cell origin. These values are subtracted from the hydrodynamic test results. Table 5.1 specifies four tests that were made.

Test	Model	Fluid		HPMM Motion		
No.	Condition	Type	Speed	Description	Frequency	Amplitude
1	No model	Air	0	none	n/a	n/a
2	Ballasted model	Air	0	none	n/a	n/a
3	Ballasted model	Air	0	rotation	0.20(Hz)	0.25(rad)
4	Ballasted model	Water	0	none	n/a	n/a

Table 5.1 Inertia test program

The analysis software developed to determine the moment of inertia, mass, buoyancy, and the centres of buoyancy and gravity are given in Appendix 4. Note in the table that 'none' refers to no motion.

5.7.5 Test Program Specifications

The manoeuvres performed using the HPMM can either be in the static or dynamic mode. The selection of the parameters for each of the manoeuvres will depend on the required full-scale motion range.

Static tests are defined by setting the yaw angle and the water flow speed. The yaw angle on the AME HPMM currently ranges between -45° and 45°. It is useful to perform the static tests at approximately 5° increments. The angle is set manually using a calibrated plate to visually determine the angle. Larger static angles can be tested once the plate is calibrated further.

The AME HPMM has two dynamic motion types that can be used in these tests. In each, the amplitude and frequency of the motion is required. The angular amplitude ranges from 0 to 0.25 radians while the translational amplitude ranges from 0 to 0.15m. The frequency can range between 0.01 and 0.20Hz.

In summary, the parameters for the HPMM tests described here are:

- Motion type
- Amplitude
- Frequency
- Model Orientation
- Flow Speed

The test program for a 1/3rd scale PAP104 model is given in Appendix 4.

The duration of oscillatory tests depends on how many cycles of motion are required for the analysis. Five cycles of data were recorded for the AME HPMM on the 1/3rd scale PAP104 model tests described in Appendix 4. Later analysis showed that further data was required when implementing Fourier techniques to determine the motion frequency.

5.8 Discussion

This chapter discussed several aspects of the design of an experimental program using a HPMM in a circulating water channel. Recommendations for the characteristics of the test model were given, taking into account effects from blockage and the imposed HPMM motions.

Two approaches to the treatment of blockage were discussed, these included the implementation of a correction factor to determine the effective flow velocity over the body, and the second was to avoid the effect altogether. The latter approach was implemented in this thesis. Specifications based on empirical relationships from the literature were developed for model testing in the AMC CWC.

The effect of the model surface roughness on the drag coefficients was reviewed. Experiments were conducted in the AMC CWC to investigate whether the affect of the

roughness of the model would be significant given the turbulence level in the flow. Even though potential errors in velocity and force measurement were accounted for, it was difficult to conclude whether differences were due to free stream turbulence or the presence of the stimulators.

To maintain similar flow conditions during model tests, the imposed motions and water flow are normally scaled by keeping constant Reynolds number between the full-scale body and the model motions. Conversely, the scaling functions can be used to determine the actual full-scale motions reproduced by the model tests.

Calibration of the load cell determined that the values given by the manufacturer were no longer applicable and had changed by up to 2.6%. Errors due to the change in the centre of pressure relative to the load cell were also determined and found to be significant. These were removed using a relationship given by Heron (1998).

The experimental program used to test the PAP104 scale model was also given. This contained an outline of the tests which were performed, detailing the motion type, frequency and amplitude of motion. Four tests are specified to provide the required data to determine the inertias of the model in the horizontal plane. Vertical plane moments of inertia are determined by performing the same tests with the model mounted on its side. These tests also enable the centre of buoyancy and mass to be determined.

Chapter 6. Analysis of PMM Data

6.1 Introduction

The objective of the PMM data analysis is to convert the raw hydrodynamic load cell data, measured from tests involving the AME PMM, into a set of hydrodynamic coefficients that characterise the manoeuvring properties of the submerged body. This chapter describes several methods for the analysis of PMM test data. The discussion highlights advantages and disadvantages of the methods. A preferred method is established.

To determine a set of hydrodynamic coefficients applicable to a particular unmanned underwater vehicle (UUV), the measured PMM data undergoes two stages of analysis. The first stage of analysis is to derive the hydrodynamic coefficients for a particular frequency and amplitude. These coefficients are then extrapolated to zero frequency in the second stage of the analysis to provide 'slow motion derivatives' that are used to represent of the hydrodynamic characteristics of the body.

The term 'slow motion derivatives' (SMD) is used to describe an approach in which the final hydrodynamic coefficients are determined by assuming the forces are based on the instantaneous motion of the body (Bishop, 1968, 1973a, 1973b, 1973c, 1974a, 1974b), which is the same as assuming a quasi-steady flow. The coefficients in this case reflect the value of the coefficient determined at zero frequency. Booth (1973) suggests that the SMD assumption is valid for oscillatory PMM tests if the body moves forward axially one model length at a rate faster than the PMM is able to complete one cycle.

An alternative to this technique is to determine oscillatory coefficients where no frequency assumptions are made. This is possible using convolution integrals to process the PMM data. The technique is regarded as linear, since the principle of

superposition still holds (Bishop, 1974b). However, the result is not a single value, rather an expression as a function of frequency.

The AME PMM was designed to operate in a significantly lower frequency range compared to that used in Bishop (1974a), where oscillatory coefficient expressions were determined (ie. a non-dimensional angular frequency of 1.2 compared to 30.3). The purpose of the low frequency design for the AME PMM was to enable SMDs to be easily determined. This has, however compromised the ability to use the mechanism to determine higher frequency dependencies.

The dependence of hydrodynamic coefficients on the relative speed of the body within the flow is obvious since the relationship of drag is dependent on the Reynolds number of the body motion. If dependency exists over the range tested then it will be necessary to express the coefficients as a function of relative speed through the water.

The techniques for analysis, like the hydrodynamic forces, are dependent on the motion of the PMM. The techniques discussed here are therefore based on the oscillatory or periodic nature of the PMM motions.

It is useful to summarise the PMM motion definitions:

Pure sway is expressed by:

$$\left.\begin{aligned} y &= y_o \sin \omega_t t \\ v &= \omega_t y_o \cos \omega_t t \\ \dot{v} &= -\omega_t^{\,2} y_o \sin \omega_t t \end{aligned}\right\} \qquad (6.1)$$

where

y_0 is the amplitude of the sinusoidal motion,

ω_t is the frequency of the translation oscillation,

v is the sway velocity, and

$\dot{v}$ is the sway acceleration.

Pure yaw is expressed by:

$$\left.\begin{aligned} \psi &= \psi_o \sin \omega_r t \\ r &= \psi_o \omega_r \cos \omega_r t \\ \dot{r} &= -\psi_o \omega_r{}^2 \sin \omega_r t \end{aligned}\right\} \qquad (6.2)$$

where

ψ_0 is the maximum amplitude of the angular oscillation,

ω_r is the frequency of the angular oscillation,

r is the yaw velocity, and

$\dot{r}$ is the yaw acceleration.

The analysis method used in this chapter assumes the data has been calibrated with the appropriate values, taking into account baseline offsets and load cell cross talk, and that it resides in ASCII format in files located on an accessible hard disk.

Software implementing the techniques discussed in this chapter has been written using the mathematical package MATLAB. Details are given in Appendix 5.

This chapter contains a discussion of the model assumptions and the form of the mathematical model for regression of the data, together with a description of several analysis techniques and their respective advantages and disadvantages. Finally, a description of the analysis technique applied to the data from the AME PMM is given.

6.2 Data Processing Model

Several mathematical models have been used to describe the hydrodynamic force on bodies. For instance, typical models for the sway force Y are given in Equations (6.3), (6.4) and (6.5).

A linear model for pure sway can be expressed in the form (Bishop, 1974b):

$$Y(t) = Y_o + \left(Y_{\dot{v}} - m \right) \dot{v} + Y_v v \tag{6.3}$$

where

Y_o, Y_v and $Y_{\dot{v}}$ are hydrodynamic coefficients,

m is the mass of the body,

v is the sway velocity,

$\dot{v}$ is the sway acceleration, and

$Y(t)$ is the body side force time history.

The non-linear model can have several forms (Bishop, 1974b). Two of these are represented by Equations (6.4) and (6.5):

$$Y(t) = Y_o + \left(Y_{\dot{v}} - m \right) \dot{v} + Y_v v + Y_{v|v|} v|v| \tag{6.4}$$

$$Y(t) = Y_o + \left(Y_{\dot{v}} - m \right) \dot{v} + Y_v v + Y_{vvv} vvv \tag{6.5}$$

By substituting the expressions for velocity and acceleration, given in Equations (6.1) and (6.2), into Equations (6.3), (6.4) and (6.5), a common form for the mathematical model is given where the force is represented explicitly by the PMM test parameters and the desired hydrodynamic terms. The resulting equations are:

$$Y(t) = Y_o - \omega_t{}^2 y_o \left(Y_{\dot{v}} - m \right) \sin \omega_t t + Y_v \omega_t y_o \cos \omega_t t \tag{6.6}$$

$$Y(t) = Y_o - \omega_t{}^2 y_o \left(Y_{\dot{v}} - m \right) \sin \omega_t t + Y_v \omega_t y_o \cos \omega_t t + Y_{v|v|} \omega_t{}^2 y_o{}^2 \cos \omega_t t |\cos \omega_t t| \tag{6.7}$$

$$Y(t) = Y_o - \omega_t{}^2 y_o \left(Y_{\dot{v}} - m \right) \sin \omega_t t + Y_v \omega_t y_o \cos \omega_t t + Y_{vvv} \omega_t{}^3 y_o{}^3 \cos^3 \omega_t t \tag{6.8}$$

Alternatively, the linear sway model can be written in the form

$$Y(t) = Y_o + Y_{mag} \sin(\omega_t t + \phi) \tag{6.9}$$

where

$$Y_{in} = Y_{mag} \cos\phi \tag{6. 10}$$

$$Y_{out} = Y_{mag} \sin\phi \tag{6. 11}$$

and Y_{mag} is the magnitude of the periodic response above the baseline.

Similarly the linear model can be written as

$$Y(t) = Y_o + a_1 \sin\omega t + b_1 \cos\omega t \tag{6. 12}$$

where a_1 and b_1 can be referred to as the out-of-phase and the in-phase component of $Y(t)$.

Bishop (1970) suggests a mathematical form that accounts for frequency dependence, where the side force may be expressed as

$$Y = Y_v\, v + Y_{\underset{v}{\cdot}}\, \dot{v} + Y_{\underset{v}{\cdot\cdot}}\, \ddot{v} + \ldots \tag{6. 13}$$

Substituting in the motion equations for pure sway

$$Y = \left(Y_v - \omega_t{}^2 Y_{\underset{v}{\cdot\cdot}} + \ldots\right)\left(y_o\, \omega_t \cos\omega_t t\right) + \left(Y_{\underset{v}{\cdot}} - \omega_t{}^2 Y_{\underset{v}{\cdot\cdot\cdot}} + \ldots\right)\left(-\, y_o \sin\omega_t t\right) \tag{6. 14}$$

the equation can be written as

$$Y = \tilde{Y}_v v + \tilde{Y}_{\underset{v}{\cdot}}\, \dot{v} \tag{6. 15}$$

where $\tilde{Y}_v$ and $\tilde{Y}_{\underset{v}{\cdot}}$ are the oscillatory form of the coefficients related by the following expressions.

As the limit of frequency goes to zero, the 'slow motion derivative' (SMD) is defined, such that

$$\lim_{\omega_t \to 0} \tilde{Y}_v = \lim_{\omega_t \to 0} \left[Y_v - \omega_t{}^2\, Y_{\underset{v}{\cdot\cdot}} + \omega_t{}^4\, Y_{\underset{v}{\cdot\cdot\cdot\cdot}} - \ldots \right] = Y_v \tag{6. 16}$$

$$\lim_{\omega_t \to 0} \tilde{Y}_{\underset{v}{\cdot}} = \lim_{\omega_t \to 0} \left[Y_{\underset{v}{\cdot}} - \omega_t{}^2\, Y_{\underset{v}{\cdot\cdot\cdot}} + \omega_t{}^4\, Y_{\underset{v}{\cdot\cdot\cdot\cdot\cdot}} - \ldots \right] = Y_{\underset{v}{\cdot}} \tag{6. 17}$$

Bishop (1973d, 1974b) gives an alternate form of Equation (6.12).

$$Y[v(t)] = \int_{-\infty}^{\infty} h_v(\tau) v(t-\tau) dt \qquad (6.18)$$

where $h_v(\tau)$ is the change in $Y(t)$ due to the input $v(t)$, subject to the conditions,

$$h_v(\tau) = 0 \quad \text{if} \quad \tau < 0 \qquad (6.19)$$

and

$$v(t-\tau) = 0 \quad \text{if} \quad \tau > t \qquad (6.20)$$

This is discussed further, later in this chapter.

The models given here are linear or non-linear depending on their relationship with velocity v. The difference between the non-linear models given in Equations (6.4) and (6.5) is in the choice of the non-linear term with respect to the velocity v. The models given by Bishop (1970, 1973d, 1974b) are linear in velocity.

The variation in the mathematical model considers not only the physics of the forces in many cases, but also the fit of the experimental data. Thus the mathematical model, while a good fit to the data, does not always resemble a physical derivation. It is important however, that for simulation to reflect the measured characteristics of the body, the choice of mathematical model in the analysis must be consistent with that in the simulation model.

6.3 Measurement Noise

Typical measurements from the AME PMM, shown in Figures 6.1 and 6.2, indicate that the recorded loads are affected by noise. The AME PMM data has been filtered during acquisition by the signal conditioner, with an effective cut-off frequency of 10 Hz. Therefore the noise threshold is less than 10Hz. Also, since the data sample rate is 30Hz, no aliasing of the data occurs.

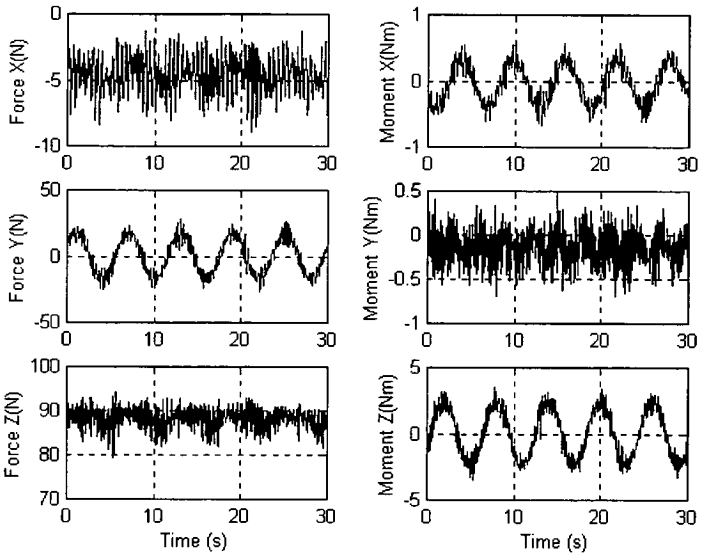

Figure 6. 1 *Typical raw PMM load measurements. Results from pure sway test on PAP104 1/3rd scale model for the six load components. Result file PAPA2404.M11: nominal frequency 0.16 Hz and amplitude of translation 0.14m.*

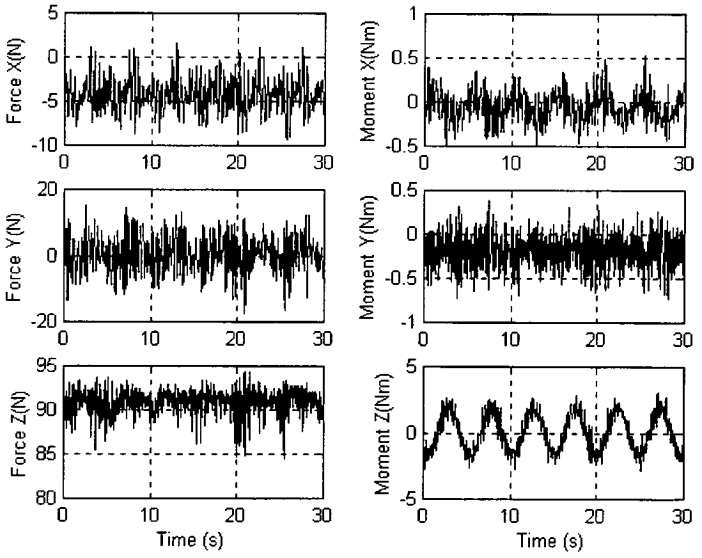

Figure 6. 2 *Typical raw PMM load measurements. Results from pure yaw test on PAP104 1/3rd scale model for the six measured load components. Result file PAPA2404.M31: nominal frequency 0.20 Hz and rotational amplitude of 0.18 radians.*

A spectral analysis of the measured loads from PMM results in 'PAPA2404.M11' and 'PAPA2404.M31' are given in Figures 6.3 - 6.4. The results are normalised with respect to the total energy of the signal.

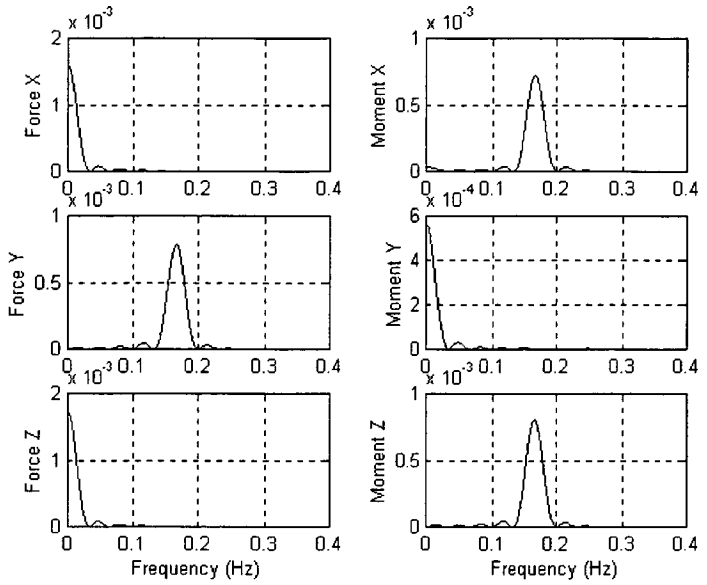

Figure 6.3 AME PMM Result file: PAPA2404.M11. Frequency response of the six measured load components. The vertical axis represents the spectral density magnitude of the given data in non-dimensional units. The PMM test frequency was 0.16Hz.

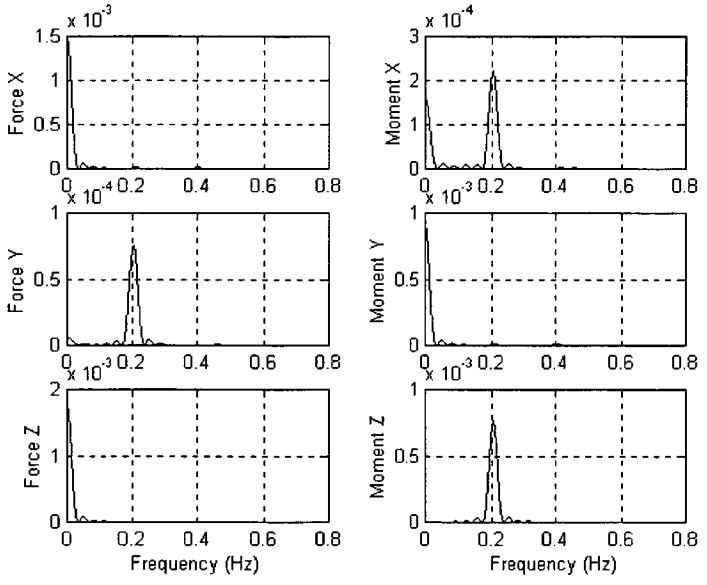

Figure 6.4 AME PMM Result file: PAPA2404.M31. Frequency response of the six load components. The vertical axis represents the spectral density magnitude of the given data in non-dimensional units. The PMM test frequency was 0.20 Hz.

6.4 Analysis Methods

6.4.1 Introduction

The following discussion describes several analysis methods including:

- Discrete Analysis
- Fourier Integration
- Switched Integration
- Systems Identification

6.4.2 Discrete Analysis

The 'Discrete Analysis' method describes a fundamental way of looking at the PMM data (Renilson, 1986). The technique selects points in the force time history so that components of the motion can be separated. In this way basic assumptions about the data can be tested before a final mathematical model is arrived at.

Assume for instance that the force is due to three factors; (1) the velocity, (2) the acceleration and (3) the memory or frequency effects. Apart from these factors no other assumptions about the mathematical model are considered at this stage of the analysis.

The motions described by 'pure yaw' and 'pure sway' are summarised in Equations (6.1) and (6.2). It is obvious from the nature of these equations that there are points where the velocity is zero and the acceleration is non-zero, and vice versa. This information can be used directly to determine values of the imposed load when there is zero velocity or zero acceleration.

The conditions for zero velocity, when $v = 0$, are given by

$$\omega_e t = \frac{\pi}{2}, \frac{3\pi}{2}, \frac{5\pi}{2}, \ldots, \frac{\pi(2n+1)}{2} \qquad (6.21)$$

where $n = 0,1,2,\ldots$

At these points the acceleration is given by

$$\dot{v} = (-1)^n \omega_t{}^2 y_o \tag{6.22}$$

The acceleration is zero at

$$\omega_t t = 0, \pi, 2\pi, ..., m\pi \tag{6.23}$$

where $m = 0,1,2,...$

At these points the velocity is given by

$$v = (-1)^{m+1} \omega_t y_o \tag{6.24}$$

The values are substituted into the expressions for force, as in Equations (6.3), (6.4), and (6.5), to give simplified expressions. For instance, the body side force Y for zero acceleration is,

$$Y(t) = Y_o + Y_v (-1)^{m+1} \omega_t y_o \tag{6.25}$$

$$Y(t) = Y_o + Y_v (-1)^{m+1} \omega_t y_o + Y_{v|v|} (-1)^{m+1} \omega_t{}^2 y_o{}^2 \tag{6.26}$$

$$Y(t) = Y_o + Y_v (-1)^{m+1} \omega_t y_o + Y_{vvv} (-1)^{m+1} \omega_t{}^3 y_o{}^3 \tag{6.27}$$

where m is given by Equation (6.23).

Therefore, the body side force, Y, for the zero velocity condition is

$$Y(t) = Y_o + \left(Y_{\dot{v}} - m \right) (-1)^n \omega_t{}^2 y_o \tag{6.28}$$

where n is given by Equation (6.21).

The discrete analysis method requires a significant amount of data to be measured. Since only four measured points per cycle are used in the analysis, many more cycles are necessary for reliable data. The method would not be economical unless the tests were completed in a circulating water channel, especially at the low frequencies. The

technique would also require that the noise be filtered from the data, should fewer points be measured.

The technique also assumes that acceleration and velocity are independent of each other; therefore the measured load when the velocity is zero is assumed to be a function of the acceleration and possibly history effects. Similarly, the load is assumed to be due to the velocity and history effects when measurements are made at zero acceleration.

The main advantage of the method is that it enables possible non-linearities and frequency effects to be studied, with no model assumptions regarding these being made. To determine the influencing factors on the force due to the velocity, it is necessary to plot the force due to velocity against velocity as measured at the discrete velocity points, when acceleration is zero. Similarly, the same is done to determine the factors on the force due to acceleration. The variation in these curves from straight lines indicates non-linearities, while deviations in the curves obtained at constant amplitude indicates frequency dependence.

While this method allows the data to be viewed simply for investigation into the effects of frequency and speed dependencies, a fit to a mathematical model producing coefficients is still required. Indeed, this method may be supplemented by one of the methods described in the following sections.

6.4.3 Fourier Integration

Fourier integration is a method of decomposing a signal into the sum of its individual components. The pure sway and yaw dynamic oscillations provided by the PMM invoke a periodic response in the model due to the induced hydrodynamic load.

Assume the hydrodynamic force due to the imposed PMM motions is periodic, therefore

$$Y(t+nT)=Y(t) \tag{6.29}$$

where

T is the period of the cycle, and

n is any integer.

The force time history can then be expressed as

$$Y(t) = a_o + \sum_{n=1}^{\infty} (a_n \cos \omega_n t + b_n \sin \omega_n t) \tag{6.30}$$

where

$$\omega_n = \frac{2\pi n}{T} \tag{6.31}$$

The Fourier coefficients (Kreyszig, 1989) are given by

$$a_o = \frac{1}{T} \int_{-T/2}^{T/2} Y(t) dt \tag{6.32}$$

$$a_n = \frac{2}{T} \int_{-T/2}^{T/2} Y(t) \cos(\omega_n t) dt \tag{6.33}$$

$$b_n = \frac{2}{T} \int_{-T/2}^{T/2} Y(t) \sin(\omega_n t) dt \tag{6.34}$$

where n=1,2,3...

The simplest form of Equation (6.30) is when n=1, this is given by

$$Y(t) = a_o + a_1 \cos(\omega t) + b_1 \sin(\omega t) \tag{6.35}$$

where

a_1, b_1 are the magnitudes of the individual waveforms,

T the motion period, and

Y_o is the base or offset force constant.

The linear equation for force Y, given in Equation (6.6), can be arranged in the form of Equation (6.30) simply by equating the two expressions.

Therefore,

$$a_o = Y_o \tag{6.36}$$

$$a_1 = Y_v \omega_t y_o \tag{6.37}$$

$$b_1 = -\left(Y_{\dot{v}} - m\right)\omega_t^2 y_o \tag{6.38}$$

Equating Equations (6.36), (6.37), and (6.38) to the Fourier coefficient expressions in (6.32), (6.33), and (6.34) enables the hydrodynamic coefficients for the linear force model to be determined.

$$Y_o = \frac{1}{T}\int_{-T/2}^{T/2} Y(t)dt \tag{6.39}$$

$$Y_v = \frac{2}{\omega_t y_o T}\int_{-T/2}^{T/2} Y(t)\cos(\omega_t t)dt \tag{6.40}$$

$$Y_{\dot{v}} = m - \frac{2}{\omega_t^2 y_o T}\int_{-T/2}^{T/2} Y(t)\sin(\omega_t t)dt \tag{6.41}$$

The Fourier integration method can also be used to determine nonlinear coefficients. Suppose that the nonlinear model given in Equation (6.8) is used as the basis of the PMM pure sway data analysis for $Y(t)$. The cubic cosine term is replaced to give a new form for Equation (6.8).

$$Y(t) = Y_o - \left(Y_{\dot{v}} - m\right)\omega_t^2 y_o \sin\omega_t t + \left(\frac{3Y_{vvv}\omega_t^3 y_o^3}{4} + Y_v \omega_t y_o\right)\cos\omega_t t + \frac{Y_{vvv}\omega_t^3 y_o^3}{4}\cos 3\omega_t t \tag{6.42}$$

In terms of a Fourier expansion, Equation (6.42) is given by

$$Y(t) = a_o + b_1 \sin\omega_t t + a_1 \cos\omega_t t + a_3 \cos 3\omega_t t \tag{6.43}$$

where

$$a_1 = \frac{3Y_{vvv}\,\omega_t^{\,3}\,y_o^{\,3}}{4} + Y_v\,\omega_t\,y_o \tag{6.44}$$

$$a_2 = 0 \tag{6.45}$$

$$a_3 = \frac{Y_{vvv}\,\omega_t^{\,3}\,y_o^{\,3}}{4} \tag{6.46}$$

and

$$b_1 = -\left(Y_{\dot{v}} - m\right)\omega_t^{\,2}\,y_o \tag{6.47}$$

By equating Equations (6.44)-(6.47) to Equations (6.32)-(6.34) the coefficients are

$$Y_{vvv} = \frac{8}{\omega_t^{\,3}\,y_o^{\,3}T}\int_{-T/2}^{T/2} Y(t)\cos(3\omega_t t)dt \tag{6.47}$$

and

$$Y_v = \frac{2}{\omega_t\,y_o T}\int_{-T/2}^{T/2} Y(t)\cos(\omega_t t)dt - \frac{3Y_{vvv}\omega_t^{\,2}y_o^{\,2}}{4} \tag{6.48}$$

As for the linear case, the coefficients Y_o and $Y_{\dot{v}}$ are given by Equations (6.39) and (6.41) respectively.

Equations (6.42)-(6.49) show that if the force response is nonlinear, then harmonics should appear in the data frequency spectrum, *ie.* a response at frequencies that are an integer multiple of the excitation. Since the nonlinear component also combines with the linear component in the principal harmonic, it is necessary to identify the nonlinear term completely to separate it out from the linear term. This may be difficult to do if the nonlinear term is not completely stimulated by the PMM excitation.

Also, the knowledge of the presence of nonlinearity does not necessarily provide its form. Obviously this can be difficult to determine, since the data processing can

become complex for various forms of the nonlinear model, making the technique difficult to implement.

It is also necessary to consider the integration technique and the numerical errors involved in the process. The algorithm is required to integrate over the period T where several periods have been measured. The integration error is a function of the sampling frequency also, since the sampled data at the end of a period will not necessarily lie on the period endpoint exactly.

The determination of the final zero frequency hydrodynamic coefficients (or slow motion derivatives) depends on the assumption of frequency. If independence of frequency is assumed, then the final coefficient can be selected from any of the tested frequencies. If independence is not assumed, the values need to be extrapolated to zero frequency.

6.4.4 Switched Integration

The method of 'Switched Integration' was implemented by the Danish Maritime Institute in the nineteen sixties (Strom-Tejsen, 1966). It assumed that the forces were directly proportional to the imposed PMM motions and were periodic. It also assumed that the sinusoidal velocity and acceleration motions were independent of each other.

The method assumes the general expression for the body Y force is given by Equation (6.35). The switched integration method works by determining the values of a_o, a_1, b_1 by polarity reversal in selected regions and then integration over the switched force signal. In the work described by Strom-Tejsen (1966), the polarity reversal was implemented electrically at the time of data acquisition, however it can be performed numerically.

If the polarity of the force signal $Y(t)$ is reversed at every half period $T/2$, then the cosine and constant component of the signal is eliminated while the sine component remains to be measured. Similarly, if the polarity of $Y(t)$ was reversed at $T/4$ and

$3T/4$, the sine and constant component would be eliminated while the cosine component would remain to be measured. If the integration is performed over $Y(t)$ without any polarity reversal then the constant remains to be measured while the sine and cosine components are eliminated. The accuracy of the method relies upon a full number of cycles being measured exactly.

The result obtained by integrating the constant over one period is given by

$$\int_0^{2\pi} a_o d(\theta) = 2\pi a_o \tag{6.49}$$

where $\theta = \omega t$, such that ω .is the angular frequency and t is the elapsed time.

The result obtained by integrating cosine over one period is given by

$$\int_0^{\pi/2} a_1 \cos(\theta) d(\theta) - \int_{\pi/2}^{3\pi/2} a_1 \cos(\theta) d(\theta) + \int_{3\pi/2}^{2\pi} a_1 \cos(\theta) d(\theta) = 4a_1 \tag{6.50}$$

Similarly, the result obtained by integrating sine over one period is given by

$$\int_0^{\pi} b_1 \sin(\theta) d(\theta) - \int_{\pi}^{2\pi} b_1 \sin(\theta) d(\theta) = 4b_1 \tag{6.51}$$

The switched integration method enables the linear coefficients to be determined in a straightforward manner. Given the linear model in Equation (6.6), the coefficients are expressed by the following:

$$Y_o = \frac{1}{2\pi} \int_0^{2\pi} Y(t) d(\theta) \tag{6.52}$$

$$Y_v = \frac{1}{4\omega y_o} \left[\int_0^{\pi/2} Y(t) d(\theta) - \int_{\pi/2}^{3\pi/2} Y(t) d(\theta) + \int_{3\pi/2}^{2\pi} Y(t) d(\theta) \right] \tag{6.53}$$

$$Y_{v}^{\bullet} = m - \frac{1}{4\omega^2 y_o}\left[\int_0^{\pi} Y(t)d(\theta) - \int_{\pi}^{2\pi} Y(t)d(\theta)\right] \qquad (6.54)$$

The method for determining nonlinear coefficients is similar. The steps outlined for the extended nonlinear analysis assume that the data has already been integrated. Assume I is the measured, integrated force data. The nonlinear expression for the force $Y(t)$ is given by Equation (6.5), which can also be expressed as

$$Y(t) = a_o + b_1 \sin\omega_t t + a_1 \cos\omega_t t + a_3 \cos^3\omega_t t \qquad (6.55)$$

where

$a_o = Y_o$,

$b_1 = -\left(Y_{v}^{\bullet} - m\right)\omega_t^{\,2}\, y_o$,

$a_1 = Y_v\, \omega_t\, y_o$, and

$a_3 = Y_{vvv}\,(\omega_t\, y_o)^3$.

If $Y(t)$ is integrated, to remove the constant and the sine component of the signal then

$$\begin{aligned} I &= \int_0^{\pi/2} Y(t)d(\theta) - \int_{\pi/2}^{3\pi/2} Y(t)d(\theta) + \int_{3\pi/2}^{2\pi} Y(t)d(\theta) \\ &= \int_0^{\pi/2}\left[a_1\cos(\theta) + a_3\cos^3(\theta)\right]d(\theta) - \int_{\pi/2}^{3\pi/2}\left[a_1\cos(\theta) + a_3\cos^3(\theta)\right]d(\theta) \\ &\quad + \int_{3\pi/2}^{2\pi}\left[a_1\cos(\theta) + a_3\cos^3(\theta)\right]d(\theta) \end{aligned} \qquad (6.56)$$

Substituting the result from Equation (6.51) gives

$$I = \int_0^{\pi/2} a_3 \cos^3(\theta) d(\theta) - \int_{\pi/2}^{3\pi/2} a_3 \cos^3(\theta) d(\theta) + \int_{3\pi/2}^{2\pi} a_3 \cos^3(\theta) d(\theta) + 4a_1 \tag{6.57}$$

The following relationship is used to simplify Equation (6.58).

$$\cos^3(\theta) = \frac{1}{4}[3\cos(\theta) + \cos 3(\theta)] \tag{6.58}$$

The integrated force time response for the cosine component is given by

$$I = 4a_1 + \frac{8a_3}{3} \tag{6.59}$$

This is rearranged to give

$$\frac{I}{4} = a_1 + \frac{2a_3}{3} \tag{6.60}$$

The measured, integrated forces are divided by four, giving $\frac{I}{4}$. The result is then fitted using the following expression, noting the form of the model representing the force.

$$\frac{I}{4} = c_1 v' + c_2 v'^3 \tag{6.61}$$

A least squares method is used to determine the coefficients c_1 and c_2.

Equating the equations gives

$$c_1 v' + c_2 v'^3 = a_1 + \frac{2a_3}{3} \tag{6.62}$$

Therefore

$$c_1 v' + c_2 v'^3 = Y_v \omega_t y_o + \frac{2}{3} Y_{vvv} (\omega_t y_o)^3 \tag{6.63}$$

The hydrodynamic coefficients are then given by

$$Y_{vvv} = \frac{3}{2} c_2 \tag{6. 64}$$

and

$$Y_v = c_1 \tag{6. 65}$$

where $v' = \omega_t y_o$.

The final value for the nonlinear coefficient is therefore derived from the theoretical integration of the assumed model and the comparison with the faired values of the measured and integrated forces.

As with the Fourier integration method, the switched integration method requires heavy manipulation of the data and integration over set intervals. Extra processing is required in the switched integration technique if the model is nonlinear. A fitting process based on least squares is used to solve for the extra terms introduced by the nonlinearity. The nonlinear model form is assumed based on best fit to the data.

Also, as in the case where the coefficients were determined at individual frequencies in the Fourier integration method, the final coefficients depend on the assumption of frequency. If independence of frequency is assumed, then the slow motion derivatives can be determined at any of the tested frequencies. Otherwise, extrapolation of the results to zero frequency is required.

6.4.5 Systems Identification

The systems identification technique is based on the method of least squares. For the purposes of this method in particular it is useful to think of the PMM output data, $Y(t)$, as related to the input data $u(t)$, where $u(t)$is the vector which represents the imposed PMM motions.

Ljung (1983) discusses systems identification for general applications. An example of the technique applied to the analysis of PMM data is given here for the model described in Equations (6.3), (6.4) and (6.5).

The input vectors are defined by the acceleration and velocity excitations for sway motion.

$$\begin{aligned} u_1(t) &= v(t) \\ &= \omega_t y_o \cos \omega_t t \end{aligned} \tag{6. 66}$$

and

$$\begin{aligned} u_2(t) &= \dot{v}(t) \\ &= -\omega_t{}^2 y_o \sin \omega_t t \end{aligned} \tag{6. 67}$$

The system input for the linear model is then given by

$$u(t) = [u_1(t), u_2(t)] \tag{6. 68}$$

In the case of a nonlinear model, terms such as $v|v|$ or v^3 are treated as another input vector, for example,

$$\begin{aligned} u_3(t) &= v|v| \\ &= \omega_t{}^2 y_o{}^2 \cos(\omega_t t)|\cos(\omega_t t)| \end{aligned} \tag{6. 69}$$

or

$$\begin{aligned} u_3(t) &= v^3 \\ &= (\omega_t y_o)^3 \cos^3(\omega_t t) \end{aligned} \tag{6. 70}$$

The input vector is simply augmented by the new excitation term, ie. $u_3(t)$, such that

$$u(t) = [u_1(t), u_2(t), u_3(t)] \tag{6. 71}$$

The relationship between the output $Y(t)$ and the input $\underline{u}$ is given by

$$Y(t) = A\underline{u} + e(t) \tag{6. 72}$$

where $A = [a_1, a_2, a_3]$ is the coefficient and $e(t)$ is the error term.

The model form given in Equation (6.9) could be solved similarly using this method.

Jensen (1986) describes an implementation of this technique for the analysis of PMM data. The described procedure averages the measured PMM load data into one period to reduce the amount of data and improve the noise characteristics. A model is assumed to represent the data, which is then fitted using least squares.

The availability of an error term in Equation (6.73) enables the various model forms to be evaluated for goodness of fit. This is useful in determining the most appropriate nonlinear terms.

Also, as in the cases above, where the hydrodynamic coefficients are determined at individual frequencies, the final coefficients depend on the assumption of frequency. If independence of frequency is assumed, the final slow motion derivatives can be determined at any of the tested frequencies. Otherwise extrapolation of the results to zero frequency is required.

6.4 6 Functional Analysis

Another approach for determining hydrodynamic coefficients is by 'functional analysis' (Booth, 1973, Bishop, 1969, 1970, 1973a, 1973b, 1973c, 1973d, 1974a, 1974b). The method assumes frequency dependent data, enabling expressions for the coefficients as a function of frequency to be determined. It is important to note that the model discussed in the literature is linear.

Recalling the functional representation of the Y force given in Equation (6.18),

$$Y[v(t)] = \int_{-\infty}^{\infty} h_v(\tau) v(t-\tau) dt$$

the frequency response $H_v(\omega)$ is given by

$$H_v(\omega) = \int_{-\infty}^{\infty} h_v(\tau) e^{-j\omega t} d\tau \qquad (6.73)$$

where

$$h_v(\tau)=\frac{1}{2\pi}\int_{-\infty}^{\infty}H_v(\omega)e^{j\omega\tau}d\tau \tag{6.74}$$

The frequency response can be expressed as

$$H_v(\omega)=\int_{-\infty}^{\infty}h_v(\tau)\cos\omega\tau\,d\tau-j\int_{-\infty}^{\infty}h_v(\tau)\sin\omega\tau\,d\tau \tag{6.75}$$

This can be written as

$$H_v(\omega)=H_v(\omega)^R+jH_v(\omega)^I \tag{6.76}$$

where

$$H_v(\omega)^R=\int_{-\infty}^{\infty}h_v(\tau)\cos\omega\tau\,d\tau \tag{6.77}$$

and

$$H_v(\omega)^I=-\int_{-\infty}^{\infty}h_v(\tau)\sin\omega\tau\,d\tau \tag{6.78}$$

If the PMM motion is given by

$$v(t)=v_o\cos\omega_t t \tag{6.79}$$

where ω_t is the translation frequency (rads/s) and the force expression is given by.

$$Y[v(t)]=a_1\cos\omega t+b_1\sin\omega t \tag{6.80}$$

then

$$H_v^R(\omega_t)=\frac{a_1}{v_o} \tag{6.81}$$

and

$$H_v^I(\omega_t)=-\frac{b_1}{v_o} \tag{6.82}$$

Assume a non-zero asymptote for $\frac{a_1}{v_o}$ and take the frequency to the limit, *i.e* $\omega_t\to\infty$.

$$\lim_{\omega_t\to\infty}\left(\frac{a_1}{v_o}\right)=Y_v(\infty) \tag{6.83}$$

Therefore

$$H_v{}^R(\omega_t)=Y_v(\infty)+H_v{}^{*R}(\omega_t) \tag{6.84}$$

such that

$$\lim_{\omega_t \to \infty} H_v^{*R}(\omega_t) = 0 \tag{6. 85}$$

and

$$H_v^{*R}(\omega_t) = \int_{-\infty}^{\infty} h_v^*(\tau).\cos\omega_t\tau.d\tau \tag{6. 86}$$

Therefore the linear velocity coefficient as a function of frequency is given by

$$Y_v(\omega_t) = Y_v(\infty) + \int_{-\infty}^{\infty} h_v^*(\tau).\cos\omega_t\tau.d\tau \tag{6. 87}$$

Since

$$\lim_{\omega_t \to \infty}\left(\frac{-b_1}{\omega_t v_o}\right) = Y_{v\bullet}(\infty) \tag{6. 88}$$

Then

$$H_v^{\,I}(\omega_t) = \omega_t Y_{v\bullet}(\infty) + H_v^{*I}(\omega_t) \tag{6. 89}$$

such that

$$\lim_{\omega_t \to \infty} H_v^{*I}(\omega_t) = 0 \tag{6. 90}$$

and

$$-H_v^{*I}(\omega_t) = \int_{-\infty}^{\infty} h_v^*(\tau).\sin\omega_t\tau.d\tau \tag{6. 91}$$

Therefore the acceleration coefficient as a function of frequency is given by

$$Y_{v\bullet}(\omega_t) = Y_{v\bullet}(\infty) - \int_{-\infty}^{\infty} h_v^*(\tau)\frac{\sin\omega_t\tau}{\omega_t}d\tau \tag{6. 92}$$

The results from PMM tests enable $H_v^{*R}(\omega_t)$ to be determined. Note that the static drift tests provide the value of $H_v^{*R}(\omega_t)$ as $\omega_t \to 0$. Since the PMM is only capable of a finite oscillation frequency it cannot achieve $\omega_t \to \infty$, therefore the value of $\frac{a_1}{v_o}$ at the maximum frequency is used for $Y_v(\infty)$. Similarly, the value of $\frac{-b_1}{\omega_t v_o}$ at the maximum measured frequency is used for the value of $Y_{\dot{v}}(\infty)$ in the calculation of $Y_{\dot{v}}(\omega_t)$.

The impulse response $h_v^*(t)$ can be determined by

$$h_v^*(t) = \frac{2}{\pi}\int_0^\infty H_v^{*R}(\omega_t).\cos\omega_t\tau.d\omega_t \qquad (6.93)$$

and

$$H_v^{*R}(\omega_t) = H_v^{R}(\omega_t) - Y_v(\infty) \qquad (6.94)$$

Once $h_v^*(t)$ is determined then $H_v^{*I}(\omega_t)$ can be found.

Note the approximation to the slow motion derivative for the acceleration coefficient is given by

$$\lim_{\omega_t \to 0}\left[\frac{b_1}{-\omega_t v_o}\right] = -\int_0^\infty \tau.h_v(\tau).d\tau \qquad (6.95)$$

To implement this method practically, the force Y should be measured at a range of frequencies, as in the earlier methods. For each response the Fourier components a_1 and b_1 of the signal are required. A curve fitting method based on least squares can be implemented, once again. While it may be possible to determine an expression for the coefficients as a function of frequency, the method applies to a linear model only.

6.5 Comparison of Methods

6.5.1 Introduction

In order to study the performance of the four analysis methods, each of the methods was coded specifically to enable the acceleration and linear velocity coefficient to be calculated from a set of data. The routines used to determine the coefficients from the generated data are given in Appendix 5. These are: 'si_yvdot.m', 'si_yv.m', 'fourint_yvdot.m', 'fourint_yv.m', 'switint_yvdot.m', 'switint_yv.m', discrete_yv.m' and 'discrete_yvdot.m'. The performance of each method was evaluated against the following criteria:

1. The amount of data required to satisfy the algorithm,
2. The sensitivity of the results to noise,
3. The reliance on integration step size, and
4. Model flexibility to incorporate non-linear terms.

To enable the results to be compared, it was decided to adopt a numerical approach where data sets could be artificially composed so that the exact values of the coefficients were known. Comparison between various data sets was decidedly problematic due to the different methods of analysis and experimental error. Therefore the software 'sway_data_gen.m', given in Appendix 5, was developed to generate data sets. The routine generates Y force data using the following expressions for velocity and acceleration:

$$v = 2\pi f_t y_o \cos 2\pi f_t t \tag{6.96}$$

$$\dot{v} = -4\pi^2 f_t^2 y_o \sin 2\pi f_t t \tag{6.97}$$

The force was given by

$$Y = Y_{\dot{v}} \dot{v} + Y_v v + n(t) \tag{6.98}$$

where

$Y_{\dot{v}}$ is the acceleration coefficient,

Y_v is the linear velocity coefficient,

y_o is the amplitude of the translation motion,

f_t (Hz) is the angular frequency of the motion, and

$n(t)$ is noise that can be specified by magnitude and frequency.

The noise model was given by

$$n(t) = n_o[\sin(2\pi f_n t) + \cos(2\pi f_n t)] \tag{6. 99}$$

where

n_o is the amplitude of the noise, and

f_n is the frequency of the noise.

Integration was completed using Simpson's rule, which was coded in Matlab in the function 'defint.m', given in Appendix 5. The integration step size was determined by the data sample rate.

6.5.2 Effect of Sample Rate

Given that two of the methods under investigation rely on integration of the data, it was reasonable to expect that the spacing of the data would affect the results. To study this, a typical data set was generated with no added noise.

Three tests were specified to consider the effect of sample rate. The sample rate was varied from 30Hz, the actual AME PMM rate, to 1000Hz in each of the three tests, denoted by A, B, and C, specified in Table 6.1. Five complete cycles were generated for each of the data sets. Tables 6.2 – 6.7 contain the values of the acceleration and linear velocity coefficient for each of the tests.

The difference between tests A, B, and C was in the set value of the linear velocity coefficient. The aim in setting these differences was to determine whether the analysis method was effected by the relative values of the coefficients.

Test	$Y_{\dot{v}}$	Y_v	y_o (m)	f_t (Hz)	n_o	f_n (Hz)	Sample Rate (Hz)	No. Cycles
A	-10	-10	0.14	0.20	0	0	30 - 1000	5
B	-10	-100	0.14	0.20	0	0	30 – 1000	5
C	-10	-1000	0.14	0.20	0	0	30 - 1000	5
D	-10	-10	0.14	0.20	0	0	30	1 - 10
E	-10	-10	0.14	0.20	0.05-1.00	0.25-2.00	30	5

Table 6.1 Test options for comparison of methods of analysis.

Sample Rate (Hz)	Fourier Int.	Systems Id.	Switched Int.	Discrete
30	-9.9867	-10.0000	-9.6538	-10.1311
50	-9.9920	-10.0000	-9.7953	-10.0792
80	-9.9950	-10.0000	-9.8732	-10.0000
100	-9.9960	-10.0000	-9.8988	-10.0000
500	-9.9992	-10.0000	-9.9800	-10.0000
1000	-9.9996	-10.0000	-9.9900	-10.0000

Table 6.2 Simulated comparison of PMM analysis methods. Acceleration coefficient, $Y_{\dot{v}}$, given for the four analysis methods with varying sample rates. Simulation parameters given by TEST A in Table 6.1.

Sample Rate (Hz)	Fourier Int.	Systems Id.	Switched Int.	Discrete
30	-9.9867	-10.0000	-9.7588	-10.0000
50	-9.9920	-10.0000	-9.8696	-10.0000
80	-9.9950	-10.0000	-9.9199	-10.0000
100	-9.9960	-10.0000	-10.0076	-10.0000
500	-9.9992	-10.0000	-10.0016	-10.0000
1000	-9.9996	-10.0000	-9.9937	-10.0000

Table 6.3 Simulated comparison of PMM analysis methods. Linear velocity coefficient, Y_v, given for the four analysis methods with varying sample rates. Simulation parameters given by TEST A in Table 6.1.

As expected the Fourier and Switched Integration techniques were affected by the sample rate, since this determined the integration spacing between points. Significantly, the Fourier method was less affected than the Switched method. Increasing the sample rate improved the performance of these methods. The Systems Identification and Discrete methods were unaffected by the change in sample rate.

Sample Rate (Hz)	Fourier Int.	Systems Id.	Switched Int.	Discrete
30	-9.9867	-10.0000	-6.6559	-11.3310
50	-9.9920	-10.0000	-7.9958	-10.7992
80	-9.9950	-10.0000	-8.7483	-10.0000
100	-9.9960	-10.0000	-8.9989	-10.0000
500	-9.9992	-10.0000	-9.8000	-10.0000
1000	-9.9996	-10.0000	-9.9000	-10.0000

Table 6.4 Simulated comparison of PMM analysis methods. Acceleration coefficient, $Y_{\dot{v}}$, given for the four analysis methods with varying sample rates. Simulation parameters given by TEST B in Table 6.1.

Sample Rate (Hz)	Fourier Int.	Systems Id.	Switched Int.	Discrete
30	-99.8668	-100.0000	-98.7968	-100.0000
50	-99.9201	-100.0000	-98.7320	-100.0000
80	-99.9500	-100.0000	-99.2132	-100.0000
100	-99.9600	-100.0000	-99.7231	-100.0000
500	-99.9920	-100.0000	-99.9450	-100.0000
1000	-99.9960	-100.0000	-99.9372	-100.0000

Table 6.5 Simulated comparison of PMM analysis methods. Linear velocity coefficient, Y_v, given for the four analysis methods with varying sample rates. Simulation parameters given by TEST B in Table 6.1.

Increasing the set value of the linear velocity coefficient relative to the acceleration coefficient reduced the accuracy of the Switched integration method. The estimate of the acceleration coefficient given by the Switched method in Table 6.4 had an error of

33% at 30 Hz. This was improved however as the sample rate was increased. The Discrete method also showed signs of being affected in the acceleration coefficient. This was however improved by the increase in sample rate. The estimates of the linear velocity coefficients by both the Discrete and Switched methods appear to be unaffected. The estimates of the acceleration and linear velocity coefficients by the Fourier and Systems methods do not appear to be affected.

Sample Rate (Hz)	Fourier Int.	Systems Id.	Switched Int.	Discrete
30	-9.9867	-10.0000	23.3221	-24.6637
50	-9.9920	-10.0000	9.9995	-17.9991
80	-9.9950	-10.0000	2.5006	-10.0000
100	-9.9960	-10.0000	0.0005	-10.0000
500	-9.9992	-10.0000	-8.0000	-10.0000
1000	-9.9996	-10.0000	-9.0000	-10.0000

Table 6.6 Simulated comparison of PMM analysis methods. Acceleration coefficient, $Y_{\dot{v}}$, given for the four analysis methods with varying sample rates. Simulation parameters given by TEST C in Table 6.1.

Sample Rate (Hz)	Fourier Int.	Systems Id.	Switched Int.	Discrete
30	-998.6684	-1000.0000	-989.1774	-1000.0000
50	-999.2006	-1000.0000	-987.3560	-1000.0000
80	-999.5002	-1000.0000	-992.1458	-1000.0000
100	-999.6002	-1000.0000	-996.8780	-1000.0000
500	-999.9200	-1000.0000	-999.3788	-1000.0000
1000	-999.9600	-1000.0000	-999.3717	-1000.0000

Table 6.7 Simulated comparison of PMM analysis methods. Linear velocity coefficient, Y_v, given for the four analysis methods with varying sample rates. Simulation parameters given by TEST C in Table 6.1.

Increasing the set value of the linear velocity coefficient demonstrates clearly the effect on the Switched Integration and Discrete methods. Large errors in the estimate of the acceleration coefficient, given by these methods, exist. Once again increasing the sample rate improves the accuracy of these coefficients.

The Systems Identification method performed well with no affect due to change in either the sample rate or the relative magnitude of the coefficients. The Fourier Integration method was only slightly affected by the change in sample rate, and not affected by the relative magnitudes of the coefficients. Increasing the sample rate improved the accuracy of the Discrete Analysis and Switched Integration methods. Both methods produced large errors in the estimates of the acceleration coefficients as the set value of the linear velocity coefficient was increased. These errors were reduced as the sample rate was increased. The Discrete method was significantly more accurate in its estimate of the linear velocity coefficients compared with the Switched method.

6.5.3 Data Requirements

To study the efficiency of the algorithms a series of tests using the data generator, where the number of cycles in each data set was varied, were performed. The model parameters were set according to option D in Table 6.1. The sample rate was set at 30Hz while the number of cycles were varied from 1 to 10. The resultant acceleration and linear velocity coefficients determined from the analysis are given in Tables 6.8 and 6.9.

All methods were largely unaffected by the amount of data provided for analysis. Although, the Fourier method did improve its accuracy slightly (error 0.7% - 0.1%) as the number of cycles were increased. It is evident also that the Switched method, with a sample rate of 30 Hz, has a consistently larger error, as shown in Tables 6.8 and 6.9.

No. Cycles	Fourier Int.	Systems Id.	Switched Int.	Discrete
1	-9.9338	-10.0000	-9.6538	-10.1645
2	-9.9668	-10.0000	-9.6538	-10.1645
3	-9.9778	-10.0000	-9.6538	-10.1089
5	-9.9867	-10.0000	-9.6538	-10.1311
7	-9.9905	-10.0000	-9.6538	-10.1407
10	-9.9933	-10.0000	-9.6538	-10.1478

Table 6.8 Simulated comparison of PMM analysis methods. Acceleration coefficient, $Y_{\dot{v}}$, for the four analysis methods with varying number of cycles ie. amount of data in set. Simulation parameters given by TEST D in Table 6.1.

No. Cycles	Fourier Int.	Systems Id.	Switched Int.	Discrete
1	-9.9338	-10.0000	-9.7588	-10.0000
2	-9.9668	-10.0000	-9.7588	-10.0000
3	-9.9778	-10.0000	-9.7588	-10.0000
5	-9.9867	-10.0000	-9.7588	-10.0000
7	-9.9905	-10.0000	-9.7588	-10.0000
10	-9.9933	-10.0000	-9.7588	-10.0000

Table 6.9 Simulated comparison of PMM analysis methods. Linear velocity coefficient, Y_v, for the four analysis methods with varying number of cycles ie. amount of data in set. Simulation parameters given by TEST D in Table 6.1.

6.5.4 Effect of Noise

A series of tests were performed using the data generator to determine the effect of noise on the determination of the acceleration coefficients. The simulation parameters are given by option E in Table 6.1. The results are contained in Table 6.10 and 6.11.

n_o	f_n (Hz)	Fourier Int.	Systems Id.	Switched Int.	Discrete
0.1000	0.2500	-9.9867	-10.0000	-9.6584	-10.1249
0.1000	0.5000	-9.9757	-9.9890	-9.6682	-10.0706
0.1000	1.0000	-9.9867	-10.0000	-9.7599	-10.5432
0.1000	2.0000	-9.9867	-10.0000	-9.6512	-10.1123
0.2000	0.2500	-9.9867	-10.0000	-9.6631	-10.1188
0.2000	0.5000	-9.9648	-9.9780	-9.6826	-10.0101
0.2000	1.0000	-9.9867	-10.0000	-9.8660	-10.9552
0.2000	2.0000	-9.9867	-10.0000	-9.6486	-10.0935
0.5000	0.2500	-9.9867	-10.0000	-9.6771	-10.1002
0.5000	0.5000	-9.9319	-9.9451	-9.7259	-9.8285
0.5000	1.0000	-9.9867	-10.0000	-10.1844	-12.1913
0.5000	2.0000	-9.9867	-10.0000	-9.6408	-10.0371
1.0000	0.2500	-9.9867	-10.0000	-9.7004	-10.0692
1.0000	0.5000	-9.8771	-9.8902	-9.7980	-9.5258
1.0000	1.0000	-9.9867	-10.0000	-10.7150	-14.2514
1.0000	2.0000	-9.9867	-10.0000	-9.6279	-9.9430

Table 6.10 Simulated comparison of PMM analysis methods. Acceleration coefficient, $Y_{\dot{v}}$, for the four analysis methods with added noise. Simulation parameters given by TEST E in Table 6.1.

The results in Tables 6.10 and 6.11 show that all four methods were affected by noise. The Fourier technique appears to be the most robust, with the Switched Integration method a close second. The Discrete method gave the largest errors. The estimates by the Systems Identification method were mostly affected by the increase in magnitude of the noise. Reasonable estimates were provided by the Systems Identification method while the magnitude of the noise was less than 2% of the signal magnitude.

n_o	f_n (Hz)	Fourier Int.	Systems Id.	Switched Int.	Discrete
0.1000	0.2500	-9.8261	-9.7858	-9.5951	-9.8236
0.1000	0.5000	-9.9523	-9.6501	-9.7045	-10.0517
0.1000	1.0000	-9.9867	-9.6089	-9.6451	-9.4316
0.1000	2.0000	-9.9867	-10.0051	-9.7692	-9.9483
0.2000	0.2500	-9.6655	-9.5715	-9.4314	-9.6472
0.2000	0.5000	-9.9179	-9.3003	-9.6502	-10.1033
0.2000	1.0000	-9.9867	-9.2179	-9.5313	-8.8632
0.2000	2.0000	-9.9867	-10.0101	-9.7797	-9.8967
0.5000	0.2500	-9.1836	-8.9288	-8.9404	-9.1179
0.5000	0.5000	-9.8146	-8.2507	-9.4873	-10.2584
0.5000	1.0000	-9.9867	-8.0447	-9.1902	-7.1579
0.5000	2.0000	-9.9867	-10.0253	-9.8111	-9.7416
1.0000	0.2500	-8.3806	-7.8576	-8.1220	-8.2358
1.0000	0.5000	-9.6425	-6.5013	-9.2159	-10.5167
1.0000	1.0000	-9.9867	-6.0895	-8.6216	-4.3159
1.0000	2.0000	-9.9867	-10.0506	-9.8634	-9.4833

Table 6.11 Simulated comparison of PMM analysis methods. Acceleration coefficient, Y_v, for the four analysis methods with added noise. Simulation parameters given by TEST E in Table 6.1.

6.5.5 Choice of Method

In the simulated study, the Fourier Integration method provided good estimates (<0.2% error) of the acceleration and linear velocity coefficient at the AME PMM sampling frequency of 30Hz. This result was little affected by the change in relative magnitudes of the acceleration coefficient to the linear velocity coefficient. The accuracy of the results was improved by increasing the sample rate. The amount of data required by the method was shown here to improve the results (0.7% error for 1 cycle compared to <0.1% for 10 cycles). The method also provided a good result in the presence of noise. On average, across all the simulations denoted by TEST E in Table 6.1, the error in the presence of noise was 1.3%. On the flexibility of the method

to incorporate various non-linear models, the Fourier method was regarded to be complex. Heavy manipulation of the data may be required to resolve non-trivial forms of a non-linear mathematical model.

The Systems Identification method provided excellent estimates of the acceleration and linear velocity coefficient at the sampling frequency of 30Hz. No error was determined for the measured accuracy. The method was also shown to be unaffected by the increase in sample frequency and the relative magnitude of the set value of the coefficients. The results from the method were however affected by the presence of noise. On average, across all the noise simulations, the error in the presence of noise was 5.4%. For implementing complex non-linear mathematical models in the analysis, the Systems Identification method was regarded as the simplest and most convenient to use.

The Switched Integration method did not provide reliable estimates of the coefficients. At the sample frequency of 30Hz, the error was up to 3.5% for the case of similar magnitude between the set coefficient values. As the relative magnitude was increased the error increased (relative magnitude of the acceleration to linear velocity coefficient was 1:10 with 33% error, and with relative magnitude of 1:100 the error was >300%). It was obvious from the results that the main error would occur in the less dominant coefficient. For instance, the error in the estimate of the acceleration coefficient increased with the set value of the linear velocity coefficient. Increasing the sample rate and the amount of data recorded improved the performance of the method. The performance of the method in the presence of noise was good, with an average error of 4.1%. Similar to the Fourier method, the Switched method would be complex to implement for non-trivial mathematical models.

The Discrete Analysis method gave reasonable estimates of the coefficients at 30Hz sample frequency. The method was affected by the relative magnitudes of the acceleration and linear velocity coefficients, with greater than 100% error in the coefficient. As with the Switched Integration method, the main error occurred in the estimate of the least significant coefficient. As in the earlier case, the error in the estimate of the acceleration coefficient increased with the increase in the set value of the linear velocity coefficient. The performance of the Discrete method was also

improved with the increase in data and sample frequency. The method had the worst response to the presence of noise with an average error of 6.7% across the simulations. The method relies on an approach similar to the Systems Identification method for determining estimates of non-linear coefficients. It does however provide a useful method for determining the presence of non-linearity in the measured data.

On the basis that the flexibility of the method to incorporate various non-linear mathematical models into the analysis was important, and that a low–pass filter can be implemented to remove noise components in the data, the following rating was determined for the four methods described:

1. Systems Identification
2. Fourier Integration
3. Discrete Analysis
4. Switched Integration

However, on the basis of a linear model only and no low-pass filter, the Fourier Integration method provided was the best results. The Fourier method also provides the most physically meaningful results while the Systems Identification method is simply a curve fitting approach which changes its meaning as easily as the model can be changed.

6.6 AME PMM Software

The Systems Identification method was developed as the basis of the AME PMM data analysis algorithm.

Six routines were developed to complete the analysis of PMM data from pure yaw, sway and static tests. Appendix 5 contains the data analysis software routines: 'xvehicle.m', 'xdynamic.m', 'xstatic.m', 'xhr.m', and 'xfilenm.m'. The filter routine called from these functions, 'bfilt.m' is given in Appendix 3. The routines are implemented using Matlab (Mathworks, 1994).

The file 'xvehicle.m' is modified with all the parameters pertaining to the series of completed PMM measurements, including the desired mathematical model to be fitted. The results are sent to an ASCII file that is also specified in 'xvehicle.m'.

6.7 Discussion

Five methods were described for the analysis of PMM data. Four of those were simulated to investigate the effects of sample frequency, relative magnitude of coefficients, amount of data and noise on the accuracy of the results. The approaches given by the Fourier Integration and the Systems Identification method were found to be superior.

The results showed the Fourier Integration method gave better results than the Systems method in the presence of noise. However, due to the perceived complexity of implementing possible arbitrary non-linear models using the Fourier approach, the method was rated second of the two. Especially since the implementation of a low-pass filter would resolve the noise performance of the Systems Identification method.

The recommended approach for the AME PMM is the Systems Identification method coupled with a low pass filter designed to remove components of noise from the measured data.

Chapter 7. PAP104 Model Results

7.1 Introduction

A series of tests were performed on a 1/3rd scale model of the PAP104 remotely operated vehicle using the Australian Maritime Engineering (AME) Planar Motion Mechanism (PMM). These experiments were conducted to provide some validation for the AME PMM data analysis techniques and software. The 1/3rd-scale model of the PAP104 vehicle was constructed and tested according to the program given in Appendix 4. The results are compared to tests undertaken at the Defence Evaluation Research Agency No.2 Towing Tank, Haslar, Gosport, Hants, U.K. (Friswell, 1985).

The AME PMM, described in Chapter Three, is situated at the Australian Maritime College Beauty Point campus in Tasmania. The PMM provides horizontal plane motions, including translation and rotation, to models attached to the mechanism and suspended in a water flow. The tests were conducted in the Circulating Water Channel (CWC) at the AMC.

Both vertical plane and horizontal plane hydrodynamic coefficients were determined for the PAP104 model. To provide vertical motions relative to the model, the body was rotated on its side.

This chapter presents the results from the testing of the PAP104 model. A detailed error analysis is conducted in the following chapter.

7.2 Vehicle Description

The first remotely operated vehicle to be characterised by the AME PMM was the French remotely operated vehicle (ROV) PAP104. Currently PAP104's are used on the Royal Australian Navy's Bay Class Inshore Minehunters.

The PAP104, shown in Figure 7.1, is remotely controlled via an umbilical cable that extends from the surface ship; its dimensions are length 2.7m, width 1.2m, and height 1.3m. The maximum operating speed of the vehicle is up to five knots relative to the water flow.

A 1:3 scale model of the PAP104 was constructed for determining the hydrodynamic coefficients using the PMM. The main interest in the vehicle's manoeuvrability is at speeds of less than two knots. The requirement is due to the need to carefully manoeuvre the vehicle in the final stages of the mine clearance operation, as the shipboard operator attempts to accurately place explosives.

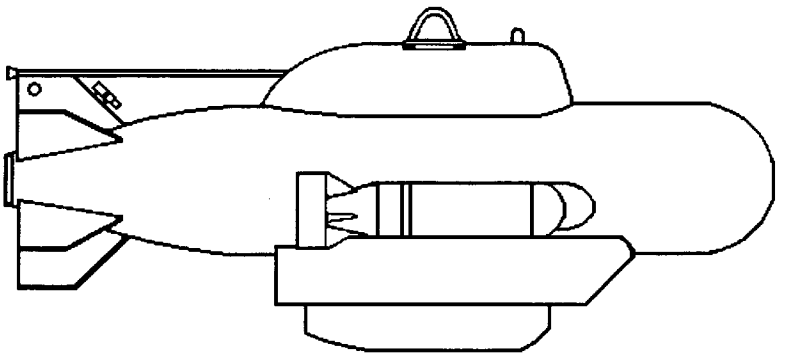

Figure 7.1 The PAP104 Remotely Operated Vehicle

The following results were obtained from the analysis of a series of tests performed using the PMM on the 1/3rd model described. The test program is outlined in Appendix 4. Dynamic oscillation and static tests were conducted with the model in an upright position to obtain sway and yaw coefficients, then on its side to obtain pitch and heave coefficients.

The nominal CWC flow speed was 1.0m/s and the Reynolds number was 0.9×10^{6}.

7.3 The HPMM Hydrodynamic Model

The general mathematical model fitted to the measured PAP104 data is given by the following for each of the motion types: static drift, dynamic yaw, dynamic sway, static pitch, dynamic heave and dynamic pitch.

Generally for all motion types tested here, the surge force was modelled by

$$X_{MODEL}(t) = X_{uu}u^2 \tag{7.1}$$

In the horizontal plane tests, the heave force was modelled by

$$Z_{MODEL}(t) = Z_o \tag{7.2}$$

The mathematical models for each of the six types of motion are:

Dynamic sway:

$$Y_{MODEL}(t) = \left(Y_{\dot{v}} - m\right)\dot{v} + Y_v v \tag{7.3}$$

$$N_{MODEL}(t) = N_v v + N_{v|v|} v|v| \tag{7.4}$$

Dynamic yaw:

$$Y_{MODEL}(t) = \left(Y_{\dot{r}} - mx_G\right)\dot{r} + (Y_r - mu)r \tag{7.5}$$

$$M_{MODEL}(t) = M_{uu}u^2 \tag{7.6}$$

$$N_{MODEL}(t) = \left(N_{\dot{r}} - I_{zz}\right)\dot{r} + (N_r - mx_G u)r \tag{7.7}$$

Static yaw:

$$Y_{MODEL}(t) = Y_v v + Y_{v|v|} v|v| \tag{7.8}$$

$$K_{MODEL}(t) = K_v v + K_{v|v|} v|v| \tag{7.9}$$

$$M_{MODEL}(t) = M_{uu}u^2 + M_{vv}v^2 + M_{vvvv}v^4 \tag{7.10}$$

$$N_{MODEL}(t) = N_v v + N_{v|v|} v|v| \tag{7.11}$$

Dynamic heave:

$$Z_{MODEL}(t) = \left(Z_{\dot{w}} - m\right)\dot{w} + Z_o + Z_w w \tag{7.12}$$

$$M_{MODEL}(t) = \left(M_{\dot{w}} + mx_G\right)\dot{w} + M_w w \tag{7.13}$$

Dynamic pitch:

$$Z_{MODEL}(t) = \left(Z_{\dot{q}} + mx_G \right)\dot{q} + Z_o + \left(Z_q + mu\right)q \qquad (7.14)$$

$$M_{MODEL}(t) = \left(M_{\dot{q}} - I_{yy} \right)\dot{q} + M_{uu}u^2 + \left(M_q - mx_G u\right)q \qquad (7.15)$$

Static pitch:

$$Z_{MODEL}(t) = Z_o + Z_w w \qquad (7.16)$$

$$M_{MODEL}(t) = M_{uu}u^2 + M_w w + M_{www} www \qquad (7.17)$$

7.4 Results

7.4.1 Horizontal Plane Inertia

The following table gives the results of the inertia tests for the PAP104 1/3rd scale model.

Variable	Dimensional Value	Non-dimensional Value
I_{yy}	0.83 kg.m^2	0.0028
I_{zz}	1.01 kg.m^2	0.0034
m	24.44 kg	0.0670
x_G	0.0005 m	0.0006
y_G	0.0097 m	0.0108
z_G	-0.0138 m	-0.0153
x_B	-0.0007 m	-0.0008
y_B	0.0002 m	0.0002
z_B	-0.0217 m	-0.0241

Table 7.1 PAP104 Model Test Inertia Results

7.4.2 Dynamic Sway

The PAP104 model was tested at a number of frequencies and amplitudes in dynamic sway. Analysis of each test run produced a value of the coefficients relevant to the

motion. The results are plotted in Figures 7.2 to 7.5. Table 7.2 contains a single non-dimensional value for each of the coefficients; which were determined by extrapolating the results to zero frequency using a zero order polynomial fit.

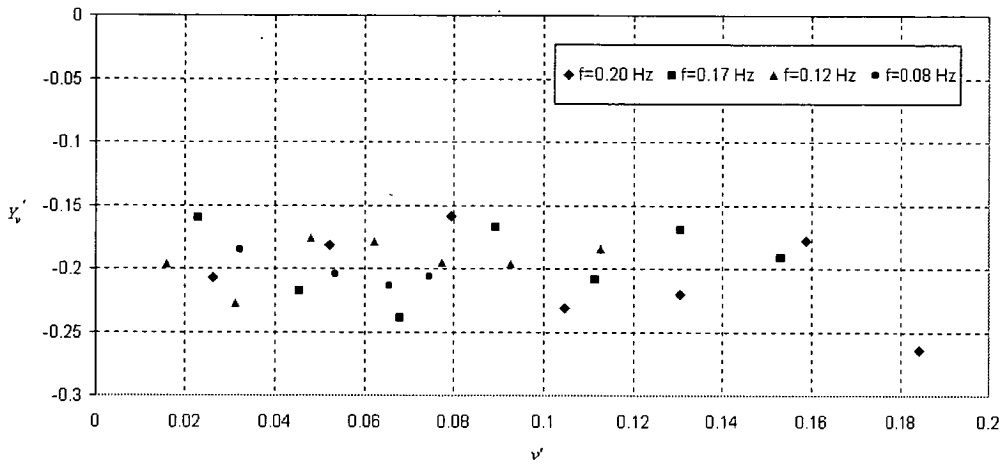

Figure 7.2 Calculated non-dimensional values of the linear coefficient Y_v' from the dynamic sway tests of the PAP104 1/3rd scale model. X-axis is the non-dimensional velocity.

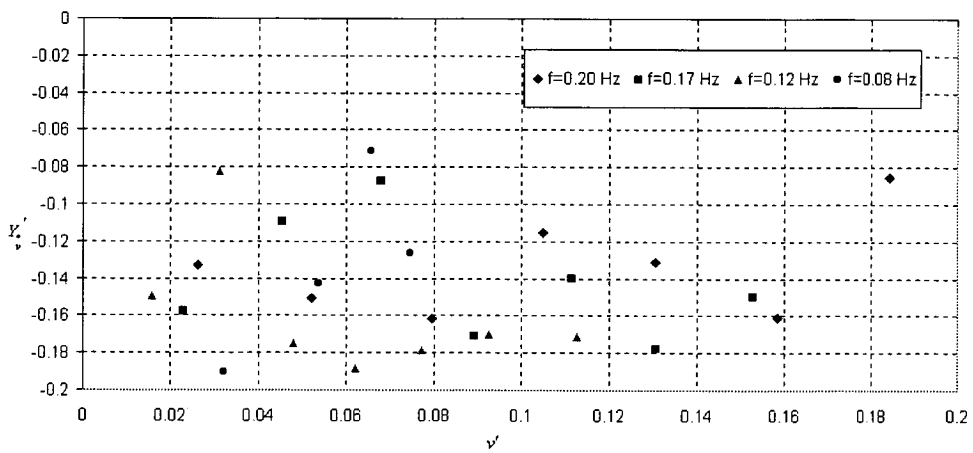

Figure 7.3 Calculated non-dimensional values of the linear coefficient Y_v' from the dynamic sway tests of the PAP104 1/3rd scale model. X-axis is the non-dimensional velocity.

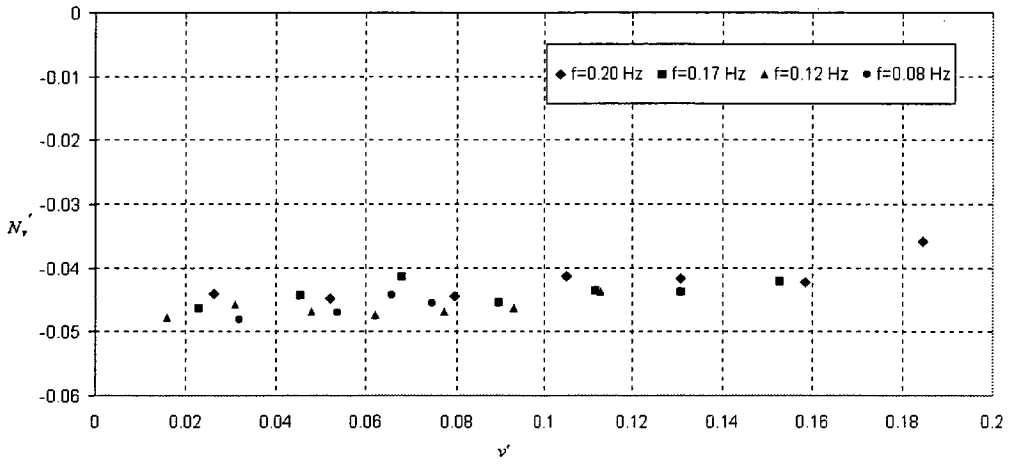

Figure 7.4 Calculated non-dimensional values of the linear coefficient N_v' from the dynamic sway tests of the PAP104 1/3rd scale model. X-axis is the non-dimensional velocity.

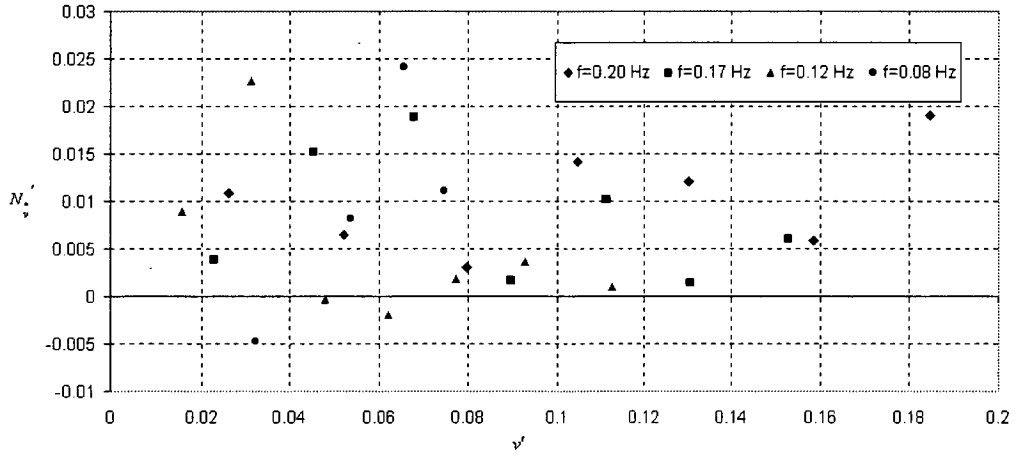

Figure 7.5 Calculated non-dimensional values of the linear coefficient $N_{\dot{v}}'$ from the dynamic sway tests of the PAP104 1/3rd scale model. X-axis is the non-dimensional velocity.

While it is difficult to draw conclusions from the results regarding frequency dependence without error bars, it would appear that no consistent frequency dependency is present. Thus it is a reasonable assumption in the case of this data to assume a zero frequency coefficient.

The variation in the data for $N_{\dot{v}}'$ illustrates the result obtained when analysing a value that is either small, ie. close to zero, or is determined from ill-defined experimental

tests. An ill-defined experiment in this case is defined as one which does not completely excite that component of the force and hence the characteristic force response is not measured. It was found that the AME PMM did not have the range of motions required to dynamically excite all the nonlinear components of the PAP104 1/3rd scale model. Therefore determining nonlinear coefficents from the measured force response was not possible from dynamic tests.

Coefficient	Non-dimensional Value
X_{uu}'	-0.0112
$Y_{\dot{v}}'$	-0.1465
Y_v'	-0.1983
$N_{\dot{v}}'$	0.0064
Z_o'	0.2202
N_v'	-0.0446

Table 7.2 Results from 1/3rd-scale PAP104 PMM dynamic pure sway model tests.

7.4.3 Static Yaw

Results from analysis of the static yaw tests are given in the following table:

Coefficient	Non-dimensional value
X_{uu}'	-0.0120
X_{vv}'	0.0431
Y_{v}'	-0.1823
$Y_{v\|v\|}'$	-0.3004
Z_{o}'	0.1978
K_{v}'	0.0016
$K_{v\|v\|}'$	0.0077
M_{uu}'	0.0017
M_{vv}'	-0.0131
M_{vvvv}'	0.0419
N_{v}'	-0.0546
$N_{v\|v\|}'$	0.0692

Table 7.3 Results from 1/3rd PAP104 PMM static yaw model tests.

7.4.4 Dynamic Yaw

The PAP104 model was tested at a number of frequencies and amplitudes in dynamic yaw. Analysis of each test run produced a value of the coefficients relevant to the motion. The results are plotted in Figures 7.6 to 7.9. Table 7.4 contains a single non-dimensional value for each of the coefficients; which were determined by extrapolating the results to zero frequency using a zero order polynomial fit.

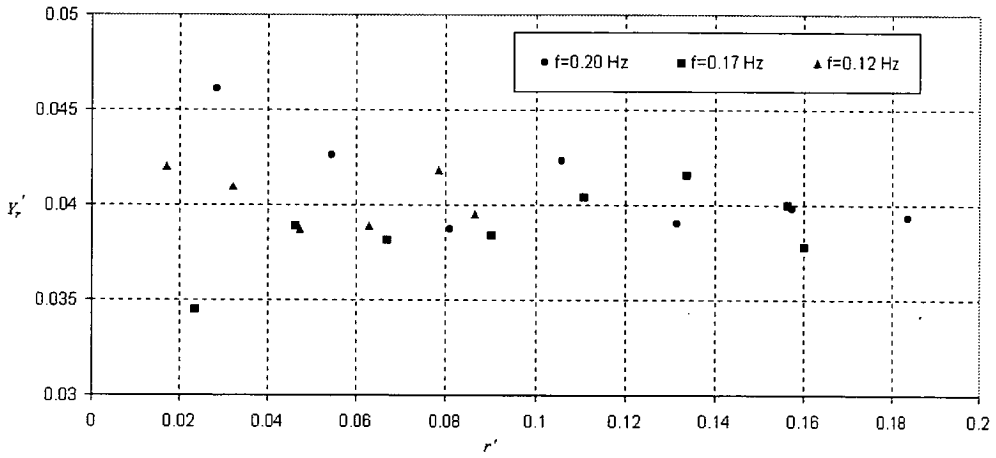

Figure 7.6 Calculated non-dimensional values of the linear coefficient Y_r' from the dynamic yaw tests of the PAP104 1/3rd scale model. X-axis is the non-dimensional angular velocity.

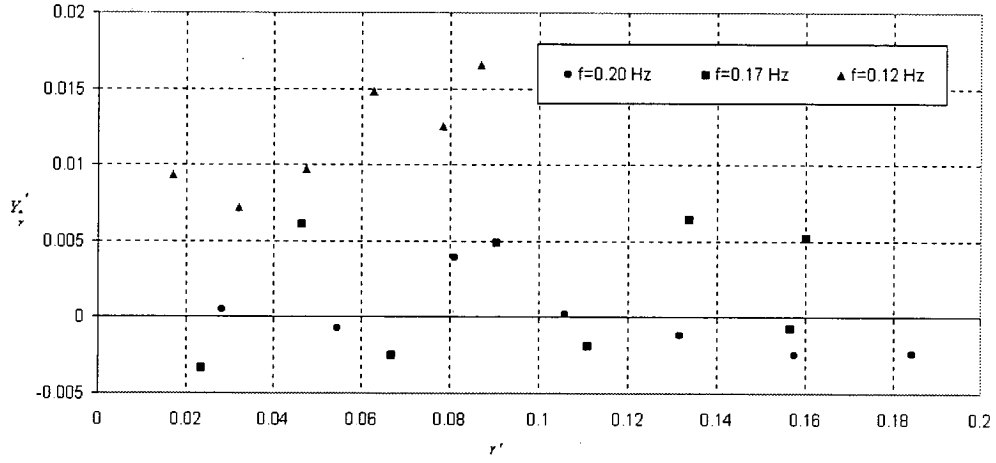

Figure 7.7 Calculated non-dimensional values of the linear coefficient $Y_{\dot{r}}'$ from the dynamic yaw tests of the PAP104 1/3rd scale model. X-axis is the non-dimensional angular velocity.

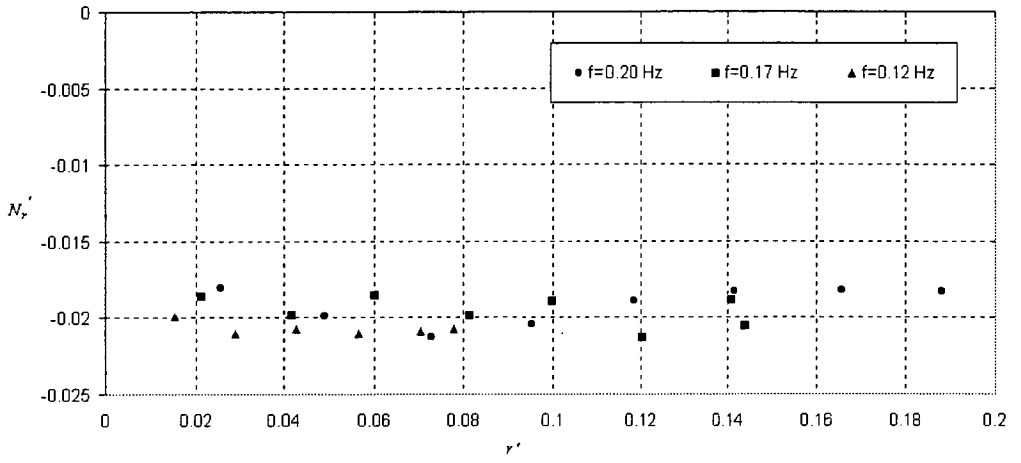

Figure 7.8 Calculated non-dimensional values of the linear coefficient N_r' from the dynamic yaw tests of the PAP104 1/3rd scale model. X-axis is the non-dimensional angular velocity.

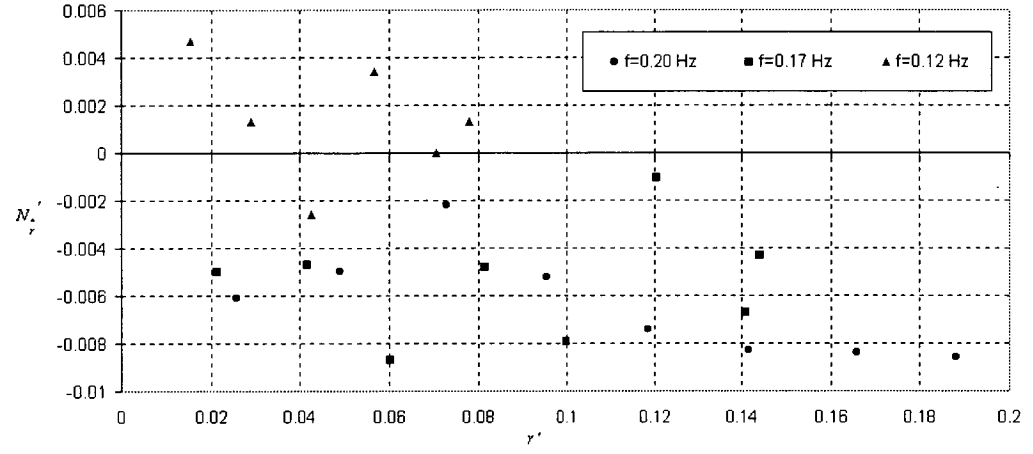

Figure 7.9 Calculated non-dimensional values of the linear coefficient $N_{\dot{r}}'$ from the dynamic yaw tests of the PAP104 1/3rd scale model. X-axis is the non-dimensional angular velocity.

Coefficient	Non-dimensional value
X_{uu}'	-0.0100
$Y_{\dot{r}}'$	0.0078
Y_r'	0.0399
Z_o'	0.2245
M_{uu}'	0.0005
N_r'	-0.0201
$N_{\dot{r}}'$	-0.0027

Table 7.4 Results from 1/3rd-scale PAP104 PMM dynamic pure yaw model tests.

7.4.5 Static Pitch

Results from analysis of the static pitch tests are given in the following table:

Coefficient	Non-dimensional value
X_{uu}'	-0.0081
Z_w'	-0.2406
M_{uu}'	0.0012
M_w'	0.0243
M_{www}'	-0.0270

Table 7.5 Results from 1/3rd PAP104 PMM static pitch model tests.

7.4.6 Dynamic Heave

The PAP104 model was tested at a number of frequencies and amplitudes in dynamic heave. The results are plotted in Figures 7.10 to 7.13. Table 7.6 contains a single non-

dimensional value for each of the coefficients; which were determined by extrapolating the results to zero frequency.

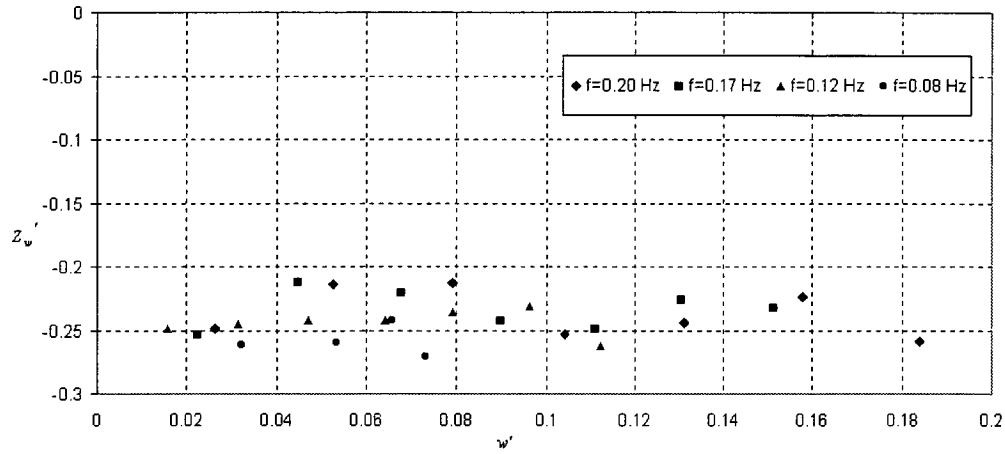

Figure 7.10 Calculated non-dimensional values of the linear coefficient Z_w' *from the dynamic heave tests of the PAP104 1/3rd scale model. X-axis is the non-dimensional heave velocity.*

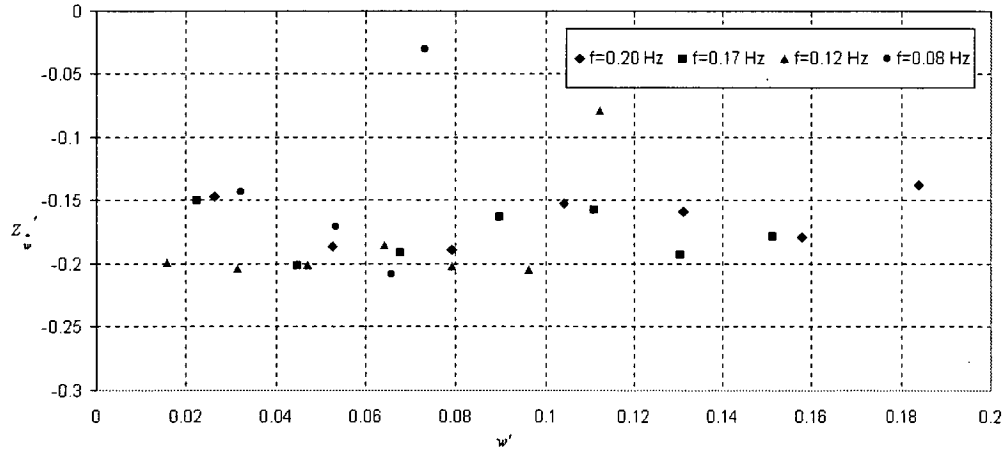

Figure 7.11 Calculated non-dimensional values of the linear coefficient $Z_{\dot{w}}'$ *from the dynamic heave tests of the PAP104 1/3rd scale model. X-axis is the non-dimensional heave velocity.*

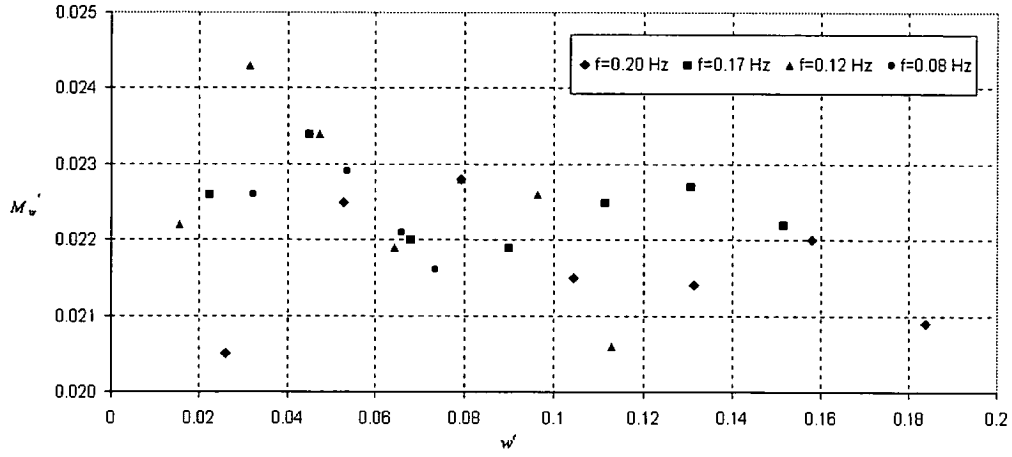

Figure 7.12 Calculated non-dimensional values of the linear coefficient M_w' from the dynamic heave tests of the PAP104 1/3rd scale model. X-axis is the non-dimensional heave velocity.

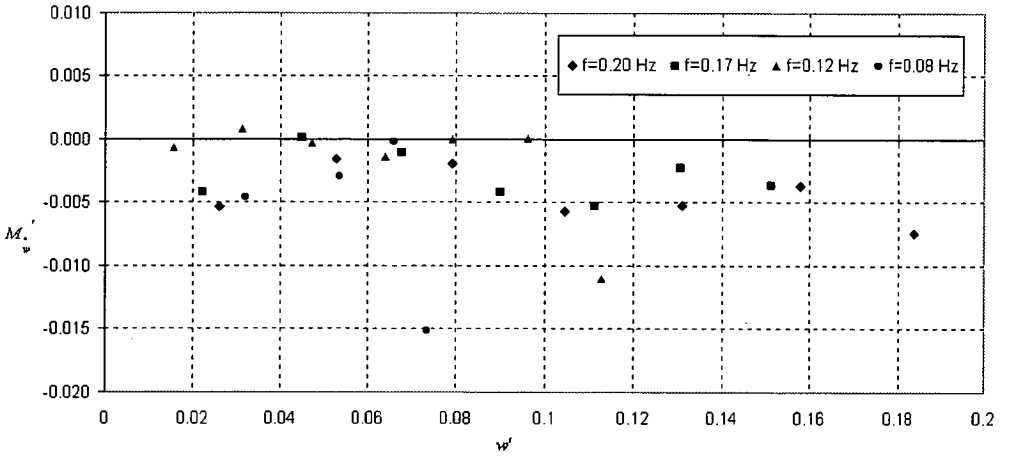

Figure 7.13 Calculated non-dimensional values of the linear coefficient $M_{\dot{w}}'$ from the dynamic heave tests of the PAP104 1/3rd scale model. X-axis is the non-dimensional heave velocity.

Coefficient	Non-dimensional value
X_{uu}'	-0.0107
Z_w'	-0.2431
$Z_{\dot{w}}'$	-0.1163
$M_{\dot{w}}'$	0.0019
M_w'	0.0224

Table 7.6 Results from 1/3rd-scale PAP104 PMM dynamic pure heave model tests.

7.4.7 Dynamic Pitch

The PAP104 model was tested at a number of frequencies and amplitudes in dynamic pitch. The results are plotted in Figures 7.14 to 7.17. Table 7.7 contains a single non-dimensional value for each of the coefficients; which were determined by extrapolating the results to zero frequency using a zero order polynomial fit.

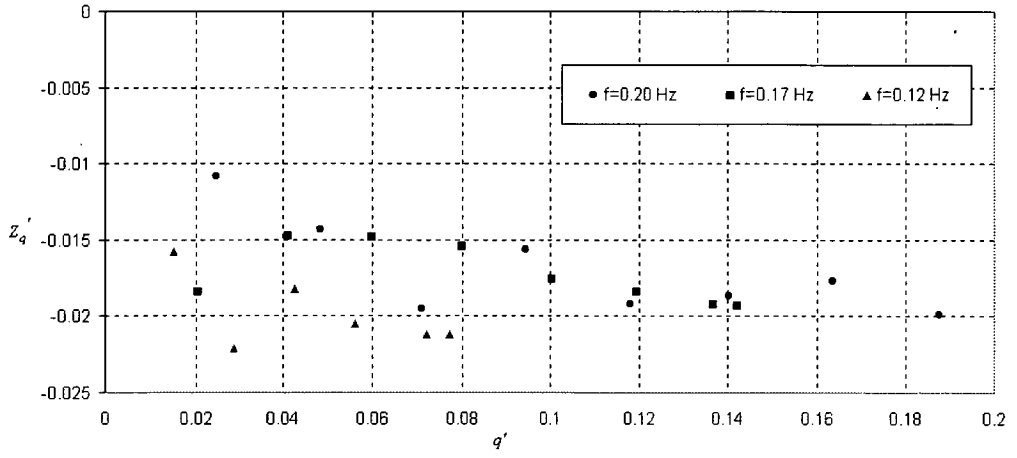

Figure 7.14 Calculated non-dimensional values of the linear coefficient Z_q' from the dynamic pitch tests of the PAP104 1/3rd scale model. X-axis is the non-dimensional angular pitch velocity.

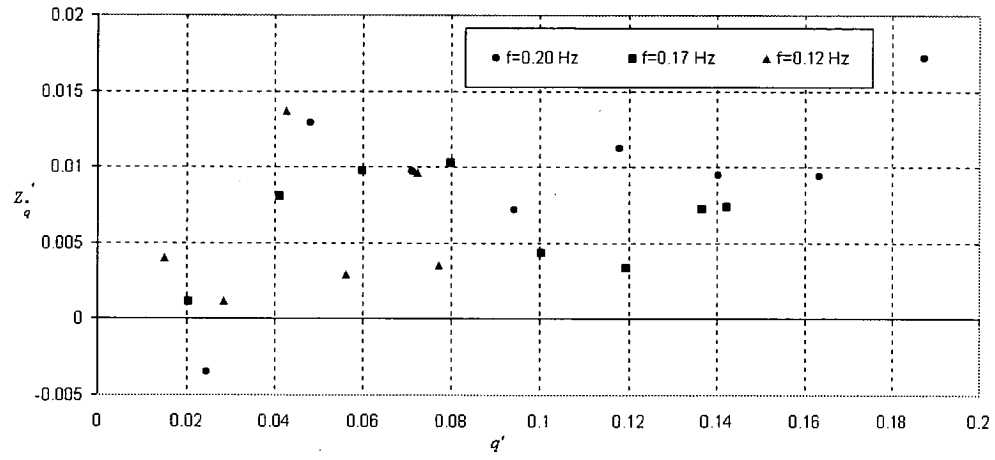

Figure 7.15 Calculated non-dimensional values of the linear coefficient Z_q' *from the dynamic pitch tests of the PAP104 1/3rd scale model. X-axis is the non-dimensional angular pitch velocity.*

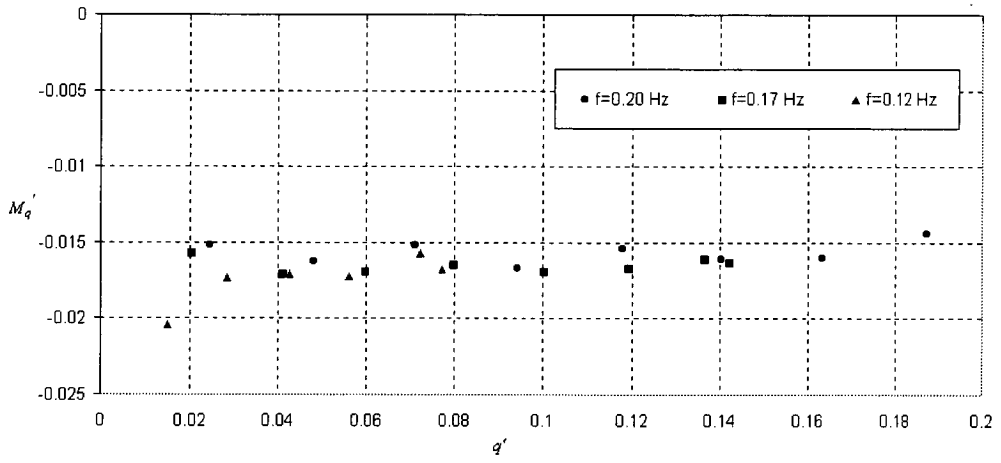

Figure 7.16 Calculated non-dimensional values of the linear coefficient M_q' *from the dynamic pitch tests of the PAP104 1/3rd scale model. X-axis is the non-dimensional angular pitch velocity.*

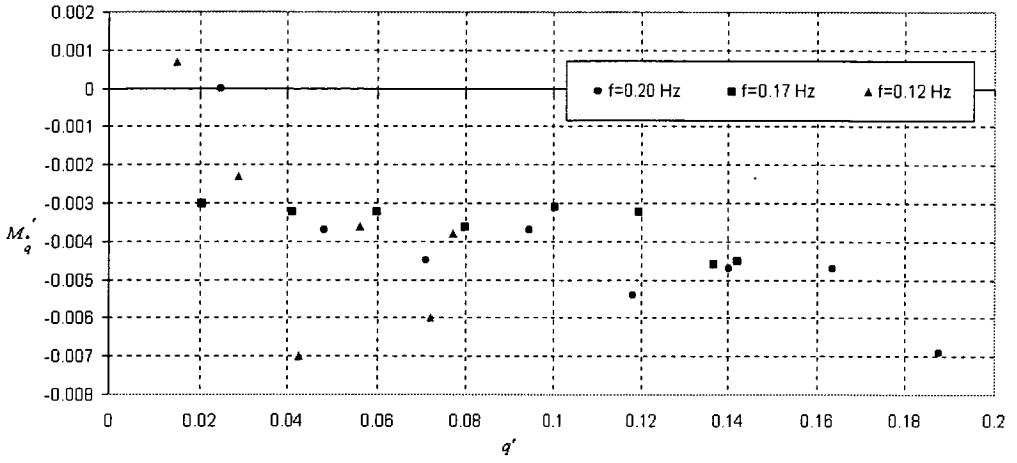

Figure 7.17 Calculated non-dimensional values of the linear coefficient $M_{\dot{q}}'$ *from the dynamic pitch tests of the PAP104 1/3rd scale model. X-axis is the non-dimensional angular pitch velocity.*

Coefficient	Non-dimensional value
X_{uu}'	-0.0089
Z_q'	-0.0190
$Z_{\dot{q}}'$	0.0057
M_q'	-0.0166
$M_{\dot{q}}'$	-0.0031

Table 7.7 Results from 1/3rd-scale PAP104 PMM dynamic pure pitch model tests.

7.4.8 Full Scale PAP104 PMM Results

Friswell (1985) tested a full size PAP104 vehicle using a vertical PMM at the ARE Portland establishment. The final estimates for the vertical derivatives given by Friswell are contained in Table 7.8 and 7.9.

Coefficient	Static	Dynamic Heave	Dynamic Pitch
Z_w'	-0.2395	-0.2493	-
M_w'	0.0218	-0.00414	-
M_{uu}'	0.00123	-	-
$Z_{\dot{w}}' - m'$	-	-0.1728	-
$M_{\dot{w}}'$	-	0.003469	-
Z_q'	-	-	-0.04416
M_q'	-	-	-0.02143
$Z_{\dot{q}}'$	-	-	-0.003434
$M_{\dot{q}}' - I_{yy}'$	-	-	-0.007427

Table 7 8 Full Scale PAP104 PMM Test Results. Flow Speed = 1.0m/s (Friswell, 1985).

Coefficient	Static	Dynamic Heave	Dynamic Pitch
Z_w'	-0.2512	-0.2292	-
M_w'	0.02125	0.01675	-
M_{uu}'	0.000999	-	-
$\left(Z_{\dot{w}} - m\right)'$	-	-0.1673	-
$M_{\dot{w}}'$	-	-0.005203	-
Z_q'	-	-	-0.03974
M_q'	-	-	-0.01958
$Z_{\dot{q}}'$	-	-	-0.000766
$\left(M_{\dot{q}} - I_{yy}\right)'$	-	-	-0.006731

Table 7.9 Full Scale PAP104 PMM Test Results. Flow Speed = 2.0m/s (Friswell, 1985).

7.5 Comparison of Results

The following table compares the PAP104 results to those determined by Friswell (1985).

Coefficient	Friswell (Re = 2.7×10^6) Flow Speed 1.0 m/s		Anderson (Re = 0.9×10^6) Flow Speed 1.0 m/s		Difference %	
	Static	Dynamic	Static	Dynamic	Static	Dynamic
$Z_{\dot{w}}'$	---	-0.0989	---	-0.1163	---	17.6
$M_{\dot{w}}'$	---	0.003469	---	0.0019	---	45.2
Z_w'	-0.2395	-0.2493	-0.2406	-0.2431	0.5	2.5
M_w'	0.0218	-0.00414	0.0243	0.0224	11.5	641.1
Z_q'	---	-0.04416	---	-0.0190	---	57.0
M_q'	---	-0.02143	---	-0.0166	---	22.5
M_{uu}'	0.00123	---	0.0012	0.0005	2.4	---

Table 7.10 Comparison of PAP104 non-dimensional coefficient values with Friswell (1985).

7.6 Discussion

While it is difficult to draw conclusions on experimental data without first analysing the errors, several observations were made. A detailed error analysis is given in the following chapter.

The dynamic test results did not appear to exhibit dependency on frequency. The scatter on each of the figures, between the different frequencies, was such that no dependency on frequency could be determined. The lack of observable frequency dependence is likely to be due to the low frequencies at which the AME HPMM could be operated. The largest non-dimensional frequency tested on the AME PMM was 1.26, compared with tests described by Bishop (1974b), which test ship models to a non-dimensional frequency of 32.30. While good estimates of SMDs may be achieved using

the AME PMM, difficultly arises if the desire is to study the potential effects due to higher frequencies.

The result suggests that future testing with the AME HPMM may only require that one frequency be tested to obtain the final SMD value. This is significant, since the number of HPMM tests performed can be reduced. It would then be unnecessary to extrapolate values of the hydrodynamic coefficient to zero frequency.

The effect of speed of the dynamic tests, on the values of the hydrodynamic coefficients, is determined by studying the dynamic result plots for a trend away from a flat straight line. This effect is separate to that of hydrodynamic coefficient dependency on flow speed or Reynolds numbers of the tests. Reynolds number effects are not considered here. The results obtained are considered valid for the Reynolds numbers tested. However, due to turbulence levels in the CWC (Chapter Four), the effective Reynolds number of the flow over the body is greater than that determined from the model and flow speed parameters alone. Considering the turbulence factor of 2.48, determined in Chapter Four, the effective Reynolds number for the PAP104 model tests is 2.2×10^{6}.

The dynamic results did not appear to exhibit dependency on the translational and rotational velocities at which the tests were conducted. Considering the data scatter aside, the plots given in the figures contained flat straight lines, indicating no dependency. If a dependency were to exist, then the mathematical model used in the analysis of the data would need modification. To that end it was useful to test the body over a range of velocities.

Given the low frequency range of the AME PMM, it would be useful to consider for future testing, that one frequency only be tested on the PMM. It is considered necessary however to test over a range of amplitudes as different vehicle models may exhibit different non-linear speed dependencies. Noting the restriction on model size due to blockage effects, it may be necessary to build and test larger models so that non-linear forces are excited during the oscillatory tests.

The comparison between the results for the 1/3rd scale PAP104 tests on the AME PMM with those determined by Friswell (1985) was inconclusive. In summary, seven

hydrodynamic coefficients were compared, three values from static model tests, and six values from dynamic tests. A comparison between static and dynamic results was made for two coefficients. The Reynolds number of the tests conducted by Friswell was 2.7×10^6 compared to 0.9×10^6 for the 1/3rd scale tests described in this chapter. However, high turbulence levels in the CWC water flow suggest that the effective Reynolds number of the 1/3rd scale tests was approximately 2.2×10^6. Therefore a closer comparison of the results can be made.

The static value comparisons were in good agreement, with the differences in the three values, Z_w', M_{uu}', and M_w', being 0.5%, 2.4% and 11.5% respectively. While the results for the dynamic tests were varied, with the differences in the seven coefficients, $Z_{\dot{w}}'$, $M_{\dot{w}}'$, Z_w', M_w', Z_q', and M_q' being 17.6%, 45.2%, 2.5%, 641.0%, 57.0%, and 22.5% respectively.

The comparison between the dynamic value of M_w' gave the largest error at 641.0%. However, the difference between the dynamic value for the 1/3rd scale tests and Friswell's value for the coefficient determined from static tests is 2.8%. Coupled with comments from Friswell (1985), this result indicates that Friwell's value for M_w' determined from dynamic tests is incorrect.

Friswell (1985) contained other coefficient values, however, the inertial components of the coefficients were not given, nor was the reference point from which the measurements were taken. Thus these values were not considered for comparison here.

Conclusions drawn in Friswell (1985) indicate that while the data was consistent, there were doubts about its accuracy. Considering that significant error was present in the results obtained from the 1/3rd model tests in the CWC, no further conclusions were made as to the validity of the data set. Further tests are required to confirm experimental error and repeatability of the results.

Chapter 8. An Analysis of Experimental Errors

8.1 Introduction

Potential sources of error are considered to determine the accuracy of hydrodynamic coefficients derived from HPMM model testing. The set-up of equipment and its performance during an experiment provide several sources of error. These include:

- Flow properties, including turbulence and non-uniformity
- Horizontal and vertical alignment of the HPMM
- Geometric similarity of the scale model to the real vehicle
- Positioning and alignment of the load cell within the model
- Load cell calibration
- Performance of the HPMM

The effect of turbulence is discussed briefly, while quantitative values for the effect of flow non-uniformity, load cell errors and the performance of HPMM motors, are determined. The other items are considered important, but should be addressed in preparing for the experiment. The effect of these errors on the simulated performance of the craft is also examined.

8.2 Turbulence

The effect of turbulence in the free-stream provides early transition of the boundary layer flow over the body, causing delayed separation of the flow and a reduction of the width of the wake, thus reducing the drag coefficient. The effect of turbulence can be considered in the same way as an increase in the flow speed.

In Chapter 5, turbulence levels were quantified by an approach given by Pope (1984). The approach, when applied to the flow in the AMC CWC, provided an estimate of the turbulence factor of 2.48, which is equivalent to a turbulence intensity level of 1.75%. Pope suggested that the Turbulence Factor is useful for determining the effective Reynolds number over the body. However the correction is not considered exact.

The Turbulence Factor is not used in determining standard errors for the coefficients. No consideration is given to turbulence effects in the HPMM data analysis. The Turbulence Factor is applied to the experimental test range to determine, as a first order approximation, the effective Reynolds range of the tests.

8.3 Non-Uniform Flow

8.3.1 Introduction

Non-uniform flow alters the drag over a submerged body through its inconsistent nature. In particular, the motions provided by the HPMM, which are based on the flow speed, are not met. The uniformity of the flow was measured in Chapter 5. The results indicate that the maximum standard deviation of the flow in the horizontal plane was 2.80% for the mean speed of 0.79m/s, while the minimum standard deviation was 1.30% for the mean speed of 1.09m/s.

8.3.2 Effect on Pure Yaw Motion

The HPMM motion most affected by the non-uniform flow is pure yaw. The equations for pure yaw motion are dependent on the flow velocity, as shown by the condition for pure yaw in the following equation:

$$\tan\psi = \frac{\dot{y}}{U_f} \tag{8. 1}$$

where

$\dot{y}$ is the translation velocity of the body across the tank,

ψ is the heading of the body with respect to the flow, and

U_f is the flow speed.

As the body is oscillated across the non-uniform flow in pure yaw motion, the error in the flow speed causes a change in the heading of the body with respect to the flow. The heading error is a quasi-steady drift angle, given by $\delta\psi$. The heading error causes a y-body velocity v and hence the condition of pure yaw is not met. The variation in the

heading $\delta\psi$ is determined as a function of the flow variation δU_f from Equation (8.1). The heading error is given by the following expression:

$$\delta\psi = \frac{|\dot{y}|}{U_f{}^2\left(1+\tan^2\psi\right)}\delta U_f \tag{8.2}$$

where

$\delta\psi$ is the heading error, and

δU_f is the error in the flow speed.

Substituting $\dot{y}$ obtained from Equation (8.1) into (8.2), the following expression for the heading error is determined:

$$\delta\psi = \frac{|\tan\psi|}{U_f\left(1+\tan^2\psi\right)}\delta U_f \tag{8.3}$$

Two simplifications can be made to Equation (8.3):

1. The error in the flow speed is given as a ratio of the absolute flow speed, ie.

$$\delta U_{f_r} = \frac{\delta U_f}{U_f} \tag{8.4}$$

2. Since $|\psi| \leq 0.26$ radians, the following approximation can be made:

$$\psi \approx \tan\psi \tag{8.5}$$

Therefore the heading error is given by the expression:

$$\delta\psi = \frac{|\psi|}{\left(1+\psi^2\right)}\delta U_{f_r} \tag{8.6}$$

The affect of the pure yaw condition not being met is an error in the forces and moments due to the additional drift component. Considering that the error in the heading equates to a drift angle, the y-body velocity is given by

$$v = -U\sin\beta \tag{8.7}$$

where

U is the net body speed, and

β is the drift angle and $\beta = \delta\psi$.

The non-dimensional y-body velocity is given by

$$v' = -\sin\beta \tag{8. 8}$$

If the error in the y-body velocity is $\delta v'$ and since $v' = 0$ in pure yaw, then the following expression gives the error in the non-dimensional y-body velocity:

$$\delta v' = |\sin\beta| \tag{8. 9}$$

If the y-body force and z-body moment due to the drift angle are given by the following linear expressions:

$$Y' = Y_v' v' \tag{8. 10}$$

and

$$N' = N_v' v' \tag{8. 11}$$

The errors are respectively given by

$$\delta Y' = |Y_v'| \delta v' \tag{8. 12}$$

and

$$\delta N' = |N_v'| \delta v' \tag{8. 13}$$

where

$\delta Y'$ and $\delta N'$ are the non-dimensional errors in the y-body force and z-body moment respectively, and

Y_v' and N_v' are the non-dimensional hydrodynamic coefficients.

Now consider the equation of motion for the rotation angle driven by the HPMM:

$$\psi = \psi_o \sin\omega t \tag{8. 14}$$

where

ψ_o is the amplitude of the motion, and

ω is the angular frequency of the motion.

If the expression for the expected heading angle is substituted into the expression for the heading error, the following expression is obtained:

$$\beta = \frac{|\psi_o \sin\omega t|}{\left(1 + \psi_o{}^2 \sin^2 \omega t\right)} \delta U_{f_r} \tag{8. 15}$$

If $|\psi_o \sin\omega t| \leq 1$,

$$\frac{|\psi_o \sin \omega t|}{1+\psi_o^2 \sin^2 \omega t} \leq \frac{|\psi_o|}{1+\psi_o^2 \sin^2 \omega t} \tag{8. 16}$$

and

$$\frac{\psi_o}{1+\psi_o^2 \sin^2 \omega t} \leq \frac{\psi_o}{1+\psi_o^2} \tag{8. 17}$$

then the heading error is simplified to the following inequality:

$$\beta \leq \frac{\psi_o}{1+{\psi_o}^2} \delta U_{f_r} \tag{8. 18}$$

Therefore the error in the y-body force and z-body moment are given by

$$\delta Y' \leq \left| Y_v' \right| \frac{\psi_o}{1+{\psi_o}^2} \delta U_{f_r} \tag{8. 19}$$

and

$$\delta N' \leq \left| N_v' \right| \frac{\psi_o}{1+{\psi_o}^2} \delta U_{f_r} \tag{8. 20}$$

Let the mathematical model for the y-body force in pure yaw motion be given by

$$Y' = \left(Y_{\dot{r}}' - m' \right) \dot{r}' + Y_r' r' \tag{8. 21}$$

where

$Y_{\dot{r}}'$, Y_r' are non-dimensional y-body force coefficients,

m' is the non-dimensional mass of the body, and

r', $\dot{r}'$ are the non-dimensional angular velocity and acceleration of the body about the z-body axis.

The expressions for the non-dimensional angular velocity and acceleration about the z-body axis are given by the following:

$$r' = \frac{2\pi f \psi_o l}{U_f} \cos(2\pi f t) \tag{8. 22}$$

and

$$\dot{r}' = -\frac{4\pi^2 f^2 \psi_o l^2}{{U_f}^2} \sin(2\pi f t) \tag{8. 23}$$

where

l is the length of the scale model, and

f is the frequency of oscillation.

The error in the hydrodynamic coefficients due to the variation in the y-body force, given by

$$\left(\delta Y_{r}^{'}\dot{r}'\right)^{2}+\left(\delta Y_{r}^{'}r'\right)^{2}=\delta Y'^{2} \tag{8.24}$$

Substituting for the angular velocity and acceleration gives the following:

$$\left(-\delta Y_{r}^{'}\frac{4\pi^{2}f^{2}\psi_{o}l^{2}}{U_{f}^{2}}\sin(2\pi ft)\right)^{2}+\left(\delta Y_{r}^{'}\frac{2\pi f\psi_{o}l}{U_{f}}\cos(2\pi ft)\right)^{2}=\delta Y'^{2} \tag{8.25}$$

To bound the error on each coefficient, the error in the force component can be attributed wholly to each term in the force equation. Hence

$$\delta Y_{r}^{'}\frac{2\pi f\psi_{o}l}{U_{f}}\left|\cos(2\pi ft)\right|\leq\delta Y' \tag{8.26}$$

and

$$\delta Y_{r}^{'}\frac{4\pi^{2}f^{2}\psi_{o}l^{2}}{U_{f}^{2}}\left|\sin(2\pi ft)\right|\leq\delta Y' \tag{8.27}$$

Given Equation (8.19), (8.26) and (8.27), the following relationships between the rotational coefficients and the error in the flow are determined:

$$\delta Y_{r}^{'}\frac{2\pi f\psi_{o}l}{U_{f}}\left|\cos(2\pi ft)\right|\leq\left|Y_{v}^{'}\right|\frac{\psi_{o}}{1+\psi_{o}^{2}}\delta U_{f_{r}} \tag{8.28}$$

and

$$\delta Y_{r}^{'}\frac{4\pi^{2}f^{2}\psi_{o}l^{2}}{U_{f}^{2}}\left|\sin(2\pi ft)\right|\leq\left|Y_{v}^{'}\right|\frac{\psi_{o}}{1+\psi_{o}^{2}}\delta U_{f_{r}} \tag{8.29}$$

Since Equations (8.28) and (8.29) hold for all values of $\left|\cos(2\pi ft)\right|$ and $\left|\sin(2\pi ft)\right|$ respectively, $\left|\cos(2\pi ft)\right|$ and $\left|\sin(2\pi ft)\right|$ can be replaced by the maximum value of 1 to give the following expressions:

$$\delta Y_{r}^{'}\frac{2\pi f\psi_{o}l}{U_{f}}\leq\left|Y_{v}^{'}\right|\frac{\psi_{o}}{1+\psi_{o}^{2}}\delta U_{f_{r}} \tag{8.30}$$

and $$\delta Y_r' \frac{4\pi^2 f^2 \psi_o l^2}{U_f^2} \leq \left|Y_v'\right| \frac{\psi_o}{1+\psi_o^2} \delta U_{f_r} \quad (8.31)$$

Rearranging the result gives the following expressions for the error in the non-dimensional coefficients:

$$\delta Y_r' \leq \left|Y_v'\right| \frac{U_f}{2\pi lf\left(1+\psi_o^2\right)} \delta U_{f_r} \quad (8.32)$$

$$\delta Y_r' \leq \left|Y_v'\right| \frac{U_f^2}{4\pi^2 l^2 f^2\left(1+\psi_o^2\right)} \delta U_{f_r} \quad (8.33)$$

Similarly the errors in the coefficients for the z-body moment are expressed as:

$$\delta N_r' \leq \left|N_v'\right| \frac{U_f}{2\pi lf\left(1+\psi_o^2\right)} \delta U_{f_r} \quad (8.34)$$

$$\delta N_r' \leq \left|N_v'\right| \frac{U_f^2}{4\pi^2 l^2 f^2\left(1+\psi_o^2\right)} \delta U_{f_r} \quad (8.35)$$

8.3.3 Scaling

The measured forces and moments are scaled to a non-dimensional form prior to the analysis that determines the hydrodynamic coefficients. Since the scaling value for the measurements is dependent on the flow speed, a variation in the flow speed will create an error in the non-dimensional value.

The non-dimensional force and moment are given by

$$F' = \frac{2F}{\rho l^2 U^2} \quad (8.36)$$

and $$M' = \frac{2M}{\rho l^3 U^3} \quad (8.37)$$

where

F, M are the magnitudes of the force and moment respectively,

F', M' are the magnitudes of the non-dimensional force and moment respectively, and

ρ is the density of the fluid.

Hence the error in the non-dimensional force and moment are given by

$$\delta F' = \frac{4|F|}{\rho l^2 U^3}\delta U \tag{8.38}$$

$$\delta M' = \frac{4|M|}{\rho l^3 U^3}\delta U \tag{8.39}$$

The expressions for U vary with the type of motion being considered:

In pure sway: $$U \le \sqrt{{U_f}^2 + \omega^2 {y_o}^2} \tag{8.40}$$

In pure yaw: $$U \le U_f \sqrt{1 + {\psi_o}^2} \tag{8.41}$$

In static drift: $$U = U_f \tag{8.42}$$

If the net speed of the body is approximated by the flow speed so that $\delta U \approx \delta U_f$, then the following inequalities for the force and moment variation holds for the three motion types:

$$\delta F' \le \frac{4|F|}{\rho l^2 {U_f}^3}\delta U_f \tag{8.43}$$

$$\delta M' \le \frac{4|M|}{\rho l^3 {U_f}^3}\delta U_f \tag{8.44}$$

If the errors are given relative to the absolute errors then the following expressions are obtained:

$$\delta F_r' \le 2\,\delta U_{f_r} \tag{8.45}$$

$$\delta M_r' \le 2\,\delta U_{f_r} \tag{8.46}$$

The relative error can be attributed to the individual force terms by equations (8.20) to (8.23) to enable an error in the coefficients to be determined.

8.4 Load Cell Errors

The AMTI M3378 load cell has been characterised by its manufacturer (AMTI, 1993) and found to contain errors due to cross-talk between channels, hysteresis, non-linearity and sensitivity to temperature change. Calibration of the load cell provides a matrix of values that are used to remove cross-talk error.

The remaining errors are given by the following:

Non-linearity:	0.20% of the full-scale output (FSO)
Hysteresis:	0.20% of the measured load (L)
Temperature Sensitivity:	0.01%/° of L

The resolution of the load cell is also considered.

Assuming the errors are independent and a maximum of 2° temperature change, the accuracy of the load cell, is given by

$$\delta L = \sqrt{\delta L_{NL}{}^2 + \delta L_H{}^2 + \delta L_T{}^2} \tag{8.47}$$

$$\Rightarrow \quad \delta L = \sqrt{\left(0.002\frac{L^2}{FSO}\right)^2 + (0.002\,L)^2 + (0.0002\,L)^2} \tag{8.48}$$

$$\Rightarrow \quad \delta L_r = \frac{\delta L}{L} = \sqrt{0.000004\frac{L^2}{FSO^2} + 0.00000404} \tag{8.49}$$

where

δL_r is the relative error of the measured load,

δL_{NL} is the variation in the load due to the non-linear effect,

δL_H is the variation in the load due to the hysteresis effect, and

δL_T is the variation in the load due to the temperature effect.

Assuming the measured load to be a maximum at the FSO, then the relative error in the measured load is given by the following:

$$\delta L_r \leq 0.0028 \tag{8.50}$$

Hence the accuracy of the load cell is approximately 0.28% of the measured load.

The resolution of the data is determined by calculating the range over the 12-bit data string. The resolution is given by

$$\delta L_R = \frac{R}{4096} \tag{8.51}$$

where δL_R is the variation in the load due to resolution of the load cell.

The range R varies with the amplifier gains, as shown in Appendix 3. The AMTI M3378 load cell has three amplifier gains: 1000, 2000, and 4000. The range resolution can therefore be given by

$$\delta L_R = \frac{1000\, R_{1000}}{4096\, G} \tag{8.52}$$

where

G is the load cell amplifier gain, and

R_{1000}. is the load range at load cell amplifier gain of 1000.

The absolute range resolution errors are given in Table 8.1 for each of the load cell amplifier gains.

Load Channel	Load Cell Amplifier Gain		
	1000	2000	4000
F_x, F_y	1.46×10^{-1} N	7.32×10^{-2} N	3.66×10^{-2} N
F_z	5.86×10^{-1} N	2.93×10^{-1} N	1.46×10^{-1} N
M_x, M_y	2.93×10^{-3} Nm	1.46×10^{-3} Nm	7.32×10^{-4} Nm
M_z	4.39×10^{-3} Nm	2.20×10^{-3} Nm	1.10×10^{-3} Nm

Table 8.1 Absolute range resolution errors for each of the six load channels of the AMTI M3378

The trade-off between increased resolution, as shown in Table 8.1, is the decrease in the load cell range by the same ratio.

8.5 Amplitude and Frequency Error

8.5.1 Amplitude Error

If we consider the mathematical models for the body forces and moments to be linear, then the relative error in the resulting coefficients due to pass-band ripple in the filter is given by the following relationship:

$$\delta C_r = \delta y_{o_r} \tag{8.53}$$

where

δC_r is the relative error in the hydrodynamic coefficient, and

δy_{o_r} is the relative error in the amplitude due to pass-band ripple in the filter.

8.5.2 Frequency Error

Assuming that both motors operate at the same frequency, the remaining error that affects the calculation of the hydrodynamic coefficients is in the determination of the frequency from displacement data. To illustrate the significance of the frequency error, consider the linear model for the y-body force, given in the following expression:

$$Y = Y_v v + \left(Y_{\dot{v}} - m \right) \dot{v} \tag{8.54}$$

where

Y is the y-body force,

m is the body mass,

Y_v is the hydrodynamic coefficient relating a change in the y-body force with respect to a perturbation in the y-body velocity v, and

$Y_{\dot{v}}$ is the hydrodynamic coefficient relating a change in the y-body force with respect to a perturbation in the y-body acceleration $\dot{v}$.

Note that the velocity and acceleration are given by

$$v = 2\pi f \, y_o \cos 2\pi f t \tag{8.55}$$

and

$$\dot{v} = -4\pi^2 f^2 y_o \sin 2\pi f t \tag{8.56}$$

where

f is the frequency of the motion,

y_o is the amplitude of the motion, and

t is the time.

Assume the components of the load can be separated such that the components due to velocity and acceleration are given by the following expressions respectively:

$$Y^{(v)} = Y_v v \tag{8.57}$$

$$Y^{\dot{(v)}} = \left(Y_{\underset{v}{\cdot}} - m\right)\dot{v} \tag{8.58}$$

Consider from that the model for the y-body force can also be expressed as:

$$Y = a_o + b_1 \sin 2\pi ft + a_1 \cos 2\pi ft \tag{8.59}$$

Similarly,

$$\left|Y^{(v)}\right| \cos 2\pi ft = Y_v 2\pi f\ y_o \cos 2\pi ft \tag{8.60}$$

and

$$\left|Y^{\dot{(v)}}\right| \sin 2\pi ft = -\left(Y_{\underset{v}{\cdot}} - m\right) 4\pi^2 f^2 y_o \sin 2\pi ft \tag{8.61}$$

Hence

$$Y_v = \frac{\left|Y^{(v)}\right|}{2\pi f\ y_o} \tag{8.62}$$

and

$$\left(Y_{\underset{v}{\cdot}} - m\right) = \frac{-\left|Y^{\dot{(v)}}\right|}{4\pi^2 f^2 y_o} \tag{8.63}$$

The following relationships for the relative error in the coefficients is determined:

$$\delta Y_{v_r}{}' = \delta f_r \tag{8.64}$$

$$\delta Y_{\underset{v_r}{\cdot}}{}' = 2\delta f_r \tag{8.65}$$

where

$\delta Y'_{v_r}$ is the relative error in the coefficient Y'_v, given by $\dfrac{\delta Y.'_{v}}{\left(Y.'_{v} - m'\right)}$

$\delta Y.'_{v_r}$ is the relative error in the coefficient $Y.'_{v}$, and

δf_r is the relative error in the frequency.

Similarly the following relationships for the relative error are given:

$$\delta N_{v_r}{}' = \delta f_r \tag{8.66}$$

$$\delta N.{}'_{v_r} = 2\delta f_r \tag{8.67}$$

$$\delta Y'_{r_r} = \delta f_r \tag{8.68}$$

$$\delta Y.'_{r_r} = 2\delta f_r \tag{8.69}$$

$$\delta N_{r_r}{}' = \delta f_r \tag{8.70}$$

$$\delta N.{}'_{r_r} = 2\delta f_r \tag{8.71}$$

where

$$\delta Y_{r_r}{}' = \frac{\delta Y_r{}'}{\left(Y_r{}' - m'\right)},\ \delta Y.{}'_{r_r} = \frac{\delta Y.{}'_{r}}{\left(Y.{}'_{r} - m'x_G{}'\right)},\ \delta N.{}'_{v_r} = \frac{\delta N.{}'_{v}}{\left(N.{}'_{v} - m'x_G{}'\right)},\ \delta N_{r_r}{}' = \frac{\delta N_r{}'}{\left(N_r{}' - m'x_G{}'\right)},$$

and $\delta N.{}'_{r_r} = \dfrac{\delta N.{}'_{r}}{\left(N.{}'_{r} - I_{zz}{}'\right)}$

8.6 Data Analysis

The AME PMM data analysis procedure provides a set of hydrodynamic coefficients for each oscillatory test run performed with the HPMM. For each of these coefficients C, the algorithm provides a standard deviation, indicating the value of C lies somewhere in the range $C \pm 2\sigma_C$, where σ_C is the standard deviation of C and the interval has 95% probability of containing the value. The final value of each coefficient, the slow motion derivative or zero frequency coefficient, is determined subsequently. The error given by the standard deviation is considered due to the fit of the mathematical model to the measured data and is consequently included in the error analysis.

8.7 Total Error

The total error in each coefficient is determined by finding the sum of the squares of the individual errors ie.

$$\delta C' = \sqrt{\sum_n \delta C_i^{2'}} \tag{8.72}$$

where $\delta C'$ is the total error in a hydrodynamic coefficient.

An analysis of the errors for the horizontal plane hydrodynamic coefficients was completed in an Excel spreadsheet. The following errors were assumed in the flow speed and, the frequency and amplitude measurements: 5.6%, 3% and 1% respectively. Table 8.1 gives the final values of the coefficients together with the estimate maximum error.

	Static Drift	Total Error	Pure Yaw	Total Error	Pure Sway	Total Error	Final Value	% Error
X'_{uu}	-0.0120	0.0005	-0.0100	0.0003	-0.0112	0.0003	-0.0120	4.2
X'_{vv}	0.0431	0.0017					0.0431	3.9
$Y'_{\dot{v}}$					-0.1465	0.0236	-0.1465	16.1
$Y'_{\dot{r}}$			0.0078	0.3240			0.0078	4153.8
Y'_{r}			0.0399	0.0369			0.0399	92.5
Y'_{v}	-0.1823	0.0076			-0.1983	0.0117	-0.1823	4.2
$Y'_{v\|v\|}$	-0.3004	0.0128					-0.3004	4.3
Z'_{o}	0.1978	0.0123	0.2245	0.0050	0.2202	0.0048	0.1978	6.2
N'_{v}	-0.0546	0.0018			-0.0446	0.0026	-0.0546	3.3
K'_{v}	0.0016	0.0003			0.0032	0.0002	0.0016	18.8
$K'_{v\|v\|}$	0.0077	0.0006					0.0077	7.8
M'_{uu}	-0.0017	0.0002	-0.0005	0.0000			-0.0017	11.8
M'_{vv}	-0.0131	0.0023					-0.0131	17.6
M'_{vvvv}	0.0419	0.0048					0.0419	11.5
$N'_{v\|v\|}$	0.0692	0.0024					0.0692	3.5
N'_{r}			-0.0201	0.0057			-0.0201	28.4
$N'_{\dot{r}}$			-0.0027	0.0487			-0.0027	1803.7
$N'_{\dot{v}}$					0.0064	0.0010	0.0064	15.6

Table 8.1 Non-dimensional coefficient values with errors.

8.8 Effect on Simulated Performance

The simulation software described in Chapter Two was used to determine the effect of the errors on the simulated performance of the PAP104 vehicle. Two manoeuvres were implemented in the investigation, these were straight line steady state manoeuvres, and zigzag manoeuvres. These manoeuvres were useful in determining the response of the vehicle to steady forward motion and unsteady rate turns.

On the steady state manoeuvre, the motion of the vehicle was initiated from rest at $t=0$. At time $t=0.5s$, full power was demanded of both thrusters on the vehicle. The simulated manoeuvre was stopped at time $t=t_{max}$, where t_{max} was varied from 60 seconds to one hour. The steady state velocity of 3.25m/s was reached at $t=15.8$ s. Simulating the errors given in Table 8.1 provided an error of 1.5% in the steady state velocity, which converted to a 1.7% error in the distance travelled.

On the zigzag manoeuvre, the motion of the vehicle was initiated from rest at $t=0$. At time $t=0.5s$, full power was demanded of both thrusters on the vehicle. At time $t=20$ s the thrusters were varied according to the thrust ratio (the relative magnitude of one thruster to the other) and the requirements of the zigzag manoeuvre. Full thrust is maintained in one thruster while the other is reduced according to the ratio.

The thrust ratio is set to a constant value during a turn until the heading of the vehicle has turned through the specified zigzag angle. Once the vehicle reaches the desired heading the thrust ratio is reversed so that the vehicle turns in the opposite direction, with the aim of turning to reach the zigzag angle in the opposite direction. The overshoot that the vehicle completes during the turning gives a measure of the response of the vehicle. Table 8.2 contains the results of several simulations that considered the effect of coefficient error, zigzag angle, and thrust ratio, on the response of the vehicle.

The simulations based on coefficients with error indicate the response time of the vehicle was approximately doubled. However, the error in the distance travelled was small at approximately 2.0% of the distance travelled.

Angle (deg)	Thrust Ratio	Response Time (s)	Distance (m)	Error Response Time (s)	Error Distance (m)	%Error Response Time	%Error Distance
5	0.2	13.0	536.1	25.6	546.0	97.0	1.8
10	0.2	17.8	535.7	35.4	546.0	98.9	1.9
20	0.2	25.4	535.3	50.0	545.9	96.9	2.0
5	0.5	16.6	579.9	33.0	589.7	98.8	1.7
10	0.5	23.6	579.8	46.6	589.7	97.5	1.7
20	0.5	35.8	579.6	67.6	589.7	88.8	1.7
5	0.8	28.2	617.5	54.2	627.4	92.2	1.6
10	0.8	43.8	617.5	81.0	627.4	84.9	1.6
20	0.8	74.4	617.5	129.2	627.4	73.7	1.6

Table 8.2 Zigzag manoeuvre response times and distance travelled.

8.9 Discussion

In this chapter a method was determined for the analysis of errors related to the measurement of PMM data. Inequalities that bounded the error on hydrodynamic coefficients were determined. These expressions were implemented in Excel where absolute errors on the hydrodynamic coefficients were determined.

Large errors of greater than 1000% were determined in the rotational acceleration coefficients. The rotational velocity coefficients were also considered large with errors between 20% and 100%. The remaining errors as determined by the analysis were less than 20%. Comparing these results with the figures of the results in Chapter Seven, the large errors for the rotational coefficients are consistent with the large variations observed in the figures.

Simulation of the manoeuvring performance of the PAP104 vehicle was completed, both with and without the errors incorporated into the values of the coefficients. The results showed that the errors in the hydrodynamic coefficients produced an error of approximately 2.0% in the distance travelled, while the turning response of the vehicle was increased by close to 100%.

The error in the distance travelled would need to be considered if the results were to be used for navigational studies on the vehicle. If the results from the simulation were to be used for analysing the response of the vehicle, maybe a stability analysis, then the error would need to be considered.

If the error bounds are considered too large then several options may need to be investigated:

- Review the assumptions of the error analysis to define tighter criteria,
- Reduce the error source and re-run the experiments, and
- Re-run the experiments to increase the statistical certainty of the results.

Chapter 9. Conclusions and Recommendations

The objective of the thesis presented here was to develop an approach for determining hydrodynamic coefficients from data obtained by testing scale models on the Australian Maritime Engineering (AME) Planar Motion Mechanism (PMM). The work described in the thesis included:

- A description of a mathematical model for an underwater vehicle,
- The development of a time domain simulation software package for an underwater vehicle,
- A description of the Australian Maritime Engineering PMM,
- The development and implementation of the motion equations for the AME PMM,
- The development and implementation of a method to analyse the displacement records of each PMM test for frequency and amplitude.
- An investigation into the flow properties of the AMC CWC and the study and implementation of methods to improve the properties of the facility,
- The design of an experimental test program for the AME PMM,
- A description of several analysis methods followed by a numerical study investigating the relative performance of each method,
- PMM testing and data analysis of a PAP104 1/3rd scale model,
- An error analysis of the PMM testing and analysis procedure,
- Simulations of the PAP104 vehicle incorporating the hydrodynamic results and the determined errors.

The following conclusions are made:

- Corrections were necessary in the PMM motion equations to provide the required motions (a non-linearity of 2%),
- Frequency and amplitude of test motions were to be analysed to enable validation of the test and accurate analysis,
- Errors were present in the PMM motors; these could be compensated for in the analysis procedure,

- The amount of recorded data for the PAP104 tests was insufficient to avoid errors due to spectral effects,
- The rectangular windowing technique used in the analysis method was not optimal for reducing spectral leakage, producing errors in the analysed value of the frequency,
- The Kaiser Filter used to reduce noise on the displacement data, from which the amplitude was determined, provided a small error of approximately 0.1%,
- The AMC CWC flow non-uniformity (of approximately 5%) had a big affect on the results of the analysis,
- The experimental program could be reduced considerably since the results appear to be independent of frequency, therefore one frequency can be chosen as the slow motion derivative, or zero frequency coefficient,
- The Fourier Integration and Systems Identification method were superior to the Discrete Analysis and Switched Integration methods. However, the noise performance of the Systems Identification method suggests the use of a low-pass filter,
- High frequency affects may be difficult to study with the AME PMM due to its range of motions,
- The comparison between the results for the 1/3rd scale PAP104 tests on the AME PMM with those determined by Friswell (1985) was inconclusive towards the validation of the method, although some good agreement with results was achieved. This would suggest that the analysis method was appropriate but the experimental errors were too great, both in the Friswell tests and those discussed in the thesis. Further results are necessary for validation of the work here to be conclusive,
- The error analysis was consistent with the measured results as shown by the spread of the results in figures,
- The simulated performance of the vehicle would be affected by errors in the hydrodynamic coefficients (approximately 2% of distance travelled and 100% increase in turning response) as given by the errors determined in the error analysis.

The following recommendations are made:

- To reduce the effects of spectral leakage, a minimum of ten cycles of data needs to be recorded together with an optimal windowing technique such as a Hanning Window,
- To improve the accuracy of estimating the amplitude consider the use of a Filter with lower pass-band ripple, such as a Butterworth filter,
- Implement a low-pass filter as part of the Systems Identification method to improve noise performance,
- Obtain further validation data,
- Analysis of the overall stiffness of the model, strut/sting and PMM system would provide further insight into the measured noise.
- Simulation of the four analysis methods, while modelling white noise passed through a 10Hz low-pass filter, would provide useful data toward discussion on the absolute performance of the analysis methods.
- A method for examining the natural frequencies of the whole system could include "plucking" the model in each of its six degrees of freedom, at zero speed through the water, then performing frequency analysis.
- Parasitic moments on the load cell could be greatly reduced by the use of two load cells fitted to the strong-back in the model.
- Added mass coefficients for sphere models could be obtained from PMM tests.
- If the error bounds are considered too large then several options may need to be investigated:
    - Review the assumptions of the error analysis to define tighter criteria,
    - Reduce the error source and re-run the experiments, and
    - Re-run the experiments to increase the statistical certainty of the results.

REFERENCES

Aage, C. and Smitt, L.W., (1994) *Hydrodynamic Manoeuvrability Data of a Flatfish Type AUV*, Oceans '94, Brest France.

Abkowitz, M.A., (1964) *Lectures on Ship Hydrodynamics – Steering and Manoeuvrability*, Hydro and Aerodynamic Laboratory Report No. Hy-5.

Abkowitz, M.A., (1969) *Stability and Motion Control of Ocean Vehicles*, M.I.T. Press, Massachusetts Institute of Technology, Cambridge, Massachusetts and London, England.

Abkowitz, M.A., (1980) *Measurement of Hydrodynamic Characteristics from Ship Manoeuvring Trials By Systems Identification*, Transactions Society of Naval Architects and Marine Engineers, Vol. 88, pp. 283-318.

Achenbach, E., (1972) *Experiments on the Flow Past Spheres at Very High Reynolds Numbers*, Journal of Fluid Mechanics, Vol. 54, Part 3, pp. 565-575, Great Britain.

Achenbach, E., (1974) *The Effects of Surface Roughness and Tunnel Blockage on the Flow Past Spheres*, Journal of Fluid Mechanics, Vol. 65, Part 1, pp 113-125, Great Britain.

Anderson, B., Campanella, G., and Walker, G.J., (1995) *Development of a Horizontal Planar Motion Mechanism for Determining Hydrodynamic Characteristics of Underwater Vehicles*, Proceedings of the Australasian Fluid Mechanics Conference, Sydney, Australia.

Anderson, B., Reynolds, E. and Walker, G.J., (1997) *Effects of Turbulence and Velocity Profile Variation in a Circulating Water Channel as Determined by Sphere and Ellipsoid Tests*, Proceedings of the International Conference on Manoeuvring and Control of Marine Craft, Croatia.

Anderson, B., and Reynolds, E., (1997) *Experimental Testing and Simulation of PAP104*, Australian Maritime Engineering CRC, Report No. 97/4, Australia

Bell, W.H., (1983) *Turbulence vs. Drag – Some Further Considerations*, Ocean Engineering, Vol. 10, No. 1, pp47-63, U.K.

Bellanger, M., (1986) *Digital Processing of Signals*, John Wiley & Sons, London.

Bishop, R.E.D., Burcher, R.K. and Price W.G., (1969) *Linear Analysis of Transient Vibration*, J. Sound Vibration 9(2), 313-337

Bishop, R.E.D. and Parkinson, A.G., (1970) *On the Planar Mechanism Used in Ship Model Testing*, Phil. Trans. R. Soc. Lond. Vol. 266, A. 1171.

Bishop, R.E.D., Burcher, R.K. and Price W.G., (1973a) *The Fifth Annual Fairey Lecture: On the Linear Representation of Fluid Forces and Moments in Unsteady Flow*, J. Sound Vibration 29(1), 113-128

Bishop, R.E.D., Burcher, R.K. and Price W.G., (1973b) *Application of Functional Analysis to Oscillatory Ship Model Testing*, Proc. R. Soc. Lond. A. 332, 37-49, U.K.

Bishop, R.E.D., and Burcher, R.K, (1973c) *Directional Stability Analysis of a Ship Allowing for Time History Effects of the Flow*, Proc. R. Soc. Lond. A. 332, 341-354, U.K.

Bishop, R.E.D., and Price W.G., (1973d) *The Uses of Functional Analysis in Ship Dynamics*, Proc. R. Soc. Lond. A. 332, 23-35, U.K.

Bishop, R.E.D., Parkinson, A.G., and Price, W.G., (1974a) *Oscillatory Testing for the Assessment of Ship Maneuvrability*, 10th Symposium on Naval Hydrodynamics.

Bishop, R.E.D., Burcher, R.K., and Price, W.G., (1974b) *A Linear Analysis of Planar Motion Mechanism Data*, Journal of Ship Research, Vol. 18, No.4, pp. 242-251.

Bishop, R.E.D., and Price, W.G., (1991) *Some Comments on Present Day Ship Dynamics*, Phil. Trans. R. Soc. Lond. A 334, 187-197

Blevins, R.D., (1990) *Flow Induced Vibration.*

Booth, T.B. and Bishop, R.E.D., (1973) *The Planar Motion Mechanism*, Admiralty Experimental Works.

Boral (1994), *Woven Wire Mesh Specification*, Manufacturer Data Sheet.

Bradshaw, P. and Pankhurst, R.C., (1964) *The Design of Low Speed Wind Tunnels*, Pergammon Presss, U.K.

Brand, R., (1964) *A Vortex Theory for the Manoeuvring Ship.* 5th Symp. On Naval Hydrodynamics, pp815-911.

Burcher, R.K., (1972) *Model Testing*, Journal of Mechanical Engineering Science, Vol. 14, pp 62-69.

Burcher, R.K., (1991) *The Prediction of the Manoeuvring Characteristics of Vessels*, Phil. Trans. R. Soc. Lond A 334 265-279.

Burchill, R.E., (1995) *A Computer Simulation and Experimental Investigation of the Manoeuvring Characteristics of an Ellipsoidal Body*, Australian Maritime College, Aus.

Chislett, M.S. and Strom-Tejsen, J., (1965) *Planar Motion Mechanism Tests and Full Scale Steering and Manoeuvring Predictions for a Mariner Class Vessel*, Hydro and Aerodynamics Laboratory Denmark, Report Hy-6.

Chislett, M.S. and Smitt, L.W., (1972) *A Brief Description of the HyA Large Amplitude PMM System*, Journal of Mechanical Engineering Science, Paper 12, Vol. 14, No. 7.

Chislett, M.S. and Smitt, L.W., (1972) *Course Stability While Stopping*, Journal of Mechanical Engineering Science, Paper 25, Vol. 14, No.7.

Chislett, M.S. and Wied S., (1985) *A Note on the Mathematical Modelling of Ship Manoeuvring in Relation to a Nautical Environment with Particular Reference to Currents*, Int. Conf on Numerical and Hydraulic Modelling of Ports and Harbours, U.K. Paper D2.

Clarke, D., Gedling, P., and Hine G., (1982) *The Application of Manoeuvring Criteria in Hull Design Using Linear Theory*, RINA

Cummins W.E., (1953) *The Forces and Moments Acting on a Body Moving in an Arbitrary Potential Stream*, David Taylor Model Basin, Report 780.

Cummins, W.E., (1957) *The Force and Moment on a Body in a Time Varying Potential Flow*, Journal of Ship Research, Vol. 1, pp. 1-18.

Dand, I.W., (1982) *Open Water Experiments on an ROV Thruster*, National Maritime Institute, R143, OT-R-8255, UK.

Dand, I.W. and Every, M.J., (1983) *An Overview of the Hydrodynamics of Umbilical Cables and Vehicles*, Subtech '83. Paper No. 10.4.

Dand, I.W., (1985) *The Naval Architecture of ROVs*, Proceedings International Symposium on Developments in Subsea Engineering Systems, London.

Dand, I.W., (1985) *Some Aspects of the Hydrodynamics of Remotely Operated Submersibles.* Proceedings of Control '85, Cambridge, U.K.

Dand, I.W., (1988) *Performance Prediction and Testing of a ROV*, Advances in Underwater Technology, Ocean Science and Offshore Engineering, Vol. 15.

Driscoll, A. and Anslow, J.F., (1990) *The Horizontal Planar Motion Mechanism Setting Up, Operating , Data Acquisition and Analysis Procedures*, Admiralty Research Establishment, U.K. ARE TM(UHU) 90313.

Feldman, J., (1966) *Model Investigations of Stability and Control Characteristics of a Preliminary Design for The Deep Sea Submergence Rescue Vessel (DSRV Scheme A)*, David Taylor Research Center Report 2249.

Feldman, J., (1987) *Straightline and Rotating Arm Captive Model Experiments To Investigate The Stability and Control Characteristics of Submarines and Other Submerged Vehicles.* David Taylor Research Center DTRC/SHD-0393-20.

Feldman, J.P., (1975) *State-of-the-Art for Predicting the Hydrodynamic Characteristics of Submarines*, Naval Ship Research and Development Center, Washington D.C., Proceedings of the Symposium on Control Theory and Naval Application, U.S. Naval Postgraduate School, Monterey, California.

Feldman, J.P., (1979) *DTNSRDC Revised Standard Submarine Equations of Motion,* Naval Ship Research and Development Center, Washington D.C., Report No. SFD-0393-09.

Friswell, M.J., (1985) *PAP104 Planar Motion Mechanism Experiments,* Defence Research Agency, Portland U.K., JH TM 35/85.

Fyfe, A.J., (1979) *Planar Motion Mechanism Experiments to Determine the Stability and Control Derivatives of the Unmanned, Cable Controlled Submersible,* ANGUS, Institute of Offshore Engineering, Report No. OT/R/7957, Heriot Watt University, Edinburgh, U.K.

Gerhart, P.M. and Gross, R.J., (1985) *Fundamentals of Fluid Mechanics,* Addison-Wesley Publishing Company, USA.

Gertler, M. and Hagen, G.R., (1967) *Standard Equations of Motion for Submarine Simulation,* Naval Ship Research and Development Center, Washington D.C.,Report No. 2510.

Gill, A.D. and Price W.G., (1976) *Determination of the Manoeuvring Derivatives of a Ship Model using a Horizontal Planar Motion Mechanism in a Circulating Water Channel,* RINA.

Gill, A.D. and Price W.G., (1977) *Experimental Evaluation of the Effects of Water Depth and Speed on the Manoeuvring Derivatives of Ship Models,* RINA.

Gill, A.D., (1979) *The Analysis and Synthesis of Ship Manoeuvring,* RINA.

Goheen, K.R., (1990) *Remotely Operated Vehicle Software Simulation Studies,* Volume I, Contractors Report 90-26, Defence Research Establishment Pacific, Canada.

Goheen, K.R. and Jeffreys E.R., *Systems Identification of Remotely Operated Vehicle Dynamics.*

Goodman, A., (1960) *Experimental Techniques and Methods of Analysis Used in Submerged Body Research,* Proceedings of the Office of Naval Research, 3rd Symposium on Navy Hydrodynamics.

Greenshields, M.C., (1987) *UCL ROV Simulation Programme-User Manual Release 1.0,* ARE Portland, UTH Memo 90/87(C).

Hawley, J.G., (1996) M. *Underwater Engineering at the US Naval Academy focussing on Novel ROV Designs,* Trans. ImarE, Vol. 108, Part 4. Pp 229-240.

He, Y., Xu, Y., and Hsiung, C.C., (1990) *Studies on the Manoeuvrability of a Submersible Approaching Sea Bottom,* Proceedings CSME Mechanical Engineering Forum, pp. 407-412.

Healey, A.J., (1992) *Experimental Verification of Autonomous Underwater Vehicle Behaviour using the NPS AUVII,* 2nd Int. Conf. Manoeuvring and Control of Marine Craft, Southampton, U.K.

Healey, A.J. and Good, M.R., (1992) *The NPS AUVII Autonomous Underwater Vehicle Testbed: Design and Experimental Verification*, Naval Engineers Journal Vol. 104, No. 3, pp 191-202.

HealeyA.J., Rock, S.M., Miles D. and Brown, J.P., (1995) *Toward an Improved Understanding of Thruster Dynamics for Underwater Vehicles*, IEEE Journal of Oceanic Engineering, Vol. 20. No 4.

Hoerner, S.F., (1958) *Fluid Dynamic Drag*, Published by the author, New Jersey USA.

Hooft, J.P., (1986) *Computer Simulations of the Behaviour of Maritime Structures*, Marine Technology, Vol. 23, No.2, pp. 139-157.

Humphreys, D.E. and Watkinson, K.W., (1978) *Prediction of Acceleration Hydrodynamic Coefficients for Underwater Vehicles from Geometric Parameters*, Naval Coastal Systems Laboratory, Panama City, Florida, Technical Report NCSL TR 327-78.

Imlay, F.H., (1961) *Complete Expressions for Added Mass of a Rigid Body Moving in an Ideal Fluid*, David Taylor Model Basin, Washington D.C., Hydromechanics Laboratory Research and Development Report.

Imlay, F.H., (1964) *Complete Expressions for the Gravitational and Buoyancy Force Terms in the Equations of Motion of a Submerged Body*, David Taylor Model Basin, Washington D.C., Hydromechanics Laboratory Research and Development Report 1845.

Jensen, A.G., (1986) *Manoeuvring in Wind and Waves*, Danish Maritime Institute

Kalske, S., (1989) *Motion Dynamics of Subsea Vehicles*, Valtion Teknillinen Tutkimuskekus, Espoo Finland, PB89-218077

Kelly, H.R., (1954) *The Estimation of Normal Force, Drag, and Pitching Moment Coefficients For Blunt Based Bodies of Revolution at Large Angles of Attack*, Journal of Aeronautical Sciences, Vol. 21, pp 549-565.

Krause, T.P., Shure, L., and Little, J.N, (1994) *Signal Processing Toolbox User's Guide*, the Mathworks Inc., Massachusetts, United States of America.

Kreyszig, E., (1989) *Advanced Engineering Mathematics*, 5th Edition, John Wiley & Sons, New York.

Krezelewski, M.J., (1994) *Some Notes on the Added Massas in Mathematical Manoeuvring Models*, 4th Int. Conf. MCMC.

Landweber, L. and Macagno, M., (1967) *Potential Flow about Series 58 Bodies in General Translational and Rotational Motion*, Naval Ship Research and Development Center Report 2505, Washington, D.C.

Lewis, D.J., Lipscombe, J.M. and Thomasson, P.G., (1984) *The Simulation of Remotely Operated Vehicles*, Cranfield Institute of Technology, Proceedings of ROV'84, pp.245-251.

Ljung, L, and Soderstrom, T., (1983) *Theory and Practice of Recursive Identification*, MIT Press, Cambridge Massachusetts.

Mackay, M., and Conway, J.T., (1991) *Modelling the Crossflow Body Separation on a Submarine using a Panel Method*, RINA Symposium on Naval Submarines, London.

Mathworks (1994) *MATLAB – High Performance Numeric Computation and Visualisation Software – User's Guide*, The Mathworks Inc,. Natick, Massachusetts.

Marker, M., (1998) *Horizontal Planar Motion Mechanism – Motion Control Software*, Australian Maritime Engineering CRC, Australia.

Mehta, R.D., (1977) *The Aerospace Design of Blower Tunnels with Wide Angle Diffusers*, Prog. Aerospace Science Vol. 18, pp 59-120, U.K.

Mehta, R.D. and Bradshaw, P., (1979) *Design Rules For Small Low Speed Wind Tunnels*, Aeronautical Journal Paper No. 718.

Mendenhall, M.R. Spangler, S.B., and Perkins, S.C. Jr, (1979) *Vortex Shedding from Circular and Non-circular Bodies at High Angles of Attack*, 17th Aerospace Sciences Meeting, New Orleans, La, AIAA Paper 79 0026.

Mendenhall, M.R., and Perkins, S.C. Jr, (1985) *Prediction of the Unsteady Hydrodynamic Characteristics of Submersible Vehicles*, Proceedings 4th International Conference on Numerical Ship Hydrodynamics, USA.

Montero, J.M, Garcia, A., and Iribarren, J.R., (1994) *New Method To Obtain Manoeuvring Coefficients by Means of Towing Tank Tests*, 4th Int. Conf. MCMC.

Morton, B.R., (1984) *An Introduction to Mechanics*, Dept. of Mathematics, Monash University, AUS.

Munk, M.M., (1924) *The Aerodynamic Forces on Airship Hulls*, National Advisory Committee for Aeronautics Report No. 184.

Myers, J.J. Holm, C., and McAlister, R.F., *Handbook of Ocean and Underwater Engineering*, North American Rockwell Corporation.

Newman, J.N., (1977) *Marine Hydrodynamics*, The Massachusetts Institute of Technology, Cambridge, Massachusetts.

Newman, J.N., (1979) *Added Moment of Inertia of Two Dimensional Cylinders*, Journal of Ship Research, Vol. 23, No. 1, pp. 1-8.

Nomoto, M. and Hattori, M., (1986) *A Deep ROV "Dolphin": Design and Performance Analysis*, IEEE Journal of Oceanic Engineering, Vol. OE-11, No.3.

Ower, E., and Hutton, C.T., (1929) *Investigation of the Boundary Layers and the Drags of Two Streamline Bodies*, Air Ministry, Aeronautical Research Committee, London.

Pope, A. and Harper J.J., (1954) *Low Speed Wind Tunnel Testing*, John Wiley & Sons, Inc., New York.

Price, W.G. and Tan, M., (1994) *A Viscous Boundary Element approach to Evaluate Slow Motion Derivatives*, 4th Int. Conf. MCMC.

Rabiner, L. R., and Gold, B., (1975) *Theory and Application of Digital Signal Processing*, Bell Telephone Laboratories and Lincoln Laboratory, Prentice Hall, United States of America

Renilson, M.R., (1986) *A Note on the Fuid Memory Effects and Non-Linearities Involved in Oscillatory Ship Model Manoeuvring Experiments*, 9th Int. Conf Australasian Fluid Mechanics, N.Z.

Sahin, I., Crane, J., and Watson, K., (1993) *Added Mass Coefficients for Submerged Bodies by a Low Order Panel Method*, Journal of Fluids Engineering, Vol. 115, pp 452-456.

Sakata, K., (1985) *Applications of CWC for Experimental Researches in Aeronautical and Mechanical Engineering*, National Aerospace Laboratory.

Sayer, P. and Baker, J.H.A., (1986) *Experimental Scaling Effects on the Hydrodynamics of ROVs*, Proceedings 5th International Conference Offshore Mechanics and Arctic Engineering Symposium, Tokyo ASME 3:272-278.

Sayer, P. and Baker, J.H.A., (1988) *Steady Flow Force and Moment Coefficients for Application to Workboat ROVs*, Proceedings 7th International Conference Offshore Mechanics and Arctic Engineering, pp 431-438, Houston.

Sharma, S.D., (1979) *Analysis and Simulation of Unsteady Nonlinear Ship Dynamics*, ONR Contract No. N00014-77-C-0701.

Smart, E.H., (1951) *Advanced Dynamics*, Vol II Dynamics of a Solid Body, MacMillan and Co., Limited St. Martin's Street, London.

Smith, D., (1984) *Calibration and Testing of the Australian Maritime College Flume Tank*, Australian Maritime College Australia.

Smith, M.J., (1991) *Notes on Data Acquisition and Analysis Software for HPMM Experiments*, Defence Research Agency, DRA/MAR TM (MTH) 91322, U.K.

SNAME (1962) *Nomenclature for Treating the Motion of a Submerged Body Through a Fluid*, The Society of Naval Architects and Marine Engineers, Technical and Research Bulletin No. 1-5, New York.

Stratford, B.S., (1958) *The Prediction of Separation of the Turbulent Boundary Layer.*

Strom-Tejsen, J. and Chislett M.S., (1966) *A Model Testing Technique and Method of Analysis for the Prediction of Steering and Manoeuvring Qualities of Surface Vessels*, Hydro and Aerodynamic Laboratory Denmark Report No. Hy-7.

Tagori, T., (1985) *Flow Visualisation Techniques in Circulating Water Channels,* University of Tokyo.

Takahei, T., (1985) *On the History and Prospect of Circulating Water Channels,* University of Tokyo.

Technisearch (1991) *Introduction to Digital signal Processing,* Department of Communication and Electrical Engineering, RMIT, Melbourne, Australia.

Tick, L.J., (1959) *Differential Equations With Frequency Dependent Coefficients.*

Tinker, S.J., (1978) *Fluid Memory Effects on the Trajectory of a Submersible,* International Shipbuilders, Vol. 25, No. 290.

Tinker, S.J., Bowman, A.R, and Booth, T.B., (1979) *Identifying Submersible Dynamics from Free Model Experiments,* RINA.

Tinker, S.J., (1988) *A Discrete Vortex Model of Separated Flows over Manoeuvring Submersibles,* Advances in Underwater Technology, Ocean Science and Offshore Engineering, Vol. 15, pp 157-176.

Ward, B., (1992) *Experiments to Improve Predictions of Submarine Manoeuvres,* Proceedings of the 2nd International Conference on Manoeuvring and Control of Marine Craft, U.K.

Ward, B., and Wilson, P.A., (1992) *Forces on a Body of Revolution in a Vortex Flow Field,* RINA.

Wellicome J.F., Wilson P.A., and Cheng, X., (1994) *The Commissioning and Operation of a Horizontal Planar Motion Mechanism,* 3rd Int. Conf. MCMC, Southampton, U.K.

Willetts, B.B., and Murray, C.G., (1981) *Lift Exerted on Stationary Spheres in Turbulent Flow,* Journal of Fluid Mechanics, Vol. 105, pp. 487-505, U.K.

Willie, C., (1980) *Methods for Prediction of Ship Manoeuvrability at the Design Stage,* Norwegian Maritime Research Report No. 1/1980.

Wright, E.A., (1959) *New Research Resources at the David Taylor Model* Basin, David Taylor Model Basin, Report 1292.

Wu, G.X., (1994) *Hydrodynamic Forces on a Submerged Sphere Undergoing Large Amplitude Motion,* Journal of Ship Research Vol. 38, No 4, pp272-277.

Zdravkovich, M.M., (1977) *Review of Flow Interference Between Two Circular Cylinders in Various Arrangements,* Journal of Fluids Engineering, pp. 618-633.

Appendix 1.

A1.1. Rigid Body Force

The derivations that follow are an expansion of results given in Greenshields (1987).

To establish the general motion of a rigid body a coordinate system must first be defined. The forces that act on a rigid body can most easily be described in a coordinate system that is defined relative to the body. A fixed point O_E is selected to represent the origin of an earth-fixed, or global, coordinate system. A point denoted by O is selected on the body to represent the origin of the body-fixed coordinate system; the selection of this point is generally one of convenience for modelling purposes, and it does not need to coincide with the centre of gravity of the body. This latter system is also called the local coordinate system.

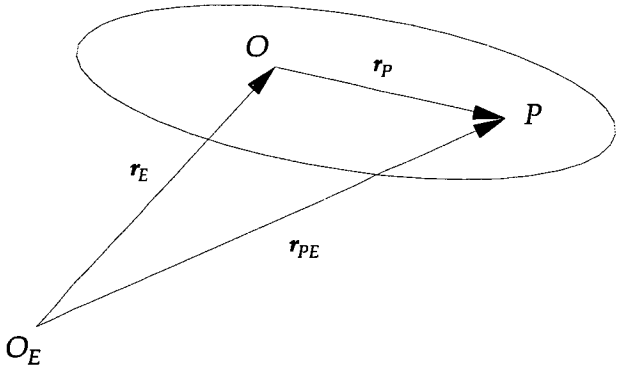

Figure A1.1. 1 Generalised body showing the origin and position vector relationships

If P is a point on a rigid body then

$$r_{PE} = r_E + r_P \qquad \text{(A1.1. 1)}$$

where

r_E is the vector from point O_E to point O,

r_P is the vector from O to point P, and

r_{PE} is the vector from point O_E to P.

v_P, the velocity of P is given by:

$$\mathbf{v}_P = \frac{d\mathbf{r}_{PE}}{dt}$$
$$\Rightarrow \mathbf{v}_P = \frac{d(\mathbf{r}_E + \mathbf{r}_P)}{dt}$$
$$\Rightarrow \mathbf{v}_P = \mathbf{v}_E + \Omega \times \mathbf{r}_P \qquad \text{(A1.1. 2)}$$

where

v_E is the velocity of O from O_E, and

Ω is the angular velocity of the body about O.

If the centre of gravity of a body is denoted by G, then let the velocity of the centre of gravity of the body with respect to O_E be given by $\boldsymbol{U}_G$. From Equation (A1.1. 2), $\boldsymbol{U}_G$ is expressed in body coordinates as

$$\boldsymbol{U}_G = \boldsymbol{U} + \boldsymbol{\Omega} \times \boldsymbol{R} \qquad \text{(A1.1. 3)}$$

where

$\boldsymbol{U}$ is the velocity of the body origin, and

$\boldsymbol{\Omega} \times \boldsymbol{R}$ is the velocity of G with respect to O.

The net force is given by the expression

$$\boldsymbol{F} = m\frac{d\left(\dot{\boldsymbol{U}}_G\right)}{dt}$$
$$\Rightarrow \boldsymbol{F} = m\frac{d}{dt}(\boldsymbol{U} + \boldsymbol{\Omega} \times \underline{\boldsymbol{R}}) \qquad \text{(A1.1. 4)}$$

The axial components of the vectors $\boldsymbol{U}$, $\boldsymbol{\Omega}$ and $\boldsymbol{R}$ are:

$$\left.\begin{aligned} \boldsymbol{U} &= (u \quad v \quad w) \\ \boldsymbol{\Omega} &= (p \quad q \quad r) \\ \boldsymbol{R} &= (x_G \quad y_G \quad z_G) \end{aligned}\right\} \qquad \text{(A1.1. 5)}$$

The axial components are substituted into Equation (A1.1. 4) to give

$$\boldsymbol{F} = m\frac{\mathrm{d}}{\mathrm{dt}}\left[(u+qz_G - ry_G)\boldsymbol{i} + (v\text{-}pz_G+rx_G)\boldsymbol{j} + (w+py_G\text{-}qx_G)\boldsymbol{k}\right] \qquad \text{(A1.1. 6)}$$

Hence

$$\mathbf{F} = m\left[\begin{array}{l}\left(\dot{u}+\dot{q}z_G - \dot{r}y_G\right)\mathbf{i} + \left(\dot{v}-\dot{p}z_G + \dot{r}x_G\right)\mathbf{j} + \left(\dot{w}+\dot{p}y_G - \dot{q}x_G\right)\mathbf{k} \\ +(u+qz_G - ry_G)\dot{\mathbf{i}} + (v\text{-}pz_G + rx_G)\dot{\mathbf{j}} + (w+py_G - qx_G)\dot{\mathbf{k}}\end{array}\right]$$

(A1.1. 7)

Since the unit vectors i, j and k are fixed in length, the derivatives of the unit vectors are simply the cross product of the unit vector with the angular velocity Ω. That is

$$\begin{aligned}\dot{\mathbf{i}} &= \Omega\times\mathbf{i} = \text{-}q\mathbf{k} + r\mathbf{j} \\ \dot{\mathbf{j}} &= \Omega\times\mathbf{j} = p\mathbf{k} - r\mathbf{i} \\ \dot{\mathbf{k}} &= \Omega\times\mathbf{k} = \text{-}p\mathbf{j} + q\mathbf{i}\end{aligned} \qquad \text{(A1.1. 8)}$$

It follows then that the components of the net force along the body axes are given by

$$X = m\left[\left(\dot{u}+qw\text{-}rv\right) - x_G\left(r^2+q^2\right) + p(qy_G + rz_G) + \left(\dot{q}z_G - \dot{r}y_G\right)\right]$$

$$Y = m\left[\left(\dot{v}+ru\text{-}pw\right) - y_G\left(p^2+r^2\right) + q(px_G + rz_G) + \left(\dot{r}x_G - \dot{p}z_G\right)\right]$$

$$Z = m\left[\left(\dot{w}+pv\text{-}qu\right) - z_G\left(p^2+q^2\right) + r(px_G + qy_G) + \left(\dot{p}y_G - \dot{q}x_G\right)\right]$$

(A1.1. 9)

The terms that contain translational and rotational velocity are separated from the acceleration terms and placed in the vector representing the rigid body forces, F_d These terms are placed on the left-hand side of Equation (A1.1.4) as if they are external forces to the body. Thus the components of the rigid body force along the body axes are

$$X_d = -m\left((qw - rv) - x_G\left(r^2 + q^2\right) + p\left(qy_G + rz_G\right)\right)$$

$$Y_d = -m\left((ru - pw) - y_G\left(p^2 + r^2\right) + q\left(px_G + rz_G\right)\right)$$

$$Z_d = -m\left((pv - qu) - z_G\left(p^2 + q^2\right) + r\left(px_G + qy_G\right)\right) \qquad \text{(A1.1. 10)}$$

A1.2. Rigid Body Moment

Let the body of total mass m, be the sum of the individual particle masses δm_i. The momentum of the particle δm_i is given by

$$\delta m_i \dot{\mathbf{r}}_i \qquad \text{(A1.2. 1)}$$

where by definition

$\boldsymbol{r}_i$ is the position of the ith particle, and

$\dot{\mathbf{r}}_i$ is the velocity from the origin O on the body.

Hence the moment about the origin O of the momentum relative to O is given by

$$\mathbf{r}_i \times \delta m_i \dot{\mathbf{r}}_i \qquad \text{(A1.2. 2)}$$

If $\boldsymbol{h}$ denotes the sum of the moments of momentum about O then

$$\boldsymbol{h} = \sum_i \boldsymbol{r}_i \times \delta m_i \dot{\boldsymbol{r}}_i \qquad \text{(A1.2. 3)}$$

Now the sum of the moments of momentum is related to the centre of gravity of the body, G. Note the expressions for the position and velocity vectors of the ith particle are

$$\boldsymbol{r}_i = \boldsymbol{R} + \boldsymbol{r}_{iG} \qquad \text{(A1.2. 4)}$$

and

$$\dot{\boldsymbol{r}}_i = \dot{\boldsymbol{R}} + \dot{\boldsymbol{r}}_{iG} \qquad \text{(A1.2. 5)}$$

where

$\boldsymbol{r}_{iG}$ and $\dot{\boldsymbol{r}}_{iG}$ denote the position and velocity respectively of the particle relative to G, and

$\boldsymbol{R}$ is the position vector of the centre of gravity, from the origin.

Substituting Equations (A1.2. 4) and (A1.2. 5) into (A1.2.3) gives

$$\boldsymbol{h} = \sum_i (\boldsymbol{R} + \boldsymbol{r}_{iG}) \times \delta m_i \left(\dot{\boldsymbol{R}} + \dot{\boldsymbol{r}}_{iG} \right)$$

$$\Rightarrow \quad \boldsymbol{h} = \sum_i \delta m_i \boldsymbol{R} \times \left(\dot{\boldsymbol{R}} + \dot{\boldsymbol{r}}_{iG} \right) + \sum_i \delta m_i \boldsymbol{r}_{iG} \times \left(\dot{\boldsymbol{R}} + \dot{\boldsymbol{r}}_{iG} \right)$$

$$\Rightarrow \quad \boldsymbol{h} = \sum_i \delta m_i \boldsymbol{R} \times \dot{\boldsymbol{R}} + \sum_i \delta m_i \boldsymbol{R} \times \dot{\boldsymbol{r}}_{iG} + \sum_i \delta m_i \boldsymbol{r}_{iG} \times \dot{\boldsymbol{R}} + \sum_i \delta m_i \boldsymbol{r}_{iG} \times \dot{\boldsymbol{r}}_{iG}$$

(A1.2. 6)

Since $\boldsymbol{r}_i = \boldsymbol{R} + \boldsymbol{r}_{iG}$ then

$$\sum_i \delta m_i \mathbf{r}_{iG} = 0 \text{ and } \sum_i \delta m_i \dot{\mathbf{r}}_{iG} = 0 \qquad \text{(A1.2. 7)}$$

Therefore

$$\sum_i \delta m_i \mathbf{R} \times \dot{\mathbf{r}}_{iG} = 0 \text{ and } \sum_i \delta m_i \mathbf{r}_{iG} \times \dot{\mathbf{R}} = 0 \qquad \text{(A1.2. 8)}$$

Hence

$$\boldsymbol{h} = m\boldsymbol{R} \times \dot{\boldsymbol{R}} + \boldsymbol{h}_G \qquad \text{(A1.2. 10)}$$

From the definition of moment of momentum in Equation (A1.2.3), the moment of momentum about G is given by

$$\boldsymbol{h}_G = \sum_i \boldsymbol{r}_{iG} \times \delta m_i \dot{\boldsymbol{r}}_{iG} \qquad \text{(A1.2. 9)}$$

The moment about O of the external forces acting on the body, denoted by $\boldsymbol{M}$ is

$$\boldsymbol{M} = \sum_i \boldsymbol{r}_i \times \boldsymbol{F}_i$$

$$\Rightarrow \quad \boldsymbol{M} = \sum_i (\boldsymbol{R} + \boldsymbol{r}_{iG}) \times \boldsymbol{F}_i$$

$$\Rightarrow \quad \boldsymbol{M} = \boldsymbol{R} \times \boldsymbol{F} + \boldsymbol{M}_G \qquad \text{(A1.2. 11)}$$

where

$$\boldsymbol{M}_G = \sum_i \boldsymbol{r}_{iG} \times \boldsymbol{F}_i \qquad \text{(A1.2. 12)}$$

$\boldsymbol{M}_G$ is the moment of external forces about the body's centre of mass G. By definition, the moment of external forces about G, is given by the rate of change of the moment of momentum with time, ie.

$$\boldsymbol{M}_G = \dot{\boldsymbol{h}}_G \qquad \text{(A1.2.13)}$$

Therefore

$$\boldsymbol{M} = \boldsymbol{R} \times \boldsymbol{F} + \dot{\boldsymbol{h}}_G \qquad \text{(A1.2. 14)}$$

Substitution for F from Equation (A1.1.4) and $\dot{\boldsymbol{h}}_G$, using the derivative of the result in Equation (A1.2.9), shows that the moment about O is

$$\boldsymbol{M} = \boldsymbol{R} \times m\dot{\boldsymbol{U}}_G + \dot{\boldsymbol{h}} - m\left(\boldsymbol{R} \times \ddot{\boldsymbol{R}}\right)$$

$$\Rightarrow \quad \boldsymbol{M} = \dot{\boldsymbol{h}} + m\boldsymbol{R} \times \left(\dot{\boldsymbol{U}}_G - \ddot{\boldsymbol{R}}\right)$$

$$\Rightarrow \quad \boldsymbol{M} = \dot{\boldsymbol{h}} + m\boldsymbol{R} \times \dot{\boldsymbol{U}} \qquad \text{(A1.2.15)}$$

Let the components of $\boldsymbol{h}$ be given by h_x, h_y, h_z and since

$$\dot{\boldsymbol{h}} = \frac{d\boldsymbol{h}}{dt}$$

$$\Rightarrow \quad \dot{\boldsymbol{h}} = \frac{\partial \boldsymbol{h}}{\partial t} + \Omega \times \boldsymbol{h} \qquad \text{(A1.2.16)}$$

then

$$\dot{\boldsymbol{h}} = \dot{h}_x \boldsymbol{i} + \dot{h}_y \boldsymbol{j} + \dot{h}_z \boldsymbol{k} + \Omega \times \boldsymbol{h} \qquad \text{(A1.2. 17)}$$

Similarly for the velocity of O,

$$\dot{\boldsymbol{U}} = \dot{u}\boldsymbol{i} + \dot{v}\boldsymbol{j} + \dot{w}\boldsymbol{k} + \boldsymbol{\Omega} \times \boldsymbol{U} \tag{A1.2.18}$$

Restating the definition for the moment of momentum about O

$$\boldsymbol{h} = \sum_i \boldsymbol{r}_i \times \delta m_i \dot{\boldsymbol{r}}_i$$

and noting that since $\boldsymbol{r}_i$ is constant in length for the ith particle the velocity is

$$\dot{\boldsymbol{r}}_i = \boldsymbol{\Omega} \times \boldsymbol{r}_i \tag{A1.2.19}$$

It can be then shown that

$$\boldsymbol{h} = \begin{bmatrix} I_{xx} & -I_{xy} & -I_{xz} \\ -I_{yx} & I_{yy} & -I_{yz} \\ -I_{zx} & -I_{zy} & I_{zz} \end{bmatrix} \begin{bmatrix} p \\ q \\ r \end{bmatrix} \tag{A1.2.20}$$

Define the components of the moment about O such that:

$$\boldsymbol{M} = K\boldsymbol{i} + M\boldsymbol{j} + N\boldsymbol{k} \tag{A1.2.21}$$

where $K, M,$ and N are the moment components about the respective axial directions.

Therefore

$$K = I_{xx}\dot{p} - I_{xy}\dot{q} - I_{xz}\dot{r} - I_{zx}pq - I_{zy}q^2 + I_{zz}qr + I_{yx}pr - I_{yy}qr + I_{yz}r^2 + m\left[\left(y_G\dot{w} - z_G\dot{v}\right) + y_G(pv - qu) - z_G(ru - pw)\right] \tag{A1.2.22}$$

$$M = -I_{yx}\dot{p} + I_{yy}\dot{q} - I_{yz}\dot{r} + I_{xx}pr - I_{xy}qr - I_{xz}r^2 + I_{zx}p^2 + I_{zy}pq - I_{zz}pr + m\left[\left(z_G\dot{u} - x_G\dot{w}\right) + z_G(qw - rv) - x_G(pv - qu)\right] \tag{A1.2.23}$$

$$N = I_{xx}\dot{p} - I_{xy}\dot{q} - I_{xz}\dot{r} - I_{yx}p^2 + I_{yy}pq - I_{yz}pr - I_{xx}qp + I_{xy}q^2 + I_{xz}qr + m\left[\left(x_G\dot{v} - y_G\dot{u}\right) + x_G(ru - pw) - y_G(qw - rv)\right] \tag{A1.2.24}$$

As described in the previous section (A1.1), the terms containing velocities are presented in the rigid body moment vector, as though the rigid body moment is an external disturbance to the body. The axial components of the rigid body moment, $K_d, M_d,$ and $N_d,$ are

$$K_d = I_{zx}pq + I_{zy}q^2 - I_{zz}qr - I_{yx}pr + I_{yy}qr - I_{yz}r^2 - m[y_G(pv - qu) - z_G(ru - pw)] \quad \text{(A1.2.25)}$$

$$M_d = -I_{xx}pr + I_{xy}qr + I_{xz}r^2 - I_{zx}p^2 - I_{zy}pq + I_{zz}pr - m[z_G(qw - rv) - x_G(pv - qu)] \quad \text{(A1.2.26)}$$

$$N_d = I_{yx}p^2 - I_{yy}pq + I_{yz}pr + I_{xx}qp - I_{xy}q^2 - I_{xz}qr - m[x_G(ru - pw) - y_G(qw - rv)] \quad \text{(A1.2.27)}$$

A1.3. UUV6DOF Simulation Input Data File

```
%=============================================================
%=== Function Name:   UUVDAT.m
%=== Description:    M-file to be used to initialise UUV6DOF
%===
%=============================================================


% Variable Declarations
% -------------------------

global MM RU S rho dia CN MLU UL;

g=9.81;     %Gravity acceleration
m=7110/g;%Mass of vehicle in air
md=700;         %Mass of displaced fluid
W=7110;         %Magnitude Weight of vehicle in air
BF=7110;   %Magnitude Buoyancy force


% Define coordinates from position of centre of gravity
% Therefore c.o.g is the origin

XG=0.0;         %Center of gravity
YG=0.0;
ZG=0.07;

XB=0.0;         %Center of buoyancy
YB=0.0;
ZB=0.0;

% Thruster positions - dimensional in meters given from body origin.
% ------------------------------------------------------------
```

```
x1=-0.481; %Position of main rear port thruster
y1=-0.437;
z1= 0.07;

x2=-0.481; %Position of main rear starboard thruster
y2= 0.437;
z2= 0.07;

x3=  0.0;   %Position of lateral port thruster
y3=-0.82;
z3= 0.07;

x4=  0.0;   %Position of lateral starboard thruster
y4= 0.82;
z4= 0.07;

x5= 0.32;   %Position of vertical forward port thruster
y5=-0.40;
z5= 0.07;

x6= 0.32;   %Position of vertical forward starboard thruster
y6= 0.40;
z6= 0.07;

x7=-0.32;   %Position of  vertical rear port thruster
y7=-0.40;
z7= 0.07;

x8=-0.32;   %Position of vertical rear starboard thruster
y8= 0.40;
z8= 0.07;

% Input thrust demands as functions of time.
%-------------------------------------------------
```

```
% The thruster model is not representative of the PAP104 thrusters

TMAX=20;
T=[0; 1; 10; TMAX];
TD1=[0; 1; 1; 1];
TD2=[0; 1; 1; 1];
TD3=[0; 0; 0; 0];
TD4=[0; 0; 0; 0];
TD5=[0; 0.3; 0.8; 1];
TD6=[0; 0.3; 0.8; 1];
TD7=[0; -0.3; -0.8; -1];
TD8=[0; -0.3; -0.8; -1];

% Thruster parameters.
% ------------------------
%
% Note: These parameters are not representative of the thrusters on
%   the PAP104 vehicle.
%      TM is the thrust magnitude.
%   TVC is the thrust/velocity coefficient.

TM1=400; TVC1=50;
TM2=400; TVC2=50;
TM3=400; TVC3=50;
TM4=400; TVC4=-50;
TM5=400; TVC5=50;
TM6=400; TVC6=50;
TM7=400; TVC7=50;
TM8=400; TVC8=50;
rho=998;

% Moments and cross products of inertia (Dimensional values)
% ------------------------------------------------------------
% Note:     These inertias are not representative of the PAP104
%   vehicle inertias.
```

```
IXX=1000; IXY=0.0; IXZ=0.0;
IYX=0.0; IYY=1000; IYZ=0.0;
IZX=0.0; IZY=0.0; IZZ=1000;

%Added Mass Values
%----------------------
% Determined from PMM tests

Xudot=0.0; Xvdot=0.0; Xwdot=0.0; Xpdot=0.0; Xqdot=0.0; Xrdot=0.0;
Yudot=0.0; Yvdot=-1989.9621; Ywdot=0.0; Ypdot=0.0; Yqdot=0.0; Yrdot=311.2263;
Zudot=0.0; Zvdot=0.0; Zwdot=-3361.5135; Zpdot=0.0; Zqdot=642.6621; Zrdot=0.0;
Kudot=0.0; Kvdot=0.0; Kwdot=0.0; Kpdot=0.0; Kqdot=0.0; Krdot=0.0;
Mudot=0.0; Mvdot=0.0; Mwdot=-141.4665; Mpdot=0.0; Mqdot=-424.3995; Mrdot=0.0;
Nudot=0.0; Nvdot=3063.7602; Nwdot=0.0; Npdot=0.0; Nqdot=0.0; Nrdot=-351.6453;

%Hydrodynamic Coefficients
%---------------------------------
% Determined from PMM tests

Xqq=0.0; Xrr=0.0; Xrp=0.0; Xvr=0.0; Xwq=0.0; Xuu=-53.8920; Xvv=193.5621;
Xww=53.4429;Xw=0.0;
Ypmp=0.0; Ypq=0.0; Yr=471.5550; Yp=0.0; Ywp=0.0; Yo=0.0; Yv=-723.0510; Yvmv=-
1774.3941;
Zq=-227.6937; Zvp=0.0; Zo=22.4550; Zw=-1153.7379; Zmw=0.0; Zwww=0.0;
Kqr=0.0; Kpq=0.0; Kpmp=0.0; Kp=0.0; Kr=0.0; Kvq=0.0; Kwp=0.0; Kwr=0.0;
Ko=0.0; Kv=0.0; Kvmv=0.0; Kvw=0.0;
Mpp=0.0; Mrr=0.0; Mrp=0.0; Mqmq=0.0; Mvr=0.0; Mvp=0.0; Mq=-711.3744;
Mqmw=0.0;
Mo=5.3892; Mw=308.5317; Mwww=-134.7300; Mvv=0.0;
Npq=0.0; Nqr=0.0; Nrmr=0.0; Nwr=0.0; Nwp=0.0; Nvq=0.0; Np=0.0; Nr=-828.5895;
Nrmv=0.0; No=0.0; Nv=-517.3632; Nvmv=431.1360; Nvw=0.0;

% Mass Inertia Matrix
% ------------------
```

```
MM=[m-Xudot -Xvdot -Xwdot -Xpdot m*ZG-Xqdot -m*YG-Xrdot,
-Yudot m-Yvdot -Ywdot -m*ZG-Ypdot -Yqdot m*XG-Yrdot,
-Zudot -Zvdot m-Zwdot m*YG-Zpdot -m*XG-Zqdot -Zrdot,
-Kudot -m*ZG-Kvdot m*YG-Kwdot IXX-Kpdot -IXY -(IZX-Krdot),
m*ZG-Mudot -Mvdot -m*XG-Mwdot -IXY IYY-Mqdot -IYZ,
-m*YG-Nudot m*XG-Nvdot -Nwdot -(IZX-Npdot) -IYZ IZZ-Nrdot];

% Global Fluid Velocity
% --------------------

TS=[0; TMAX];
S=[0,0,0;0,0,0];

% Initial state vector
% -------------------

POSX=0;
POSY=0;
POSZ=50;
PHI=0;
THETA=0;
PSI=0;
VELU=0;
VELV=0;
VELW=0;
VELP=0;
VELQ=0;
VELR=0;

t=0;

STATE=[POSX,POSY,POSZ,PHI,THETA,PSI,VELU,VELV,VELW,VELP,VELQ,VELR]';

POS=[POSX;POSY;POSZ]';
```

```
ANG=[PHI;THETA;PSI]';
VEL=[VELU;VELV;VELW;VELP;VELQ;VELR]';
```

A1.4. UUV6DOF MATLAB/SIMULINK

The simulation package consists of four files: UUV6DOF.M, ACCEL2.M, UUVOUT.M and UUVDAT.M. The files should be copied under a single directory, preferably named UUV6DOF.

To begin the UUV6DOF simulation program, it is necessary to first start MATLAB. At the MATLAB command line, enter the directory under which the UUV6DOF files have been stored. Type <cd d:\uuv6dof\> and press enter.

Next type <simulink> at the command line and then press enter.

The simulink window should now be open. With the simulink window activated, press <Ctrl+O>, select 'UUV6DOF.M' and press <OK>. The opening screen for UUV6DOF should now appear (Fig. A1.4.1).

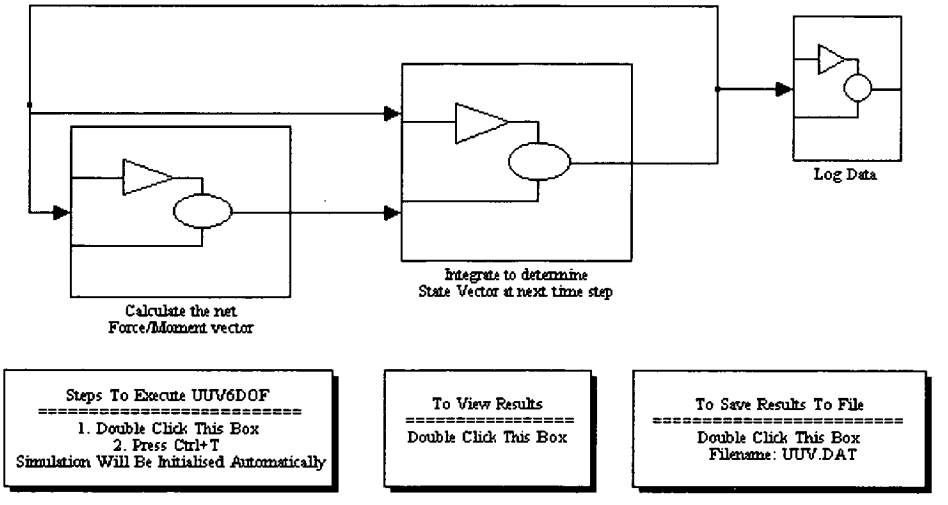

Figure A1.4.1 UUV6DOF Simulation Software

Each vehicle simulated with UUV6DOF requires its own data set. The individual characteristics such as mass, weight and hydrodynamic coefficients, are entered into the data file, 'UUVDAT.M'. The data file is also used to control the thruster operation and the environmental variables during the simulation. Both the thruster and sea current variables are required as a function of time. Since UUVDAT.M is a MATLAB m-file that is run prior to the simulation beginning, time series commands can be

generated using standard MATLAB commands embedded in the data file. A typical data file is given in Appendix A1.3.

The data files are edited prior to a simulation to incorporate the desired commands. Once completed, the data file is saved and the edit window can either be closed or minimised.

Before the simulation can commence, the simulation parameters may need to be set. These are found under the Simulink Menu <Options><Parameters>. Once these are checked the simulation can be run. This can be done in either of two ways:

1. Double Click the left hand box on UUV6DOF, then press <Ctrl+T> or
2. Enter <UUVDAT> at the Matlab command line then press <Ctrl+T>.

Once the simulation is complete the results can be viewed by double clicking the middle UUV6DOF box or saved by double clicking the third box. The data will be stored in the filename 'UUV.DAT'. This file is used to write the data from each simulation, therefore it is advised that the data from previous runs is copied to other files before continuing with new simulations.

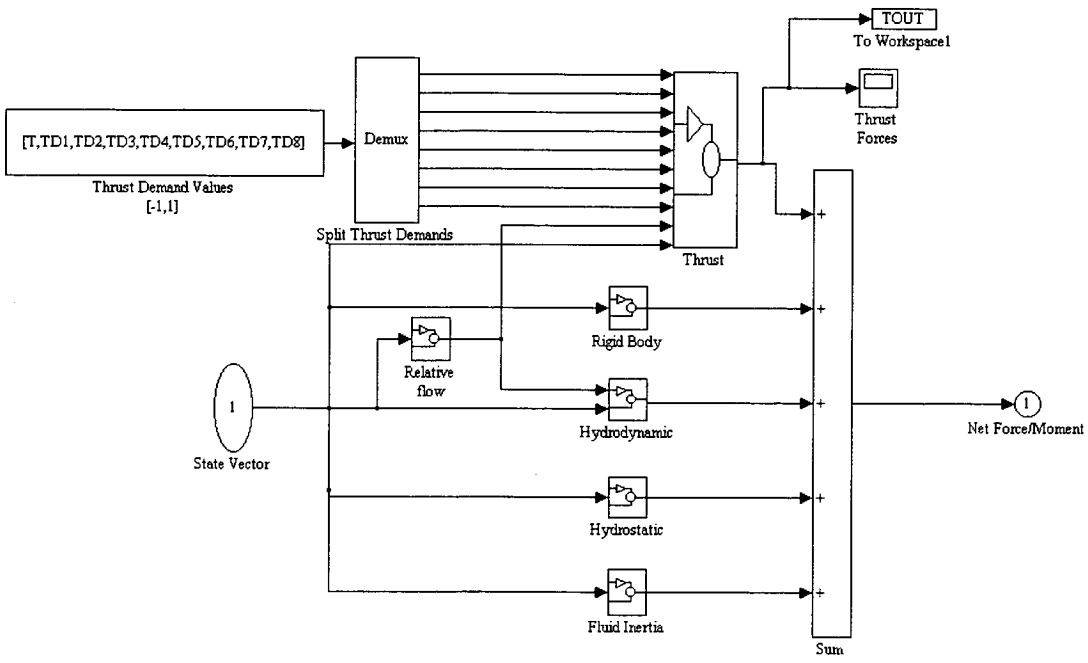

Figure A1.4.2 UUV6DOF Matlab/Simulink Block that calculates the forces and moments on the body

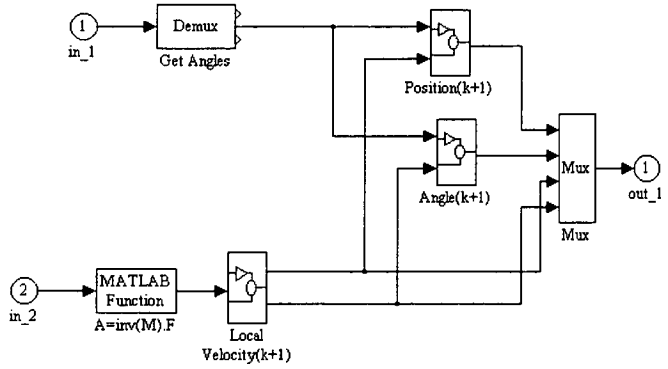

Figure A1.4.3 UUV6DOF Matlab Simulink Block that determines the acceleration, velocity and position of the body at the next time step.

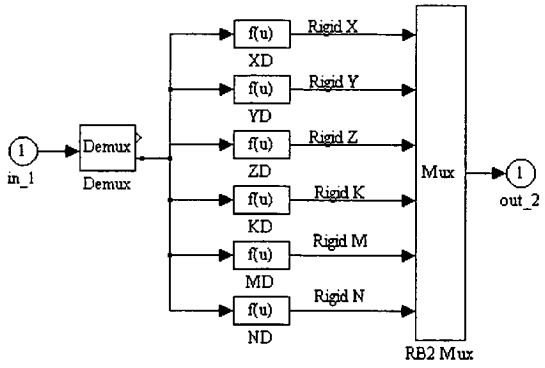

Figure A1.4.4 UUV6DOF Matlab/Simulink Block to determine rigid body forces.

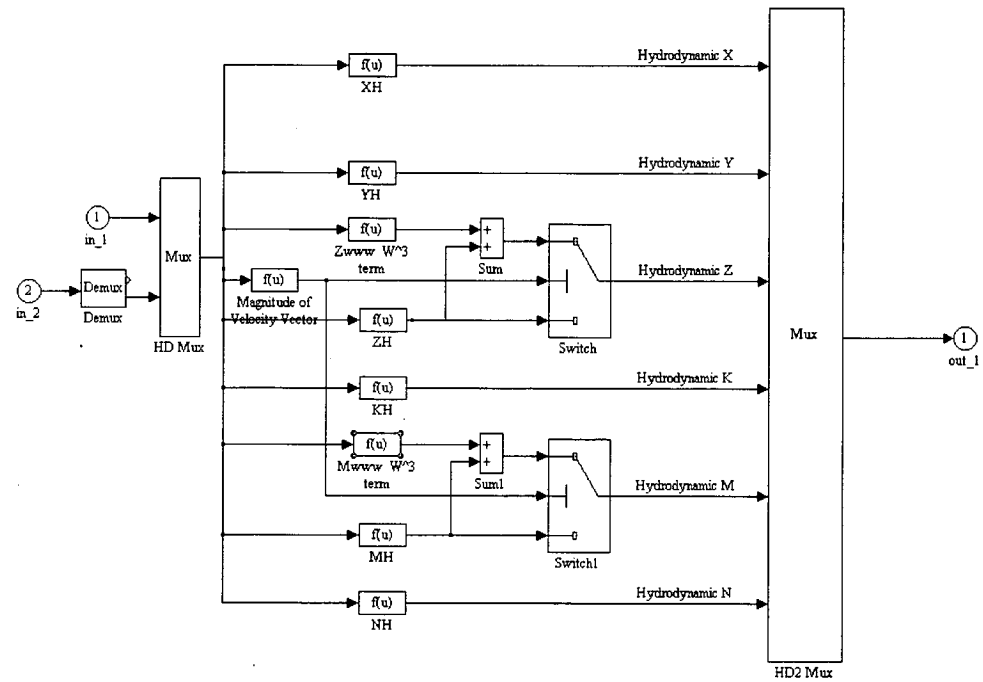

Figure A1.4.5 UUV6DOF Matlab/Simulink Block to determine hydrodynamic forces

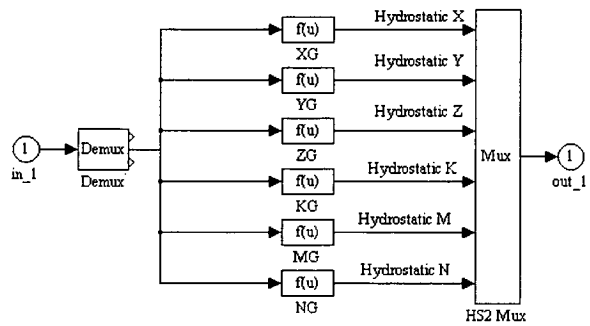

Figure A1.4.6 UUV6DOF Matlab/Simulink Block to determine hydrostatic forces

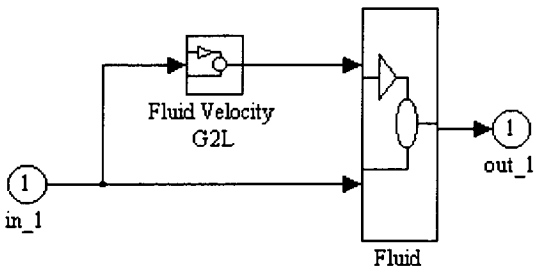

Figure A1.4.7 UUV6DOF Matlab/Simulink Block to determine the input flow variables to the fluid block that determines the hydrostatic forces

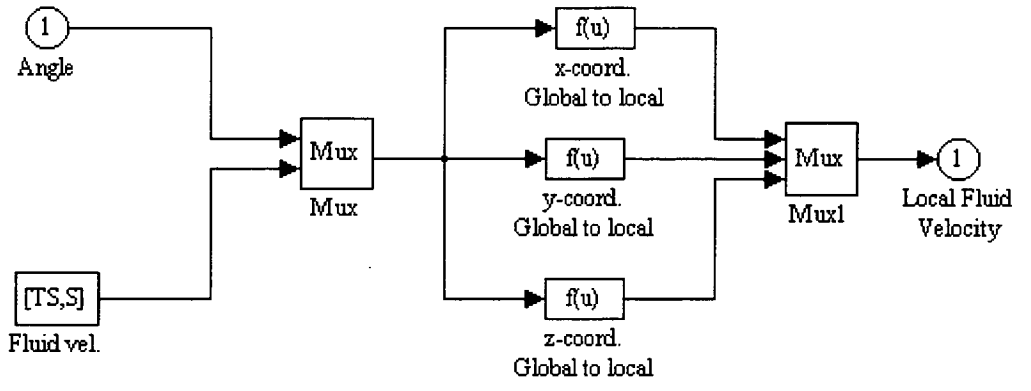

Figure A1.4.8 UUV6DOF Matlab/Simulink Block to transform the fluid velocities to local coordinate axes

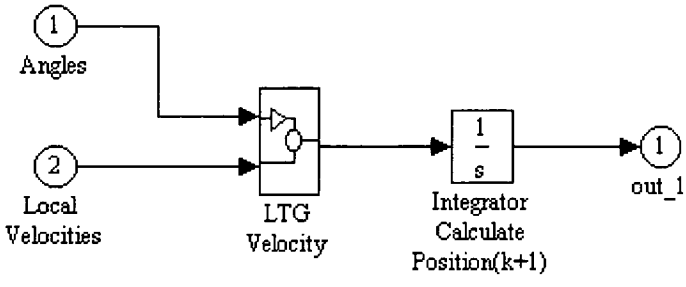

Figure A1.4.9 UUV6DOF Matlab/Simulink Block to determine position of the body at the next time step, k+1

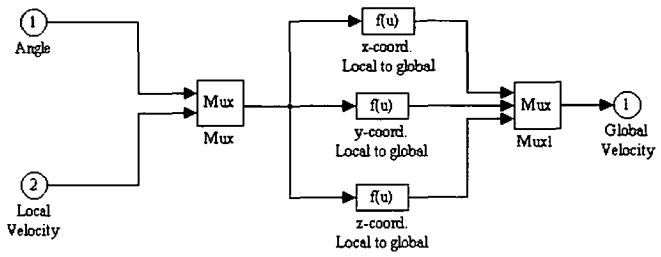

Figure A1.4.10 UUV6DOF Matlab/Simulink Block to transform local body axes velocity to absolute earth fixed velocities.

Appendix 2.

A2.1 Hydrodynamic Coefficients In A Potential Flow

	X	Y	Z	K	M	N
$\dot{u}$	$X_{\dot{u}}$	$Y_{\dot{u}} = X_{v}$	$Z_{\dot{u}} = X_{v}$	$K_{\dot{u}} = X_{p}$	$M_{\dot{u}} = X_{q}$	$N_{\dot{u}} = X_{r}$
$\dot{v}$	$X_{\dot{v}}$	$Y_{\dot{v}}$	$Z_{\dot{v}} = Y_{w}$	$K_{\dot{v}} = Y_{p}$	$M_{\dot{v}} = Y_{q}$	$N_{\dot{v}} = Y_{r}$
$\dot{w}$	$X_{\dot{w}}$	$Y_{\dot{w}}$	$Z_{\dot{w}}$	$K_{\dot{w}} = Z_{p}$	$M_{\dot{w}} = Z_{q}$	$N_{\dot{w}} = Z_{r}$
$\dot{p}$	$X_{\dot{p}}$	$Y_{\dot{p}}$	$Z_{\dot{p}}$	$K_{\dot{p}}$	$M_{\dot{p}} = K_{q}$	$N_{\dot{p}} = K_{r}$
$\dot{q}$	$X_{\dot{q}}$	$Y_{\dot{q}}$	$Z_{\dot{q}}$	$K_{\dot{q}}$	$M_{\dot{q}}$	$N_{\dot{q}} = M_{r}$
$\dot{r}$	$X_{\dot{r}}$	$Y_{\dot{r}}$	$Z_{\dot{r}}$	$K_{\dot{r}}$	$M_{\dot{r}}$	$N_{\dot{r}}$
u^2	---	---	---	---	$-X_{w}$	X_{v}
uv	---	---	---	X_{w}	$-Z_{v}$	$Y_{v} - X_{u}$
uw	---	---	---	$-X_{v}$	$X_{u} - Z_{w}$	Z_{v}
up	---	$-X_{w}$	X_{v}	---	$-Z_{p} - X_{r}$	$X_{q} + Y_{p}$
uq	X_{w}	---	$-X_{u}$	X_{r}	$-Z_{q}$	$Y_{q} - X_{p}$
ur	$-X_{v}$	X_{u}	---	$-X_{q}$	$X_{p} - Z_{r}$	Y_{r}
v^2	---	---	---	Z_{v}	---	$-X_{v}$
vw	---	---	---	$Z_{w} - Y_{v}$	X_{v}	$-X_{w}$
vp	---	$-Z_{v}$	Y_{v}	Z_{p}	$-Y_{r}$	$Y_{q} - X_{p}$
vq	Z_{v}	---	$-X_{v}$	$Y_{r} + Z_{q}$	---	$-X_{q} - Y_{p}$
vr	$-Y_{v}$	X_{v}	---	$Z_{r} - Y_{q}$	Y_{p}	$-X_{r}$
w^2	---	---	---	$-Z_{v}$	X_{w}	---
wp	---	$-Z_{w}$	Z_{v}	$-Y_{p}$	$X_{p} - Z_{r}$	Z_{q}

	X	Y	Z	K	M	N
wq	Z_{w}	---	$-X_{w}$	$Z_{r} - Y_{q}$	X_{q}	$-Z_{p}$
wr	$-Z_{v}$	X_{w}	---	$-Y_{r} - Z_{q}$	$Z_{p} + X_{r}$	---
p^2	---	$-Z_{p}$	Y_{p}	---	$-K_{r}$	K_{q}
pq	Z_{p}	$-Z_{q}$	$Y_{q} - X_{p}$	K_{r}	$-M_{r}$	$M_{q} - K_{p}$
pr	$-Y_{p}$	$X_{p} - Z_{r}$	Y_{r}	$-K_{q}$	$K_{p} - N_{r}$	M_{r}
q^2	Z_{q}	---	$-X_{q}$	M_{r}	---	$-K_{q}$
qr	$Z_{r} - Y_{q}$	X_{q}	$-X_{r}$	$N_{r} - M_{q}$	K_{q}	$-K_{r}$
r^2	$-Y_{r}$	X_{r}	---	$-M_{r}$	K_{r}	---

Table A2.1.1 Hydrodynamic coefficient relationships for an arbitrary body in an inviscid fluid.

When symmetry exists in the xz-plane then the following acceleration coefficients are zero:

$$Z_{v}\ Y_{w}\ Y_{u}\ X_{v}\ M_{r}\ N_{q}\ K_{q}\ M_{p}\ X_{p}\ K_{u}\ Y_{q}\ M_{v}\ Z_{r}\ N_{w}\ Z_{p}\ K_{w}\ X_{r}\ N_{u}$$

When symmetry exists in the xy-plane then the following acceleration coefficients are zero:

$$Z_{v}\ Y_{w}\ X_{w}\ Z_{u}\ M_{r}\ N_{q}\ K_{r}\ N_{p}\ X_{p}\ K_{u}\ Y_{q}\ M_{v}\ Z_{r}\ N_{w}\ X_{q}\ M_{u}\ Y_{p}\ K_{v}$$

When symmetry exists in the yz-plane then the following acceleration coefficients are zero:

$$X_{w}\ Z_{u}\ X_{v}\ Y_{u}\ K_{r}\ N_{p}\ K_{q}\ M_{p}\ X_{p}\ K_{u}\ Y_{q}\ M_{v}\ Z_{r}\ N_{w}\ Y_{r}\ N_{v}\ Z_{q}\ M_{w}$$

A2.2 Non-Dimensional Coefficients

Mass and moment of inertia:

$$m' = \frac{m}{\frac{1}{2}\rho l^3} \qquad I' = \frac{I}{\frac{1}{2}\rho l^5}$$

Distance, time and velocity:

$$x' = \frac{x}{l} \qquad t' = \frac{tU}{l} \qquad v' = \frac{v}{U}$$

Added Mass coefficients with respect to translational acceleration:

$$X'_{\dot{u}} = \frac{X_{\dot{u}}}{\frac{1}{2}\rho l^3} \qquad X'_{\dot{v}} = \frac{X_{\dot{v}}}{\frac{1}{2}\rho l^3} \qquad X'_{\dot{w}} = \frac{X_{\dot{w}}}{\frac{1}{2}\rho l^3}$$

Added Mass coefficients with respect to rotational acceleration:

$$X'_{\dot{r}} = \frac{X_{\dot{r}}}{\frac{1}{2}\rho l^4}$$

Added Moment coefficients with respect to translational acceleration:

$$N'_{\dot{u}} = \frac{N_{\dot{u}}}{\frac{1}{2}\rho l^4} \qquad N'_{\dot{v}} = \frac{N_{\dot{v}}}{\frac{1}{2}\rho l^4}$$

Added Moment coefficients with respect to rotational acceleration:

$$N'_{\dot{r}} = \frac{N_{\dot{r}}}{\frac{1}{2}\rho l^5}$$

A complete listing of non-dimensionalised formulae are given in SNAME (1962) and Humphreys (1978).

Appendix 3.

A3.1 Data File Sample

The following is a sample data file from the AME PMM data acquisition system:

```
**********************
*   PMM DATA FILE    *
**********************

THIS DATA HAS CROSS TALK COMPONENTS

Date            05/12/1996

Time            14:33

Sampling rate   30 Hz

Model type      PAP_104

Location        FLUME TANK

Flow speed      N/A

Motion type     N/A

Run type        N/A

Loadcell        M3378 250lbs

Amplitude       N/A

Frequency       N/A

Offset angle    N/A

Logging time    30 sec

Sample Force Y Force X Force Z Moment Y Moment X Moment Z EM log Back_DP Pitot Tran Rot

0 9.0110 -10.3223 -35.8170 0.7801 1.0876 -1.2441 -0.5380 -0.5914 0.3776 0.0324 0.3522
1 9.3864 -9.7693 -36.5480 0.7281 1.0701 -1.2541 -0.5380 -0.5973 0.3759 0.0324 0.3566
2 9.9496 -9.2163 -37.8272 0.7246 1.0561 -1.2591 -0.5378 -0.5899 0.3740 -0.1405 0.3517
3 10.1373 -9.2163 -39.4718 0.8911 1.0491 -1.1741 -0.5381 -0.5929 0.3759 -0.0417 0.3528
4 10.3251 -9.2163 -40.0201 0.9257 1.0386 -1.1092 -0.5375 -0.5973 0.3759 -0.0170 0.3555
5 9.9496 -9.4007 -39.2891 0.6934 1.0561 -1.1791 -0.5374 -0.5899 0.3740 -0.3134 0.3512
```

A3.2 AMTI Load Cell M3378 Properties

The characteristics of the AMTI M3378 Load Cell (AMTI 1993) follow:

Load Capacities:

Fx: 556.1 N – Shear force

Fy: 556.1 N – Shear force

Fz: 1112.2 N – Normal force

Mx: 28.3 Nm – Moment

My: 28.3 Nm – Moment

Mz: 14.1 Nm – Torque

Nominal Bridge Supply Voltages: 2.5V, 5.0V, 10.0V

Amplifier Gains: 1000, 2000, 4000

Load Ranges for different Amplifier Gains:

	1000	2000	4000
Fx	± 300 N	± 150 N	± 75 N
Fy	± 300 N	± 150 N	± 75 N
Fz	± 1200 N	± 600 N	± 300 N
Mx	±600 Ncm	± 300 Ncm	± 150 Ncm
My	±600 Ncm	± 300 Ncm	± 150 Ncm
Mz	±900 Ncm	± 450 Ncm	± 225 Ncm

Amplifier Output Channels are denoted Fx', Fy', Fz', Mx', My', Mz'

Excitation Voltage: 10V

Temperature Range: 0 to $125^{o}F$

Sensitivity change to temperature: $0.01\%/^{\circ}C$

Crosstalk: Less than 2% on all channels

Weight: 0.9kg

Stiffness:

Fz 7.88×10^{6} N/m

Fx, Fy 0.53×10^{6} N/m

Mz 0.57×10^{4} N-m/radian

Non-linearity: Fx, Fy, Fz 0.20 +/- %Full scale output

Hysteresis: Fx, Fy, Fz 0.20 %Full scale output

Resonant frequency: Mx, My 500Hz

Connector Type: Burndy BTO2E16-26P

Mounting Screw Holes:

4 x Threaded ¼-20 inserts in 50.8mm centres on top surface

4 x 6.76mm through holes on 60.3mm centres on bottom surface.

The output voltage of the load cell is related to the input loads by:

$$\boldsymbol{O}(i)=0.000001\,\boldsymbol{S}(i,j)G\,V_o\,\boldsymbol{I}(j) \qquad \text{(A3. 1)}$$

where

$\boldsymbol{O}(i)$ is the output voltage in volts

$\boldsymbol{S}(i,j)$ is the sensitivity

V_o is the bridge excitation voltage

G is the amplifier gain

$\boldsymbol{I}(j)$ is the input force or moment in newtons or newton-metres

The input load to the ith channel is given by

$$\boldsymbol{I}(i)=\frac{\boldsymbol{O}(j)\boldsymbol{C}(i,j)}{(0.000001\,G\,V_o)} \qquad \text{(A3. 2)}$$

where $\boldsymbol{C}(i,j)$ is the calibration matrix, which is also the inverse of the sensitivity matrix.

The manufacturer's sensitivity matrix:

$$\mathbf{S} = \begin{bmatrix} 2.594 & 0.025 & -0.002 & -0.044 & 0.533 & 0.641 \\ 0.001 & 2.577 & 0.006 & -0.232 & -0.615 & 0.249 \\ -0.005 & 0.0003 & 0.662 & 0.032 & -0.209 & 0.185 \\ -0.008 & -0.020 & -0.092 & 138.593 & 1.142 & -0.084 \\ 0.002 & -0.001 & -0.000 & 1.079 & 137.182 & 0.148 \\ 0.035 & -0.001 & 0.008 & 0.326 & -0.226 & 95.283 \end{bmatrix}$$

The manufacturer's calibration matrix:

$$\mathbf{C} = \begin{bmatrix} 0.38552 & -0.00373 & 0.00145 & 0.00013 & -0.00152 & -0.000258 \\ -0.00008 & 0.38814 & -0.00354 & 0.00064 & 0.00173 & -0.00101 \\ 0.00268 & -0.00203 & 1.51046 & -0.00037 & 0.00228 & -0.00294 \\ 0.00002 & 0.00005 & 0.00100 & 0.00722 & -0.00006 & 0.00000 \\ -0.00001 & 0.00010 & -0.00000 & -0.00006 & 0.00729 & -0.00001 \\ -0.00014 & 0.00001 & -0.00013 & -0.00002 & 0.00002 & 0.01050 \end{bmatrix}$$

A3.3 Software listing PURESWAY.M

```
% ==========================================
%      Function:  PureSway.m
%      Name:      Brendon Anderson
%     Date:       1998
%     Description:Pure Sway motion simulation
% ==========================================

y0=0.15;        %Max. Translation Amplitude
ft=0.20;        %Translation Frequency (Hz)
psi=0;          %Heading angle

t=[0:0.01:10];  %Time
wt=2*pi*ft;     %Translation frequency (rad/s)

% Pure sway motion

y=y0*sin(wt*t);

plot(t,y,'black');
xlabel('Time (s)');
ylabel('Displacement (m)');
set(gca,'ydir','reverse','ylim',[-0.2 0.2]);
grid on;

% End Function
```

A3.4 Software Listing Pure Yaw Motion

A3.4.1 Pureyaw.m

```
%=====================================================
%  Name: PureYaw.m
%  Author: brendon anderson
%  Decsription: Produces simulation of pure yaw mation
%  Function Calls beta.m (t,Uf,psi_0,wr)
%=====================================================

psi_0=0.25;      %Rotation max. amplitude
fr=0.20;       %Frequency (Hz) of rotation
wr=2*pi*fr;      %Frequency (rad/s) of rotation
Uf=0.5;        %Flow Speed (m/s)
delta=0.01;
t=[0:delta:10];

psi=psi_0*sin(wr*t-0.5*pi*ones(size(t)));

for i=1:length(t)
   k1=delta*beta(t(i),Uf,psi_0,wr);
   k2=delta*beta(t(i)+0.5*delta,Uf,psi_0,wr);
   k3=delta*beta(t(i)+0.5*delta,Uf,psi_0,wr);
   k4=delta*beta(t(i)+delta,Uf,psi_0,wr);

   if i==1,
      y(1)=(k1+2*k2+2*k3+k4)/6;
   else
      y(i)=y(i-1)+(k1+2*k2+2*k3+k4)/6;
   end;
end;
plot(t,psi,'k--',t,y,'k');
xlabel('Time (s)');
ylabel('Displacement');
set(gca,'ydir','reverse','ylim',[-0.3 0.3]);
grid on;
```

```
% End Function
```

A3.4.2 Beta.m

```
%=====================================================
%  Name: beta.m
%  Author: brendon anderson
%  Decsription: Function for pureyaw.m
%=====================================================

function [Out]=beta(time,Uf,psi_0,wr);

   Out=Uf*tan(psi_0*sin(wr*time-pi/2));

end;
```

A3.5 Motion Analysis Software Listings

A3.5.1 Hr.m

The following Matlab algorithm is based on the data file format described in Sections (4.5) and (A3.1). The program removes the header from AME PMM data files and places the data into a matrix.

```
%================================================================
%=== Name:    hr.m
%=== Created:31/1/96
%=== Author: B. Anderson
%=== Description: Removes header off PMM data files
%=== Modified:  31/1/96
%================================================================
   global A;

   fid=fopen(fname);
   fstr=fscanf(fid,'%s',1);
   while strcmp(fstr,'Rot')==0,
      fstr=fscanf(fid,'%s',1);
   end;
   [A,count]=fscanf(fid,'%f  %f  %f  %f  %f  %f  %f  %f  %f  %f  %f
%f',[12,inf]);
   A=A';
   fclose(fid);
%
%  End routine
%
```

A3.5.2 Bfilt.m

```
%================================================================
%===
%===   Name:       BFILT.m
%===   Author:       B. Anderson
%===   Description:
%===   Filter the data using an FIR filter which implements a
%===   kaiser window. The return vector will be corrected for the
%===   phase shift.
%===
%===   Input Variables:
%===  Y    is the data vector to be filtered
%===  c    is the passband cutoff frequency
%===   Output Variables:
%===     YFILT_PH    is the filtered vector with phase shift
%===        correction
%===  b    is the FIR filter parameters
%===
%================================================================

function [YFILT_PH,b]=BFILT(Y,c);

      wn=c/15.00015;
      n=round(32/(2.285*0.01*pi)+1);
      b=fir1(n-1,wn,kaiser(n,0.5842*(19^0.4)+0.07886*19));
      YFILT=filter(b,1,Y);
      if rem(n,2)~=0,
         n=n+1;
      end;
      YFILT_PH=YFILT(n/2:length(YFILT));
end;

%================================================================
%=== End function BFILT
%================================================================
```

A3.5.3 Motion_analysis.m

```
%================================================================
%=== Name:    Motion_Analysis.m
%=== Author: B. Anderson
%=== Description: Analyses PMM motion data; outputs
%=== frequency, amplitude of displacement
%================================================================

     ftitle='papa2404.m56';
      mot_type='py';

      fname=['d:\pmm0496\',ftitle];

     hr;

     if mot_type=='ps',
        y=A(:,11)./100; %Convert cm to m
     else
         y=A(:,12);
         trans=A(:,11)./100;
     end;

     sam=A(:,1);

  %Set sample frequency
     fs=30.003;

  %Set filter cutoff frequency
     if mot_type=='py',
         [y1,b]=bfilt(y,0.5);
         rot_amp=max(abs(y1))
         [trans_filt,b]=bfilt(trans,0.5);
         trans_amp=max(abs(trans_filt))
      else
         [y1,b]=bfilt(y,0.5);
        trans_amp=max(abs(y1))
      end;
```

```
freqz(b,1,256,fs);

%Determine maximum amplitude
amp=max(abs(y1));

% Step 1. Perform fft with n=1024 points;
% Note if s>n then increase the size of n by powers of 2
n=2^(18);

% Step 2. Find the power spectrum magnitudes
yf=fft(y,n);
Syy=yf.*conj(yf)/n;

figure;
f=fs*(0:(n/2-1))/n;
title(ftitle);

subplot(1,2,1);
plot(f(1:n/2),Syy(1:n/2),'k');
grid on;
xlabel('Frequency (Hz)');
ylabel('Energy Density Magnitude');

subplot(1,2,2);
plot(f(1:500),Syy(1:500),'k');
grid on;
xlabel('Frequency (Hz)');

% Step 3. Determine the peak magnitude
maxSyy=max(Syy);

% Step 4. Determine the sample at which the peak value occurs
peakSam=find(Syy==maxSyy);

% Step 5. Determine the frequency from the sample
ft=(peakSam(1)-1)/n*fs;
wt=2*pi*ft;
```

```
% Determine the time delay between measured and analytic motion
% ------------------------------------------------------------
      t=[0:1/fs:1/ft]';
      tl=length(t)-1;
      y2=amp*sin(wt*t);
      Ryy=xcorr(y(1:tl),y2(1:tl));
      maxRyy=max(Ryy);
      tsam=find(Ryy==maxRyy);
      td=(tsam(1)-1)/fs;

   %Regenerate signal
      ylength=length(y);
      t=[0:1/fs:(ylength-1)/fs];
      newy=amp*sin(wt*(t+td));

   % Generate program output

      frequency=ft

      figure;
      subplot(3,1,1);
      plot(sam./fs,y,'k');
      xlabel('Time (s)');
      ylabel('Raw Displacement');
      grid on;
      title(ftitle);

      subplot(3,1,2);
      plot(sam./fs,newy,'k');
      xlabel('Time (s)');
      ylabel('Fitted Displacement');
      grid on;

      subplot(3,1,3);
      plot(sam./fs,y,'k',sam./fs,newy,'r');
      xlabel('Time (s)');
      ylabel('Comparison');
```

```
    grid on;
% End routine
```

A3.6 Raw Displacement Output

The following Figures (A3.1) – (A3.18) correspond to the measured data referred to in Table (4.1):

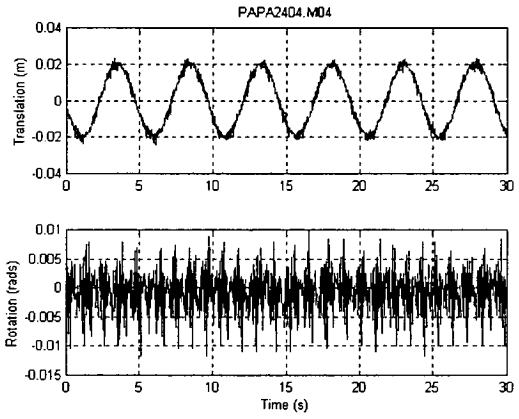

Figure A3.1 PAPA2404.M04

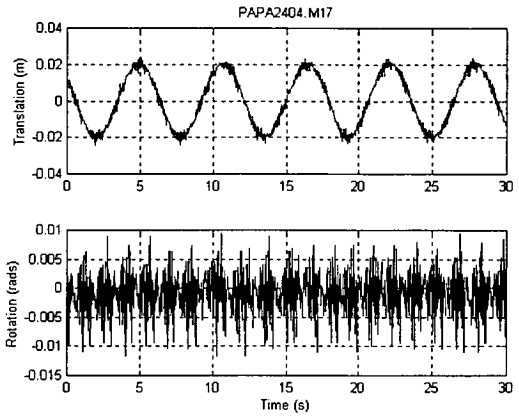

Figure A3.2 PAPA2404.M17

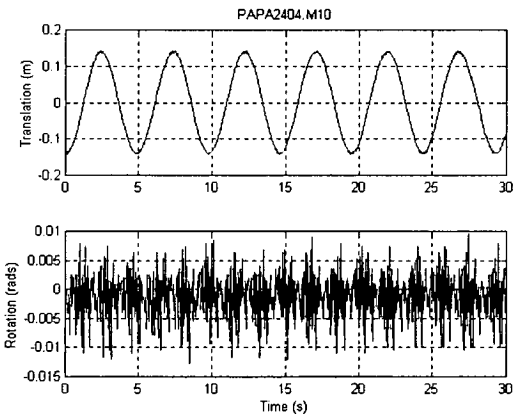

Figure A3.3 PAPA2404.M10

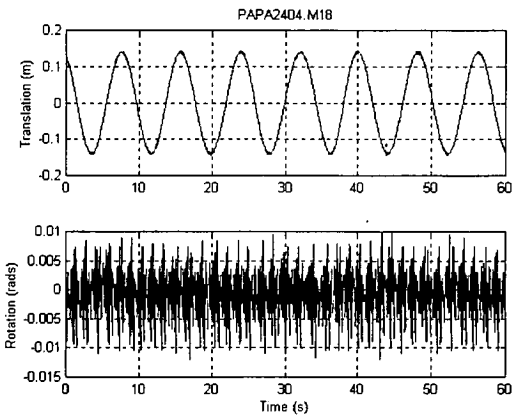

Figure A3.4 PAPA2404.M18

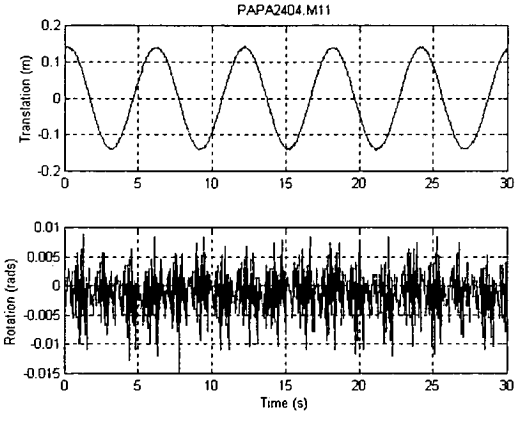

Figure A3.5 PAPA2404.M11

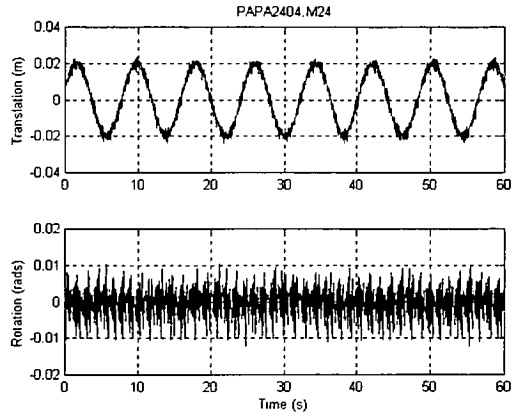

Figure A3.6 PAPA2404.M24

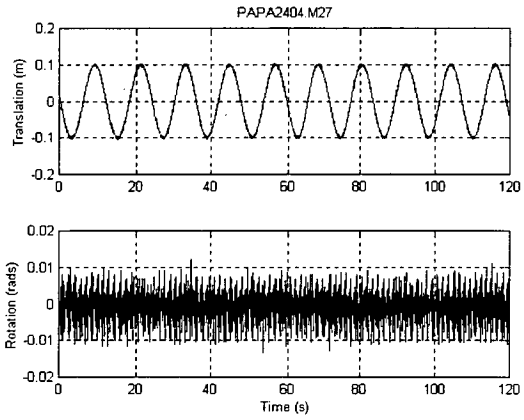

Figure A3.7 PAPA2404.M27

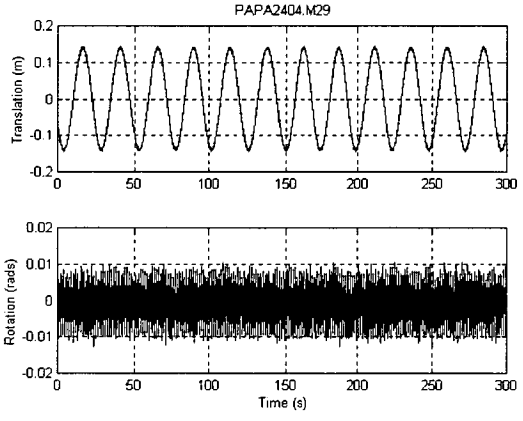

Figure A3.9 PAPA2404.M29

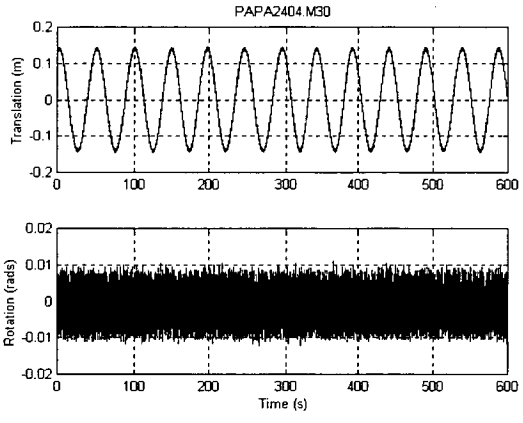

Figure A3.11 PAPA2404.M30

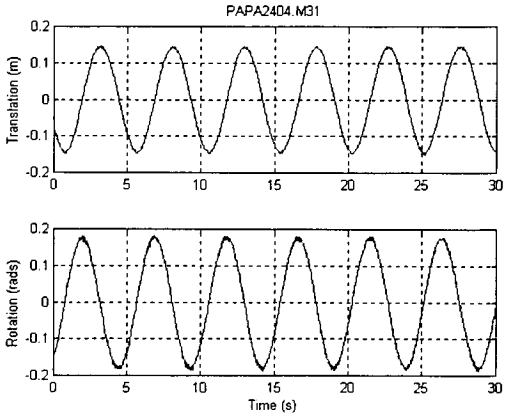

Figure A3.8 PAPA2404.M31

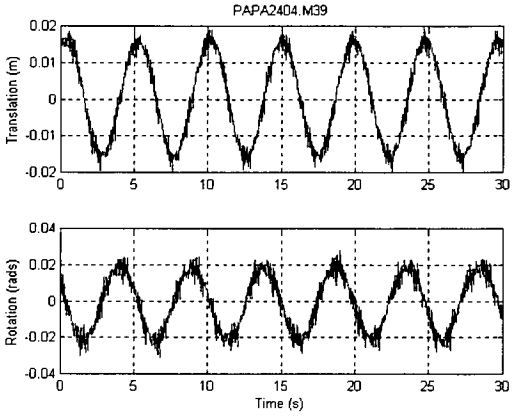

Figure A3.10 PAPA2404.M39

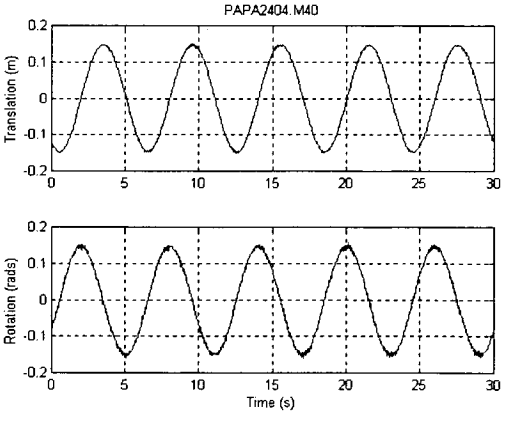

Figure A3.12 PAPA2404.M40

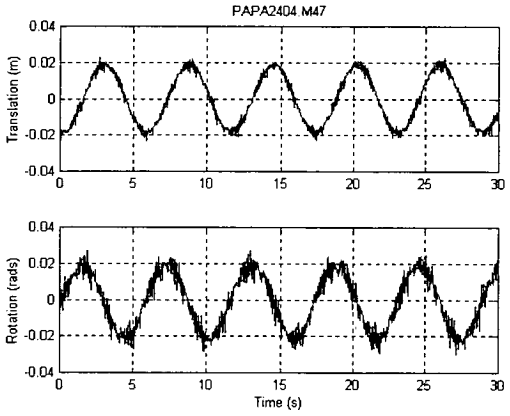

Figure A3.13 PAPA2404.M47

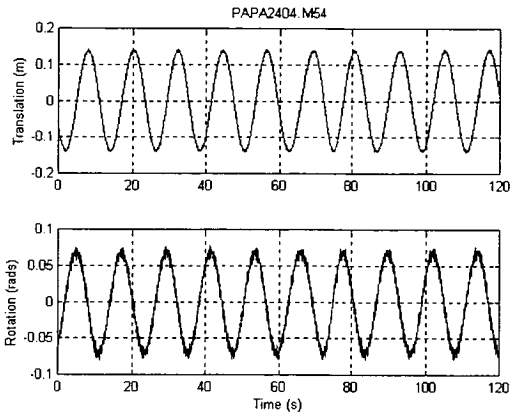

Figure A3.14 PAPA2404.M54

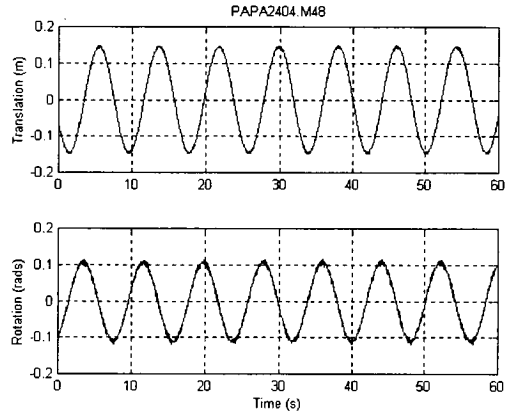

Figure A3.15 PAPA2404.M48

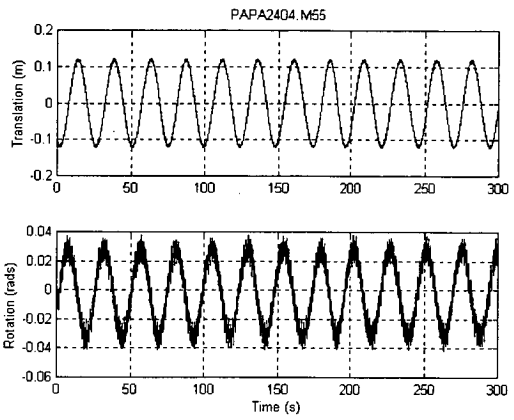

Figure A3.16 PAPA2404.M55

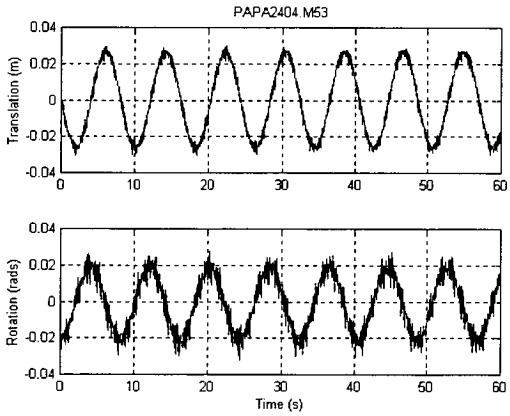

Figure A3.17 PAPA2404.M53

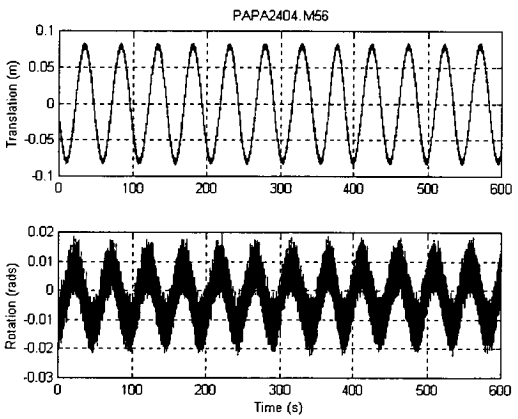

Figure A3.18 PAPA2404.M56

A3.7 Software Listing - ROTATION_MOTION.M

```
% ========================================
%  rotation_motion.m
%  Brendon Anderson
%  1998
%  Function calculates the number of motor
%  steps required to generate rotation
% ========================================

a=462.50;
b=300.00;
L0=352.00;
L1=5.08;
G=1.92;
S=8000;

num_elems=1000;
psi_range=30*pi/180; %Angle in radians
psi_initial=-15*pi/180; %Angle in radians
psi_inc=psi_range/num_elems;

alpha=acos((a^2+b^2-L0^2)/(2*a*b)); %Angle in radians

for i=1:num_elems,

   psi(i)=psi_initial+(i-1)*psi_inc;
   L(i)=sqrt(a^2+b^2-2*a*b*cos(psi(i)+alpha));
   n(i)=S*(L(i)-L0)/(G*L1)/10000;
   n2(i)=S*b*psi(i)/(G*L1)/10000;
   errorn(i)=(n2(i)-n(i))/n(i)*100;

end;


plot(psi,n,'k');
grid on;
```

```
xlabel('Rotation Angle (rads)');
ylabel('Step Number (x10^4)');

figure;
plot(psi,errorn,'k');
grid on;
xlabel('Rotation Angle (rads)');
ylabel('Relative Angle Error %');
% End function
```

A3.8 Fitted Displacement Data

The following Figures (A3.19) – (A3.36) correspond to the data files referred to in Table (4.1). The figures show the regenerated displacement using the software 'motion_analysis.m'.

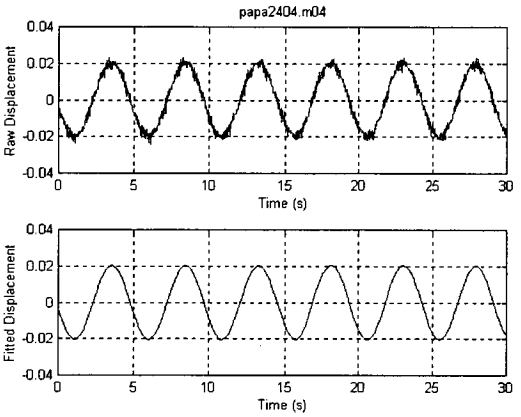

Figure A3.19 PAPA2404.M04

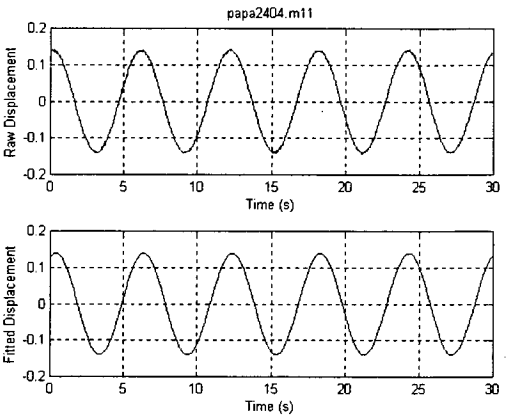

Figure A320 PAPA2404.M11

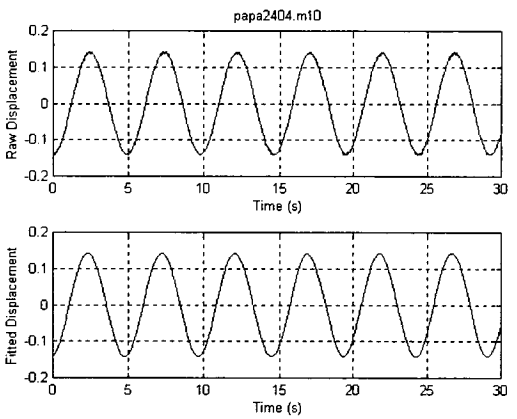

Figure A3.21 PAPA2404.M10

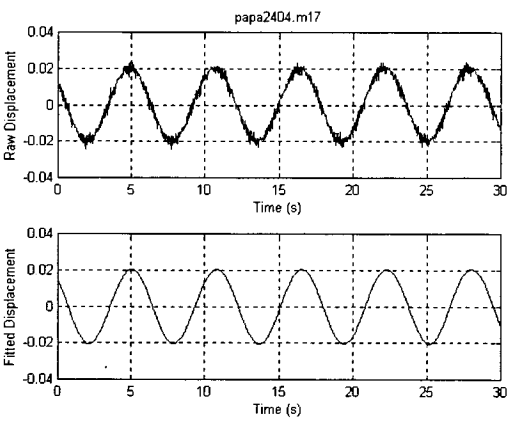

Figure A3.22 PAPA2404.M17

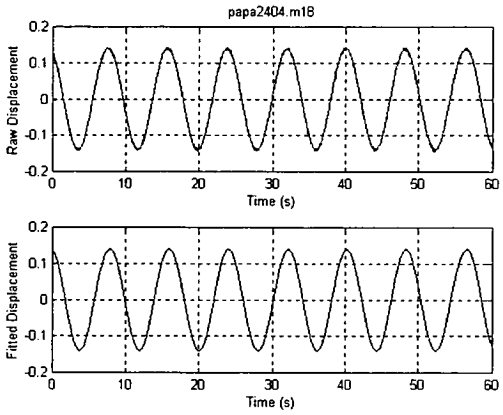

Figure A3.23 PAPA2404.M18

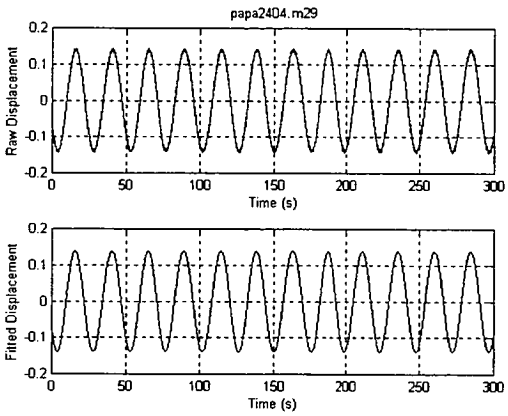

Figure A3.24 PAPA2404.M29

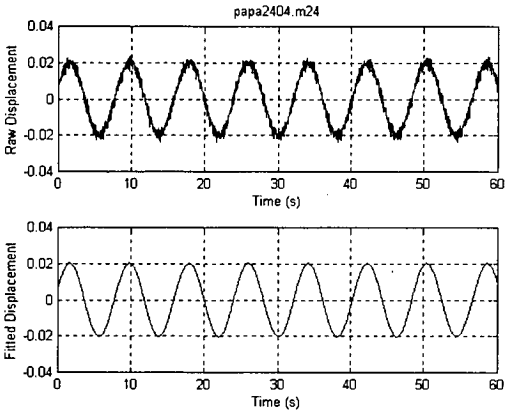

Figure A3.25 PAPA2404.M24

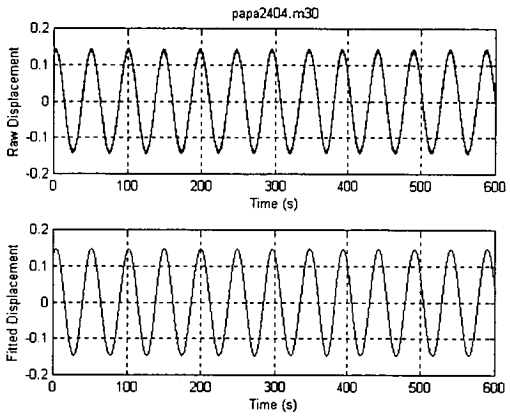

Figure A3.26 PAPA2404.M30

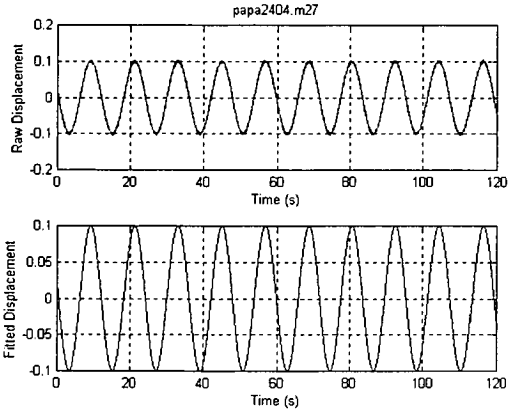

Figure A3.27 PAPA2404.M27

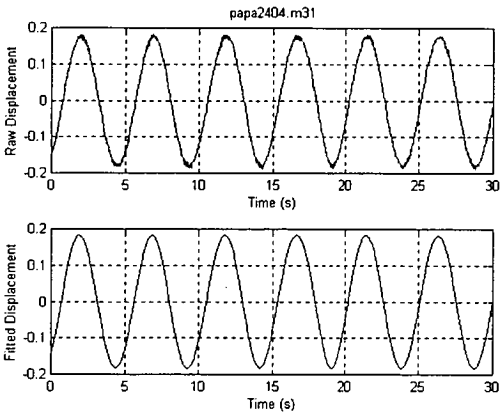

Figure A3.28 PAPA2404.M31

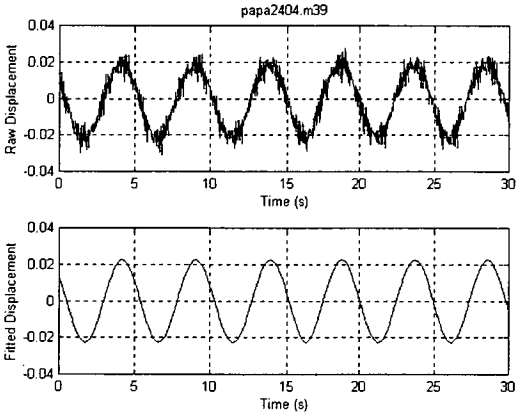

Figure A3.29 PAPA2404.M39

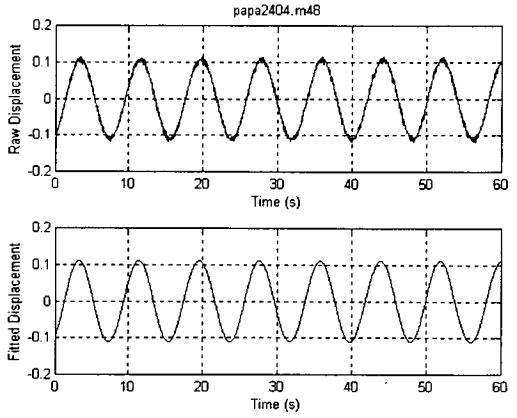

Figure A3.30 PAPA2404.M48

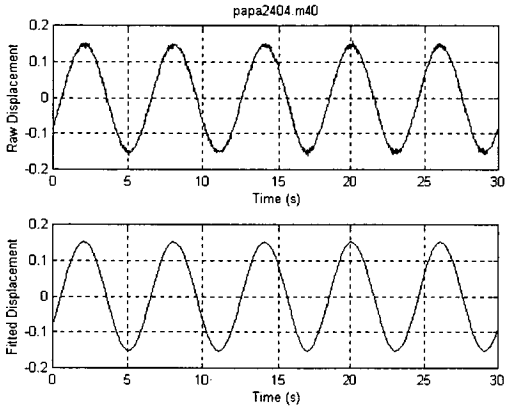

Figure A3.31 PAPA2404.M40

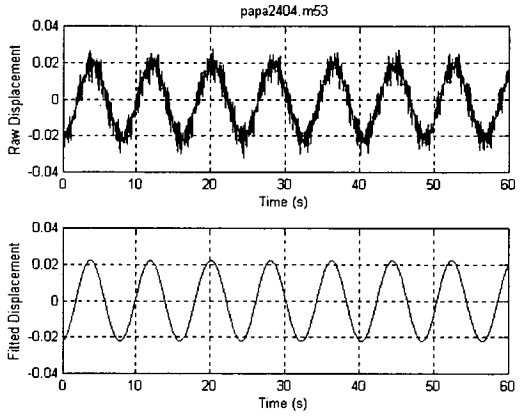

Figure A3.32 PAPA2404.M53

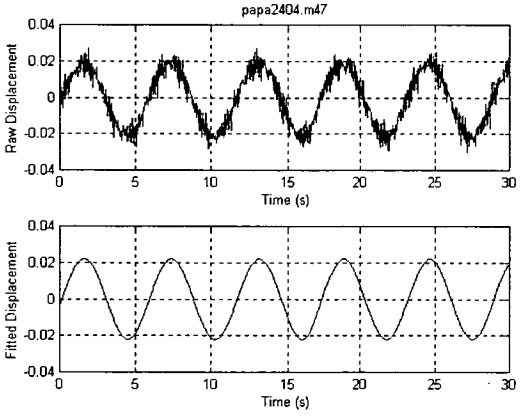

Figure A3.33 PAPA2404.M47

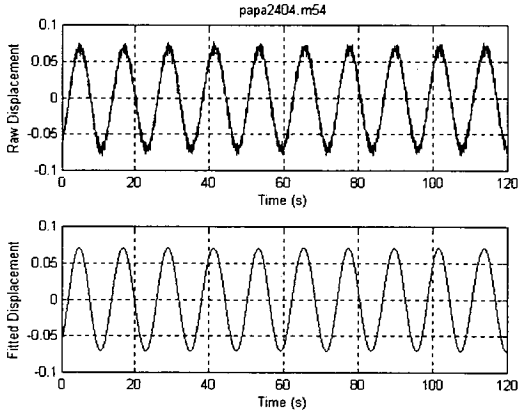

Figure A3.34 PAPA2404.M54

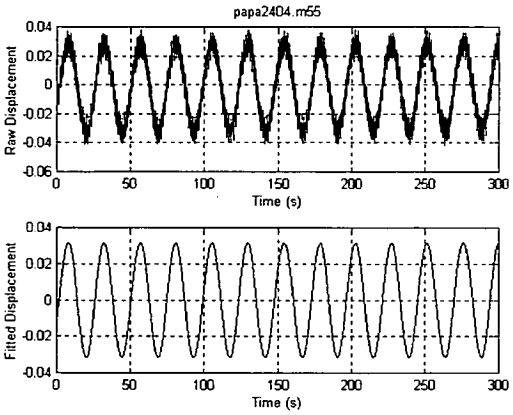

Figure A3.35 PAPA2404.M55

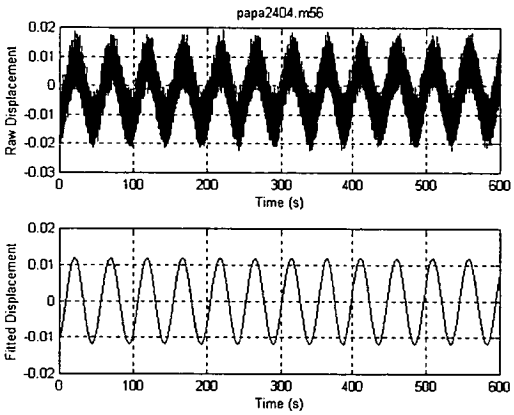

Figure A3.36 PAPA2404.M56

Appendix 4.

4.1 Sample Experimental Program for 1/3rd PAP104 Model

The following experimental test program is designed specifically for the Australian Maritime Engineering Cooperative Research Centre's (AMECRC) Planar Motion Mechanism (PMM) to be used in the Australian Maritime College's (AMC) Circulating Water Channel (CWC) Beauty Point Tasmania.

Equipment:

Facility:	AMC's CWC
Apparatus:	DSTO/AME CRC's PMM
	PMM Motion Control console
	Strut/Sting mounting arrangement
	250lb/500lb load cell
	Load cell calibrator
Data Acquisition:	PMM Data acquisition console
	105Mb Syquest Disk/1.44Mb Floppy Disks
Model:	Weight less than 50kg in air
	Internal bracket to suit sting/strut
	Bracket to allow model to be mounted on its side
	Ballasted to be approximately neutrally buoyant in water
Flow Measurement:	8mm diameter pitot static tube
	Differential Pressure Cell (DPC)
	DPC Signal Conditioner
	Plastic tubing & connectors
	Streamlined mount for pitot tube

Procedure:

1. Setup PMM on CWC carriage, including both the data acquisition and motion control consoles. Refer to the AMECRC PMM user's manual for installation instruction.

2. Select the load cell to be used for the tests; base the selection on the estimate of the forces expected on the submerged model. Note the 250lb load cell was selected for the testing described in this thesis. Mount the load cell to the sting/strut and connect electrical wiring. See AMECRC PMM user's manual for wiring diagrams.

3. Setup the flow measurement device. Connect the pitot tube to the DPC via the tubing and lower the pitot into the water in its streamlined mount. Bleed the system, removing all air bubbles. Connect the DPC signal conditioner and power it up. Prior to tests the readout will require taring to remove the baseline offset from measurements. Connect the DPC signal conditioner to the PMM data acquisition console.

4. Move the carriage to position 'F' marked on the CWC wall. The flow profile of the CWC has been measured at this point for various reference velocities.

5. Set the pitot tube 1.5m from the window side wall at depth of 1.2m from tank floor.

6. Select the model orientation and mount it to the PMM sting/strut.

7. Perform the experimental tests according to the specifications for the motions. Refer to the AMECRC PMM user's manual for specific instructions relating to the operation of the PMM.

The following table specifies the test program for a series of PMM tests using the sting mounting arrangement and the PAP104 1/3rd scale model:

(I) INERTIA TESTS:

The following tests are required to determine the centre of gravity and buoyancy of the test model, and the moment of inertia about the vertical axis around the load cell origin. These values are important for the analysis of the static and dynamic test data. Also, they establish a baseline from which the force and moment measurements are determined. The tests require the model to be mounted to the strut or sting while load cell measurements are recorded. 30 seconds is adequate for these tests.

Note that the tests may be performed before, or after the remaining tests. However, if they are performed before the static and dynamic tests are conducted, then it is important that the load cell balances are not changed once test one is done. If they are changed the baseline offsets for the tests will be changed, significantly affecting the results.

Test	Ballasted Model	Fluid		PMM Motion		
	Mounted	Type	Speed	Description	Frequency	Amplitude
1	no	Air	0	none	n/a	n/a
2	yes	Air	0	none	n/a	n/a
3	yes	Air	0	rotation	0.20(Hz)	0.25(rad)
4	yes	Water	0	none	n/a	n/a

Table A.4.1 Inertia test program

(II) STATIC

The following static yaw tests are an example of the type of program which might be undertaken for a particular body. The yaw angle presently ranges between -45 and 45 degrees. The angle is set manually using a calibrated plate to visually determine the angle. Larger static angles can be tested once the plate is calibrated further.

Flow Speed: 1.0m/s
CWC Pump Motor Demand: 50.1%
Pump Ratios: 0.95:1.24:1.01:1.16
Duration: 30 seconds

Test	Yaw (deg)	Test	Yaw (deg)	Test	Yaw (deg)
5	-45	10	-5	15	20
6	-30	11	0	16	30
7	-20	12	5	17	45
8	-15	13	10		
9	-10	14	15		

Table A.4.2 Test Program: Static Yaw

(III) DYNAMIC

The following table is an example program for testing a model in both the dynamic motions pure sway and pure yaw.

Flow Speed: 1.0m/s

CWC Pump Motor Demand: 50.1%

Pump Ratios: 0.95:1.24:1.01:1.16

The test program as outlined in Tables A.4.1-A.4.3 are all repeated when the model is tested on its side. The motions then become static pitch, dynamic pure heave and pure pitch with respect to the model. The duration of the tests depends on how many cycles of motion are required for the analysis.

Pure Sway				Pure Yaw			
Test	Freq. (Hz)	Amp. (m)	Dur. (s)	Test.	Freq. (Hz)	Amp. (rad)	Dur. (s)
18	0.20	0.02	30	45	0.20	0.18	30
19	0.20	0.04	30	46	0.20	0.16	30
20	0.20	0.06	30	47	0.20	0.14	30
21	0.20	0.08	30	48	0.20	0.12	30
22	0.20	0.10	30	49	0.20	0.10	30
23	0.20	0.12	30	50	0.20	0.08	30
24	0.20	0.14	30	51	0.20	0.06	30
25	0.16	0.02	30	52	0.20	0.04	30
26	0.16	0.04	30	53	0.20	0.02	30
27	0.16	0.06	30	54	0.16	0.15	30
28	0.16	0.08	30	55	0.16	0.14	30
29	0.16	0.10	30	56	0.16	0.12	30
30	0.16	0.12	30	57	0.16	0.10	30
31	0.16	0.14	30	58	0.16	0.08	30
32	0.12	0.02	60	59	0.16	0.06	30
33	0.12	0.04	60	60	0.16	0.04	30
34	0.12	0.06	60	61	0.16	0.02	30
35	0.12	0.08	60	62	0.12	0.11	60
36	0.12	0.10	60	63	0.12	0.10	60
37	0.12	0.12	60	64	0.12	0.08	60
38	0.12	0.14	60	65	0.12	0.06	60
39	0.08	0.14	120	66	0.12	0.04	60
40	0.08	0.12	120	67	0.12	0.02	60
41	0.08	0.10	120	68	0.08	0.07	120
42	0.08	0.06	120	69	0.04	0.03	300
43	0.04	0.14	300	70	0.02	0.01	600
44	0.02	0.14	600				

Table A.5.3 Pure Sway and Pure Yaw Test Program

4.2 Model Dimension Algorithm – Boundary.m

```
%=====================================================
% Function Name:  Boundary.m
% Author:         B. Anderson
% Date:           1998
% Description:      Determine model size limits due to
%                 boundaries.
%=====================================================

delta_y=0.3;
theta=pi/12;
delta_y2=0.0;
theta2=pi/4;

L=0;
AR=0;
x=0;
y=0;
i=0;

for AR =0.10:0.1:150,
   i=i+1;
   L=(1-delta_y)/(sin(atan(1/AR)+theta));
   x(i)=AR;
   y(i)=L;
end;

i=0;

for AR =0.10:0.1:150,
   i=i+1;
   L=(1-delta_y2)/(sin(atan(1/AR)+theta2));
   x2(i)=AR;
   y2(i)=L;
end;
```

```
for i=1:length(y),
   if (y(i)>y2(i))&(y2(i)<=1.5),
      y(i)=y2(i);
   elseif (y(i)>y2(i))&(y2(i)>1.5),
      y(i)=1.5;
   elseif (y(i)<=y2(i))&(y(i)>1.5),
      y(i)=1.5;
   end;
end;


semilogx(x,y,'k');
xlabel('Model Aspect Ratio');
ylabel('Maximum Model Length (m)');
grid on;
```

4.3 Inertia Analysis Software – Inertia.m

```
%============================================================
%
%     Function: Inertia.m
%     Description: Calculate the COG COB W and G
%     Author: Brendon Anderson
%     Date: 2/5/96
%
%============================================================

     clc;
     fprintf(1,'%s\n\n','INERTIAL TEST ANALYSIS');
     rep=input('Is the model mounted Upright or on its Side
[U/S] ? ','s');

     if rep=='U',
         FZVec=4;
         MYVec=5;
     else
         FZVec=2;
         MYVec=7;
     end;

     MXVec=6;

     fprintf(1,'\n%s\n','Enter the filenames for the data
acquired in the following tests:');

     fname=input('In air; no model; no motion ? ','s');
     hr;
     P3=mean(A(:,FZVec));
     P4=mean(A(:,MXVec));
     P5=mean(A(:,MYVec));
     if rep=='S',
        P5=-P5;
     end;
```

```
      fname=input('In air; ballasted model; no motion ? ','s');
      hr;
      Q3=mean(A(:,FZVec));
      Q4=mean(A(:,MXVec));
      Q5=mean(A(:,MYVec));
      if rep=='S',
         Q5=-Q5;
      end;

   % Calculate the weight of the ballasted model in air
      W=Q3-P3;

   % Calculate the COG position
      YG=(Q4-P4)/W;
      XG=-(Q5-P5)/W;

      fname=input('In water; ballasted model; no motion ?
','s');
      hr;

      R3=mean(A(:,FZVec));
      R4=mean(A(:,MXVec));
      R5=mean(A(:,MYVec));
      if rep=='S',
         R5=-R5;
      end;

   % Calculate the buoyancy of the ballasted model
   % B is the magnitude of the buoyancy force
      B=-(R3-Q3);

   % Calculate the COB position
      YB=-(R4-Q4)/B;
      XB=(R5-Q5)/B;

      %if rep=='S',
      %   posB='ZB';
      %   posG='ZG';
```

```
      %else
      %   posB='YB';
      %   posG='YG';
      %end;

      fprintf(1,'\n%s\n','The following are relative to the PMM
axes:');
      fprintf(1,'\n\n%s%f7.4%s\n  ','Weight    ',W,'N');
      fprintf(1,'%s%f7.4%s\n  ','XG        ',XG,'m');
      fprintf(1,'%s%f7.4%s\n','YG        ',YG,'m');
      fprintf(1,'\n%s%f7.4%s\n  ','Buoyancy  ',-B,'N');
      fprintf(1,'%s%f7.4%s\n  ','XB        ',XB,'m');
      fprintf(1,'%s%f7.4%s\n','YB        ',YB,'m');


%=================================================================
```

4.4 Moment of Inertia Analysis Software- Rotan.m

```
%============================================================
%===        Name:       rotan.m
%===        Author:     Brendon Anderson
%===        Created:    11/1/96
%===        Description:     Analysis of pure yaw motion
%===        Modified:   30/4/96
%============================================================

      clc;

      fprintf(1,'\n\n\n\n\n%s\n\n','            DYNAMIC ROTATION
ANALYSIS');
      fprintf(1,'%s\n\n','          In Air Moment of Inertia
Test');

      fname=input('          Enter the filename to be Analysed:
','s');
      fprintf(1,'\n\n\n\n');

  % Load in the data file and read in the relevant force to be
analysed

      hr;
      s=size(A,1);
      r=A(:,12)-mean(A(:,12));

      R=A(:,5);


   % Define sample frequency
      fs=30.0003;

   % Define density of the water
      rho=1000;
```

```
% Define the length of the vehicle
   l=0.9;

% Define the amplitude of the motion
         amp=0.25;

%
% Determine motion frequency
% --------------------------
%
% Step 1. Perform fft with n=1024 points;
%       Note if s>n then increase the size of n by powers of
2
   n=2^(15);

% Step 2. Find the autocorrelation of Yf
   rf=fft(r,n);
   Srr=rf.*conj(rf)/n;

% Step 3. Determine the peak magnitude
   maxSrr=max(Srr);

% Step 4. Determine the sample at which the peak value occurs
   peakSam=find(Srr==maxSrr);

% Step 5. Determine the frequency from the sample
   fr=(peakSam(1)-1)/n*fs;
   Freq=fr;
   wr=2*pi*fr;

%
% Determine the time delay between the measured and analytic
motion
% ------------------------------------------------------------
------
%
   t=[0:1/fs:1/fr]';
   tl=length(t)-1;
   r2=amp*sin(wr*t(1:tl));
```

```
   Rrr=xcorr(r(1:tl),r2);
   maxRrr=max(Rrr);
   tsam=find(Rrr==maxRrr);
   td=(tsam(1)-1)/fs;


%
% Define the pure yaw motion vectors
% ----------------------------------
%
   t=[0:1/fs:(s-1)/fs]';
   r=amp*sin(wr*(t+td));
   velR=amp*wr*cos(wr*(t+td));
   accR=-amp*wr^2*sin(wr*(t+td));



%
% Define the input vectors (model) for the regression
algorithm
%
   In1=accR;

%
% Perform the regression
%
   z=[R In1];
   th=arx(z,[0 1 0]);
   present(th);


   rfit=th(3,1)*In1;

% Define plotting Vectors
   num=round(fs/fr);
   Time=t(1:num);
   Fit=rfit(1:num);
   Meas=R(1:num);
   plot(Time,Meas,'w',Time,Fit,'w')
```

```
%
%=====================================================
%===              End of RotAn.m
%=====================================================
```

Appendix 5.

A5.1 Software Listing: XVEHICLE.M

```
%=============================================================
%=== Name: xvehicle.m
%=== Description: Parent program used to analyse vehicle model
%===
%=============================================================

% Declare the global variables
   global sampl_freq rho model_ln flow_vel flpth flbs resbs ...
      resfl zfl file_vect driftangle notstr motiontype;

% Define the experimental test parameters:
% ========================================
% 1. Define sample frequency
   sampl_freq = 30.0003;

% 2. Define density of the water
   rho = 1000;

% 3. Define the length of the vehicle
   model_ln = 0.90;

% 4. Define the flow velocity
   flow_vel = 1.0;

% 5. Define the file path
   flpth='d:\pmm0496\';

% 6. Define the filename base
   flbs='papa2404';
   resbs='test';
   resfl = [flpth, resbs, '.res'];
```

```
% 7. Define zerofile and file vector
   zfl = 3;
   file_vect = [4:4];

% 8. Add comment to result file
   notstr = 'Analysis of papa2404.004 to 030 - flow velocity
1.0m/s - Pure sway';

% 9. Select analysis program and motion type
%  motiontype = 0; %for static drift angle
   motiontype = 1;  %for pure sway
%  motiontype = 2;  %for pure yaw

% 10. Set mean rotation vector in degrees
% Drift angles are in degrees
%driftangle = [45 40 35 30 25 20 15 10 5 0 -5 -10 -15 -20];

   Anal_vect = [2];
   imp_filt = 0;
   Av_lngth = length(Anal_vect);
   Fv_lngth = length(file_vect);%file vector length
   zero_mean = [];
   zero_std = [];

   if motiontype == 0
      xstatic;
   else
      xdynamic;
   end;

%  end program
```

A5.2 Software Listing: XDYNAMIC.M

```
% ========================================================
% === Function name:   xdynamic.m
%===  Previous name:   SysId.m
% === Purpose:    Pmm data analysis routine
% === Based on the systems identidication method
% === For determining an arbitrary model.
% ========================================================

% This routine is called by xvehicle to determine dynamic
maneouvring co-efficients
%  for pure sway and pure yaw experiments.  Fourier analysis is
used to determine the
%  principle frequency of the motion vector (which is the
translation or rotation
%  trace against time for sway and yaw respectively).  The time
delay to the first cycle
%  of the motion vector is then calculated and use to calculated
velocity vectors in the
%  x and y directions, accelerated in y, and the angular and the
absolute velocity of
%  the model.  The velocities, accelerations and force vectors
are all non-dimensionalised
%  and scaled using absolute model velocity, which in this case
is a function of time.
%  Maneouvring co-efficients are determined using the arx model
and are currently use
%  (v', u^2, uv) for asymmetric functions (Fy, Mx, Mz) and (v',
u^2, v^2) for symmetric
%  functions (Fx, Fz, My).
%
%  This routine draws flpth, flbs, zfl, Anal_vect, AV_lngth,
resfl, file_vect,
%  Fv_lngth, motiontype, sampl_freq, amp_vect, flow_vel,
model_ln, fil_freq and rot_amp
%  from the parent program xvehicle
```

```
%============================%
%  Initialise local varibles  %
%============================%
   resmat = []; coefmat = []; scalef = [];scalem = [];
   fname = []; rawdata = []; raw_ln = 0; cyc = [];
   zero_mean = []; zero_std = []; datarow = 0; datacol = 0;
   title = 0; zv_cnt = 0; prnt_cnt = 0; file_cnt = 0; coefcnt =
0;
   scalecnt = 0; motion_v = []; mv_ideal = []; fourier_mv = [];
   freq_mv = []; maxfreq = 0;maxposfq = [];freq_prin = 0; wt =
0;
   Vo=[]; Ao=[];t = [];t1 = [];Ryy = [];maxRyy = [];tsam = 0;
   timedel = 0;velx = [];vely = [];accy = [];absvel = [];r = [];
   velxn = [];velyn = [];accyn = [];In1 = [];In2 = [];In3 = [];
   In4 = [];In5 = [];z = [];th = []; analysis_model=[];

%====================%
%  Analyse zero file  %
%====================%

   fname = xfilenm(flpth,flbs,zfl);
   fid1 = fopen(fname,'r');
   xhr;
   cyc(zfl) = cycle;

   for zv_cnt = 1:Av_lngth,
      datarow = Anal_vect(zv_cnt);
      zero_mean(zv_cnt) = mean(rawdata(datarow,:));
      zero_std(zv_cnt) = std(rawdata(datarow,:));
   end;
   fclose(fid1);

%==================================%
%  Add Titles to the Results File  %
%==================================%

   fidw = fopen(resfl,'w');
```

```
   fprintf(fidw, '%s\n', notstr);
   fprintf(fidw, '%s', 'File Motion Vo Ao Freq Amp ');
   for prnt_cnt = 1:Av_lngth
      title = Anal_vect(prnt_cnt);
      if title == 2,   fprintf(fidw, '%s', 'Yc1 sYc1 Yc2 sYc2 Yc3
sYc3 Yc4 sYc4 Yc5 sYc5 Yerr ');end;
      if title == 3,   fprintf(fidw, '%s', 'Xc1 sXc1 Xc2 sXc2 Xc3
sXc3 Xc4 sXc4 Xc5 sXc5 Xerr ');end;
      if title == 4,   fprintf(fidw, '%s', 'Zc1 sZc1 Zc2 sZc2 Zc3
sZc3 Zc4 sZc4 Zc5 sZc5 Zerr ');end;
      if title == 5,   fprintf(fidw, '%s', 'Mc1 sMc1 Mc2 sMc2 Mc3
sMc3 Mc4 sMc4 Mc5 sMc5 Merr ');end;
      if title == 6,   fprintf(fidw, '%s', 'Kc1 sKc1 Kc2 sKc2 Kc3
sKc3 Kc4 sKc4 Kc5 sKc5 Kerr ');end;
      if title == 7,   fprintf(fidw, '%s', 'Nc1 sNc1 Nc2 sNc2 Nc3
sNc3 Nc4 sNc4 Nc5 sNc5 Nerr ');end;
   end;

   fprintf(fidw, '%s\n', 'cycle ');

%============================%
%  Principle Data Analysis  %
%============================%

   for file_cnt = 1:Fv_lngth, %this loop contains most of the
program
      fname = xfilenm(flpth,flbs,file_vect(file_cnt));
      fid1 = fopen(fname,'r');
      xhr;
      cyc(file_cnt) = cycle;

      file_vect(file_cnt)%used as a visual progress reporter
      rawdata = rawdata';
      raw_ln = size(rawdata,1);
      resmat = rawdata;

      if motiontype == 1,
```

```
        motion_v = rawdata(:,11)./100;   %motion vector -
translation vector in pure sway
      elseif motiontype == 2,     % or rotation vector if pure
yaw
        motion_v = rawdata(:,12);
      end;

% Remove zero file

      for rv_cnt = 1:Av_lngth,
        datacol = Anal_vect(rv_cnt);
        resmat(:,datacol) = (rawdata(:,datacol) -
zero_mean(rv_cnt) * ones(raw_ln,1));
      end;

%==============================
% Determine the motion amplitude
%==============================
      [filt_motion_v,b]=bfilt(motion_v,0.3);
      amplitude=max(abs(filt_motion_v));

%==============================%
%  Determine motion frequency  %
%==============================%

% Step 1. Perform fft with n points;
%     Note if s>n then increase the size of n by powers of 2

      n = 2^(17);

% Step 2. Find the power spectrum magnitudes

      %motion_v = motion_v - mean(motion_v);
      fourier_mv = fft(motion_v,n);
      freq_mv = fourier_mv .* conj(fourier_mv) / n;

% Step 3. Determine the peak magnitude

      maxfreq = max(freq_mv);
```

```
% Step 4. Determine the sample at which the peak value occurs

      maxposfq = find(freq_mv == maxfreq);

% Step 5. Determine the frequency from the sample

      freq_prin = (maxposfq(1) - 1) / n * sampl_freq;
      wt = 2 * pi * freq_prin;

      Vo = [Vo amplitude*freq_prin*(2*pi/flow_vel)];
      Ao = [Ao amplitude*((freq_prin*(2*pi))^2)/(flow_vel^2)];

%=========================================%
%  Determine the time delay between       %
%  the measured and ideal motion vectors  %
%=========================================%

      t = [0 : 1/sampl_freq : 1/freq_prin]';
      tl = length(t) - 1;

      mv_ideal = amplitude*sin(wt*t);

      Ryy = xcorr(motion_v(1:tl),mv_ideal(1:tl));
      maxRyy = max(Ryy);
      tsam = find(Ryy == maxRyy);
      timedel = (tsam(1) - 1) / sampl_freq;

%=========================================================%
%  Determine velocity and accelerations for regression  %
%=========================================================%

      t = [0 : 1/sampl_freq : (raw_ln-1)/sampl_freq]';

      if motiontype == 1,
         velx = flow_vel * ones(raw_ln,1);
         vely = amplitude * wt * cos(wt*(t+timedel));
         accy = -amplitude * wt^2 * sin(wt*(t+timedel));
         absvel = sqrt(velx.^2+vely.^2);
```

```
      elseif motiontype == 2,
         r = amplitude * sin(wt*(t+timedel));
         vely = amplitude * wt * cos(wt*(t+timedel));
         accy= -amplitude * wt^2 * sin(wt*(t+timedel));
         velx = sqrt(flow_vel^2 * (ones(length(t),1) +
tan(r).*tan(r)));
         absvel = velx;
      end;


%=============================================================%
% Nondimensionalise the force, velocities and accelerations  %
%=============================================================%
% Note the output coefficients are nondimensional

      scalef = (0.5 * rho * model_ln^2 .* absvel.^2);
      scalem = (0.5 * rho * model_ln^3 .* absvel.^2);

      for scalecnt = 1:Av_lngth
         datacol = Anal_vect(scalecnt);
         if datacol <= 4,
            resmat(:,datacol) = resmat(:,datacol) ./ scalef;
         else
            resmat(:,datacol) = resmat(:,datacol) ./ scalem;
         end;
      end;

      velxn = velx./absvel;

      if motiontype==1,
         velyn = vely./absvel;
         accyn = model_ln * accy ./ absvel.^2;
      elseif motiontype==2,
         velyn = model_ln * vely ./ absvel;
         accyn = model_ln^2 * accy ./ absvel.^2;
      end;

%======================%
%  Regression Analysis  %
```

```
%=======================%
      num_inputs=5;

      In1 = accyn;
      In2 = velxn.^2;
      In3 = velyn.^2;
      In4 = velxn .* velyn;
      In5 = velyn .* abs(velyn);

      if motiontype==1
         if datacol==3 | datacol==4 | datacol==5
               analysis_model=[1 1 1 0 0];
         else
               analysis_model=[1 1 0 1 0];
         end;
      elseif motiontype==2
         if datacol==3 | datacol==4 | datacol==5
            analysis_model=[1 1 1 0 0];
         else
            analysis_model=[1 1 0 1 0];
         end;
      end;

%
% Analyse the output
%
      for i=1:num_inputs,
          c(i)=analysis_model(i);
       end;

      first_entry=find(analysis_model);
      for i=1:num_inputs,
         if i<=first_entry(1) d(i)=1;
            else d(i)=d(i-1)+analysis_model(i);
         end;
      end;


       for coefcnt = 1:Av_lngth
```

```
        datacol = Anal_vect(coefcnt);
        z = [resmat(:,datacol) In1 In2 In3 In4 In5];

         th = arx(z,[0 analysis_model 0 0 0 0 0]);

         coefmat(coefcnt,1) = c(1)*th(3,d(1));
        coefmat(coefcnt,2) = sqrt(c(1)*th(3+d(1),d(1)));
        coefmat(coefcnt,3) = c(2)*th(3,d(2));
        coefmat(coefcnt,4) = sqrt(c(2)*th(3+d(2),d(2)));
        coefmat(coefcnt,5) = c(3)*th(3,d(3));
         coefmat(coefcnt,6) = sqrt(c(3)*th(3+d(3),d(3)));
         coefmat(coefcnt,7) = c(4)*th(3,d(4));
        coefmat(coefcnt,8) = sqrt(c(4)*th(3+d(4),d(4)));
        coefmat(coefcnt,9) = c(5)*th(3,d(5));
        coefmat(coefcnt,10) = sqrt(c(5)*th(3+d(5),d(5)));
        coefmat(coefcnt,11) = th(1,d(1));

      end;

%  Note: the coefficient matrix is only set up at the moment to
%  handle three regression coefficents.  If more coefficients
are added
%  to the model then this will need to be reviewed.

%=========================%
%  Print Results to File  %
%=========================%

      fprintf(fidw, '%1.0f %s', file_vect(file_cnt),' ');
      if motiontype == 1
         fprintf(fidw, '%s', ' Sway ');
      else
         fprintf(fidw, '%s', ' PYaw ');
      end

      fprintf(fidw, '%7.4f %s', Vo(file_cnt), ' ');
      fprintf(fidw, '%7.4f %s', Ao(file_cnt), ' ');
      fprintf(fidw, '%7.4f %s', freq_prin, ' ');
      fprintf(fidw, '%7.4f %s', amplitude, ' ');
```

```
      for prnt_cnt = 1:Av_lngth
         fprintf(fidw, '%7.4f %s', coefmat(prnt_cnt,1), ' ');
         fprintf(fidw, '%7.4f %s', coefmat(prnt_cnt,2), ' ');
          fprintf(fidw, '%7.4f %s', coefmat(prnt_cnt,3), ' ');
         fprintf(fidw, '%7.4f %s', coefmat(prnt_cnt,4), ' ');
         fprintf(fidw, '%7.4f %s', coefmat(prnt_cnt,5), ' ');
          fprintf(fidw, '%7.4f %s', coefmat(prnt_cnt,6), ' ');
          fprintf(fidw, '%7.4f %s', coefmat(prnt_cnt,7), ' ');
         fprintf(fidw, '%7.4f %s', coefmat(prnt_cnt,8), ' ');
         fprintf(fidw, '%7.4f %s', coefmat(prnt_cnt,9), ' ');
         fprintf(fidw, '%7.4f %s', coefmat(prnt_cnt,10), ' ');
         fprintf(fidw, '%7.4f %s', coefmat(prnt_cnt,11), ' ');
      end;

       fprintf(fidw, '%7.4f %s\n', cyc(file_cnt),' ');
   end;


fclose(fidw);
cyc

%================================
% End Routine - xdynamic.m
%================================
```

A5.3 Software Listing: XFILENM.M

```
%=============================================================
%=== Name:    xfilenm.m
%=== Description:  Determine file ending
%=============================================================

%  xfilenm.m is designed specifically to generate a filename
%  from a file number.  The sub-routine uses global variables
%  'flnum', 'flpth', and 'flbs' to generate 'fname', which is
%  used by the parent program.
%
%  Variables used:
%  flnum - the file number defined in the parent program
%  flpth - file path name defined in the parent program
%  flbs -  file name base defined in the parent program
%  fname - complete file name

function fname = xfilenm(fpth,fbs,flnum)


if flnum <= 9,
   fname=[fpth,fbs,'.00', num2str(flnum)];
elseif flnum <= 99,
   fname=[fpth,fbs,'.0', num2str(flnum)];
else
   fname=[fpth,fbs,'.', num2str(flnum)];
end;

%  end routine
```

A5.4 Software Listing: XSTATIC.M

```
%============================================================
%=== Name: xstatic.m
%=== Description: Used to analyse static drift angle data
%============================================================

   %======================%
   %  Initialise Varibles  %
   %======================%


result_mean=[];  %results matrix - mean values
result_std=[];   %results matrix - standard deviations
coefmat=[];   %coefficient matrix
calcmat = [];

velxn=[]; velyn=[];      %non-dimension velocities in x and y
directions
scalef = (0.5 * rho * model_ln^2 * flow_vel^2);  %scale factor
for the forces
scalem = (0.5 * rho * model_ln^3 * flow_vel^2);  %scale factor
for moments

In1=[]; In2=[]; In3=[];  %used in regression function arx
In4=[]; In5=[];       %used in regression function arx
regvec1=[]; regvec2=[];     %regression vectors used to adjust
angular error
regcoeff = [];
angerr = 0;

file_cnt = 0; %counters
zv_cnt = 0;
rm_cnt = 0;
regcnt=1;
coefcnt = 0;
calcnt = 0;
```

```
cyc = [];  %records the number of poor entries in the raw data
datarow = 0;
datacol = 0;


   %====================%
   %  Analyse zero file  %
   %====================%

fname=xfilenm(flpth,flbs,zfl);
fid1=fopen(fname,'r');
xhr;
cyc(zfl) = cycle;

for zv_cnt = 1:Av_lngth,
   datarow = Anal_vect(zv_cnt);
   zero_mean(zv_cnt) = mean(rawdata(datarow,:));
   zero_std(zv_cnt) = std(rawdata(datarow,:));
end;
fclose(fid);


   %============================%
   %  Principle Data Analysis  %
   %============================%

for file_cnt = 1:Fv_lngth,
   fname = xfilenm(flpth,flbs,file_vect(file_cnt))
   fid1 = fopen(fname,'r');
   xhr;
   cyc(file_cnt) = cycle;

%  file_vect(file_cnt)%used as a visual progress reporter

   for rm_cnt = 1:Av_lngth,
      datarow = Anal_vect(rm_cnt);

      if datarow == 2 | datarow == 3 | datarow == 4
```

```
        result_mean(file_cnt,rm_cnt) = (mean(rawdata(datarow,:))
- zero_mean(rm_cnt)) ...
            / scalef;

      elseif datarow == 5 | datarow == 6 | datarow == 7,

        result_mean(file_cnt,rm_cnt) = (mean(rawdata(datarow,:))
- zero_mean(rm_cnt)) ...
            / scalem;
      else
        result_mean(file_cnt,rm_cnt) = (mean(rawdata(datarow,:))
- zero_mean(rm_cnt));
      end;

      result_std(file_cnt,rm_cnt) = std(rawdata(datarow,:));
   end;

   fclose(fid);
end;


   %============================%
   %  Determine Angular Offset  %
   %============================%

for file_cnt = 1:Fv_lngth,
   if abs(driftangle(file_cnt)) < 15,
      regvec1(regcnt) = driftangle(file_cnt);
      regvec2(regcnt) = result_mean(file_cnt,2);
      regcnt = regcnt + 1;
   end;
end;

regcoef = polyfit(regvec1, regvec2, 1);
angerr = -regcoef(2) / regcoef(1);
%driftangle = driftangle - angerr;  %VE
```

```
   %============================================================
=%
   %  Regression analysis to determine maneouvring coefficients
%
   %============================================================
=%

% Non-dimensional velocities in the x and y directions

velxn = cos(pi * driftangle / 180); %VE
velyn = -sin(pi * driftangle / 180);   %VE

% Define the input vectors model for the regression algorithm

In1 = velxn'.^2;    %VE
In2 = velyn'.*velxn';    %VE
In3 = velyn'.^2;    %VE
In4 = velyn'.*abs(velyn)'; %VE
In5 = velyn'.*velyn'.*velyn'; %VE

for coefcnt = 1:Av_lngth,
   datacol = Anal_vect(coefcnt);
   z = [result_mean(:,coefcnt) In1 In2 In3 In4 In5];%VE
   if datacol == 2 | datacol == 6 | datacol == 7,
      th = arx(z,[0 1 1 0 1 0 0 0 0 0 0]);
      coefmat(coefcnt,1) = th(3,1);
      coefmat(coefcnt,2) = th(3,2);
      coefmat(coefcnt,4) = th(3,3);
      coefmat(coefcnt,5) = sqrt(th(4,1));
      coefmat(coefcnt,6) = sqrt(th(5,2));
      coefmat(coefcnt,8) = sqrt(th(6,3));
   else
      th = arx(z,[0 1 1 1 0 0 0 0 0 0 0]);
      coefmat(coefcnt,1) = th(3,1);
      coefmat(coefcnt,2) = th(3,2);
      coefmat(coefcnt,3) = th(3,3);
      coefmat(coefcnt,5) = sqrt(th(4,1));
      coefmat(coefcnt,6) = sqrt(th(5,2));
      coefmat(coefcnt,7) = sqrt(th(6,3));
```

```
   end;
end;

   %================================%
   %  Calculate Forces and Moments  %
   %================================%

for calcnt = 1:Av_lngth,
   calcmat(:,calcnt) = In1.*coefmat(calcnt,1) +
In2.*coefmat(calcnt,2) + ...
      In3.*coefmat(calcnt,3) + In4.*coefmat(calcnt,4);
end;


   %=========================%
   %  Print Results to File  %
   %=========================%

fidw = fopen(resfl,'w');

%titles
fprintf(fidw, '%s\n', notstr);
fprintf(fidw, '%s', 'File_Number Rot Fy Fycalc Fx Fxcalc Fz
Fzcalc ');
fprintf(fidw, '%s', 'My Mycalc Mx Mxcalc Mz Mzcalc ');
fprintf(fidw, '%s', 'velxn velyn cycle ');
fprintf(fidw, '%s', 'Std_Fy Std_Fx Std_Fz ');
fprintf(fidw, '%s\n', 'Std_My Std_Mx Std_Mz');

%zero file
fprintf(fidw, '%1.0f %s %7.4f %s', zfl, ' N/A ', zero_mean(1), '
N/A ');
fprintf(fidw, '%7.4f %s %7.4f %s', zero_mean(2), ' N/A ',
zero_mean(3), ' N/A ');
fprintf(fidw, '%7.4f %s %7.4f %s', zero_mean(4), ' N/A ',
zero_mean(5), ' N/A ');
fprintf(fidw, '%7.4f %s %7.4f %s', zero_mean(6), ' N/A N/A N/A
', cyc(zfl), ' ');
```

```
fprintf(fidw, '%7.4f %s %7.4f %s %7.4f %s', zero_std(1), ' ',
zero_std(2),' ', zero_std(3), ' ');
fprintf(fidw, '%7.4f %s %7.4f %s %7.4f\n', zero_std(4), ' ',
zero_std(5), ' ', zero_std(6));

%main files
for file_cnt = 1:Fv_lngth,
   fprintf(fidw, '%1.0f %s', file_vect(file_cnt),' ');
   fprintf(fidw, '%7.4f %s', driftangle(file_cnt),' ');
   for datacol = 1:6,
      fprintf(fidw, '%7.4f %s', result_mean(file_cnt,datacol),'
');
      fprintf(fidw, '%7.4f %s', calcmat(file_cnt,datacol),' ');
      fprintf(fidw, '%7.4f %s', result_std(file_cnt,datacol),'
');
   end;
   fprintf(fidw, '%7.4f %s', velxn(file_cnt),'   ');
   fprintf(fidw, '%7.4f %s', velyn(file_cnt),'   ');
   fprintf(fidw, '%7.4f %s\n', cyc(file_cnt),' ');
end;

%coefficients
fprintf(fidw, '%s\n', ' c1   c2   c3  c4  c1err c2err c3err
c4err');
coefstr = ['Fy ' 'Fx ' 'Fz ' 'My ' 'Mx ' 'Mz '];
for coefcnt = 1:Av_lngth
   fprintf(fidw,'%s',coefstr(coefcnt*3-2:coefcnt*3));
   for coefcol = 1:8
      fprintf(fidw,'%7.4f %s',coefmat(coefcnt,coefcol),'  ');
   end;
   fprintf(fidw,'%s\n',' ');
end;

%angular offset
fprintf(fidw,'%s %7.4f\n','Angle_error ',angerr);

fclose(fidw);
```

A5.5 Software Listing: XHR.M

```
%============================================================
%=== Name:    xhr.m
%=== Description:  Removes header off PMM data files
%============================================================

%  xhr.m takes the global variable 'fname' from the parent
program
%  and produced a raw data matrix 'A' which is subsequently used
%  by the parent program.  A varible 'cycle', which represents
%  the number of corrupted lines in the raw data file, is also
%  generated.
%
%  xhr.m is designed specifically to remove the header from the
%  raw data files produced by the PMM Data Acquasition Software.
%  The subroutine was modified to check (and correct) the raw
%  data for errors.
%  Each string is read individually from the file fname until
%  'Rot' is found.  The raw data is saved immediately after the
%  string 'Rot'.  The data is read into 'tmpA' (a 12 x Inf
matrix)
%  and each column is check for errors and modified if
necessary.
%  Finally the raw data matrix 'A' is generated from 'tmpA'.

%  Variables used:
%  fname - file name, which contains the raw data, obtained
%     from parent program.
%  fstr -  used to read each string in turn at the beginning of
the
%     raw data file, until the string 'Rot' is identified.
%  check - loop variable to check each line of the raw data for
errors.
%  tmpA -  temporary raw data matrix
%  sizetmpA - size of the matrix tmpA.
```

```
%  cyclecnt - runnining count of the number of corrupted lines
in the
%        raw data file.
%  end_chk - boolean toggle to advance the error checking loop.
%  cycle - final value of cyclecnt.  Used by parent program.
%  tmpB -  temporary column vector of corrupted data.
%  rawdata -  raw data matrix used by parent program.

rawdata = [];
cycle = 0;

fid = fopen(fname,'r');
fstr = fscanf(fid,'%s',1);

while strcmp(fstr,'Rot') == 0,
   fstr = fscanf(fid,'%s',1);
end;



%  Proceeds through each line of the raw data file and modifies
any
%  which are corrupted.  Stores each line in tmp before adding
to A.

check = 0;
tmpA = [];
tmpA = fscanf(fid1, '%f %f %f %f %f %f %f %f %f %f %f %f', [12
Inf]);
sizetmpA = size(tmpA);
cyclecnt=0;

for check = 1:sizetmpA(2),
   end_chk = 1;
   while end_chk == 1
      if rem(tmpA(1,check),1) == 0,
         cycle = cyclecnt;
         end_chk = 0;
      else
```

```
            tmpB = tmpA(:,check);
            tmpA(1:2,check) = tmpB(11:12);
            tmpA(3:12,check) = tmpB(1:10);
            cyclecnt = cyclecnt+1;
        end;
    end;
end;

rawdata = tmpA;


%
%  End routine
%
```

A5.6 Discrete Analysis Software – Discrete_yvdot.m

```
% ============================================================
% Name: discrete_yvdot.m
% Descr:   Discrete Analysis Method
%     To be used for the analysis of pure sway dynamic data.
%     Dimensional force values will be returned.
%     imp_filt is zero for no filter else it is the cutoff
%     frequency.
%
================================================================

function [yvdot]=discrete_yvdot(data,ft,td,fs,amp);


% Implement discrete analysis technique
% =====================================
           i=0;
           svdot=0;
           n=0;
      f_yvdot=0.0;
      wt=2*pi*ft;

           while svdot<=length(data),
           n=n+1;
         svdot=round(fs*((pi+2*(n-1)*pi)/(2*wt)-td)+1);
         if (svdot>0)&(svdot<=length(data)),
                 i=i+1;
              f_yvdot(i)=data(svdot);
         end;
      end;
      yvdot=-mean(abs(f_yvdot))/(amp*wt^2);
%=========================================================
%===   End function
%=========================================================
```

A5.7 Fourier Integration Analysis Software – Fourint_yvdot.m

```
% ====================================================
% === Function name:   fourint_yvdot.m
% === Author:          Brendon Anderson
% === Purpose:   Pmm data analysis routine
% === Fourier Integration used to determine acceleration
coefficient
% === in phase components of the force
% === Child:           DefInt.m
%====================================================

function [Yvdot]=fourint_yvdot(ft, fs, td, Y, amp);

% Define the linear fourier coefficients
% ======================================
      s=length(Y);
      t=[0:1/fs:(s-1)/fs]';
      angle=(2*pi*ft*(t+td));
      YIn=Y.*sin(angle);

% Define the number of complete cycles in the data vector
      n=s*ft/fs;
      b=2*ft/n*defint(YIn,1/fs);
      Yvdot=-b/((2*pi*ft)^2*amp);

% End function
```

A5.8 Switch Integration Analysis Software – Switint_yvdot.m

```
% ========================================================
% === Function name:   switInt_yvdot.m
% ========================================================

function [yvdot]=switint_yvdot(ft,fs,td,amp,Ynoise);


% Perform switched integration
% ============================

           YIn=0.0;
           n=0;
           sv1=0;
           sv2=0;
           p=0;
      wt=2*pi*ft;

 % Determine the inphase component of the force

           while sv2<length(Ynoise),
          n=n+1;
          if n==1,
             sv1=1;
          else
               sv1=sv2+1;
            end;
          sv2=round(fs*(n*pi/wt-td));
          if (sv1>0)&(sv2<length(Ynoise)),
                p=p+1;
                ts=(sv2+sv1)/(2*fs);
                angle=(2*pi*ft*(ts+td));
             if rem(angle,2*pi)<=pi,
                YIn=YIn+defint(Ynoise(sv1:sv2),1/fs);
             else
                YIn=YIn-defint(Ynoise(sv1:sv2),1/fs);
```

```
                end;
            end;
        end;

            YIn=wt*YIn/p;
            yvdot=-YIn/(2*wt^2*amp);

% End function
```

A5.9 Systems Identification Analysis Software – Si_yvdot.m

```
% ========================================================
% === Function name: si_yvdot
% ========================================================

function [yvdot]=si_yvdot(Ynoise,vel,acc);

%
% Define the input vectors for the regression algorithm
%
           In1=acc;
           In2=vel;
           In3=vel.*abs(vel);
           In4=vel.*vel.*vel;

%
% Perform the regression, 'av'
%
           av=[1 1 1 0];
      c1=av(1); c2=av(2); c3=av(3); c4=av(4);
      z=[Ynoise In1 In2 In3 In4];
           th=arx(z,[0 c1 c2 c3 c4 0 0 0 0]);

%
% Analyse the output
%
     s=find(av);
           for i=1:4,
           if i<=s(1) d(i)=1;
           else d(i)=d(i-1)+av(i);
           end;
           end;

           fprintf('%8.4f %s',c1*th(3,d(1)),',  ')
           fprintf('%8.4f %s',sqrt(c1*th(3+d(1),d(1))),',  ')
           fprintf('%8.4f %s',c2*th(3,d(2)),',  ')
```

```
            fprintf('%8.4f %s',sqrt(c2*th(3+d(2),d(2))),',  ')
            fprintf('%8.4f %s',c3*th(3,d(3)),',  ')
            fprintf('%8.4f %s',sqrt(c3*th(3+d(3),d(3))),',  ')
            fprintf('%8.4f %s',c4*th(3,d(4)),',  ')
            fprintf('%8.4f %s',sqrt(c4*th(3+d(4),d(4))),',  ')
            fprintf('%10.8f\n',th(1,d(1)))

            yvdot=c1*th(3,d(1));
%=============================================
%== End function
%=============================================
```

A5.10 Data Generation Software – Sway_data_gen.m

```
% ================================================
% Function: sway_data_gen.m
% Description: Function generates PMM data to test
% analysis routines.
%
% ================================================

%function [output]=sway_data_gen(amplitude,...
%sample_rate,frequency,Yo,Yvdot,Yv,Yvmvm,Yvvv);

% Define variables
frequency=0.2;
amplitude=0.14;
sample_rate=30.00;

% Define mathematical model

Yvdot=-10; Yv=-1000; Yvmvm=-10; Yvvv=0; Yo=0;

% Define motions
no_cycles=5;
t=[0:1/sample_rate:no_cycles/frequency]';
wt=2*pi*frequency;
vel=amplitude*wt*cos(wt*t);
acc=-amplitude*wt^2*sin(wt*t);

% Define measurement noise -
% Normal distribution: mean 0, var 1
randn('seed',0);
%noise=randn(length(t),1);
level1=sqrt(Yv^2+Yvmvm^2+Yvvv^2)*amplitude*wt*0.5;
level2=Yvdot*amplitude*wt^2*0.5;
noise1=level1*cos(2*pi*2*t);
noise2=level2*sin(2*pi*2*t);
```

```
%Define output vector
Y=Yo.*ones(length(t),1) + Yvdot*acc + Yv*vel +
Yvmvm*vel.*abs(vel)...
   + Yvvv*vel.^3;
Ynoise=Y+level1*noise1+level2*noise2;

% FFT of data
pts=2^17;
Yfft=fft(Ynoise,pts);
Syy=Yfft.*conj(Yfft)/pts;
f=sample_rate*(0:(pts/2-1))/pts;
%figure;
%plot(f(1:2000),Syy(1:2000));
%figure;
%plot(f(1:pts/2),Syy(1:pts/2));

output=Y;
%figure;
%plot(t,Ynoise,'k',t,Y,'r');
%grid on;
%xlabel('Time (s)');
%ylabel('Force (N)');

%Fourier integration
delay=0;
est_yvdot_fourint=fourint_yvdot(frequency,sample_rate,delay,Ynoi
se,amplitude)
est_yvdot_si=si_yvdot(Ynoise,vel,acc)
est_yvdot_switint=switint_yvdot(frequency,sample_rate,delay,ampl
itude,Ynoise)
est_yvdot_discrete=discrete_yvdot(Ynoise,frequency,delay,sample_
rate,amplitude)


%end;
```

A5.11 Integration Routine – Defint.m

```
% ============================================================
% === Function name:   defint.m
% === Purpose:    Integrate stored data using Simpson's Rule
% ============================================================

 function [Out]=defint(X,h);

      ns=length(X);
   yn=0.0;
   yn1=0.0;


% The method requires an even number of panels for the method to
work.
% Truncate the last point if there are even numbers of points.

      if ( rem((ns-1),2) ~= 0 )
           ns=ns-1;
      end;

      for i=1:2:ns-2,
           yn1=yn+h/3*((X(i))+4*(X(i+1))+(X(i+2)));
           yn=yn1;
      end;

   Out=yn1;


% End function defint
```

Appendix 6.

A6.1 Raw Static Measurements

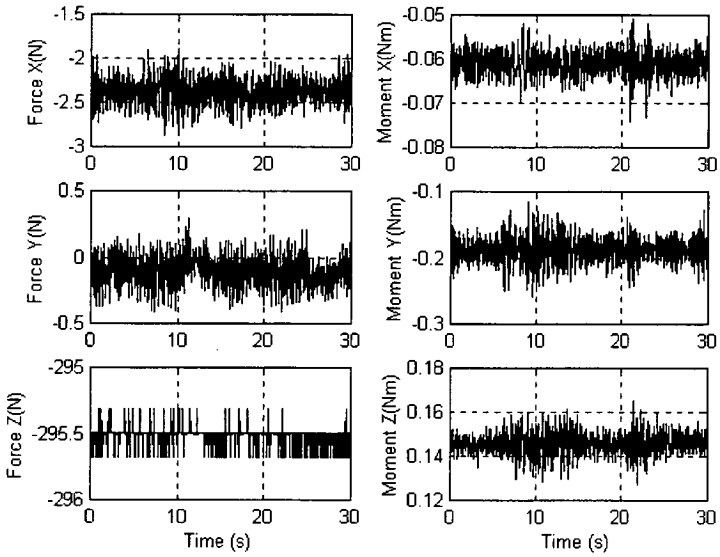

Figure A6.1.1 AME PMM Result file: PAPA2404.003. Raw Measurement Data – zero flow velocity, no model motion.

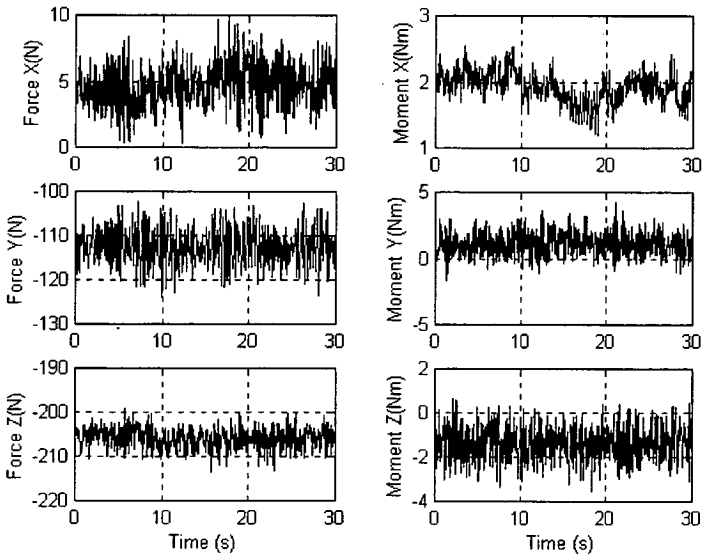

Figure A6.1.2 AME Result File: PAPA2404.057. Static drift angle of -45°.

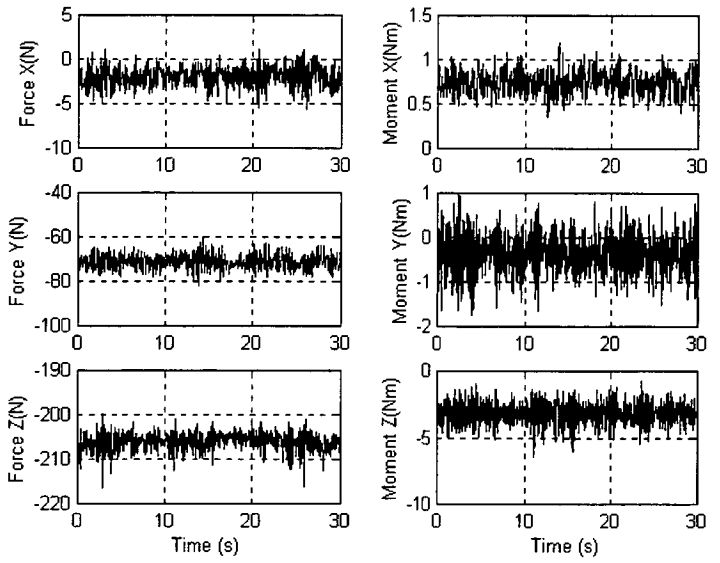

Figure A6.1.3 AME PMM Result File: PAPA2404.058. Static drift angle of -30°.

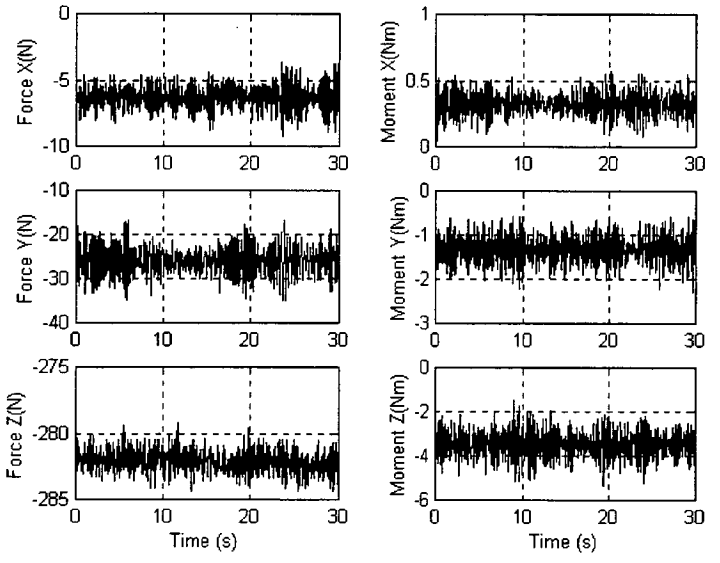

Figure A6.1.4 AME PMM Result File: PAPA2404.060. Static drift angle of -15°.

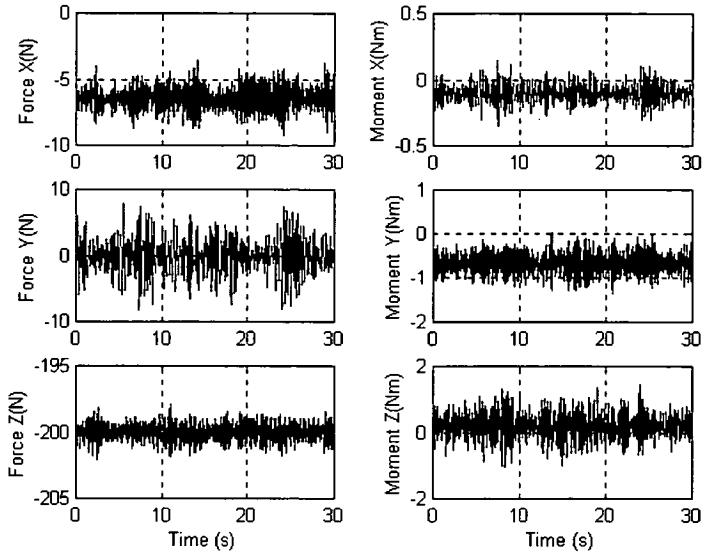

Figure A6.1.5 AME PMM Result File: PAPA2404.063. Static drift angle of 0°.

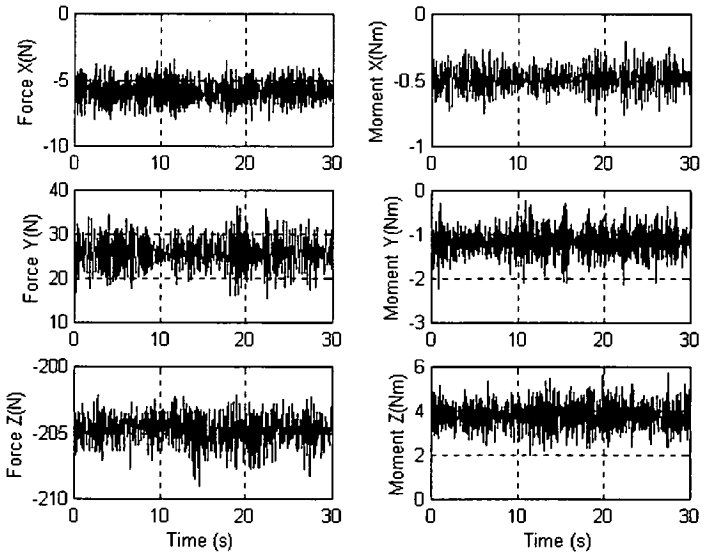

Figure A6.1.6 AME PMM Result File: PAPA2404.066. Static drift angle of 15°.

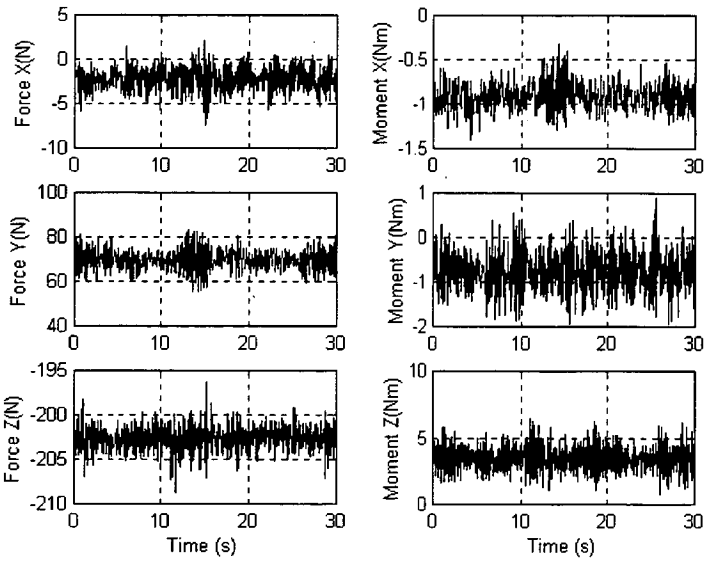

Figure A6.1.7 AME PMM Result File: PAPA2404.068. Static drift angle of 30°.

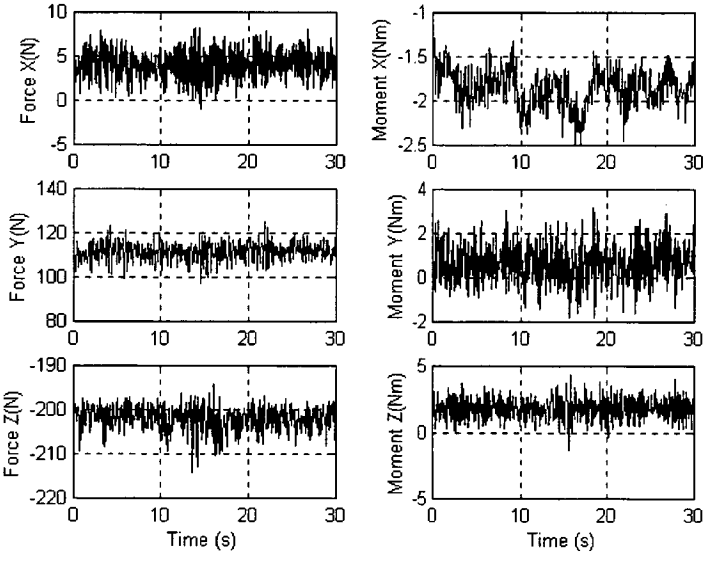

Figure A6.1.8 AME PMM Result File: PAPA2404.69. Static drift angle of 45°.

A6.2 Dynamic Test Results

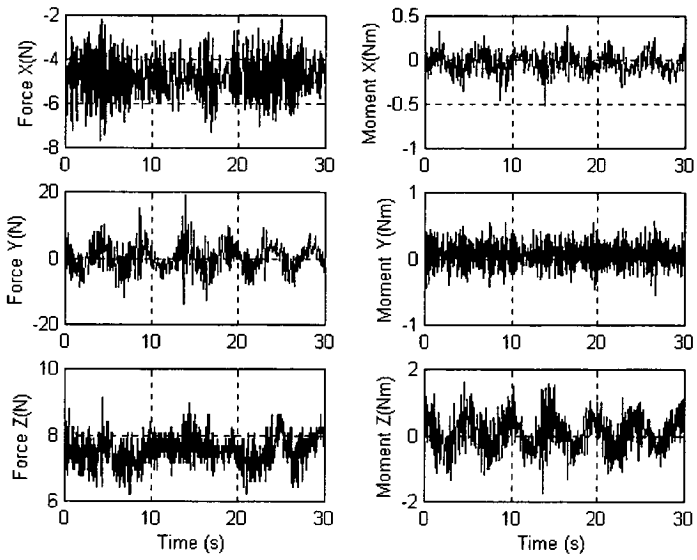

Figure A6.2. 1 AME PMM Result file: PAPA2404.004. Nominal frequency 0.20Hz and amplitude 0.02m.

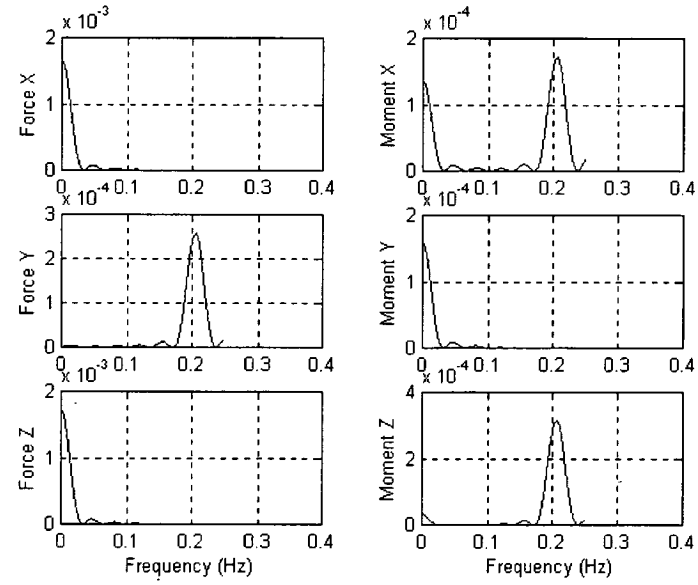

Figure A6.2.2 AME PMM Result file: PAPA2404.004. Frequency response of the six measured load components; nominal frequency 0.20Hz and amplitude 0.02m.

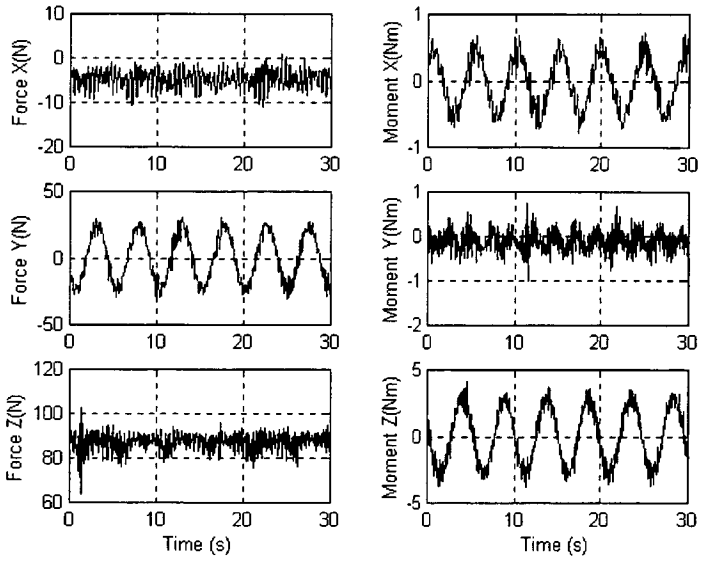

Figure A6.2.3 AME PMM Result file: PAPA2404.010. Nominal frequency 0.20Hz and amplitude 0.14m.

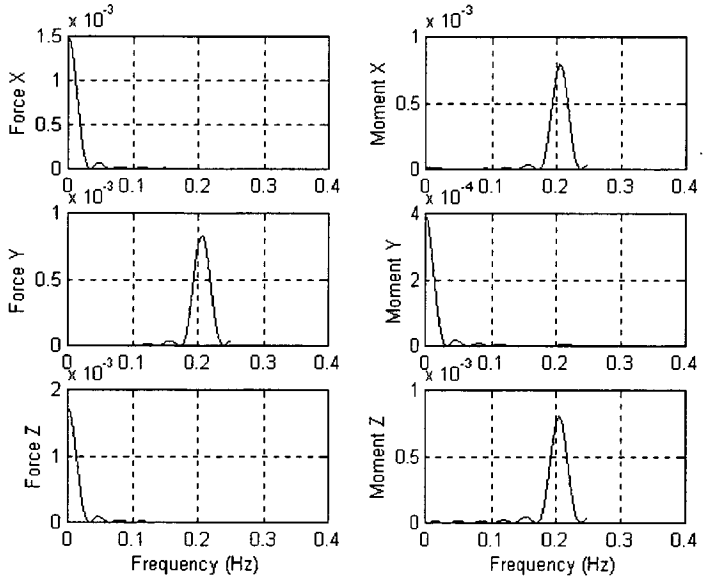

Figure A6.2.4 AME PMM Result file: PAPA2404.010. Frequency response of the six measured load components; nominal frequency 0.20Hz and amplitude 0.14m.

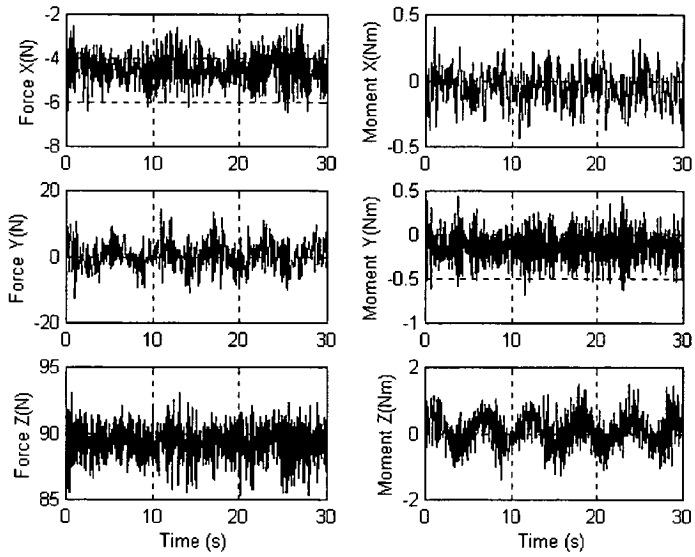

Figure A6.2.5 AME PMM Result file: PAPA2404.017. Nominal frequency 0.16Hz and amplitude 0.02m.

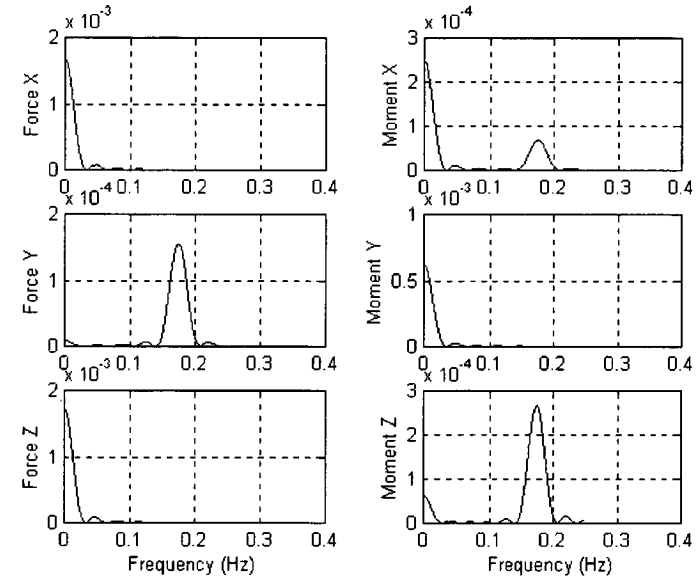

Figure A6.2.6 AME PMM Result file: PAPA2404.017. Frequency response of the six measured load components; nominal frequency 0.16Hz and amplitude 0.02m.

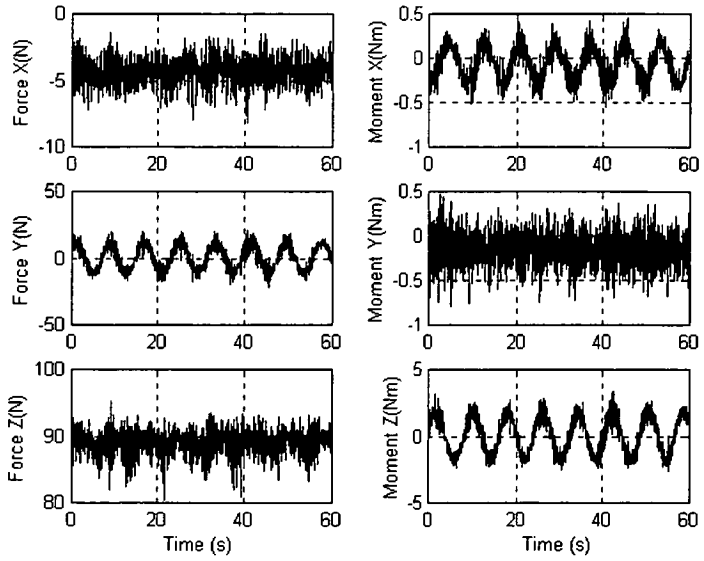

Figure A6.2.7 AME PMM Result file: PAPA2404.018. Nominal frequency 0.12Hz and amplitude 0.14m.

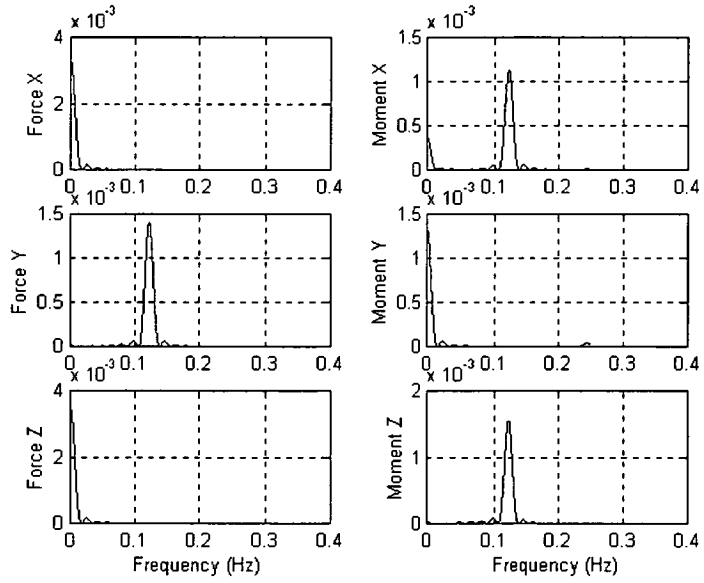

Figure A6.2.8 AME PMM Result file: PAPA2404.018. Frequency response of the six measured load components; nominal frequency 0.12Hz and amplitude 0.14m.

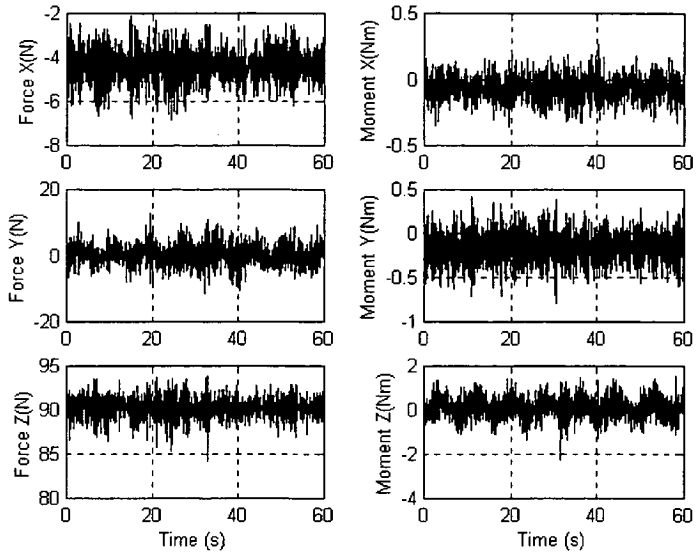

Figure A6.2.9 AME PMM Result file: PAPA2404.024. Nominal frequency 0.12Hz and amplitude 0.02m.

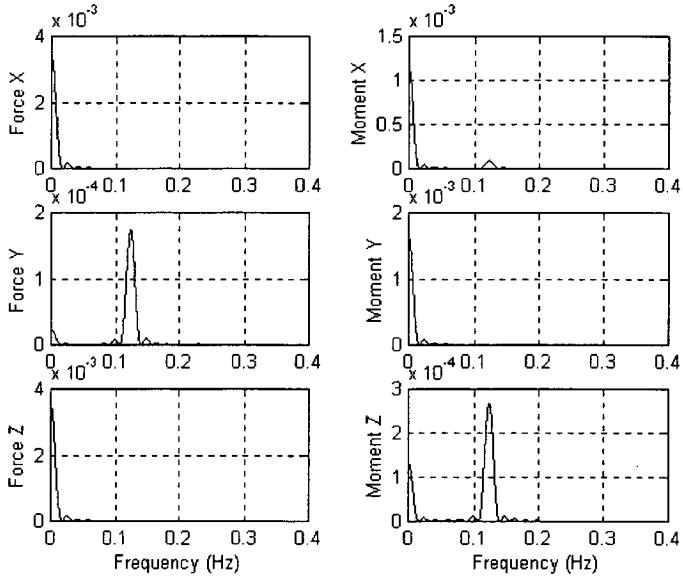

Figure A6.2.10 AME PMM Result file: PAPA2404.024. Frequency response of the six measured load components; nominal frequency 0.12Hz and amplitude 0.02m.

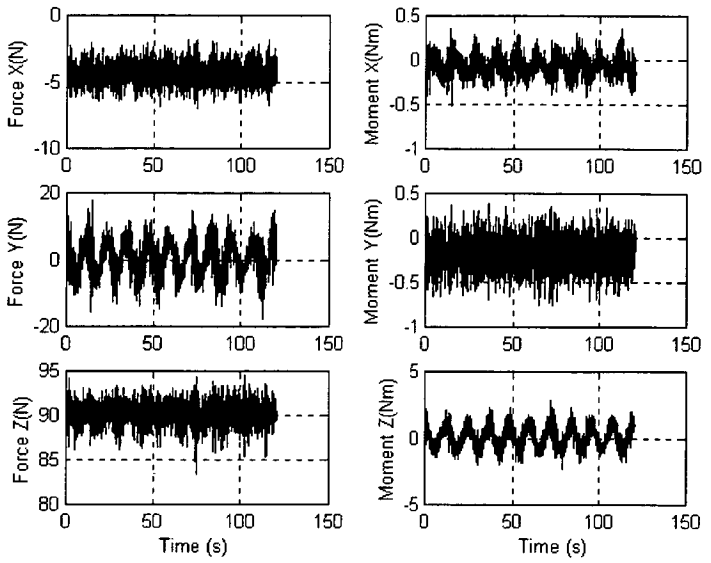

Figure A6.2.11 AME PMM Result file: PAPA2404.027. Nominal frequency 0.08Hz and amplitude 0.10m.

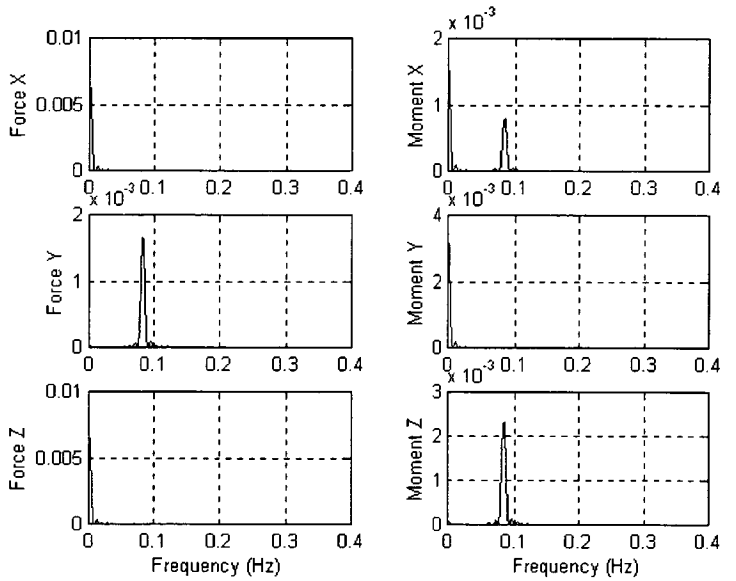

Figure A6.2.12 AME PMM Result file: PAPA2404.027. Frequency response of the six measured load components; nominal frequency 0.08Hz and amplitude 0.10m.

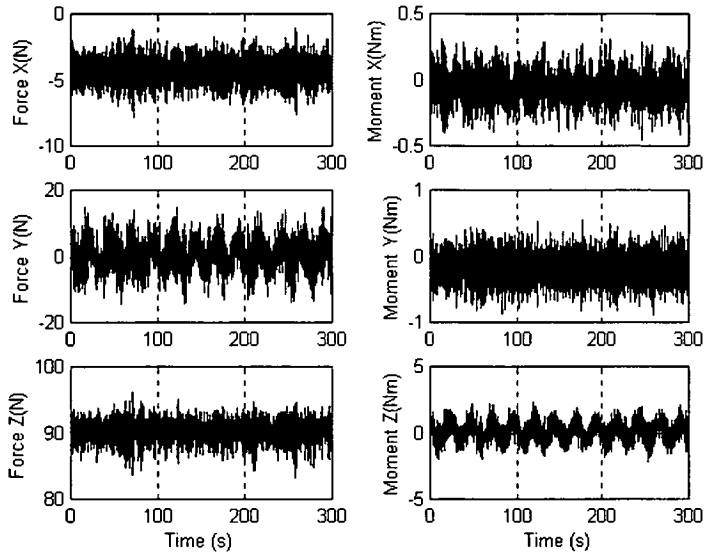

Figure A6.2.13 AME PMM Result file: PAPA2404.029. Nominal frequency 0.04Hz and amplitude 0.14m.

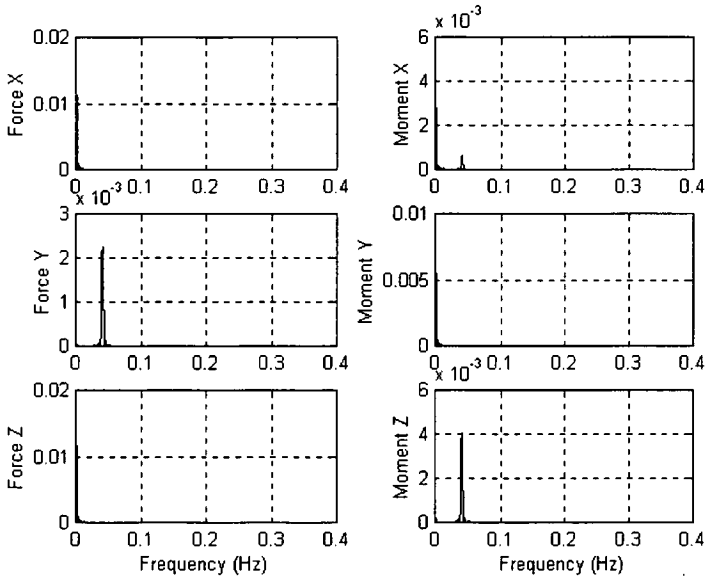

Figure A6.2.14 AME PMM Result file: PAPA2404.029. Frequency response of the six measured load components; nominal frequency 0.04Hz and amplitude 0.14m.

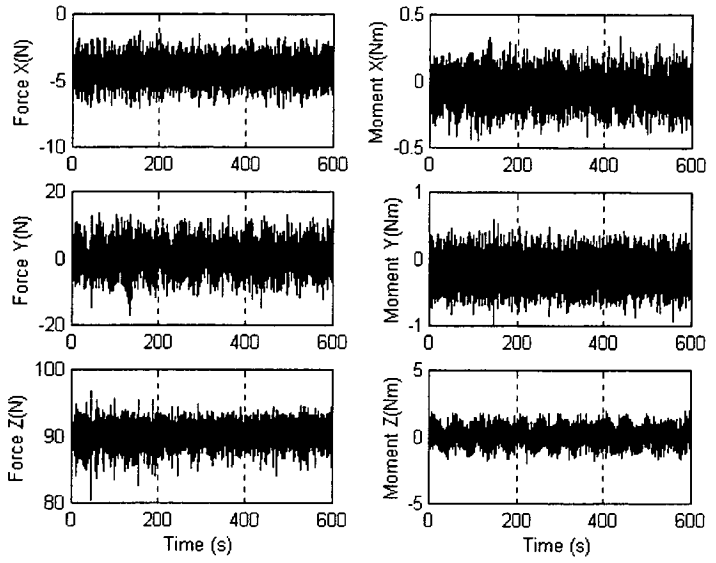

Figure A6.2.15 AME PMM Result file: PAPA2404.030. Nominal frequency 0.02Hz and amplitude 0.14m.

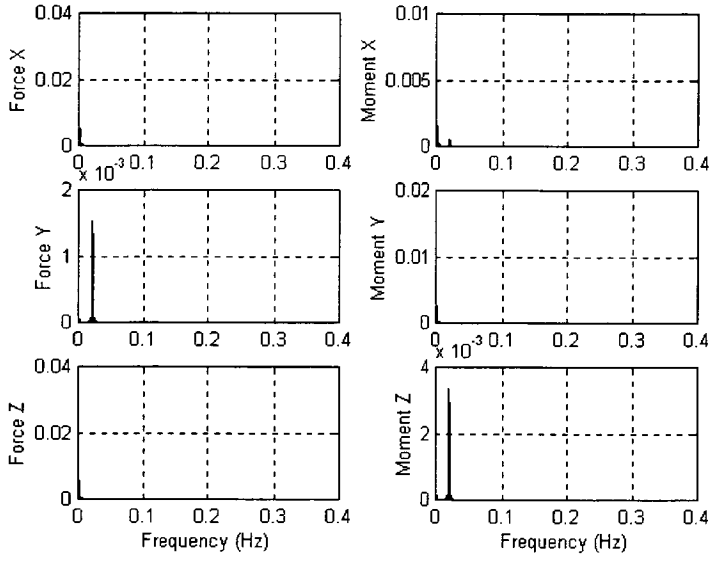

Figure A6.2.16 AME PMM Result file: PAPA2404.030. Frequency response of the six measured load components; nominal frequency 0.02Hz and amplitude 0.14m.

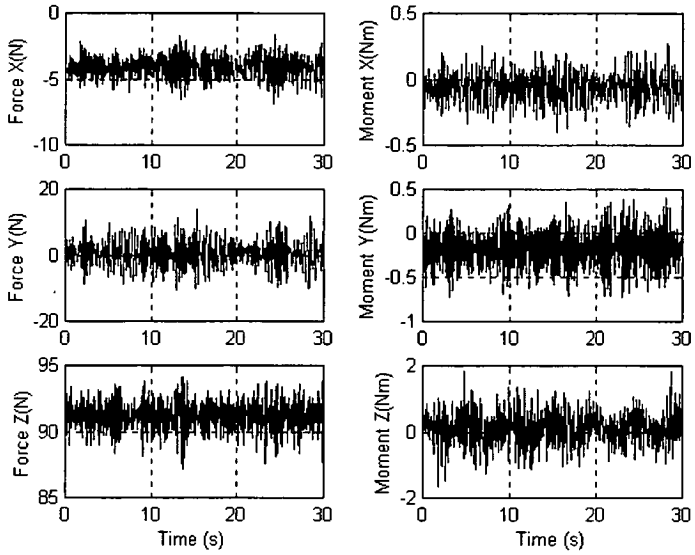

Figure A6.2.17 AME PMM Result file: PAPA2404.039. Nominal frequency 0.2Hz and amplitude 0.02radians.

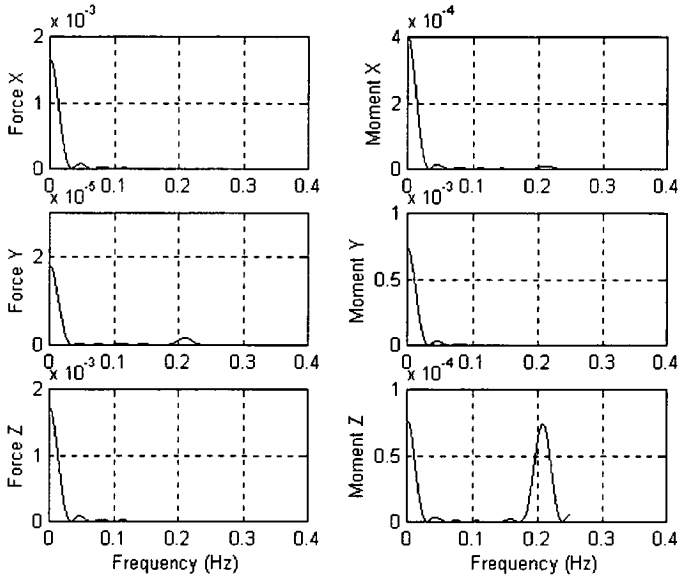

Figure A6.2.18 AME PMM Result file: PAPA2404.039. Frequency response of the six measured load components; nominal frequency 0.2Hz and amplitude 0.02radians.

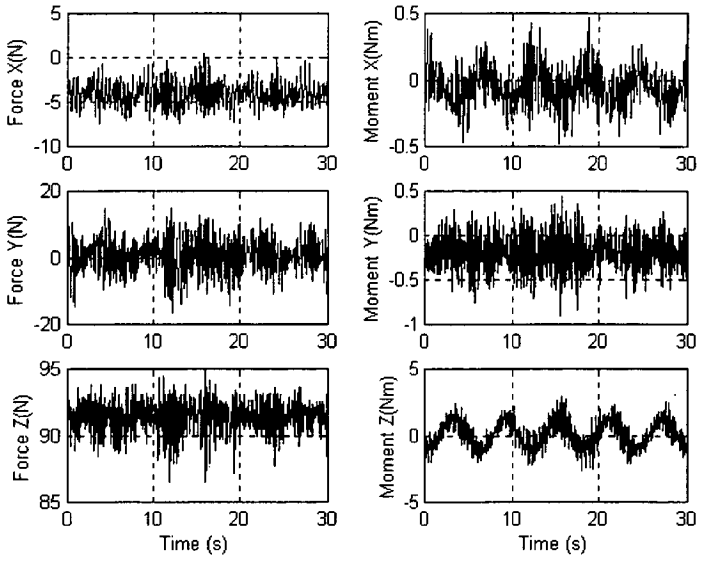

Figure A6.2.19 AME PMM Result file: PAPA2404.040. Nominal frequency 0.16Hz and amplitude 0.15radians.

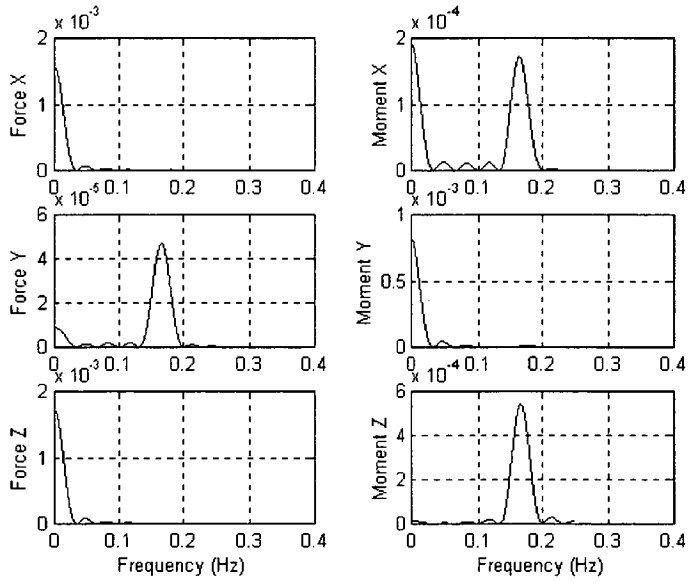

Figure A6.2.20 AME PMM Result file: PAPA2404.040. Frequency response of the six measured load components; nominal frequency 0.16Hz and amplitude 0.15radians.

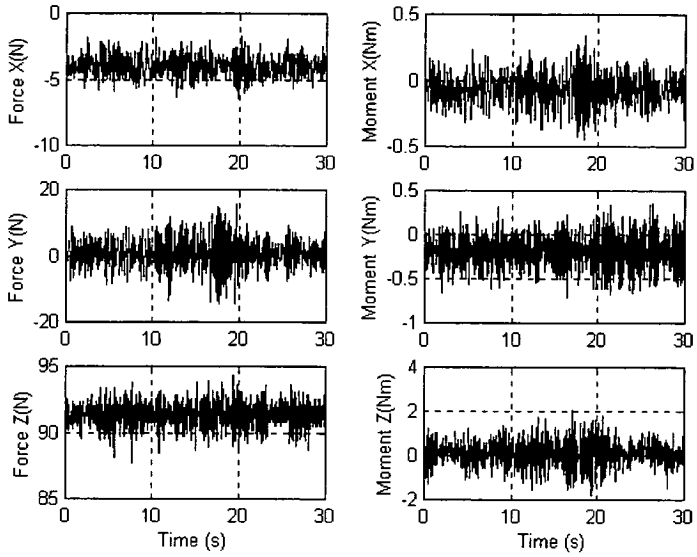

Figure A6.2.21 AME PMM Result file: PAPA2404.047. Nominal frequency 0.16Hz and amplitude 0.02radians.

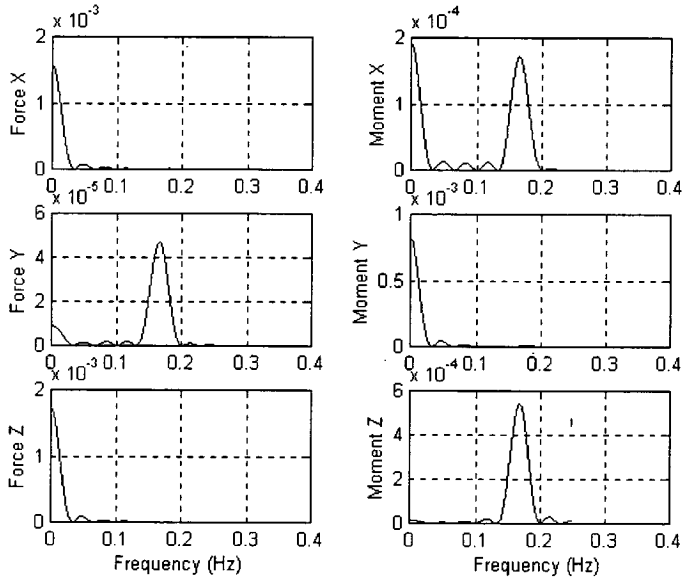

Figure A6.2.22 AME PMM Result file: PAPA2404.047. Frequency response of the six measured load components; nominal frequency 0.16Hz and amplitude 0.02radians.

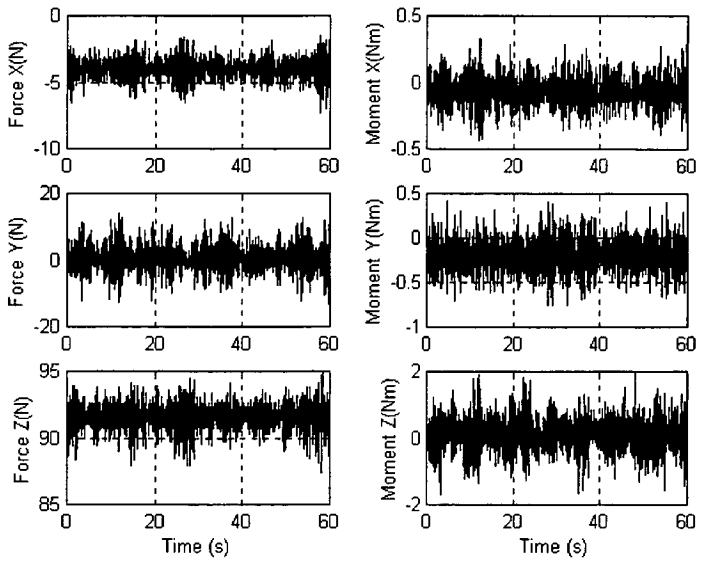

Figure A6.2.23 AME PMM Result file: PAPA2404.053. Nominal frequency 0.12Hz and amplitude 0.02radians.

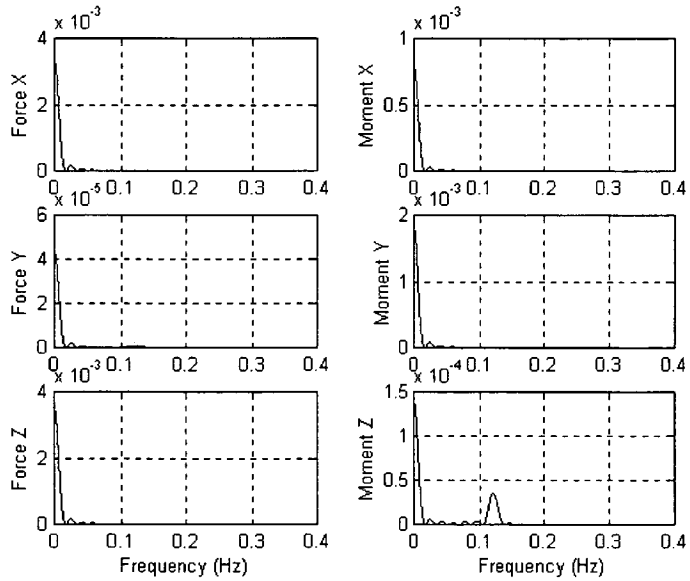

Figure A6.2.24 AME PMM Result file: PAPA2404.053. Frequency response of the six measured load components; nominal frequency 0.12Hz and amplitude 0.02radians.

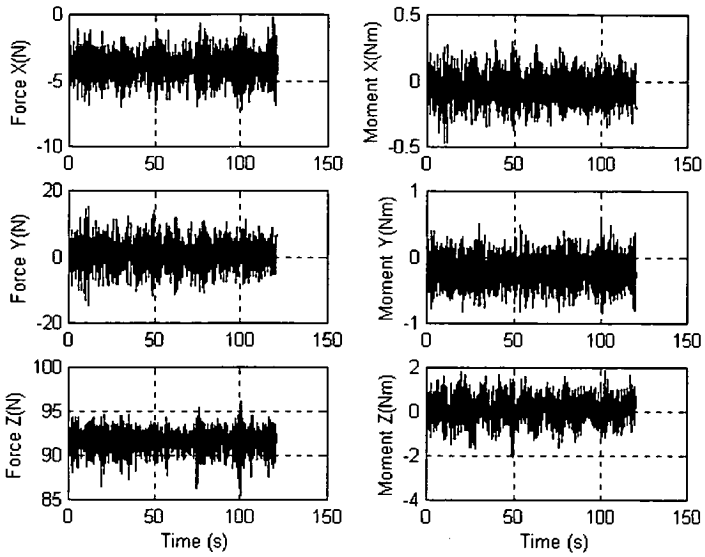

Figure A6.2.25 AME PMM Result file: PAPA2404.054. Nominal frequency 0.08Hz and amplitude 0.07radians.

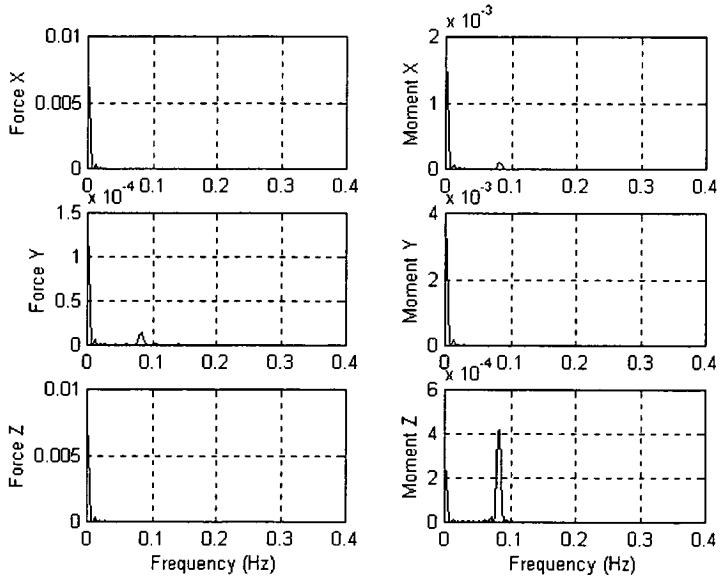

Figure A6.2.26 AME PMM Result file: PAPA2404.054. Frequency response of the six measured load components; nominal frequency 0.08Hz and amplitude 0.07radians.

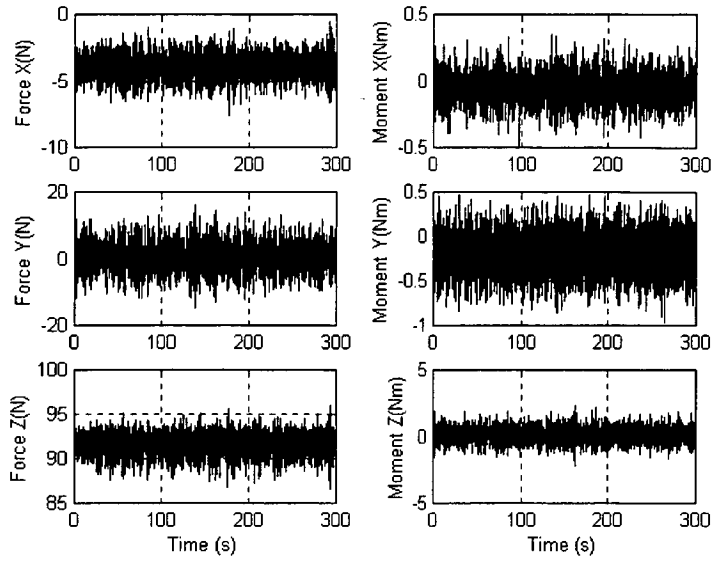

Figure A6.2.27 AME PMM Result file: PAPA2404.055. Nominal frequency 0.04Hz and amplitude 0.03radians.

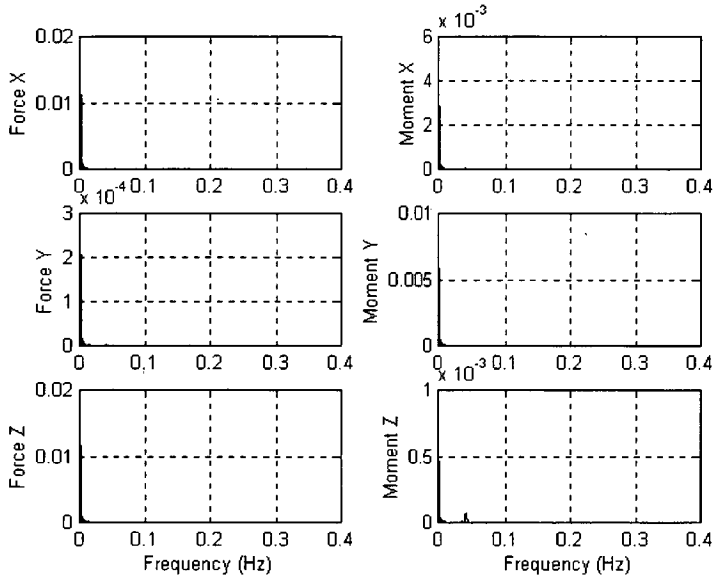

Figure A6.2.28 AME PMM Result file: PAPA2404.055. Frequency response of the six measured load components; nominal frequency 0.04Hz and amplitude 0.03radians.

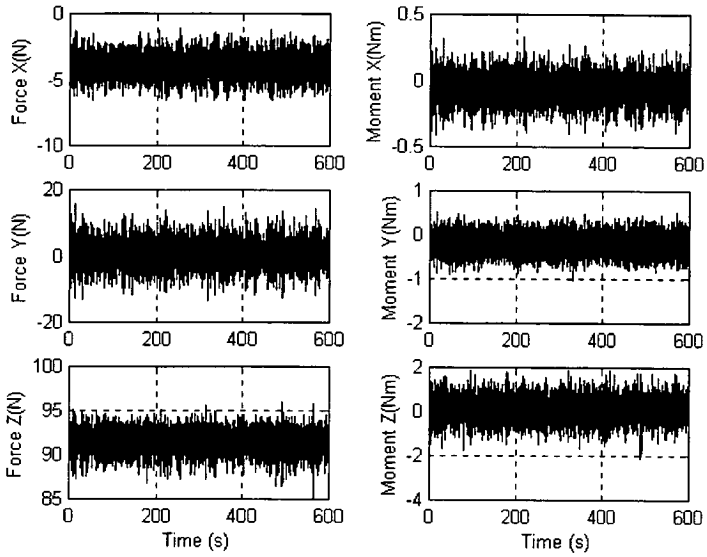

Figure A6.2.29 AME PMM Result file: PAPA2404.056. Nominal frequency 0.02Hz and amplitude 0.01radians.

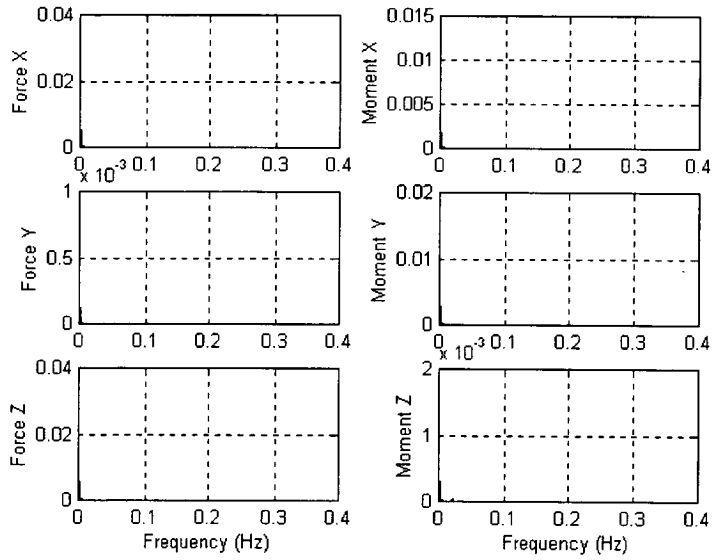

Figure A6.2.30 AME PMM Result file: PAPA2404.056. Frequency response of the six measured load components; nominal frequency 0.02Hz and amplitude 0.01radians.